Forward and Inverse Problems in Microwave Remote Sensing of Objects in Complex Media

by

Yan Zhang

B.S. Electrical Engineering
Tsinghua University, Beijing, P.R. China (1985)
M.S. Electrical Engineering
Tsinghua University, Beijing, P.R. China (1987)
M.A. Physics
The City University of New York (1993)

Submitted to the Department of Electrical Engineering and Computer Science
in partial fulfillment of the requirements for the degree of

Doctor of Philosophy

at the

MASSACHUSETTS INSTITUTE OF TECHNOLOGY

November 1999

Author ....
Department of Electrical Engineering and Computer Science
November 5, 1999

Certified by...... ....
Professor Jin Au Kong
Thesis Supervisor

Certified by......... ....
Dr. Y. Eric Yang
Thesis Supervisor

Accepted by ....
Professor Arthur C. Smith
Chairman, Department Committee on Graduate Students

Forward and Inverse Problems in Microwave Remote Sensing of Objects in Complex Media

by

Yan Zhang

Submitted to the Department of Electrical Engineering and Computer Science
on November 5, 1999, in partial fulfillment of the
requirements for the degree of
Doctor of Philosophy

Abstract

In this thesis, hybrid numerical and analytical methods are developed for solving forward and inverse microwave remote sensing problems. The primary motivation for using hybrid methods is that many electromagnetic scattering problems cannot be solved based on purely analytical or numerical approaches because of the complexity of the problems and limitations of computer resources. Three electromagnetic problems solved by using hybrid methods are analyzed. First, an electromagnetic model is developed to calculate the radar cross section of a conducting object on a rough surface by combining the method of moments (MoM) and the small perturbation method (SPM). Second, the thermal emission of foam-covered rough ocean surface with the consideration of atmospheric emission and attenuation is investigated by using the radiative transfer theory (RT). Finally, the electromagnetic inverse problem for a plasma medium based on the Gel'fand-Levitan-Marchenko (GLM) integral equation is solved numerically by matrix inversion.

The electromagnetic wave scattering models based on the method of moments (MoM) and small perturbation method (SPM) are developed for the microwave remote sensing of a perfectly conducting object on rough surface. The perfectly conducting object is constructed using planar triangular patches, and the basis functions are defined to yield current continuity and charge conservation and reduction of the order of singularity of the Green's function in the self-impedance matrix elements. The integral equations from Huygens' principle are expanded in terms of the rough surface height function, so that each equation with the same order of roughness is equivalent to one of an object on a flat surface with an equivalent source.

As an example of the application of hybrid numerical and analytical methods to passive microwave remote sensing, thermal emission from a wind-driven and foam-covered ocean surface is modeled and analyzed. The foam on the ocean surface is modeled as a layer of randomly distributed water bubbles. The radiative transfer (RT) theory is used to calculate the polarimetric brightness temperature from the foam and atmospheric layer, and the small perturbation method (SPM) is used to compute the scattered field from the ocean surface up to the second order. The numerical results from the composite model are validated by using measurement data.

In the last part of the thesis, a numerical method using matrix inversion is developed for solving the Gel'fand-Levitan-Marchenko (GLM) inverse scattering problem for an arbitrary reflection coefficient of an inhomogeneous plasma medium. A uniform electron density profile reconstructed from a closed form reflection coefficient is used to validate the numerical model. It is shown that the numerical method provides an accurate and efficient solution for the GLM inverse problem.

Thesis Supervisor: Jin Au Kong
Title: Professor of Electrical Engineering

Thesis Supervisor: Y. Eric Yang
Title: Research Scientist, MIT Research Laboratory of Electronics

Acknowledgments

First of all, I would like to express my sincerest thanks to Professor Kong for his continued support and guidance throughout my graduate research. It was his energetic and clear-as-crystal teaching that stimulated me to study and finally start to make my own contribution to the area of Electromagnetics.

I would like to thank Dr. Y. Eric Yang for his helpful advice, guidance, and concern throughout every stage of my research. Without his fruitful criticism and suggestions, this thesis would have never materialized.

I would also like to thank Professor David H. Staelin, my thesis reader, for his helpful suggestions.

Special thanks are extended to Dr. Arthur K. Jordan of the Naval Research Laboratory for his guidance and encouragement; to Dr. Tarek M. Habashy for his supervising and support during my summer internship at Schlumberger-Doll Research in 1996.

I also wish to thank my colleagues over the years for their friendship, Hong Tat Ewe, Chih-Chien Hsu, Joel Johnson, Kevin Li, John Oates, Sean Shih, Ali Tassoudji, Murat Veysoglu, Li-Fang Wang, Lars Bomholt, Kung-Hau Ding, Jean-Claude Souyris, Jerry Akerson, Nayon Tomsio, Chen-Pang Yeang, Makkalon Em, Fabio del Frate, Chi O. Ao, Henning Braunisch, Chris Moss, Peter Orondo, Bae-Ian Wu, and Ben Barrowes. Many thanks to Henning Braunisch for his moment method (MoM) code used in this thesis for comparison. The discussions in the group meetings, and the questions and suggestions in my seminars helped me to understand and solve problems in my research work. Our late secretary Kit Lai's kindness and help will never be forgotten.

Finally, I would like to thank my wife Jie (Jennifer) Sun for her love, patience, and support during my student life at MIT; to my children Jacob and Alicia, both of whom were born during my stay at MIT. They made my school life enjoyable.

Contents

List of Figures

Chapter 1

Introduction

Since the fundamental electromagnetic theory was established in the nineteenth century, the applications of microwave remote sensing in target detection, meteorology, and non-destructive profile reconstruction have been greatly developed. The microwave spectrum band is superior to others such as optics and infrared frequencies due to its capability to penetrate the atmosphere layer and more deeply into the earth terrain. However, with the increasing need to consider more complex structures and media in the microwave remote sensing applications, solving Maxwell's equations for the theoretical investigation becomes more difficult. Thus the motivation of this thesis is to develop hybrid/composite methods and increase the range of available numerical or analytical methods to solve more complicated microwave remote sensing problems, and accordingly to obtain a deeper understanding of the electromagnetic waves.

1.1 Review of Previous Work

Recently, there has been a great interest in studying the microwave scattering of an object situated near a rough surface [1]–[11]. The problem can be generalized to the electromagnetic wave scattering of local scatterers near a rough surface from which a better understanding of how the presence of the rough surface affects the direct scattering from the object can be obtained. The model was applied to radar detection and identification of targets near the ground and water surfaces [12].

Electromagnetic wave scattering by arbitrarily shaped objects in free space has been studied by many researchers. Wire mesh was first used to construct a conducting object [13]. The wire mesh method is however not suited for calculate the near field, surface current distribution, and input impedance because of the presence of fictitious loop currents in the solution, ill-conditioned impedance matrix, and resonant problems [14, 15]. Early work using surface mesh model to construct a conducting object can be found in [16]–[22]. In 1982, Rao developed a triangular patch model to construct an arbitrarily shaped object in free space [23] and solved the electric field integral equation (EFIE) using the method of moments to obtain object surface current and scattering field. For numerical purposes, the surface of object is discretized using planar triangular patches. A set of subdomain-type basis functions is defined on pairs of adjacent triangular patches which yields a current representation free of line and point charges at subdomain boundaries.

The theory and numerical approaches associated with a conducting object near the interface of a layered medium is significantly more difficult than the free space problems because the Green's function in the integral equation involves Sommerfeld integrals. Only when the surface is perfectly conducting, can the Sommerfeld integral be evaluated in a closed form. In the past, problems with a simple 2-D object in half space with flat interface have been studied by some researchers. A simple conducting strip residing on a planar interface between two homogeneous half space media was analyzed by Butler [24]. In his study, it was shown that the kernel in the integral equation for the induced current is in general a Sommerfeld-type integral, and can be expressed in closed form when the permeabilities of the two media are the same. However this simplification of kernel integral cannot be obtained for the 3-D problem with a dielectric interface. Later Butler et al. [25]–[27] used a similar method to calculate the induced current on an infinitely long perfectly conducting cylinder located near a planar interface between two homogeneous half space media. It was shown that the choices of the Sommerfeld-type integral are not unique, and that they affect the efficiency of evaluation, as was also discovered later by Michalski et al. [28, 29]. Using a similar Green's function approach, Cottis et al. [11] considered the problem of electromagnetic scattering from 2-D infinitely long conducting cylinders located above the ground. The unknown surface current on the conducting cylinder is determined by solving the integral equation using MoM and the scattering field is calculated using the steepest descent method of integration. A solution for the 2-D problem of an infinitely long circular cylinder buried in a lossy half space was also obtained by Mahmoud [30], who used an iterative scheme and derived the scattered field as the contribution of induced multipole line sources located at the cylinder's axis. Both the dielectric and conducting cylinder can be treated using this scheme, however it is difficult to apply the scheme to a cylinder with arbitrary cross section. Other works concerning 2-D scattering from infinitely long cylinder can be found in [31, 32].

The consideration of a rough surface for the interface is a new challenge. Previously, the problem of scattering from a conducting cylinder above a lossy medium with a sinusoidal profile interface was studied by Vazouras et.al. [33] using an integral equation approach with the extended boundary condition method. Since the rough surface is specified to be sinusoidal, the unknown expansion coefficients in the integral equation are deterministic and can be solved using MoM. O'Neill et al. [7] applied standard integral equation methods for 2-D perfectly conducting object near rough surface of an isotropic lossy dielectric, and performed Monte Carlo simulation for a selection of ensembles of rough surface profiles. Tsang et al. [34] used a similar method to calculate the scattering field from a 2-D conducting object buried under a random rough surface and investigated the memory effect of the angular correlation function of scattering. Ripoll et al. [35] used the 2-D model to study the effect on the angular distribution of mean far-field intensity due to the presence of an arbitrary body located over a random rough surface. All these approaches are based on the method of moments and need to sample the unknowns on the rough surface. Therefore in the above works, only a two dimensional object has been investigated in order to speed up the computation. The finite difference time domain (FDTD) method has been used to compute the scattering from 3-D objects embedded in a homogeneous medium with a rough surface [36, 37]. The boundary finite element method was also used to calculate the scattering field from an object buried under a rough interface by Saillard et al. [38]. However, the FDTD and finite element methods cannot improve the efficiency of computation, especially when the statistics of the scattering field for the randomly rough surface is to be computed. In the latter case, the Monte Carlo simulation must be performed.

In this thesis, we develop a hybrid technique which combines the method of moments (MoM) for 3-D object and small perturbation method (SPM) for the rough surface. Numerically, only the surface currents on the object need to be solved. This leads to a much higher computational efficiency.

In the microwave remote sensing of ocean surface, the use of polarimetric passive techniques, originally proposed in [39], has shown potential for enhancing the retrieval of wind speed and directions [40]. The recent theoretical and experimental research activities have concentrated on studies of polarimetric thermal emissions regarding the anisotropic ocean surface by assuming a smoothly varying surface profile [40, 41]. However, under high wind conditions, the presence of breaking water waves, foam patches and water bubbles will significantly affect the polarimetric brightness temperatures of the open ocean surface. The significance of foam on the ocean surface was recognized a long time ago [42], and several subsequent experiments performed have verified its importance [43, 44]. The previous studies of the foam contribution to the emissivity of ocean surface were based on empirical formulations [45, 46] derived from experimental data. Although several attempts at modeling the foam theoretically have been presented [47, 48], it is difficult to incorporate them with rough ocean surface.

This thesis presents a theoretical study of the polarimetric thermal emission from foam covered ocean surface based on a composite volume and rough surface scattering model using the radiative transfer theory. For the foam layer, the sea form is modeled as a layer contains randomly distributed thin-film water bubbles. The small perturbation method (SPM) is used for random rough ocean surface, where the bistatic scattering is calculated up to second order. The radiative transfer equations with a rough interface are solved using an iterative technique. Model predictions are compared with empirical expressions from [46] for the foam emissivity and with the WINDRAD measurement data [49].

The Gel'fand-Levitan-Marchenko (GLM) integral equation was derived from the one-dimensional Helmholtz wave equation for 1-D plasma-like inhomogeneous medium [50]. It has been shown by Gel'fand and Levitan that given the inverse Fourier transformation of the reflection coefficient, the kernel function in the GLM integral equation is unique, furthermore the profile of the medium can be determined. In previous work, analytical solutions for the GLM integral equation were obtained for reflection coefficients which are rational functions without zeroes [51]. To obtain a numerical solution to the GLM integral equation for a general reflection coefficient, an iterative technique has been used by Ge et al. [52]. A reasonable accuracy of the iterative solution can be achieved by setting low-error criteria with the tradeoff of computing efficiency. However the iterative solution is divergent for thick layers as shown in [52].

The GLM integral equation for electromagnetic inverse scattering problem was solved numerically using matrix inversion [53]. For the special case in which the reflection coefficient is a rational function, the numerical result has an excellent agreement with the analytic result. The algorithm can be applied to the GLM integral equation with general reflection coefficient for which the analytic solution to the GLM integral equation does not exist. The algorithm can also be used to the GLM inverse problem given the reflection coefficient from measurement data.

1.2 Overview of the Thesis

This thesis explores the method combining numerical and analytical approaches to solve electromagnetic remote sensing problems. The particular problems analyzed in this thesis are (1) the electromagnetic wave scattering by a perfectly conducting object on a rough surface; (2) polarimetric thermal emission by wind-driven and foam-covered ocean surface; and (3) electromagnetic inverse scattering method to reconstruct the electron density profile of a plasma medium.

In Chapter 2, first we discuss the method of moments to solve the electromagnetic scattering problem by a perfectly conducting body in free space using Rao's approach [23] where he used the electric field integral equation to set up the matrix equation and meshed the conducting object using planar triangular patches. The advantage of using the vector and scalar potential in the EFIE is the reduction of the order of singularity in the integrand, so that the impedance matrix can be accurately evaluated. We then employ the method to derive the vector and scalar potential (or Green's function) for our problem: a conducting object on a flat surface. The main purpose of the work in this chapter is to develop the zeroth order MoM solver (i.e. the MoM code for object on a flat surface) which can then be applied to the rough surface problem in Chapter 3, so that the interaction of the electromagnetic waves between the object and the flat surface can be easily understood.

In Chapter 3, the rough surface is introduced to the problem in Chapter 2. We examine the integral equation obtained by Huygens' principle, and expand the unbounded Green's function in Taylor series. We then group the terms in the order of the rough surface height and try to solve them separately. We find that the equations of each order represent the problem with flat surface and excited by an "equivalent source" on the mean surface. Under the assumption of small roughness, we solve the problem iteratively up to the first order and compare the result with the standard method of moments, in which the surface of the object as well as the rough surface are discretized. Comparing the hybrid method with the standard method of moments, we obtain a good agreement in addition to the much higher computational efficiency.

In Chapter 4, we use the radiation field of the "equivalent source" due to the rough surface derived in Chapter 3 to show the consistency of the scattered field by the traditional small perturbation method (SPM) for open rough surface. For the perfectly conducting rough surface, we show that the radiation field plus the reflection of the "equivalent source" on the mean surface is exactly the same as that from traditional SPM.

Chapter 5 studies the polarimetric brightness temperature of ocean surface under high-wind conditions. In this study, the emissions by foam and atmospheric layers are taken into account. The ocean surface is modeled as a composite rough surface with small and large scale waves. The small perturbation method up to second order is applied to model small-scale waves. Large-scale waves are considered by modulating the local polar angle and averaging the local brightness temperature weighted by the slope distribution. The foam layer is modeled using the radiative transfer (RT) theory by considering the foam as a layer with water bubbles. The atmospheric layer is also modeled using the RT theory by neglecting the scattering of the particles in the air. The absorption coefficient of atmosphere is calculated by using Liebe's millimeter wave propagation model (MPM) [54]. The atmospheric profiles, such as temperature, pressure and humidity, are obtained from the US Standard Atmosphere [55]. The couplings among the ocean surface, the foam, and the atmosphere are fully considered in the formulation. The interaction mechanism is illustrated by examining individual terms.

Chapter 6 demonstrates the numerical method of solving the GLM integral equation for the electromagnetic inverse problem to reconstruct the electron density profile of a plasma medium. The transient reflection coefficient and the kernel function in the GLM integral equation are discretized in space and time domains, hence the integral equation is transformed to a matrix equation. The solution for the matrix equation exhibits faster convergence, better accuracy, and less computation time in comparison with other numerical methods, such as the iterative scheme with relaxation [52, 56].

Chapter 7 summarizes the work presented in this thesis, highlights the most significant results, and suggests future work and directions for the research related to this thesis.

Chapter 2

Electromagnetic Wave Scattering by Object on a Flat Surface

2.1 Introduction

Before fast computers were available, the electromagnetic scattering by arbitrarily-shaped conducting object in free space could only be solved with a wire-grid model or only for some very simple and symmetrical geometries such as a body of revolution [57]–[62]. The wire-grid model for conducting surface was considered as the state-of-the-art approach before the nineteen-eighties. The current on the wires can be considered to be one-dimensional which is convenient for programming [13, 14]. However, the wire mesh model for the conducting surface fails when the near field has to be considered or the current on a patch cannot be simplified along the local wires [15]. Before it was able to consider the conducting body to be arbitrarily shaped, the problem of electromagnetic radiation and scattering from perfectly conducting bodies of revolution was studied as early as 1969 by Mautz and Harrington [57]. An integro-differential equation was obtained from the potential integrals plus boundary conditions on the body of revolution and a solution was obtained by the method of moments. Later Wilton and Mittra (1972) solved the electromagnetic scattering problem of two-dimensional cylindrical scatterers of arbitrary cross section for TM polarization [63]. Perhaps Wang and Papanicolopulos (1979) were the first to consider the arbitrary shape of conducting body using the planar triangle patches [64]. In their approach, the amplitude and phase of the current on these patches are calculated by the method of moments. However the basis functions they used in the integral equation finally resulted in an impedance matrix that depends on the incident field. By using special basis functions, Rao, Wilton and Glisson [23] combined the advantages of triangular patch modeling and the electric field integral equation (EFIE) to develop a simple and efficient numerical model to calculate the surface current on an arbitrary conducting body. The EFIE formulation is preferable to the magnetic field integral equation (MFIE) because the former can be applied to open bodies, whereas the MFIE can only be applied to closed surfaces [23]. However in the approach provided by Rao et al. [23], the conducting object is considered only in free space. If an infinite conducting flat surface is placed near the object and it is treated in the same way, Rao's method becomes infeasible due to the large number of patches.

In this chapter, we first consider the electromagnetic wave scattering by an arbitrary conducting body in free space, and then reconsider the problem by placing the object above a perfectly conducting flat surface. Starting from Huygens' principle, we derive the electric field integral equations to obtain the expression of scattered field in terms of vector and scalar potentials which reduces the order of singularity of the dyadic Green's function. In the rest of this chapter, by introducing the layered Green's function for a perfectly conducting half space, we reformulate the problem for an object above a perfectly conducting flat surface. The layered Green's function for vector and scalar potentials will be derived from the layered Green's function for the electric field.

2.2 Field Scattered by Object in Free Space

Consider an electric wave $\overline{E}_i(\bar{r})$ incident upon a perfectly conducting (PEC) object in free space as shown in Fig. (2-1). Based on Huygens' principle [65], the electromagnetic fields outside the surface take the following forms:

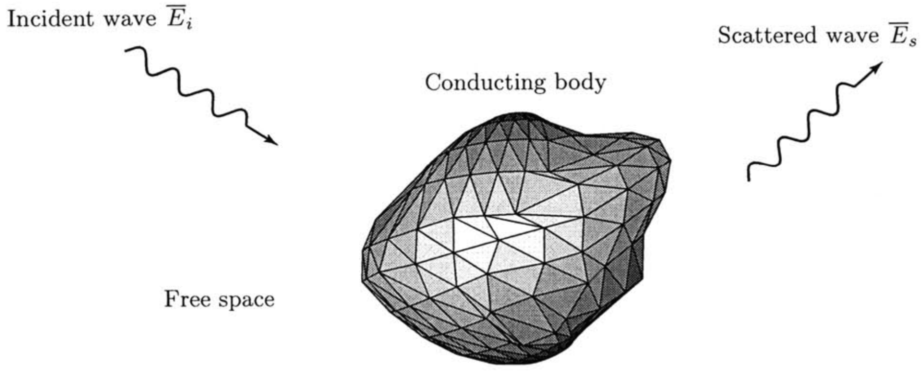

Figure 2-1: An electromagnetic wave incident upon an arbitrarily-shaped perfectly conducting (PEC) body in free space.

$$\begin{aligned}&\int_{S'} dS' \left\{ i\omega\mu_o \overline{\overline{G}}(\bar{r},\bar{r}')\cdot\left[\hat{n}(\bar{r}')\times\overline{H}(\bar{r}')\right] + \nabla\times\overline{\overline{G}}(\bar{r},\bar{r}')\cdot\left[\hat{n}(\bar{r}')\times\overline{E}(\bar{r}')\right]\right\}\\ &+\overline{E}_i(\bar{r}) = \overline{E}(\bar{r}),\end{aligned} \tag{2.1}$$

$$\begin{aligned}&\int_{S'} dS' \left\{ -i\omega\epsilon_o \overline{\overline{G}}(\bar{r},\bar{r}')\cdot\left[\hat{n}(\bar{r}')\times\overline{E}(\bar{r}')\right] + \nabla\times\overline{\overline{G}}(\bar{r},\bar{r}')\cdot\left[\hat{n}(\bar{r}')\times\overline{H}(\bar{r}')\right]\right\}\\ &+\overline{H}_i(\bar{r}) = \overline{H}(\bar{r}),\end{aligned} \tag{2.2}$$

where S' denotes the surface of the conducting object with normal vector $\hat{n}(\bar{r}')$, and $\overline{\overline{G}}(\bar{r},\bar{r}')$ is the Green's function in free space. Equation (2.1) is called the electric field integral equation (EFIE) and Equation (2.2) is called the magnetic field integral equation (MFIE). The MFIE [Eq. (2.2)] can be derived from the EFIE [Eq. (2.1)] by taking the curl on both sides of the EFIE, and using the Maxwell equations $\nabla \times \overline{E} = i\omega\mu\overline{H}$ and $\nabla \times \overline{H} = -i\omega\epsilon\overline{E}$. Since the tangential electric field on the surface of the conducting object is zero, i.e., $\hat{n}(\bar{r}') \times \overline{E}(\bar{r}') = 0$, the integral term that is referred to as the field $\overline{E}_s$ scattered by the object, can be written as

$$\overline{E}_s(\bar{r}) = \int_{S'} dS' \left\{ i\omega\mu_o \overline{\overline{G}}(\bar{r}, \bar{r}') \cdot \overline{J}_s(\bar{r}') \right\}, \tag{2.3}$$

where $\overline{J}_s(\bar{r}')$ is the induced surface current on the conducting object which can be written as $\overline{J}_s(\bar{r}') = \hat{n}(\bar{r}') \times \overline{H}(\bar{r}')$.

By using the Green's function

$$\overline{\overline{G}}(\bar{r}, \bar{r}') = \left(\overline{\overline{I}} + \frac{1}{k^2} \nabla\nabla \right) g(\bar{r}, \bar{r}'), \tag{2.4}$$

the scattered field is written as

$$\overline{E}_s(\bar{r}) = \int_{S'} dS' \left\{ i\omega\mu_o \left[g(\bar{r}, \bar{r}') \cdot \overline{J}_s(\bar{r}') + \frac{1}{k^2} \left(\nabla\nabla g(\bar{r}, \bar{r}') \right) \cdot \overline{J}_s(\bar{r}') \right] \right\}. \tag{2.5}$$

Using the identity

$$\nabla \left(\bar{u} \cdot \bar{v} \right) = (\nabla \bar{v}) \cdot \bar{u} + (\nabla \bar{u}) \cdot \bar{v}, \tag{2.6}$$

we obtain

$$\begin{aligned} \left(\nabla\nabla g(\bar{r}, \bar{r}') \right) \cdot \overline{J}_s(\bar{r}') &= -\left(\nabla\nabla' g(\bar{r}, \bar{r}') \right) \cdot \overline{J}_s(\bar{r}') \\ &= -\nabla \left(\overline{J}_s(\bar{r}') \cdot \nabla' g(\bar{r}, \bar{r}') \right) + \left(\nabla \overline{J}_s(\bar{r}') \right) \cdot \nabla' g(\bar{r}, \bar{r}') \\ &= -\nabla \left(\overline{J}_s(\bar{r}') \cdot \nabla' g(\bar{r}, \bar{r}') \right). \end{aligned} \tag{2.7}$$

Therefore the scattered electric field can be written as

$$\overline{E}_s(\bar{r}) = i\omega\mu_o \int_{S'} dS' g(\bar{r}, \bar{r}') \cdot \overline{J}_s(\bar{r}') - \frac{i\omega\mu_o}{k^2} \nabla \int_{S'} dS' \overline{J}_s(\bar{r}') \cdot \nabla' g(\bar{r}, \bar{r}'). \tag{2.8}$$

On the other hand, by using the identity

$$\nabla \cdot (\phi \bar{v}) = \bar{u} \cdot (\nabla \phi) + \phi \nabla \cdot \bar{u}, \tag{2.9}$$

we get the continuity relation as

$$\overline{J}_s(\bar{r}') \cdot \nabla' g(\bar{r}, \bar{r}') = \nabla' \cdot \left(g(\bar{r}, \bar{r}') \overline{J}_s(\bar{r}') \right) - g(\bar{r}, \bar{r}') \nabla' \cdot \overline{J}_s(\bar{r}'). \tag{2.10}$$

Using the continuity law for the surface current and charge,

$$\nabla' \cdot \overline{J}_s(\bar{r}') = i\omega \rho(\bar{r}'), \tag{2.11}$$

we get

$$\begin{aligned} \overline{E}_s(\bar{r}) &= i\omega\mu_o \int\limits_{S'} dS' g(\bar{r}, \bar{r}') \cdot \overline{J}_s(\bar{r}') - \frac{i\omega\mu_o}{k^2} \nabla \int\limits_{S'} dS' \left[\nabla' \cdot \left(g(\bar{r}, \bar{r}') \overline{J}_s(\bar{r}') \right) \right] \\ & -\nabla \frac{1}{\epsilon_o} \int\limits_{S'} dS' \left[\rho(\bar{r}') g(\bar{r}, \bar{r}') \right]. \end{aligned} \tag{2.12}$$

Since the surface current is normal to the surface vector, we have

$$\nabla' \cdot \left(g(\bar{r}, \bar{r}') \overline{J}_s(\bar{r}') \right) = \nabla'_s \cdot \left(g(\bar{r}, \bar{r}') \overline{J}_s(\bar{r}') \right). \tag{2.13}$$

By using the identity from [66], and assuming that the surface current has no component normal to the edge, we arrive at

$$\int dS' \left[\nabla'_s \cdot \left(g(\bar{r}, \bar{r}') \overline{J}_s(\bar{r}') \right) \right] = \oint\limits_{C} dl' \, \hat{n}_{l'} \cdot g(\bar{r}, \bar{r}') \overline{J}_s(\bar{r}') = 0, \tag{2.14}$$

where $\hat{n}_l$ is the unit vector normal to the edge and tangent to the surface. Therefore the wave scattered by the conducting object can be written as

$$\overline{E}_s(\bar{r}) = i\omega\overline{A}(\bar{r}) - \nabla\phi(\bar{r}), \tag{2.15}$$

where $\overline{A}(\bar{r})$ and $\phi(\bar{r})$ are vector and scalar potential, respectively, given by

$$\overline{A}(\bar{r}) = \mu_o \int_{S'} dS' g(\bar{r}, \bar{r}')\overline{J}_s(\bar{r}') = \mu_o \int_{S'} dS' \frac{e^{ik|\bar{r}-\bar{r}'|}}{4\pi\,|\bar{r}-\bar{r}'|}\overline{J}_s(\bar{r}'), \tag{2.16}$$

$$\phi(\bar{r}) = \frac{1}{\epsilon_o} \int_{S'} dS' g(\bar{r}, \bar{r}')\rho(\bar{r}') = \frac{1}{\epsilon_o} \int_{S'} dS' \frac{e^{ik|\bar{r}-\bar{r}'|}}{4\pi\,|\bar{r}-\bar{r}'|}\rho(\bar{r}'). \tag{2.17}$$

By considering the surface current as an unknown, and noticing that the tangential electric field vanishes on the surface of the conducting object, we obtain the equation for the surface current ($\bar{r} \in S$) from Eq. (2.1)

$$\left(\overline{E}_i(\bar{r}) + \overline{E}_s(\bar{r})\right)_{\tan} = 0, \tag{2.18}$$

or

$$\left(\overline{E}_i(\bar{r}) + i\omega\mu_o \int_{S'} dS' \frac{e^{ik|\bar{r}-\bar{r}'|}}{4\pi\,|\bar{r}-\bar{r}'|}\overline{J}_s(\bar{r}') - \nabla\frac{1}{\epsilon_o}\int_{S'} dS' \frac{e^{ik|\bar{r}-\bar{r}'|}}{4\pi\,|\bar{r}-\bar{r}'|}\rho(\bar{r}')\right)_{\tan} = 0. \tag{2.19}$$

After the surface current $\overline{J}_s(\bar{r}')$ is solved from the above equation, the scattered field can be calculated using Eq. (2.15).

2.3 Field Scattered by Object on Flat PEC Surface

Similar to Eq. (2.3), the electric field scattered by object on a flat surface as shown in Fig. (2-2) can be written as

$$\overline{E}_s(\bar{r}) = \int_{S'} dS' \left\{ i\omega\mu_o \overline{\overline{G}}_L(\bar{r}, \bar{r}') \cdot \overline{J}_s(\bar{r}') \right\}, \tag{2.20}$$

where $\overline{\overline{G}}_L(\bar{r}, \bar{r}')$ is the Green's function for layered media. The total field in the upper half space of the layered medium can be written as

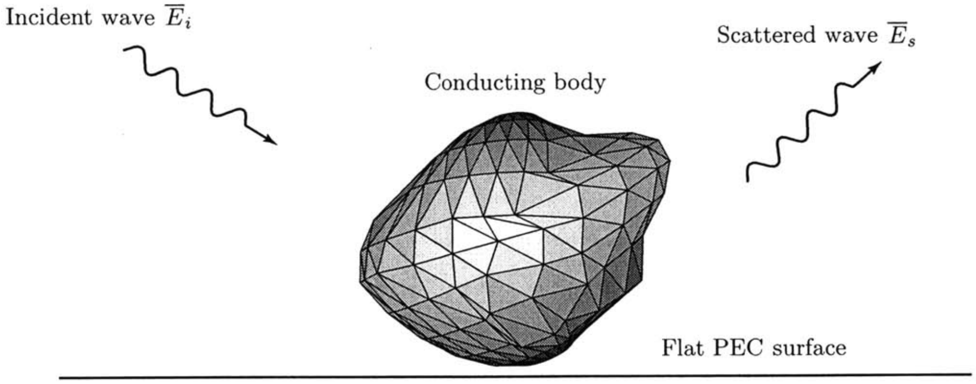

Figure 2-2: An electromagnetic wave incident upon an arbitrarily-shaped perfectly conducting (PEC) body above a flat PEC surface.

$$\overline{E}(\bar{r}) = \overline{E}_i(\bar{r}) + \overline{E}_r(\bar{r}) + \overline{E}_s(\bar{r}), \tag{2.21}$$

where $\overline{E}_r(\bar{r})$ is the field reflected by the layered interface in the absence of the PEC object. By applying the boundary condition on the surface of the conducting object, the electric field integral equation is obtained as

$$\left(\overline{E}_i(\bar{r}) + \overline{E}_r(\bar{r}) + \overline{E}_s(\bar{r})\right)_{\tan} = 0 \qquad \text{for } \bar{r} \in S. \tag{2.22}$$

2.3.1 Green's Function of Layered Media with PEC Half Space

Considering an object above a perfectly conducting flat surface, the layered Green's function can be written as [65, page 473]

$$\overline{\overline{G}}_L(\bar{r}, \bar{r}') = \overline{\overline{G}}_1(\bar{r}, \bar{r}') - \overline{\overline{G}}_1\left(\bar{r}, \bar{r}' \cdot (\overline{\overline{I}} - 2\hat{z}\hat{z})\right) \cdot (\overline{\overline{I}} - 2\hat{z}\hat{z}), \tag{2.23}$$

where $\overline{\overline{G}}_1(\bar{r},\bar{r}')$ is the Green's function in unbounded space. Using the definition of the dyadic Green's function in free space,

$$\overline{\overline{G}}_1(\bar{r},\bar{r}') = \left(\overline{\overline{I}} + \frac{1}{k^2}\nabla\nabla\right) g_1(\bar{r},\bar{r}'), \tag{2.24}$$

we write

$$\begin{aligned}\overline{\overline{G}}_L(\bar{r},\bar{r}') &= \overline{\overline{I}}g_1(\bar{r},\bar{r}') - \overline{\overline{I}}g_1\left(\bar{r},\bar{r}'\cdot(\overline{\overline{I}}-2\hat{z}\hat{z})\right) + 2g_1\left(\bar{r},\bar{r}'\cdot(\overline{\overline{I}}-2\hat{z}\hat{z})\right)\cdot\hat{z}\hat{z} \\ &+\frac{1}{k^2}\left(\nabla\nabla g_1(\bar{r},\bar{r}')\right) - \frac{1}{k^2}\left[\nabla\nabla g_1\left(\bar{r},\bar{r}'\cdot(\overline{\overline{I}}-2\hat{z}\hat{z})\right)\right] \\ &+2\frac{1}{k^2}\left[\nabla\nabla g_1\left(\bar{r},\bar{r}'\cdot(\overline{\overline{I}}-2\hat{z}\hat{z})\right)\right]\cdot\hat{z}\hat{z}.\end{aligned} \tag{2.25}$$

Thus the scattered field is

$$\begin{aligned}\overline{E}_s(\bar{r}) &= \int_{S'} dS'\left\{i\omega\mu_o\overline{\overline{G}}_L(\bar{r},\bar{r}')\cdot\overline{J}_s(\bar{r}')\right\} \\ &= \int_{S'} dS'\left\{i\omega\mu_o\overline{\overline{K}}_A(\bar{r},\bar{r}')\cdot\overline{J}_s(\bar{r}')\right\} \\ &+\int_{S'} dS'\left\{i\omega\mu_o\frac{1}{k^2}\left(\nabla\nabla g_1(\bar{r},\bar{r}')\right)\cdot\overline{J}_s(\bar{r}')\right\} \\ &-\frac{1}{k^2}\int_{S'} dS'\left\{i\omega\mu_o\left[\nabla\nabla g_1\left(\bar{r},\bar{r}'\cdot(\overline{\overline{I}}-2\hat{z}\hat{z})\right)\right]\cdot(\overline{\overline{I}}-2\hat{z}\hat{z})\cdot\overline{J}_s(\bar{r}')\right\},\end{aligned} \tag{2.26}$$

where

$$\overline{\overline{K}}_A(\bar{r},\bar{r}') = \begin{bmatrix} g_1(\bar{r},\bar{r}') - g_1(\bar{r},\bar{r}'') & 0 & 0 \\ 0 & g_1(\bar{r},\bar{r}') - g_1(\bar{r},\bar{r}'') & 0 \\ 0 & 0 & g_1(\bar{r},\bar{r}') + g_1(\bar{r},\bar{r}'') \end{bmatrix}, \tag{2.27}$$

and

$$\bar{r}'' = \bar{r}'\cdot(\overline{\overline{I}}-2\hat{z}\hat{z}). \tag{2.28}$$

By using the relation in Eq. (2.7), we have

$$(\nabla\nabla g_1(\bar{r},\bar{r}'))\cdot\overline{J}_s(\bar{r}') = -\nabla\left(\overline{J}_s(\bar{r}')\cdot\nabla' g_1(\bar{r},\bar{r}')\right), \tag{2.29}$$

$$\left(\nabla\nabla g_1\left(\bar{r},\bar{r}'\cdot(\overline{\overline{I}}-2\hat{z}\hat{z})\right)\right)\cdot\hat{z}\hat{z}\cdot\overline{J}_s(\bar{r}') = -\nabla\left(\overline{J}_s(\bar{r}')\cdot\left(\nabla' g_1\left(\bar{r},\bar{r}'\cdot(\overline{\overline{I}}-2\hat{z}\hat{z})\right)\cdot\hat{z}\hat{z}\right)\right), \tag{2.30}$$

thus the scattered electric field can be found to be

$$\begin{aligned}\overline{E}_s(\bar{r}) \;=\;& \int\limits_{S'} dS'\left\{i\omega\mu_o\overline{\overline{K}}_A(\bar{r},\bar{r}')\cdot\overline{J}_s(\bar{r}')\right\}\\ &-\frac{i\omega\mu_o}{k^2}\nabla\int\limits_{S'} dS'\left\{\left(\overline{J}_s(\bar{r}')\cdot\nabla' g_1(\bar{r},\bar{r}')\right)\right\}\\ &+\frac{i\omega\mu_o}{k^2}\nabla\int\limits_{S'} dS'\left\{\left((\overline{\overline{I}}-2\hat{z}\hat{z})\cdot\overline{J}_s(\bar{r}')\cdot\nabla' g_1\left(\bar{r},\bar{r}'\cdot(\overline{\overline{I}}-2\hat{z}\hat{z})\right)\right)\right\}.\end{aligned} \tag{2.31}$$

For the third surface integral in Eq. (2.31), we change the sign of the coordinate of z', so that the new surface is the image with respect to the flat surface. By letting $\overline{J}''_s(\bar{r}'') = (\overline{\overline{I}}-2\hat{z}\hat{z})\cdot\overline{J}_s(\bar{r}'')$, the third surface integral becomes

$$\overline{E}_{s3}(\bar{r}) = \frac{i\omega\mu_o}{k^2}\nabla\int\limits_{S''} dS''\left\{\left(\overline{J}''_s(\bar{r}'')\cdot\nabla'' g_1(\bar{r},\bar{r}')\right)\right\}. \tag{2.32}$$

Notice that $\overline{J}''_s(\bar{r}'') = (\overline{\overline{I}}-2\hat{z}\hat{z})\cdot\overline{J}_s(\bar{r}'')$ is the surface current on the image surface S''. This can be shown by defining a normal vector $\hat{n}' = x'\hat{x}+y'\hat{y}+z'\hat{z}$ on the surface S', such that the corresponding normal vector on the image surface is $\hat{n}'' = x'\hat{x}+y'\hat{y}-z'\hat{z}$. Since $\overline{J}_s(\bar{r}')$ is the surface current on S', $\overline{J}_s(\bar{r}')\cdot\hat{n}'=0$, therefore $(\overline{\overline{I}}-2\hat{z}\hat{z})\cdot\overline{J}_s(\bar{r}'')\cdot\hat{n}'' = \overline{J}_s(\bar{r}')\cdot\hat{n}' = 0$.

By using the identity

$$\overline{J}_s(\bar{r}')\cdot\nabla' g_1(\bar{r},\bar{r}') = \nabla'\cdot\left(g_1(\bar{r},\bar{r}')\overline{J}_s(\bar{r}')\right) - g_1(\bar{r},\bar{r}')\nabla'\cdot\overline{J}_s(\bar{r}'), \tag{2.33}$$

and noticing that the surface integral of the first term is zero, we write the term as

$$\overline{E}_{s3}(\bar{r}) = -\frac{i\omega\mu_o}{k^2}\nabla \int_{S'} dS'' \left\{ g_1(\bar{r},\bar{r}')\nabla'' \cdot \overline{J}''_s(\bar{r}'') \right\}. \tag{2.34}$$

Using the continuity law for the current and charge distributions

$$\nabla'' \cdot \overline{J}''_s(\bar{r}'') = i\omega\rho(\bar{r}''), \tag{2.35}$$

the third term of the scattered electric field can be written as an integral in terms of the surface charge density

$$\overline{E}_{s3}(\bar{r}) = \frac{1}{\epsilon_o}\nabla \int_{S''} dS'' g_1(\bar{r},\bar{r}')\rho(\bar{r}''). \tag{2.36}$$

Changing the component z'' back to $-z'$, it yields

$$\overline{E}_{s3}(\bar{r}) = \frac{1}{\epsilon_o}\nabla \int_{S'} dS' g_1(\bar{r},\bar{r}'')\rho(\bar{r}'). \tag{2.37}$$

Finally, we obtain the electric field scattered by the conducting object on a flat PEC surface as following:

$$\overline{E}_s(\bar{r}) = i\omega\mu_o \int_{S'} dS' \overline{\overline{K}}_A(\bar{r},\bar{r}') \cdot \overline{J}_s(\bar{r}') - \nabla\frac{1}{\epsilon_o} \int_{S'} dS' K_\phi(\bar{r},\bar{r}')\rho(\bar{r}'), \tag{2.38}$$

where $K_\phi(\bar{r},\bar{r}') = g_1(\bar{r},\bar{r}') - g_1(\bar{r},\bar{r}'')$. Defining the vector and scalar potentials

$$\overline{A}(\bar{r}) = \mu_o \int_{S'} dS' \overline{\overline{K}}_A(\bar{r},\bar{r}') \cdot \overline{J}_s(\bar{r}'), \tag{2.39}$$

$$\phi(\bar{r}) = \frac{1}{\epsilon_o} \int_{S'} dS' K_\phi(\bar{r},\bar{r}')\rho(\bar{r}'), \tag{2.40}$$

the total electric field scattered by the object on a flat PEC surface can also be written as

$$\overline{E}_s(\bar{r}) = i\omega\overline{A}(\bar{r}) - \nabla\phi(\bar{r}). \tag{2.41}$$

2.3.2 Formulations for the Solution by Method of Moments

In the electric field integral equation for the conducting object on a flat PEC surface, the unknown function is the surface current on the object. The charge distribution $\rho_s(\bar{r}')$ is related to the surface current by the continuity law $\nabla'_s \cdot \overline{J}_s(\bar{r}') = i\omega\rho_s(\bar{r}')$, therefore $\rho_s(\bar{r}')$ is not an independent unknown. In this section, we will use the triangular patch model introduced by Glisson [67] to formulate the equation used in the MoM. In the triangular patch model, the surface current on the object is approximated in terms of the basis function $\overline{f}_n(\bar{r}')$, i.e.,

$$\overline{J}_s(\bar{r}') = \sum_{n=1}^{N} I_n \overline{f}_n(\bar{r}'), \tag{2.42}$$

where N is the number of interior edges and I_n is the unknown on the interior edge n. The basis function $\overline{f}_n(\bar{r}')$ is defined for an adjacent pair of triangles:

$$\overline{f}_n(\bar{r}') = \begin{cases} \dfrac{l_n}{2A_n^+}\bar{\rho}_n^+(\bar{r}') & \bar{r}' \text{ on } T_n^+, \\ \dfrac{l_n}{2A_n^-}\bar{\rho}_n^-(\bar{r}') & \bar{r}' \text{ on } T_n^-, \\ 0 & \text{otherwise.} \end{cases} \tag{2.43}$$

One triangle (T_n^+) of the pair with the area denoted by A_n^+ is named "positive" and the other (T_n^-) with the area labeled by A_n^- is called "negative", and they share a common interior edge with the edge length l_n as shown in Fig. (2-3). If the tip of the position vector $\bar{r}'$ is located on the triangle T_n^+, then the local position vector $\bar{\rho}_n^+(\bar{r}')$ points from the free vertex V to the tip of the vector $\bar{r}'$. If the tip of the position vector $\bar{r}'$ on the triangle T_n^-, then the local position vector $\bar{\rho}_n^-(\bar{r}')$ points from the tip of the vector $\bar{r}'$ to the free vertex V'. For example, the surface current on the triangle

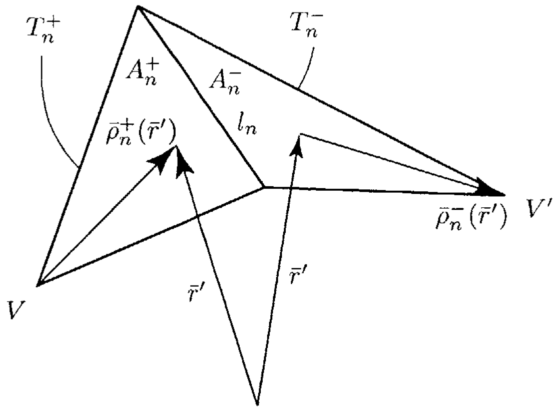

Figure 2-3: Triangular patch pair used in the modeling of conducting objects.

is approximated as

$$\begin{aligned}\bar J_s(\bar r') &= \sum_{n=1}^{N} I_n \bar f_n(\bar r') \\ &= I_a \frac{l_a}{2A}\bar\rho_a(\bar r') + I_b \frac{l_b}{2A}\bar\rho_b(\bar r') + I_c \frac{l_c}{2A}\bar\rho_c(\bar r'), \qquad (2.44)\end{aligned}$$

where the subscripts a, b, and c are the labels for the edges. Note that there is a maximum of 3 terms contributing to the surface current on a triangle patch. There is no surface current flowing across an open edge because no unknowns are assigned to such edges. However, if an open edge touches a perfectly conducting surface, the unknown associated with this edge is treated as the one for a regular interior edge so that the current crossing this edge is continuous. With the definition of the basis vector function $\bar f_n(\bar r')$, we also get the surface charge density

$$\rho(\bar r') = \frac{1}{i\omega}\nabla'_s \cdot \bar J_s(\bar r') = \frac{1}{i\omega}\sum_{n=1}^{N} I_n \nabla'_s \cdot \bar f_n(\bar r'), \qquad (2.45)$$

where the surface divergence of the basis functions is constant and is given by

$$\nabla'_s \cdot \bar{f}_n(\bar{r}') = \begin{cases} \dfrac{l_n}{A_n^+} & \bar{r}' \text{ in } T_n^+, \\ -\dfrac{l_n}{A_n^-} & \bar{r}' \text{ in } T_n^-, \\ 0 & \text{otherwise.} \end{cases} \tag{2.46}$$

Therefore, associated with the vector basis function, the scattered electric field is

$$\begin{aligned} \overline{E}_s(\bar{r}) &= i\omega\overline{A}(\bar{r}) - \nabla\phi(\bar{r}) \\ &= i\omega\mu_o \int_{S'} dS' \overline{\overline{K}}_A(\bar{r},\bar{r}') \cdot \overline{J}_s(\bar{r}') - \nabla\frac{1}{\epsilon_o}\int_{S'} dS' K_\phi(\bar{r},\bar{r}')\rho(\bar{r}') \\ &= i\omega\mu_o \sum_{n=1}^{N} I_n \int_{S'} dS' \overline{\overline{K}}_A(\bar{r},\bar{r}') \cdot \bar{f}_n(\bar{r}') \\ &\quad -\nabla\frac{1}{i\omega\epsilon_o}\sum_{n=1}^{N} I_n \int_{S'} dS' K_\phi(\bar{r},\bar{r}')\nabla'_s \cdot \bar{f}_n(\bar{r}'), \end{aligned} \tag{2.47}$$

and the total electric field is

$$\overline{E}(\bar{r}) = \overline{E}_i(\bar{r}) + \overline{E}_r(\bar{r}) + \overline{E}_s(\bar{r}). \tag{2.48}$$

By choosing the testing function as the basis function $\bar{f}_m(\bar{r})$, we calculate the inner product for the total electric field on the surface of the conducting object, and get

$$\int_S dS\overline{E}(\bar{r}) \cdot \bar{f}_m(\bar{r}) = \int_S dS \left[\overline{E}_i(\bar{r}) + \overline{E}_r(\bar{r}) + \overline{E}_s(\bar{r})\right] \cdot \bar{f}_m(\bar{r}). \tag{2.49}$$

Noting that $\overline{E}(\bar{r}) \cdot \bar{f}_m(\bar{r}) = 0$ since the tangential electric field is zero on the PEC object, we find

$$\int_S dS \left[\overline{E}_i(\bar{r}) + \overline{E}_r(\bar{r}) + \overline{E}_s(\bar{r})\right] \cdot \bar{f}_m(\bar{r}) = 0, \tag{2.50}$$

where

$$\begin{aligned}
&\int_S dS\left[\overline{E}_i(\bar{r})+\overline{E}_r(\bar{r})\right]\cdot\overline{f}_m(\bar{r})\\
&\quad=\frac{l_m}{2A_m^+}\int_{T_m^+} dS\left[\overline{E}_i(\bar{r})+\overline{E}_r(\bar{r})\right]\cdot\bar{\rho}_m^+(\bar{r})+\frac{l_m}{2A_m^-}\int_{T_m^-} dS\left[\overline{E}_i(\bar{r})+\overline{E}_r(\bar{r})\right]\cdot\bar{\rho}_m^-(\bar{r})\\
&\quad\approx\frac{l_m}{2}\left[\overline{E}_i(\bar{r}_m^{c+})+\overline{E}_r(\bar{r}_m^{c+})\right]\cdot\bar{\rho}_m^{c+}+\frac{l_m}{2}\left[\overline{E}_i(\bar{r}_m^{c-})+\overline{E}_r(\bar{r}_m^{c-})\right]\cdot\bar{\rho}_m^{c-}. \qquad (2.51)
\end{aligned}$$

and the superscript c denotes the centroid of the corresponding triangle. A detailed derivation is given in Appendix A. The inner product of the scattered electric field with the vector basis function is

$$\begin{aligned}
&\int_S dS\overline{E}_s(\bar{r})\cdot\overline{f}_m(\bar{r})\\
&\approx\ i\omega l_m\left[\overline{A}(\bar{r}_m^{c+})\cdot\frac{\bar{\rho}_m^+(\bar{r}_m^{c+})}{2}+\overline{A}(\bar{r}_m^{c-})\cdot\frac{\bar{\rho}_m^-(\bar{r}_m^{c-})}{2}\right]\\
&\quad+l_m\left[\phi(\bar{r}_m^{c+})-\phi(\bar{r}_m^{c-})\right]. \qquad (2.52)
\end{aligned}$$

Thus Eq. (2.50) becomes

$$\begin{aligned}
&\frac{l_m}{2}\left[\overline{E}_i(\bar{r}_m^{c+})+\overline{E}_r(\bar{r}_m^{c+})\right]\cdot\bar{\rho}_m^{c+}+\frac{l_m}{2}\left[\overline{E}_i(\bar{r}_m^{c-})+\overline{E}_r(\bar{r}_m^{c-})\right]\cdot\bar{\rho}_m^{c-}\\
&\quad+i\omega l_m\left[\overline{A}(\bar{r}_m^{c+})\cdot\frac{\bar{\rho}_m^+(\bar{r}_m^{c+})}{2}+\overline{A}(\bar{r}_m^{c-})\cdot\frac{\bar{\rho}_m^-(\bar{r}_m^{c-})}{2}\right]+l_m\left[\phi(\bar{r}_m^{c+})-\phi(\bar{r}_m^{c-})\right]=0, \quad (2.53)
\end{aligned}$$

where

$$\begin{aligned}
\overline{A}(\bar{r}_m^{c\pm}) &= \mu_o\sum_{n=1}^{N} I_n\int_{S'} dS'\,\overline{\overline{K}}_A(\bar{r}_m^{c\pm},\bar{r}')\cdot\overline{f}_n(\bar{r}')=\sum_{n=1}^{N} A_{mn}^{\pm}I_n, \qquad (2.54)\\
\phi(\bar{r}_m^{c\pm}) &= \frac{1}{i\omega\epsilon_o}\sum_{n=1}^{N} I_n\int_{S'} dS'K_\phi(\bar{r}_m^{c\pm},\bar{r}')\nabla_s'\cdot\overline{f}_n(\bar{r}')=\sum_{n=1}^{N}\phi_{mn}^{\pm}I_n. \qquad (2.55)
\end{aligned}$$

and

$$A^{\pm}_{mn} = \mu_o \int_{S'} dS' \overline{\overline{K}}_A(\bar{r}^{c\pm}_m, \bar{r}') \cdot \bar{f}_n(\bar{r}'), \tag{2.56}$$

$$\phi^{\pm}_{mn} = \frac{1}{i\omega\epsilon_o} \int_{S'} dS' K_\phi(\bar{r}^{c\pm}_m, \bar{r}') \nabla'_s \cdot \bar{f}_n(\bar{r}'). \tag{2.57}$$

Define the element

$$V_m = \frac{l_m}{2}\left[\overline{E}_i(\bar{r}^{c+}_m) + \overline{E}_r(\bar{r}^{c+}_m)\right] \cdot \bar{\rho}^{c+}_m + \frac{l_m}{2}\left[\overline{E}_i(\bar{r}^{c-}_m) + \overline{E}_r(\bar{r}^{c-}_m)\right] \cdot \bar{\rho}^{c-}_m, \tag{2.58}$$

and the impedance element

$$Z_{mn} = l_m \left[-i\omega\left(A^{+}_{mn} \cdot \frac{\bar{\rho}^{+}_m(\bar{r}^{c+}_m)}{2} + A^{-}_{mn} \cdot \frac{\bar{\rho}^{-}_m(\bar{r}^{c-}_m)}{2}\right) - \left(\phi^{+}_{mn} - \phi^{-}_{mn}\right)\right] I_n, \tag{2.59}$$

for Eq. (2.53), we write the above as a linear equation

$$V_m = \sum_{n=1}^{N} Z_{mn} I_n. \tag{2.60}$$

This is the matrix equation for the MoM with impedance matrix $Z = [Z_{mn}]$, source vector $V = [V_m]$, and unknown vector $I = [I_n]$.

2.3.3 Induced Surface Current and Scattered Field

Surface Current on the Object

Once we solve the unknown vector $I = [I_n]$ from Eq. (2.60), we can calculate the induced current anywhere on the object using Eq. (2.44),

$$J_{se}(\bar{r}') = \hat{e} \cdot \sum_{n=1}^{N} I_n \bar{f}_n(\bar{r}'), \tag{2.61}$$

where $e = x, y$ or z. There are three terms contributing to the current. The direction of the local coordinate vectors $\bar{\rho}_a(\bar{r}')$, $\bar{\rho}_b(\bar{r}')$, and $\bar{\rho}_c(\bar{r}')$ are associated with the definition of "positive" or "negative" triangle patches as shown in Fig. (2-4).

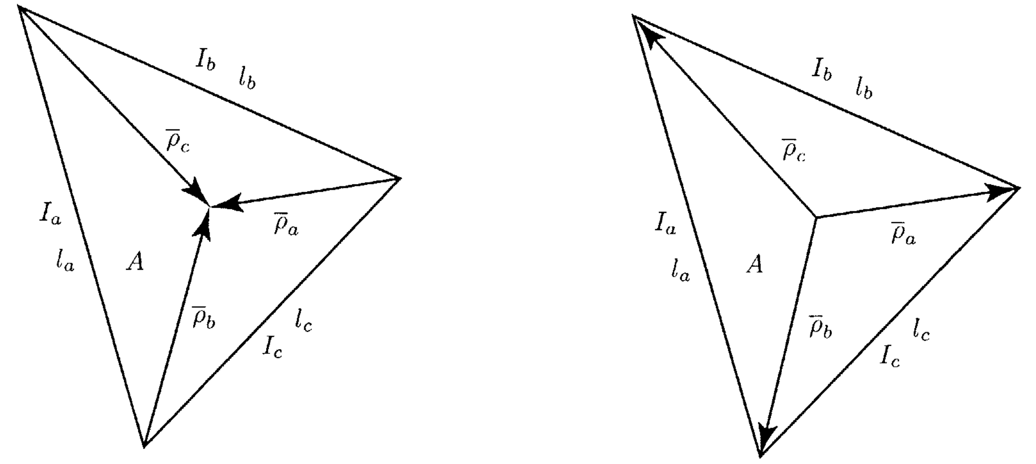

(a) The "positive" triangle patch (b) The "negative" triangle patch

Figure 2-4: Surface current on triangular patches.

Surface Current on the Flat Surface

The surface current on the conducting flat surface can be calculated by

$$\overline{J}(\bar{r}) = \hat{n} \times \left(\overline{H}_i(\bar{r}) + \overline{H}_r(\bar{r}) + \overline{H}_s(\bar{r})\right), \tag{2.62}$$

where $\overline{H}_i(\bar{r})$ and $\overline{H}_r(\bar{r})$ are the incident and reflected magnetic fields in the absence of the object, respectively. $\overline{H}_s(\bar{r})$ is the magnetic field scattered by the object in the presence of the flat surface. It is convenient to define the vector

$$\overline{a}(\bar{r}) = \eta_o \overline{J}(\bar{r}) \tag{2.63}$$

with the unit of the electric field (Volt/meter).

The Field Scattered by the Object

As in Eq. (2.47), the field scattered by the conducting object can be calculated after the unknown vector $I = [I_n]$ is solved from Eq. (2.60),

$$\begin{aligned}\overline{E}_s(\bar{r}) &= i\omega\overline{A}(\bar{r}) - \nabla\phi(\bar{r}) \\ &= i\omega\mu_o \sum_{n=1}^{N} I_n \int_{S'} dS' \overline{\overline{K}}_A(\bar{r},\bar{r}') \cdot \overline{f}_n(\bar{r}') \\ &\quad -\nabla\frac{1}{i\omega\epsilon_o}\sum_{n=1}^{N} I_n \int_{S'} dS' K_\phi(\bar{r},\bar{r}')\nabla'_s \cdot \overline{f}_n(\bar{r}'). \end{aligned} \tag{2.64}$$

In the iterative method for the scattering problem of the object on a rough surface (Chapter 3), the near field $\overline{E}_s(\bar{r})$ needs to be calculated. However the far field formulation of $\overline{E}_s(\bar{r})$ is also useful for each iteration. In the far field region, $|\bar{r} - \bar{r}'| \approx r - \hat{r}\cdot\bar{r}'$, we have

$$g_1(\bar{r},\bar{r}') \approx \frac{e^{ikr}e^{-ik\hat{r}\cdot\bar{r}'}}{4\pi r}, \tag{2.65}$$

and

$$\begin{aligned}\overline{\overline{K}}_A(\bar{r},\bar{r}') &= \begin{bmatrix} g_1(\bar{r},\bar{r}') - g_1(\bar{r},\bar{r}'') & 0 & 0 \\ 0 & g_1(\bar{r},\bar{r}') - g_1(\bar{r},\bar{r}'') & 0 \\ 0 & 0 & g_1(\bar{r},\bar{r}') + g_1(\bar{r},\bar{r}'') \end{bmatrix} \\ &\approx \frac{e^{ikr}}{4\pi r}\begin{bmatrix} e^{-ik\hat{r}\cdot\bar{r}'} - e^{-ik\hat{r}\cdot\bar{r}''} & 0 & 0 \\ 0 & e^{-ik\hat{r}\cdot\bar{r}'} - e^{-ik\hat{r}\cdot\bar{r}''} & 0 \\ 0 & 0 & e^{-ik\hat{r}\cdot\bar{r}'} + e^{-ik\hat{r}\cdot\bar{r}''} \end{bmatrix}, \end{aligned} \tag{2.66}$$

$$K_\phi(\bar{r},\bar{r}') = g_1(\bar{r},\bar{r}') - g_1(\bar{r},\bar{r}'') \approx \frac{e^{ikr}}{4\pi r}\left(e^{-ik\hat{r}\cdot\bar{r}'} - e^{-ik\hat{r}\cdot\bar{r}''}\right). \tag{2.67}$$

The far field approximation is important in numerical calculation because evaluation of $|\bar{r} - \bar{r}'|$ cannot be carried out correctly if the ratio r'/r is small compared to a computer's digital accuracy.

2.4 Numerical Results

2.4.1 Validation of the Code against Mie Theory

We first simulate the radar cross section (RCS) of a conducting sphere above a conducting flat surface using the MoM and compare the result with the one from an approximated Mie's theory [68, 69, 70] as shown in Fig. (2-5). The incident electric field $\overline{E}_i = \hat{x} E_o e^{-ikz}$ is a plane wave with frequency $f = 300\,\text{MHz}$ normal to the conducting surface coincident xy plane. The bistatic radar cross section is calculated by

$$\text{RCS} = \lim_{r \to \infty} 4\pi r^2 \frac{\left|\overline{E}_s\right|^2}{\left|E_o\right|^2}, \tag{2.68}$$

where $\overline{E}_s$ is the bistatic scattered field of the conducting sphere. The radius of the sphere is $r = 0.5\lambda$ and the gap between the sphere and the flat surface is $\delta h = 0$. The small deviation of the simulation result using MoM from Mie's theory may be due to the discretization of the spherical surface and the asymmetry of the patches. The number of triangular patches is 528 and the number of unknowns is 792.

2.4.2 Surface Current on a Conducting Object

Figure (2-6-a) and (2-6-b) are the calculated surface current $|J_z|$ and $\sqrt{|J_x|^2 + |J_y|^2}$ on a conducting cylinder above a flat conducting surface, respectively. The surface current intensity is normalized to gray levels from 0 to 1. The incident wave is TE polarized with $\theta_i = 40°$ illuminating the front-end of the cylinder ($\phi_i = 0°$). The cylinder is along the x-axis with length $L = 2.0\lambda$, radius $r = 0.5\lambda$, and the gap from the flat surface $\delta h = 0.1\lambda$. The incident wave is tapered with $g = 3.0\lambda$ and 64×64 plane waves (see Chapter 3).

Figure (2-7-a) and (2-7-b) are the induced surface current $|J_z|$ and $\sqrt{|J_x|^2 + |J_y|^2}$, respectively, by TM incident wave with $\theta_i = 40°$ and $\phi_i = 0°$. The cylinder has the same geometry and orientation as in Fig. (2-7). Notice that the dominant component

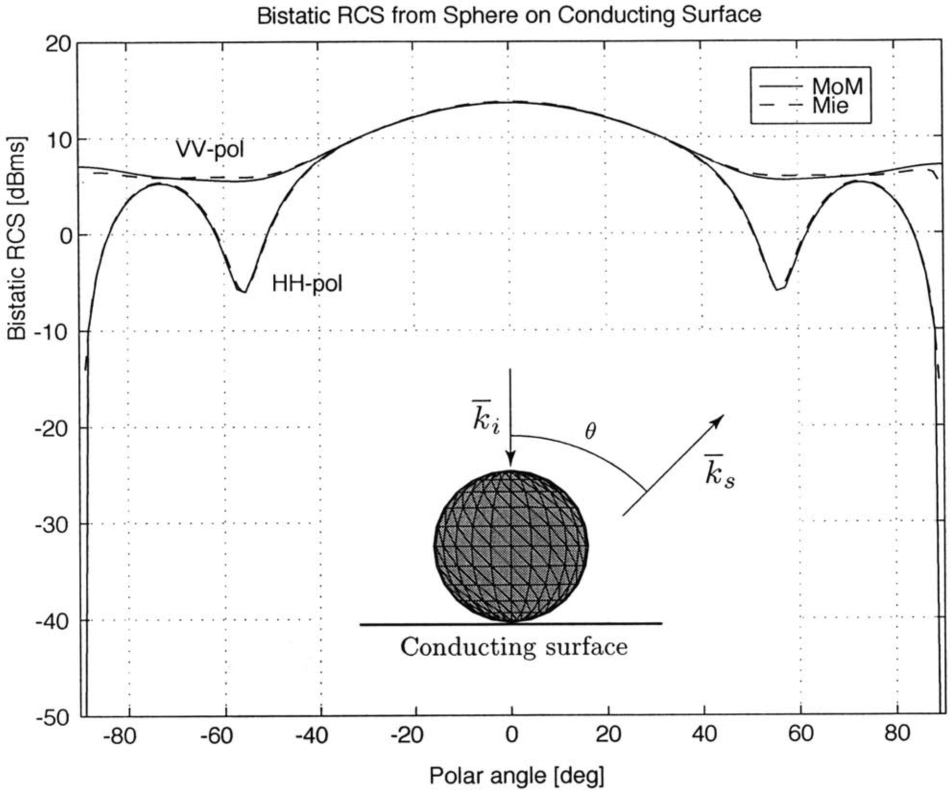

Figure 2-5: Bistatic radar cross section (RCS) of a conducting sphere with $r = 0.5\lambda$ above a conducting flat surface. The gap between the sphere and the flat surface is $\delta h = 0$.

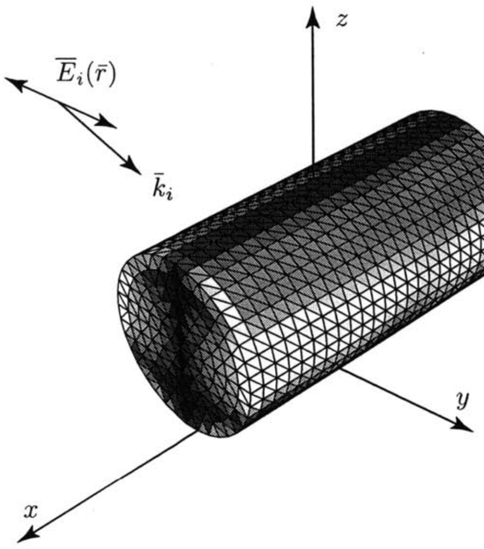

(a) TE incident wave, $|J_z|$

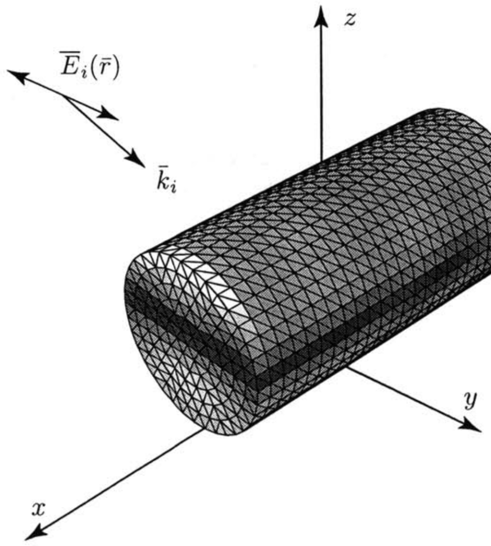

(b) TE incident wave, $J_s = \sqrt{|J_x|^2 + |J_y|^2}$

Figure 2-6: The induced surface current on a conducting cylinder above a flat surface using TE incident wave.

of the surface current has the same direction as the polarization of the incident wave.

2.4.3 Surface Current on Flat PEC Surface

Figure (2-8) is the simulation result of the x and y components of the surface current multiplied by the characteristic impedance η_o. The incident wave is tapered with TE polarization, $g = 3.0\lambda$, $\theta_i = 40°$, and $\phi_i = 0°$. The object is a horizontal cylinder along the x-axis with the length $L = 2.0\lambda$, radius $r = 0.5\lambda$ and the gap between the cylinder and the flat surface $\delta h = 0.1\lambda$.

Figure (2-9) is the simulation result of the x and y components of the surface current multiplied by the characteristic impedance η_o for TM incident tapered wave.

2.4.4 Scattered Field of a Conducting Cylinder above a Conducting Surface

Consider the same perfectly conducting cylinder as in Fig. (2-6) and (2-7) horizontally placed above a PEC flat surface. After the induced current on the cylinder has been solved, the scattered fields are calculated as shown in Fig. (2-10)–(2-13). The co-polarized and cross-polarized bistatic scattered fields are calculated by using the method of layered Green's function in comparison with the standard MoM that considers both the object and the PEC interface as scattering bodies. However, in the layered Green's function approach, the only unknown is the surface current on the conducting object above the PEC surface. Therefore a much higher computational efficiency for the layered Green's function approach can be achieved. Notice that the scattered fields for TM incident wave agree better than the TE incident wave in comparison with the standard MoM. This is because the scattered field excited by a TE wave may cause higher artificial edge currents at the truncated boundary of the

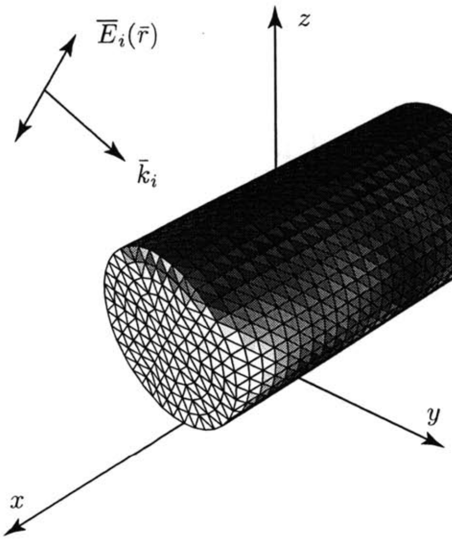

(a) TM incident wave, $|J_z|$

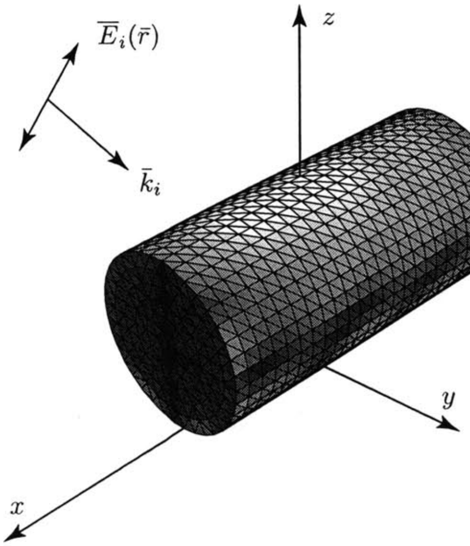

(b) TM incident wave, $J_s = \sqrt{|J_x|^2 + |J_y|^2}$

Figure 2-7: The induced surface current on a conducting cylinder above a flat surface using TM incident wave.

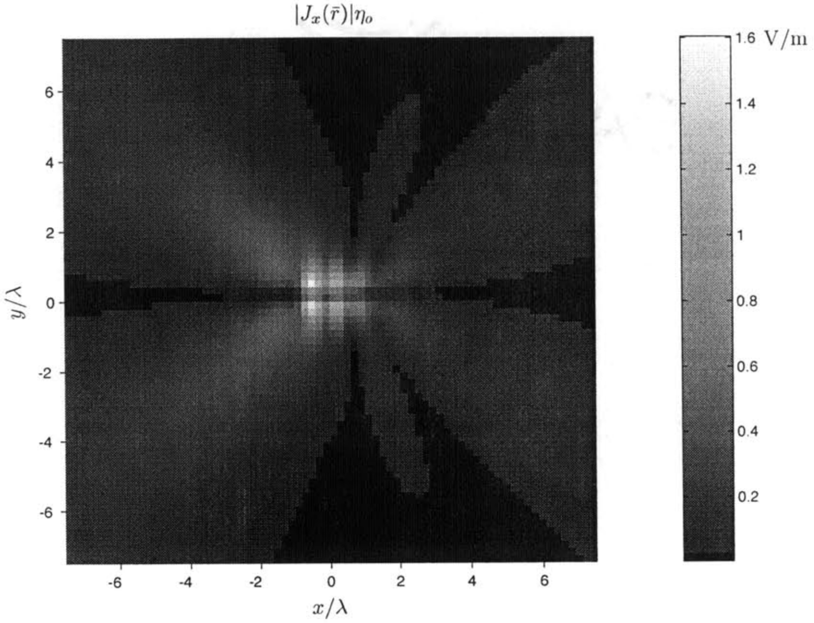

(a) The x component of the surface current

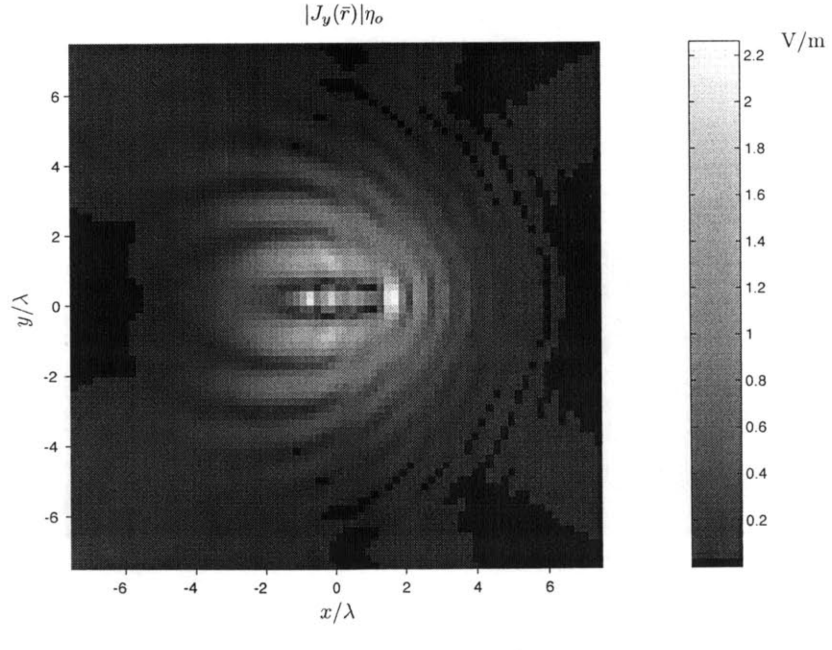

Figure 2-8: The x and y components of the surface current on a conducting object for the TE incident tapered wave.

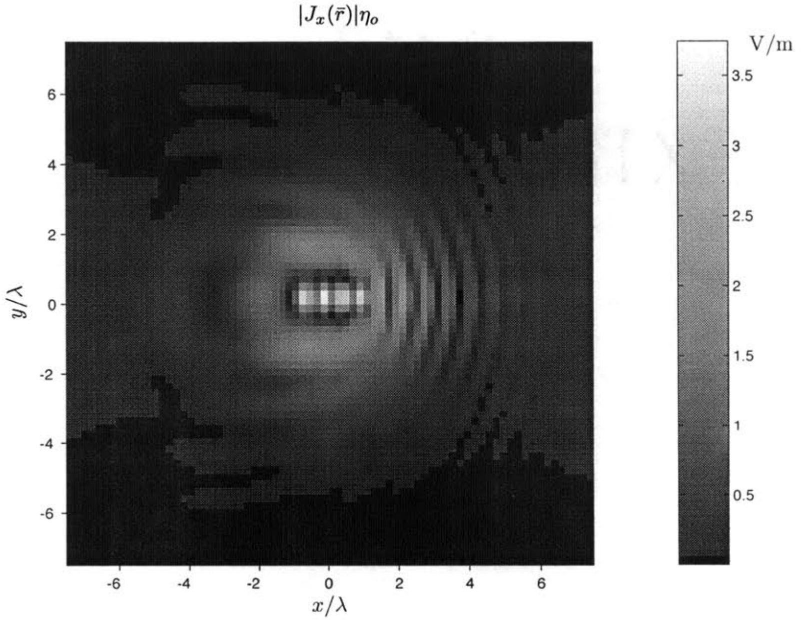
$|J_x(\bar{r})|\eta_o$

(a) The x component of the surface current

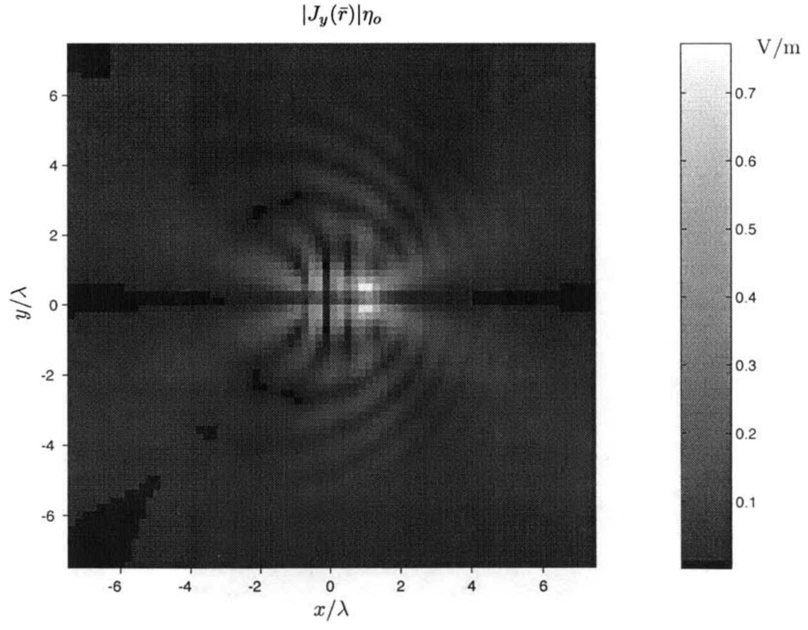
$|J_y(\bar{r})|\eta_o$

(b) The y component of the surface current

Figure 2-9: The x and y components of the surface current on a conducting object for the TM incident tapered wave.

PEC flat surface in the standard MoM. The large value at 180° azimuthal angle for the co-polarized scattered fields as in Fig. (2-10) and (2-12) are the specular reflection from the PEC flat surface. The small but visible non-symmetry in the plots for the cross-polarized scattered fields as shown in Fig. (2-11) and (2-11) are caused by the unsymmetry of the triangular patches on the cylinder. An overall good agreement has been achieved for the scattered field for all polarizations.

2.4.5 Object Half Buried in a Conducting Surface

Figure (2-14) is the gray level plot of the induced surface current on the horizontal cylinder half buried in a conducting flat surface. The incident wave is TM with the polar angle $\theta_i = 40°$ and azimuth angle $\phi_i = 0°$. In Fig. (2-14-a), the total induced surface current, $J_s = \sqrt{|J_x|^2 + |J_y|^2 + |J_z|^2}$, is plotted. It shows that the largest amount of surface current is induced at the front end of the cylinder. Figure (2-14-b) is the plot of the induced surface current in the z direction. Notice that the current crosses the edges touching the flat surface. The length of the cylinder is $L = 2\lambda$ and the radius is $r = 0.5\lambda$. The maximum current intensity is normalized to 1.

Figure (2-15) is the numerical simulation result of the bistatic radar cross section (RCS) for the conducting cylinder horizontally half buried in a flat conducting surface. The incident wave is a TE tapered wave with the frequency $f = 300\,\text{MHz}$. The g factor of the tapered incident wave is $g = 3.0\lambda$. The wave vector $\overline{k}_i$ of the incident wave is on the xz plane ($\phi_i = 0°$) with the polar angle $\theta_i = 40°$. The bistatic scattered field is calculated for the scattering polar angle $\theta_s = \theta_i = 40°$ and the azimuth angle ϕ_s varying from 0° to 360°, so $\phi_s = 0°$ or $\phi_s = 360°$ is the backscattering direction. The solid curve is the simulation result by using the method described in this chapter. The dashed curve is the simulation result by using the standard method of moments (MoM). In the standard MoM, the flat surface as well as the cylinder are discretized into triangular patches. The size of the flat surface is chosen as $15\lambda \times 15\lambda$ so that the illuminating field at the edges is small enough to avoid the edge effect due to

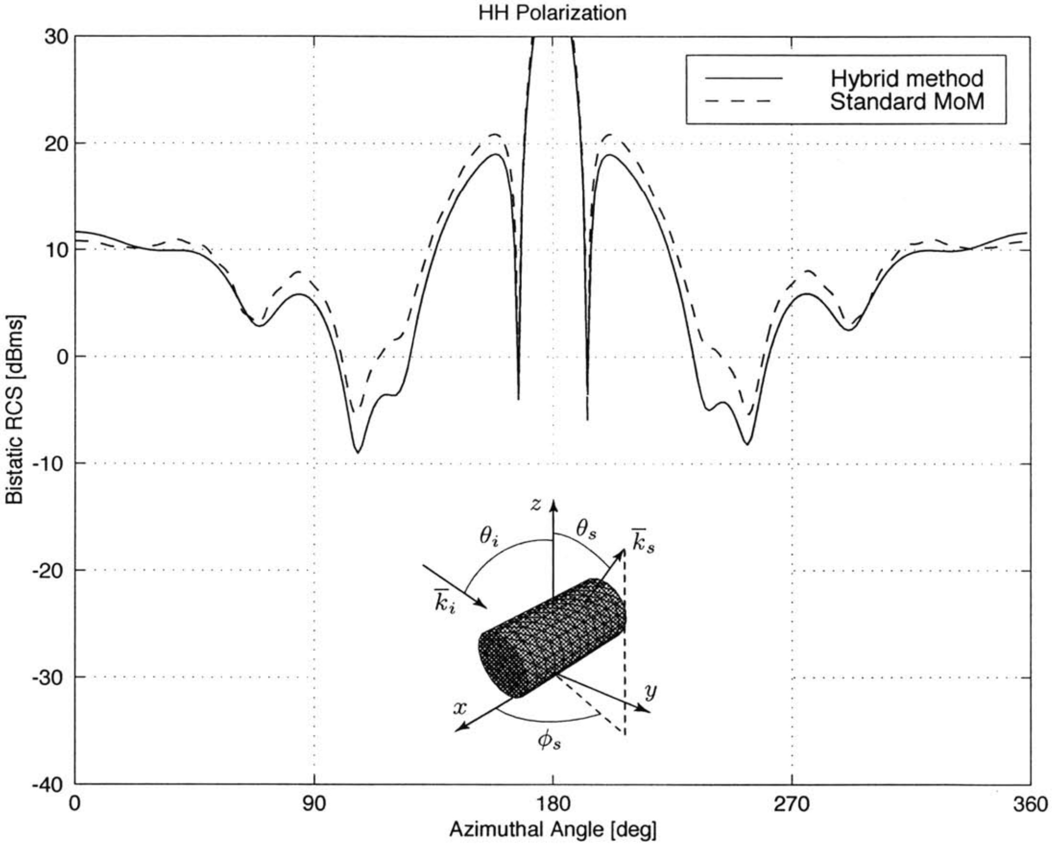

Figure 2-10: The co-polarized bistatic radar cross section (RCS) solved by the layered Green's function approach for a conducting cylinder above a PEC flat surface in comparison with the result from the standard MoM.

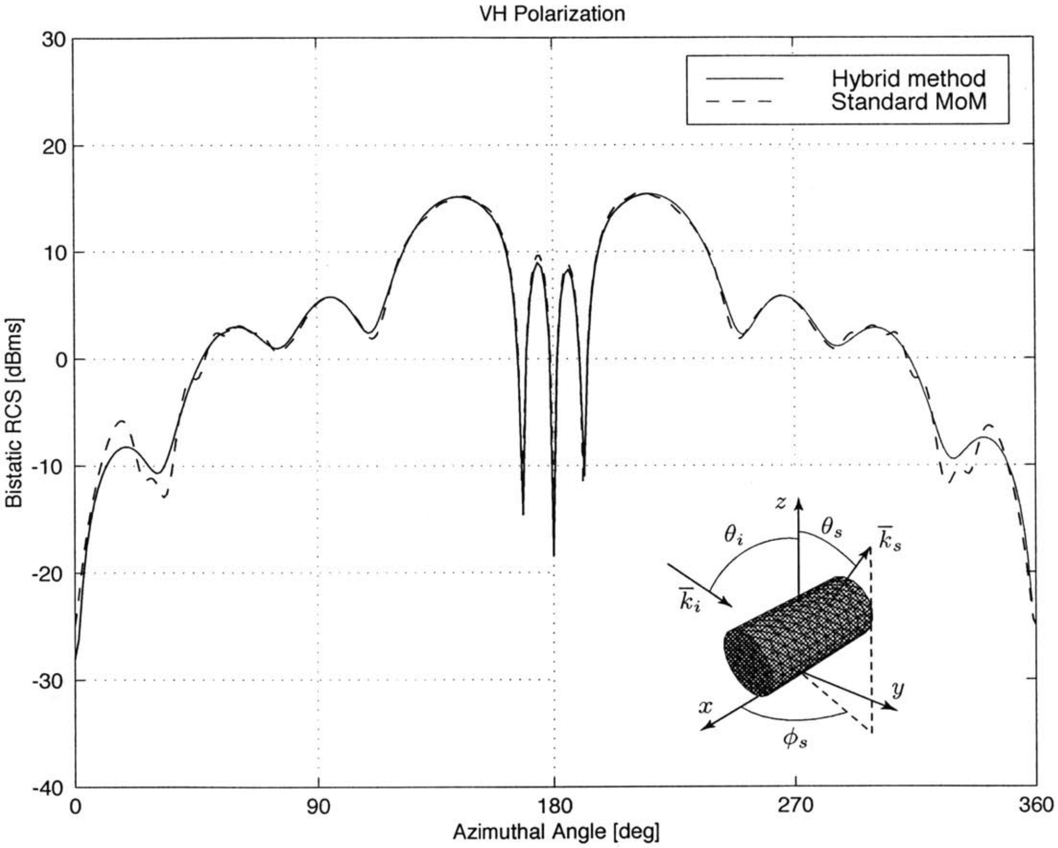

Figure 2-11: The cross-polarized bistatic radar cross section (RCS) solved by the layered Green's function approach for a conducting cylinder above a PEC flat surface in comparison with the result from the standard MoM.

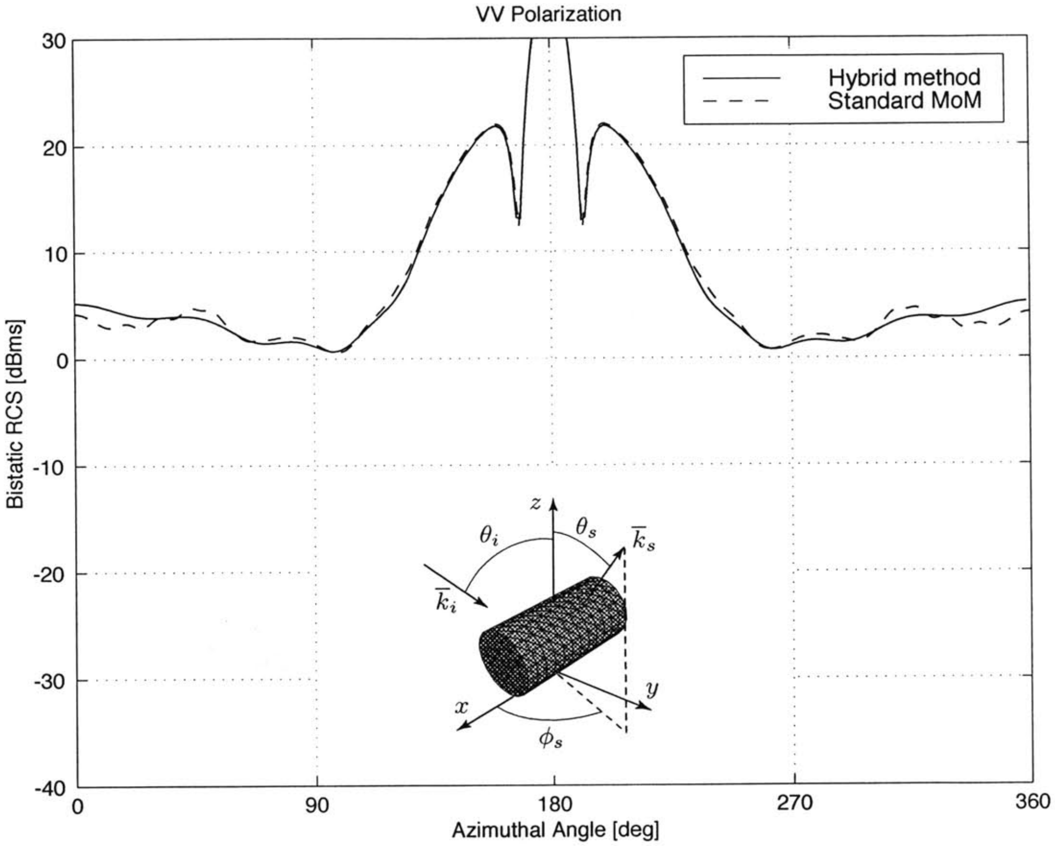

Figure 2-12: The co-polarized bistatic radar cross section (RCS) solved by the layered Green's function approach for a conducting cylinder above a PEC flat surface in comparison with the result from the standard MoM.

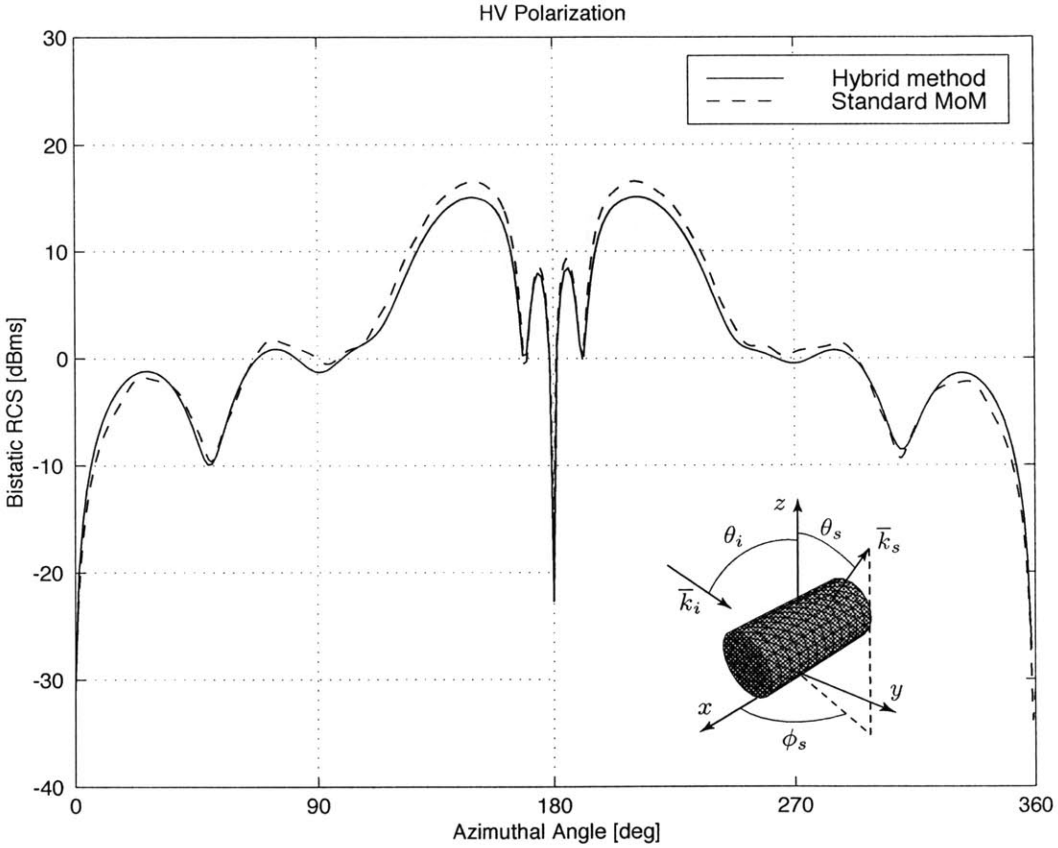

Figure 2-13: The cross-polarized bistatic radar cross section (RCS) solved by the layered Green's function approach for a conducting cylinder above a PEC flat surface in comparison with the result from the standard MoM.

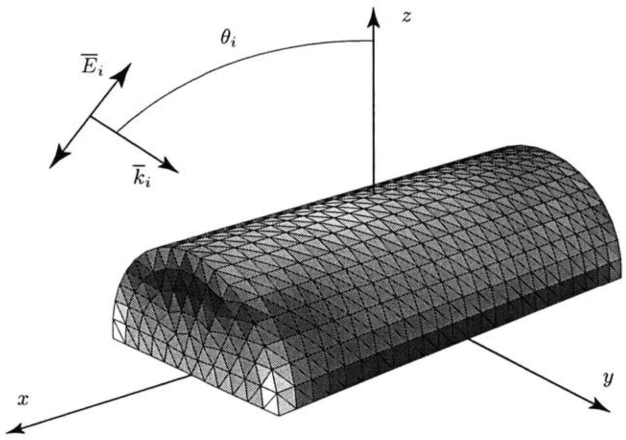

(a) The total surface current $J_s = \sqrt{J_x^2 + J_y^2 + J_z^2}$

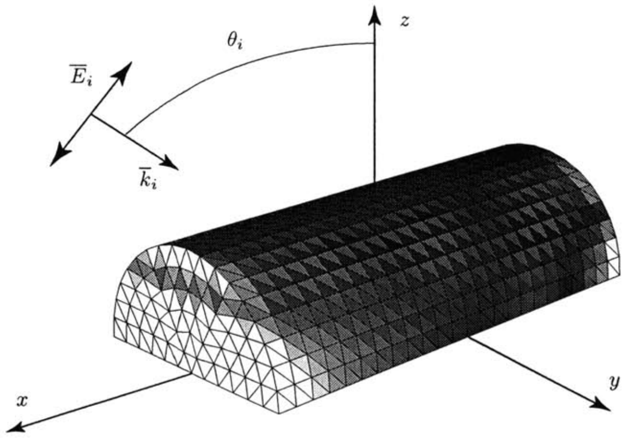

(b) The vertical surface current J_z

Figure 2-14: The induced surface current on a conducting cylinder half buried in a conducting flat surface by a TM incident electric wave.

the truncation of the computational domain. The radar cross section (RCS) of a half cylinder in free space is also calculated and shown by using the dash-dotted line in comparison with the RCS of the cylinder half buried in the conducting surface. Notice that, due to the electromagnetic wave interaction between the object and the surface, the total RCS of the buried cylinder is enhanced in comparison with the RCS of the half cylinder in free space. Also notice that there is a strong specular reflection in the forward direction $\phi_s = 180^\circ$ for the cylinder half buried in the flat surface. The dash-dotted curve is calculated by using the standard MoM. The cross-polarization of the bistatic radar cross section (RCS) is shown in Fig. (2-16). The discrepancy of the simulation results at $\phi_s \approx 0^\circ$ or 360° may be caused by the edge effect in the standard MoM calculation where the flat surface is treated as finite. In the layered Green's function approach, the flat surface is taken to be infinite.

Figure (2-17) and (2-18) are the numerical simulation results for TM incident wave. In these simulations, all other parameters are the same as in Fig. (2-15) and Fig. (2-16). Notice that the bistatic RCS patterns are similar to that of a cylinder half buried in flat surface or in free space. However the RCS for a cylinder half buried in flat surface is about 10 dB higher than in the free space. In Fig. (2-17) the enhancement of the RCS with flat conducting surface demonstrates that the dominant portion of the induced surface current is on the object. This is due to the fact that the TM incident wave is vertically polarized, and that the image of the vertically polarized surface current on the object points in the same direction as the original surface current.

2.5 Conclusions

In this chapter, by modification of the vector and scalar potentials, the EFIE solver of object in free space was applied to the problem for the object on a flat PEC surface. By using the vector and scalar potential as in [23], the integration for the

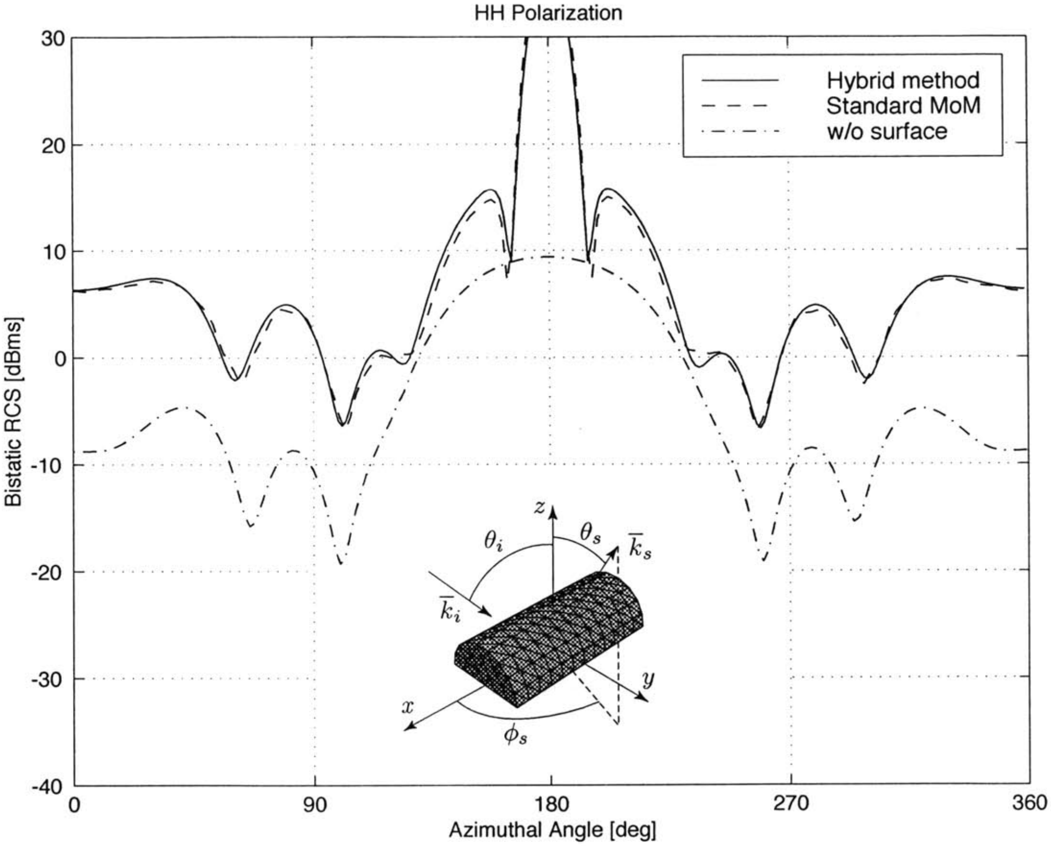

Figure 2-15: The co-polarized bistatic radar cross section (RCS) of a conducting cylinder half buried in a conducting surface in comparison with the RCS of a half cylinder in free space.

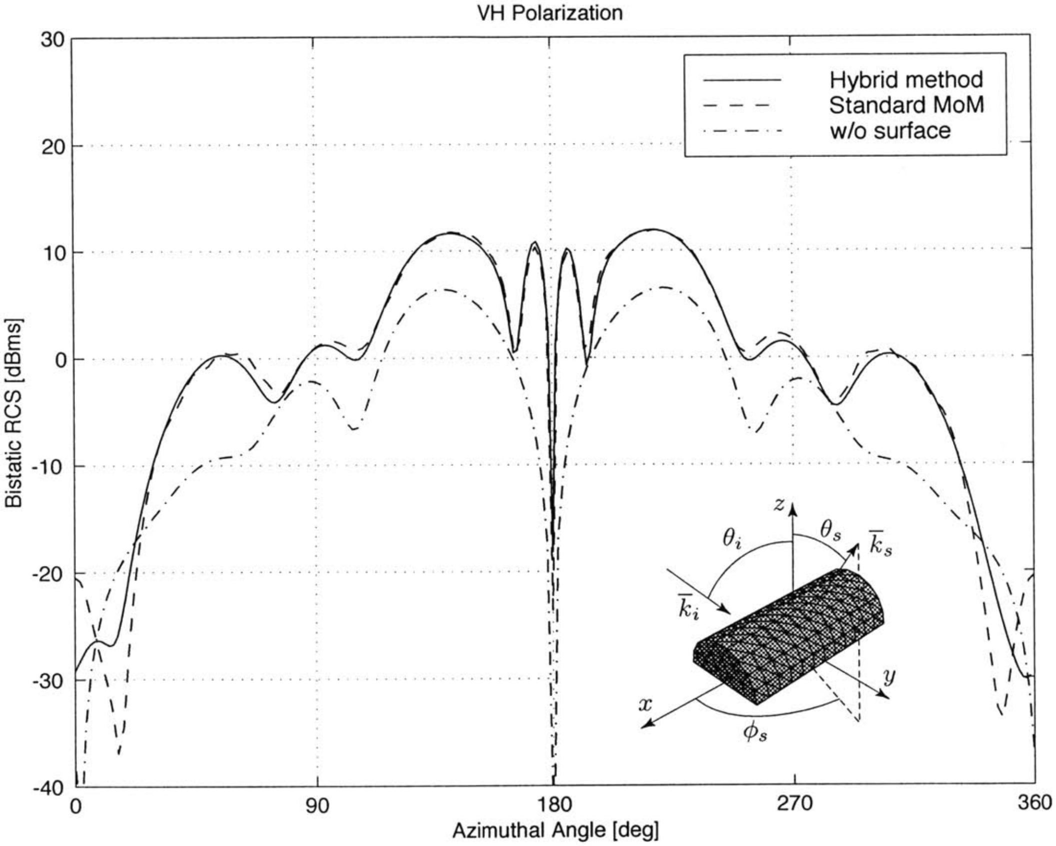

Figure 2-16: The cross-polarized bistatic radar cross section (RCS) of a conducting cylinder half buried in a conducting surface in comparison with the RCS of a half cylinder in free space.

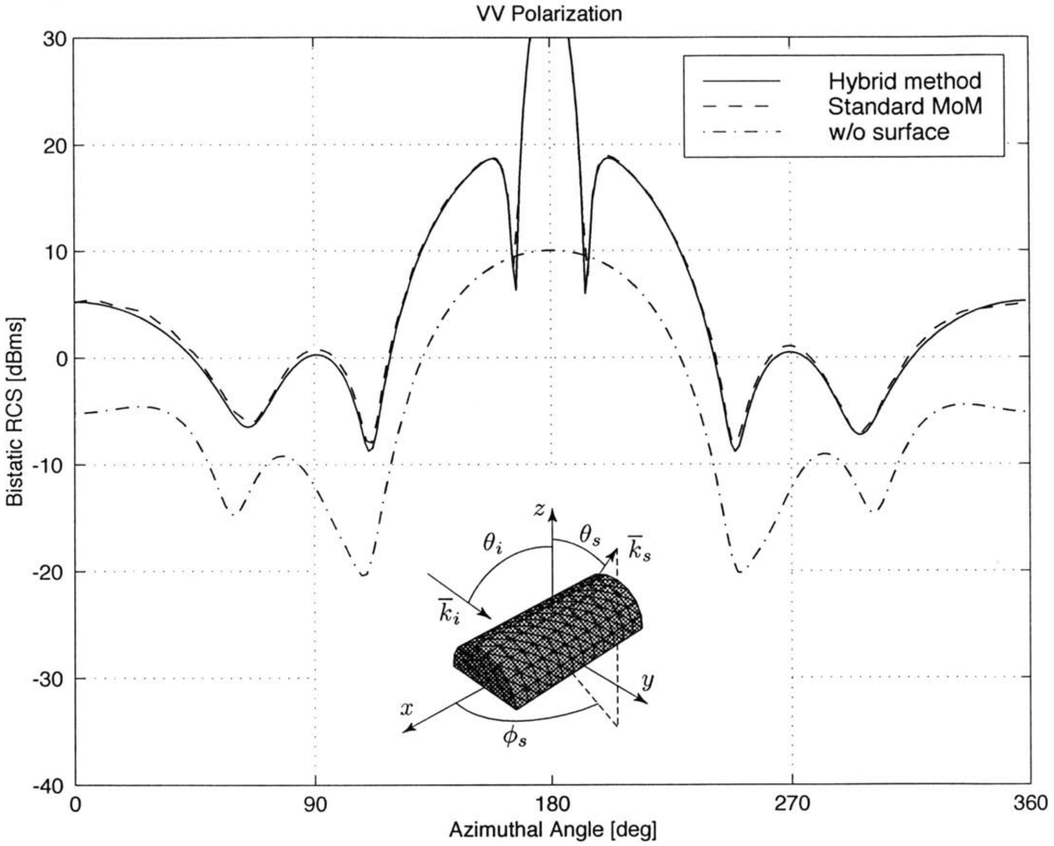

Figure 2-17: The co-polarized bistatic radar cross section (RCS) of a conducting cylinder half buried in a conducting surface in comparison with the RCS of a half cylinder in free space.

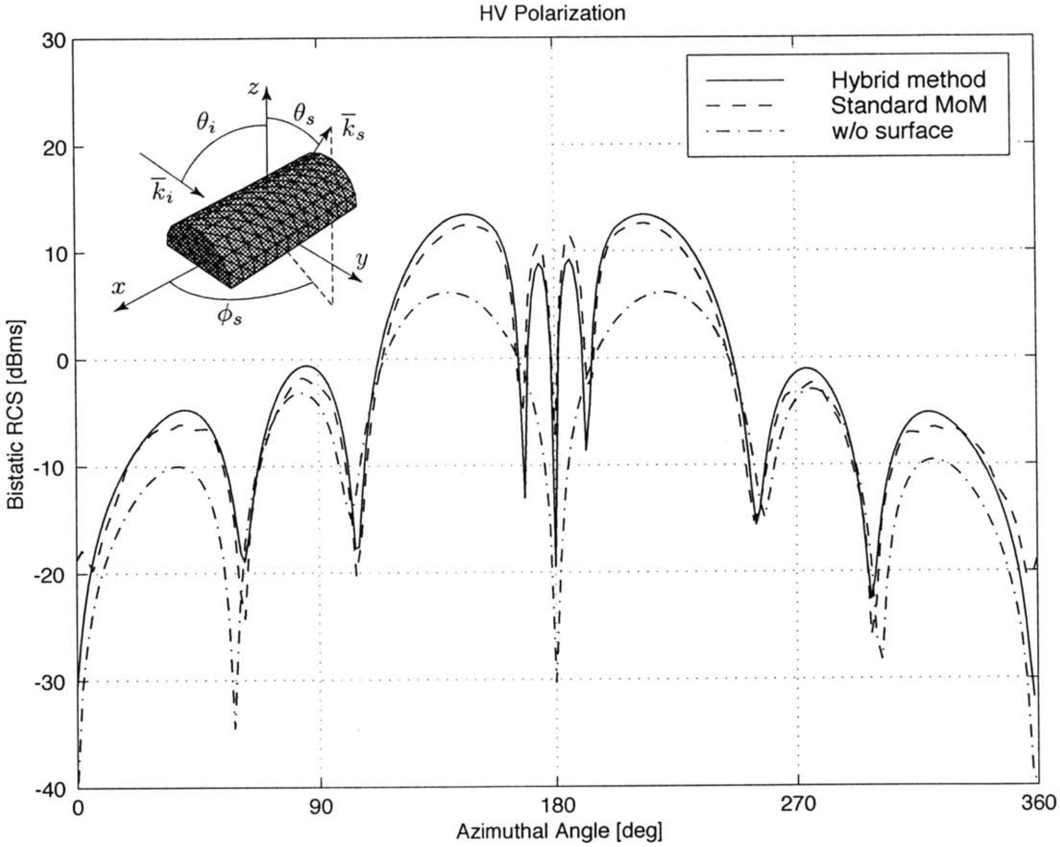

Figure 2-18: The cross-polarized bistatic radar cross section (RCS) of a conducting cylinder half buried in a conducting surface in comparison with the RCS of a half cylinder in free space.

scattered field is simplified with lower order of singularity in comparison with the original integral equation. We have considered the electromagnetic wave scattering by an arbitrary conducting object above a PEC flat surface by writing the scattered field as the integral of induced current multiplied by the Green's function for a PEC half space. The vector and scalar potentials for the object-on-surface problem are derived from the layered Green's function. We compared the numerical results by the layered Green's function approach with the standard method of moments, and good agreements were obtained. In addition, the layered Green's function approach is much more computationally efficient, since unknowns are only associated with the triangular patches on the conducting object. This is in contrast to the standard MoM approach where the unknowns are associated with the patches on the object as well as the flat surface. The interface we considered in this chapter is flat; it is eventually the zeroth order problem of a conducting object above a PEC rough surface which will be discussed in the next chapter.

Chapter 3

Electromagnetic Wave Scattering of Conducting Objects on Rough Surfaces

3.1 Introduction

Recently, there has been a great interest in studying the electromagnetic wave scattering from an object situated above a rough surface [1]–[11]. Simulation techniques for electromagnetic wave scattering by arbitrarily shaped objects in free space are well developed using wire [13]–[15] and surface-patch models [16]–[23]. The theory and numerical approaches associated with objects near flat interfaces of layered media have also been studied extensively by many researchers [11], [32]–[72]. However the consideration of a rough surface interface is a new challenge, and little work has been reported. In theory, the standard MoM can be used to solve for the unknowns both on the object and the rough surface [7, 34, 35]. However, the discretization of the rough surface significantly increases the computational resource requirements compared to calculating the scattering from the object alone. Therefore little literature exists on the study of scattering for full-scale geometry.

In this chapter, we present a hybrid SPM/MoM technique to calculate the EM scattering from a 3-D conducting object above a rough surface [73, 74]. In this hybrid technique, the Green's function and surface variables are expanded in terms of the surface height function on the mean surface, and the electric integral equations based on the extinction theorem and the surface boundary conditions are decomposed into different orders. Each order represents a flat-surface scattering problem with the same geometry and different equivalent sources, so that it can be solved efficiently by using the dyadic Green's function for layered media as discussed in the previous chapter. The separation of the solution into different orders also helps us identify and characterize the individual interaction terms between the object and the rough surface.

3.2 Configuration and Formulations

Consider an electric wave $\overline{E}_i(\bar{r})$ incident upon a perfectly conducting object with arbitrary shape S_1 above a rough surface S_r as shown in Fig. (3-1). The upper and lower spaces V_1 and V_2 are homogeneous, isotropic media characterized by (ϵ_1, μ_1) and (ϵ_2, μ_2), respectively. The rough surface profile is defined by the surface height function $f(\bar{r}'_\perp)$ with mean surface S_o coincident with the xy plane.

3.2.1 Electric Field Integral Equation

On the perfectly conducting surface of the object, the tangential electric field is zero. Thus we can write the electric field integral equation for $\bar{r} \in S_1$ as

$$\begin{aligned}\Bigg(\overline{E}_i(\bar{r}) \; + \; & \int_{S_r} dS' \left\{ i\omega\mu_1 \overline{\overline{G}}_1(\bar{r},\bar{r}') \cdot \left[\hat{n}_1(\bar{r}') \times \overline{H}_1(\bar{r}')\right] + \nabla \times \overline{\overline{G}}_1(\bar{r},\bar{r}') \cdot \left[\hat{n}_1(\bar{r}') \times \overline{E}_1(\bar{r}')\right]\right\} \\ & + i\omega\mu_1 \int_{S_1} dS' \, \overline{\overline{G}}_1(\bar{r},\bar{r}') \cdot \overline{J}_1(\bar{r}') \Bigg) \times \hat{n}_o(\bar{r}) = 0. \qquad (3.1)\end{aligned}$$

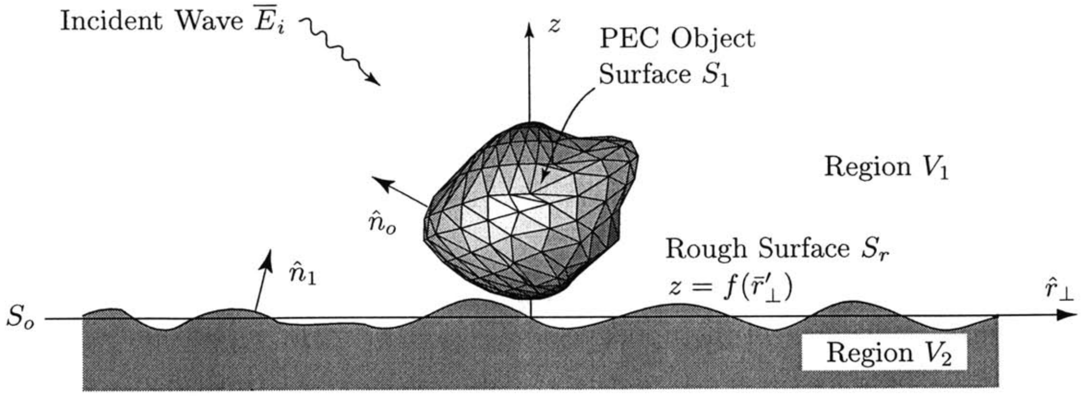

Figure 3-1: Configuration of the problem: An electromagnetic wave incident upon a PEC body above a rough surface.

By applying the extinction theorem, we get for $\bar{r} \in V_2$

$$\begin{aligned}\overline{E}_i(\bar{r}) \quad + \quad & \int_{S_r} dS' \left\{ i\omega\mu_1 \overline{\overline{G}}_1(\bar{r},\bar{r}') \cdot \left[\hat{n}_1(\bar{r}') \times \overline{H}_1(\bar{r}')\right] + \nabla \times \overline{\overline{G}}_1(\bar{r},\bar{r}') \cdot \left[\hat{n}_1(\bar{r}') \times \overline{E}_1(\bar{r}')\right]\right\} \\ & + i\omega\mu_1 \int_{S_1} dS' \, \overline{\overline{G}}_1(\bar{r},\bar{r}') \cdot \overline{J}_1(\bar{r}') = 0, \end{aligned} \tag{3.2}$$

and for $\bar{r} \in V_1$

$$\int_{S_r} dS' \left\{ i\omega\mu_2 \overline{\overline{G}}_2(\bar{r},\bar{r}') \cdot \left[\hat{n}_2(\bar{r}') \times \overline{H}_2(\bar{r}')\right] + \nabla \times \overline{\overline{G}}_2(\bar{r},\bar{r}') \cdot \left[\hat{n}_2(\bar{r}') \times \overline{E}_2(\bar{r}')\right]\right\} = 0, \tag{3.3}$$

where $\overline{\overline{G}}_1$ and $\overline{\overline{G}}_2$ are dyadic Green's functions for unbounded regions with (ϵ_1, μ_1) and (ϵ_2, μ_2), respectively. The vector $\hat{n}_1(\bar{r}')$ denotes a local normal pointing from the rough surface S_r to the upper region V_1. The vector $\hat{n}_2(\bar{r}')$ is anti-parallel to $\hat{n}_1(\bar{r}')$, i.e., $\hat{n}_2(\bar{r}') = -\hat{n}_1(\bar{r}')$. $\overline{E}_1(\bar{r}')$ and $\overline{H}_1(\bar{r}')$ are electric and magnetic fields on the rough surface in region V_1, while $\overline{E}_2(\bar{r}')$ and $\overline{H}_2(\bar{r}')$ are surface fields on S_r in region V_2. $\overline{J}_1(\bar{r}')$ is the induced surface current on the object. If region V_2 is dielectric, the tangential fields are continuous, thus

$$\hat{n}_1(\bar{r}') \times \overline{H}_1(\bar{r}') = \hat{n}_1(\bar{r}') \times \overline{H}_2(\bar{r}') \equiv \frac{1}{\eta_1}\frac{d\bar{r}'_\perp}{dS'}\bar{a}(\bar{r}'_\perp), \tag{3.4}$$

$$\hat{n}_1(\bar{r}') \times \overline{E}_1(\bar{r}') = \hat{n}_1(\bar{r}') \times \overline{E}_2(\bar{r}') \equiv \frac{d\bar{r}'_\perp}{dS'}\bar{b}(\bar{r}'_\perp), \tag{3.5}$$

where $\bar{a}(\bar{r}'_\perp)$ and $\bar{b}(\bar{r}'_\perp)$ are new surface variables defined on the mean surface S_o, η_1 is the intrinsic impedance of the upper region V_1, i.e., $\eta_1 = (\mu_1/\epsilon_1)^{1/2}$, and $d\bar{r}'_\perp$ is the projection of the infinitesimal area dS' on the mean surface S_o. With the new surface variables, we can rewrite the integral equations as

$$\begin{aligned}&\Big(\overline{E}_i(\bar{r}) + \int_{S_o} d\bar{r}'_\perp \left\{ik_1 \overline{\overline{G}}_1(\bar{r},\bar{r}') \cdot \bar{a}(\bar{r}'_\perp) + \nabla \times \overline{\overline{G}}_1(\bar{r},\bar{r}') \cdot \bar{b}(\bar{r}'_\perp)\right\}\\ &+i\omega\mu_1 \int_{S_1} dS' \overline{\overline{G}}_1(\bar{r},\bar{r}') \cdot \overline{J}_1(\bar{r}')\Big) \times \hat{n}_o(\bar{r}) = 0 \qquad \text{for } \bar{r} \in S_1,\end{aligned} \tag{3.6}$$

$$\begin{aligned}\overline{E}_i(\bar{r}) \quad + \quad & \int_{S_o} d\bar{r}'_\perp \left\{ik_1 \overline{\overline{G}}_1(\bar{r},\bar{r}') \cdot \bar{a}(\bar{r}'_\perp) + \nabla \times \overline{\overline{G}}_1(\bar{r},\bar{r}') \cdot \bar{b}(\bar{r}'_\perp)\right\}\\ & +i\omega\mu_1 \int_{S_1} dS' \overline{\overline{G}}_1(\bar{r},\bar{r}') \cdot \overline{J}_1(\bar{r}') = 0 \qquad \text{for } \bar{r} \in V_2,\end{aligned} \tag{3.7}$$

$$\int_{S_o} d\bar{r}'_\perp \left\{ik_2 \frac{\eta_2}{\eta_1} \overline{\overline{G}}_2(\bar{r},\bar{r}') \cdot \bar{a}(\bar{r}'_\perp) + \nabla \times \overline{\overline{G}}_2(\bar{r},\bar{r}') \cdot \bar{b}(\bar{r}'_\perp)\right\} = 0 \qquad \text{for } \bar{r} \in V_1. \tag{3.8}$$

Theoretically, given the rough surface S_r and the object surface profile S_1, the unknown surface variables $\bar{a}(\bar{r}'_\perp)$, $\bar{b}(\bar{r}'_\perp)$ and the induced current $\overline{J}_1(\bar{r}')$ can be solved from Eqs. (3.6)–(3.8). For the special case in which the interface is flat, the surface variables $\bar{a}(\bar{r}'_\perp)$ and $\bar{b}(\bar{r}'_\perp)$ have only horizontal components and the local coordinate $\bar{r}'$ in the dyadic Green's functions $\overline{\overline{G}}_1(\bar{r},\bar{r}')$ and $\overline{\overline{G}}_2(\bar{r},\bar{r}')$ can be replaced by $\bar{r}'_\perp$.

3.2.2 Expansion of Green's Function and Surface Variables

As shown in Fig. (3-2), the local position vector $\bar{r}'$ on the rough surface can be expressed as the sum of the horizontal vector $\bar{r}'_\perp$ and the vertical vector $\hat{z}\, f\,(\bar{r}'_\perp)$. Therefore the scalar Green's function g_α in region V_α (where $\alpha = 1, 2$) can be expanded in terms of the surface height function $f(\bar{r}'_\perp)$ on the mean surface S_o,

$$\begin{aligned} g_\alpha(\bar{r},\bar{r}') &= \frac{e^{ik_\alpha|\bar{r}-\bar{r}'|}}{4\pi\,|\bar{r}-\bar{r}'|} \\ &= g_\alpha\left(\bar{r},\bar{r}'_\perp + \hat{z}f(\bar{r}'_\perp)\right) \\ &= \sum_{m=0}^{\infty}\frac{1}{m!}\frac{\partial^m}{\partial z'^m}g_\alpha\left(\bar{r},\bar{r}'_\perp\right)f^m(\bar{r}'_\perp) \\ &= \sum_{m=0}^{\infty}\frac{1}{m!}\frac{\partial^m}{\partial z^m}g_\alpha\left(\bar{r},\bar{r}'_\perp\right)\left(-f(\bar{r}'_\perp)\right)^m, \end{aligned} \tag{3.9}$$

in which the following property of the scalar Green's function has been used:

$$\frac{\partial^m}{\partial z'^m}g_\alpha\left(\bar{r},\bar{r}'\right) = (-1)^m\frac{\partial^m}{\partial z^m}g_\alpha\left(\bar{r},\bar{r}'\right). \tag{3.10}$$

Thus the dyadic Green's function can be expressed as

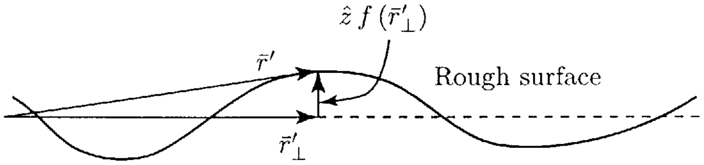

Figure 3-2: The local position vector $\bar{r}'$ on the rough surface is the sum of the horizontal and vertical vectors.

$$\overline{\overline{G}}_\alpha(\bar{r},\bar{r}') = \left(\overline{\overline{I}} + \frac{1}{k_\alpha^2}\nabla\nabla\right)g_\alpha(\bar{r},\bar{r}') = \sum_{m=0}^{\infty}\frac{1}{m!}\left(-f(\bar{r}'_\perp)\right)^m\frac{\partial^m}{\partial z^m}\overline{\overline{G}}_\alpha\left(\bar{r},\bar{r}'_\perp\right). \tag{3.11}$$

Similarly, the surface variables and induced current can be written as series expansions as follows:

$$\overline{J}_1(\bar{r}') = \sum_{m=0}^{\infty} \overline{J}_1^{(m)}(\bar{r}'), \tag{3.12}$$

$$\bar{a}(\bar{r}'_\perp) = \sum_{m=0}^{\infty} \left[\bar{a}_\perp^{(m)}(\bar{r}'_\perp) + \hat{z}a_z^{(m)}(\bar{r}'_\perp)\right], \tag{3.13}$$

$$\bar{b}(\bar{r}'_\perp) = \sum_{m=0}^{\infty} \left[\bar{b}_\perp^{(m)}(\bar{r}'_\perp) + \hat{z}b_z^{(m)}(\bar{r}'_\perp)\right]. \tag{3.14}$$

In Eqs. (3.13) and (3.14), the separation of the z-components for the surface variables $\bar{a}$ and $\bar{b}$ allows the only unknown surface variables to become the tangential components since the z-components of the m-th order can be expressed in terms of the tangential components of order $(m-1)$, as we will see below.

By the definition of $\bar{a}$ and $\bar{b}$ [Eqs. (3.4) and (3.5)], the following identities hold:

$$\hat{n}_1(\bar{r}'_\perp) \cdot \bar{a}(\bar{r}'_\perp) = 0, \tag{3.15}$$

$$\hat{n}_1(\bar{r}'_\perp) \cdot \bar{b}(\bar{r}'_\perp) = 0, \tag{3.16}$$

where

$$\hat{n}_1(\bar{r}'_\perp) = \frac{-\nabla'_\perp f(\bar{r}'_\perp) + \hat{z}}{|-\nabla'_\perp f(\bar{r}'_\perp) + \hat{z}|}. \tag{3.17}$$

Substituting the series expansions of $\bar{a}$ and $\bar{b}$, Eqs. (3.13) and (3.14), into Eqs. (3.15) and (3.16), respectively, and assuming that $\partial f(\bar{r}'_\perp)/\partial x'$ and $\partial f(\bar{r}'_\perp)/\partial y'$ are of the same order as $k_1 f(\bar{r}'_\perp)$, we then get the m-th order z-components of the surface variables $\bar{a}$ and $\bar{b}$ in terms of their $(m-1)$-th order tangential components:

$$a_z^{(m)}(\bar{r}'_\perp) = \nabla'_\perp f(\bar{r}'_\perp) \cdot \bar{a}_\perp^{(m-1)}(\bar{r}'_\perp), \tag{3.18}$$

$$b_z^{(m)}(\bar{r}'_\perp) = \nabla'_\perp f(\bar{r}'_\perp) \cdot \bar{b}_\perp^{(m-1)}(\bar{r}'_\perp). \tag{3.19}$$

3.2.3 The n-th Order Equation

Substituting the series expansion for the dyadic Green's function Eq. (3.11) and the surface variables $\bar{a}$ and $\bar{b}$ as in Eqs. (3.13) and (3.14) into the integral equations (3.6)–(3.8), we can derive the following n-th order equations in terms of the surface height function $f(\bar{r}'_\perp)$:

$$\begin{aligned}\Big(\overline{E}_i^{(n)}(\bar{r}) + \int_{S_o} d\bar{r}'_\perp \left\{ik_1 \overline{\overline{G}}_1(\bar{r},\bar{r}'_\perp)\cdot\bar{a}_\perp^{(n)}(\bar{r}'_\perp) + \nabla\times\overline{\overline{G}}_1(\bar{r},\bar{r}'_\perp)\cdot\bar{b}_\perp^{(n)}(\bar{r}'_\perp)\right\}\\ +i\omega\mu_1\int_{S_1} dS'\,\overline{\overline{G}}_1(\bar{r},\bar{r}')\cdot\overline{J}_1^{(n)}(\bar{r}')\Big)\times\hat{n}_o(\bar{r}) = 0 \qquad \text{for } \bar{r}\in S_1,\end{aligned} \tag{3.20}$$

$$\begin{aligned}\overline{E}_i^{(n)}(\bar{r}) \;+\; & \int_{S_o} d\bar{r}'_\perp \left\{ik_1 \overline{\overline{G}}_1(\bar{r},\bar{r}'_\perp)\cdot\bar{a}_\perp^{(n)}(\bar{r}'_\perp) + \nabla\times\overline{\overline{G}}_1(\bar{r},\bar{r}'_\perp)\cdot\bar{b}_\perp^{(n)}(\bar{r}'_\perp)\right\}\\ & +i\omega\mu_1\int_{S_1} dS'\,\overline{\overline{G}}_1(\bar{r},\bar{r}')\cdot\overline{J}_1^{(n)}(\bar{r}') = 0 \qquad \text{for } \bar{r}\in V_2,\end{aligned} \tag{3.21}$$

$$\begin{aligned}\overline{E}_{i2}^{(n)}(\bar{r}) \;+\; \int_{S_o} d\bar{r}'_\perp \left\{ik_2\frac{\eta_2}{\eta_1} \overline{\overline{G}}_2(\bar{r},\bar{r}'_\perp)\cdot\bar{a}_\perp^{(n)}(\bar{r}'_\perp) + \nabla\times\overline{\overline{G}}_2(\bar{r},\bar{r}'_\perp)\cdot\bar{b}_\perp^{(n)}(\bar{r}'_\perp)\right\} = 0\\ \text{for } \bar{r}\in V_1,\end{aligned} \tag{3.22}$$

where for $n = 0$,

$$\overline{E}_i^{(0)}(\bar{r}) = \overline{E}_i(\bar{r}), \tag{3.23}$$

$$\overline{E}_{i2}^{(0)}(\bar{r}) = 0, \tag{3.24}$$

and for $n \geq 1$,

$$\begin{aligned}\overline{E}_i^{(n)}(\bar{r}) \;=\; & \sum_{m=1}^{n}\frac{1}{m!}\int d\bar{r}'_\perp\,[-f(\bar{r}'_\perp)]^m\\ & \frac{\partial^m}{\partial z^m}\left\{ik_1 \overline{\overline{G}}_1(\bar{r},r'_\perp)\cdot a_\perp^{(n-m)}(r'_\perp) + \nabla\times\overline{\overline{G}}_1(r,r'_\perp)\cdot\bar{b}_\perp^{(n-m)}(\bar{r}'_\perp)\right\}\\ & +\sum_{m=1}^{n}\frac{1}{(m-1)!}\int d\bar{r}'_\perp\,[-f(\bar{r}'_\perp)]^{m-1}\end{aligned}$$

$$\begin{aligned}
&\frac{\partial^{m-1}}{\partial z^{m-1}}\left\{ik_1\overline{\overline{G}}_1\left(\bar{r},\bar{r}'_\perp\right)\cdot\hat{z}\left[\nabla'_\perp f(\bar{r}'_\perp)\cdot\bar{a}_\perp^{(n-m)}(\bar{r}'_\perp)\right]\right.\\
&\left.+\nabla\times\overline{\overline{G}}_1\left(\bar{r},\bar{r}'_\perp\right)\cdot\hat{z}\left[\nabla'_\perp f(\bar{r}'_\perp)\cdot\bar{b}_\perp^{(n-m)}(\bar{r}'_\perp)\right]\right\},
\end{aligned}\tag{3.25}$$

$$\begin{aligned}
\overline{E}_{i2}^{(n)}(\bar{r}) \;=\; &\sum_{m=1}^{n}\frac{1}{m!}\int d\bar{r}'_\perp\left[-f(\bar{r}'_\perp)\right]^m\\
&\frac{\partial^m}{\partial z^m}\left\{ik_2\frac{\eta_2}{\eta_1}\overline{\overline{G}}_2\left(\bar{r},\bar{r}'_\perp\right)\cdot\bar{a}_\perp^{(n-m)}(\bar{r}'_\perp)+\nabla\times\overline{\overline{G}}_2(\bar{r},\bar{r}'_\perp)\cdot\bar{b}_\perp^{(n-m)}(\bar{r}'_\perp)\right\}\\
&+\sum_{m=1}^{n}\frac{1}{(m-1)!}\int d\bar{r}'_\perp\left[-f(\bar{r}'_\perp)\right]^{m-1}\\
&\frac{\partial^{m-1}}{\partial z^{m-1}}\left\{ik_2\frac{\eta_2}{\eta_1}\overline{\overline{G}}_2\left(\bar{r},\bar{r}'_\perp\right)\cdot\hat{z}\left[\nabla'_\perp f(\bar{r}'_\perp)\cdot\bar{a}_\perp^{(n-m)}(\bar{r}'_\perp)\right]\right.\\
&\left.+\nabla\times\overline{\overline{G}}_2(\bar{r},\bar{r}'_\perp)\cdot\hat{z}\left[\nabla'_\perp f(\bar{r}'_\perp)\cdot\bar{b}_\perp^{(n-m)}(\bar{r}'_\perp)\right]\right\}.
\end{aligned}\tag{3.26}$$

Comparing the zeroth order ($n = 0$) integral equations with Eqs. (3.6)–(3.8) for the flat interface ($f(\bar{r}'_\perp) = 0$), we see that they are the same except for an additional superscript (0) to the surface variables $\bar{a}_\perp$ and $\bar{b}_\perp$ and to the induced current $\overline{J}_1$. Therefore, the solutions $\bar{a}_\perp^{(0)}$, $\bar{b}_\perp^{(0)}$, and $\overline{J}_1^{(0)}$ for the zeroth order equations should be the same as the ones for Eqs. (3.6)–(3.8) in which the rough surface is considered to be flat. For the higher order equations ($n \geq 1$), we find that they are also in the same form as the zeroth order equations, except for the substitution of $\overline{E}_i$ by $\overline{E}_i^{(n)}$, and the additional "source" term $\overline{E}_{i2}^{(n)}$ in the lower region. Therefore we only need to solve the zeroth order equations, i.e., the equations for an object over a flat interface.

Since the equations of any order are equivalent to the ones for a flat interface, they can be rewritten by introducing the dyadic Green's function for layered media. The advantage of this approach is that it avoids solving surface unknowns $\bar{a}_\perp^{(n)}$ and $\bar{b}_\perp^{(n)}$ on the interface. Only the induced current $\overline{J}_1^{(n)}$ on the conducting body need be solved. Therefore both the computational time and memory requirement are dramatically reduced.

3.2.4 Application to PEC Rough Surface

As an example, we now consider the rough surface to be perfectly conducting. In this case the zeroth order electric field integral equation (EFIE) can be written as

$$\hat{n}_o(\bar{r}) \times \left(\overline{E}_i^{(0)}(\bar{r}) + \overline{E}_r^{(0)}(\bar{r}) + i\omega\mu_1 \int_{S_1} dS' \,\overline{\overline{G}}_L(\bar{r}, \bar{r}') \cdot \overline{J}_1^{(0)}(\bar{r}') \right) = 0 \qquad \text{for } \bar{r} \in S_1, \tag{3.27}$$

and the n-th order ($n \geq 1$) EFIE can be written as

$$\hat{n}_o(\bar{r}) \times \left(\overline{E}_i^{(n)}(\bar{r}) + \overline{E}_r^{(n)}(\bar{r}) + i\omega\mu_1 \int_{S_1} dS' \,\overline{\overline{G}}_L(\bar{r}, \bar{r}') \cdot \overline{J}_1^{(n)}(\bar{r}') \right) = 0 \qquad \text{for } \bar{r} \in S_1, \tag{3.28}$$

where

$$\begin{aligned} \overline{E}_i^{(n)}(\bar{r}) \;=\; & \sum_{m=1}^{n} \frac{1}{m!} \int d\bar{r}'_\perp \left[-f(\bar{r}'_\perp)\right]^m \frac{\partial^m}{\partial z^m} \left\{ ik_1 \overline{\overline{G}}_1\left(\bar{r}, \bar{r}'_\perp\right) \cdot \bar{a}_\perp^{(n-m)}(\bar{r}'_\perp) \right\} \\ & + \sum_{m=1}^{n} \frac{1}{(m-1)!} \int d\bar{r}'_\perp \left[-f(\bar{r}'_\perp)\right]^{m-1} \\ & \frac{\partial^{m-1}}{\partial z^{m-1}} \left\{ ik_1 \overline{\overline{G}}_1\left(\bar{r}, \bar{r}'_\perp\right) \cdot \hat{z} \left[\nabla'_\perp f(\bar{r}'_\perp) \cdot \bar{a}_\perp^{(n-m)}(\bar{r}'_\perp)\right] \right\}, \end{aligned} \tag{3.29}$$

and the dyadic Green's function for a conducting interface is [cf. Ch. 2.3.1]

$$\overline{\overline{G}}_L(\bar{r}, \bar{r}') = \overline{\overline{G}}_1(\bar{r}, \bar{r}') - \overline{\overline{G}}_1(\bar{r}, (\overline{\overline{I}} - 2\hat{z}\hat{z}) \cdot \bar{r}') \cdot (\overline{\overline{I}} - 2\hat{z}\hat{z}), \tag{3.30}$$

where $\overline{\overline{G}}_1$ is the dyadic Green's function in the unbounded medium of region V_1. The singularities of the dyadic Green's functions in Eqs. (3.27) and (3.28) can be reduced by using a triangular patch model in [23] for the conducting surface of the object.

The surface field $\bar{a}_\perp$ of lower order can be obtained from the lower order scattered field due to object and equivalent source. For example, the first order surface variable $\bar{a}_\perp^{(1)}$ can be calculated by using the solution of the zeroth order induced current $\overline{J}_1^{(0)}$

and the incident and reflected magnetic fields in absence of the object,

$$\bar{a}_{\perp}^{(0)}(\bar{r}'_{\perp}) = \eta_1 \hat{z} \times \left(\overline{H}_{i1}(\bar{r}'_{\perp}) + \overline{H}_{r1}(\bar{r}'_{\perp}) + \int_{S_1} dS'' \nabla' \times \overline{\overline{G}}_L(\bar{r}'_{\perp}, \bar{r}'') \cdot \overline{J}_1^{(0)}(\bar{r}'') \right). \quad (3.31)$$

The higher order ($n \geq 2$) surface variable $\bar{a}_{\perp}^{(n)}$ can be obtained similarly but involves a lot of manipulations.

Up to the first order, the total returned field can be written as

$$\overline{E}_s(\bar{r}) = \overline{E}_r(\bar{r}) + \overline{E}_b(\bar{r}) + \overline{E}_c(\bar{r}) + \overline{E}_d(\bar{r}), \quad (3.32)$$

where

$$\begin{aligned} \overline{E}_b(\bar{r}) &= i\omega\mu_1 \int_{S_1} dS' \overline{\overline{G}}_L(\bar{r}, \bar{r}') \cdot \overline{J}_1^{(0)}(\bar{r}'), && (3.33) \\ \overline{E}_c(\bar{r}) &= \overline{E}_i^{(1)}(\bar{r}) + \overline{E}_r^{(1)}(\bar{r}), && (3.34) \\ \overline{E}_d(\bar{r}) &= i\omega\mu_1 \int_{S_1} dS' \overline{\overline{G}}_L(\bar{r}, \bar{r}') \cdot \overline{J}_1^{(1)}(\bar{r}'). && (3.35) \end{aligned}$$

and

$$\begin{aligned} \overline{E}_i^{(1)}(\bar{r}) &= -ik_1 \int d\bar{r}'_{\perp} f(\bar{r}'_{\perp}) \frac{\partial}{\partial z} \overline{\overline{G}}_1(\bar{r}, \bar{r}'_{\perp}) \cdot \bar{a}_{\perp}^{(0)}(\bar{r}'_{\perp}) \\ &\quad + ik_1 \int d\bar{r}'_{\perp} \overline{\overline{G}}_1(\bar{r}, \bar{r}'_{\perp}) \cdot \hat{z} \left[\nabla'_{\perp} f(\bar{r}'_{\perp}) \cdot \bar{a}_{\perp}^{(0)}(\bar{r}'_{\perp}) \right]. \quad (3.36) \end{aligned}$$

In Eq. (3.32), $\overline{E}_r(\bar{r})$ is simply the reflected field from the flat interface in absence of the conducting object. In the expression for $\overline{E}_b(\bar{r})$ [Eq. (3.33)], the induced current $\overline{J}_1^{(0)}$ is obtained by solving the integral equation (3.27) with layered Green's function, therefore the returned field $\overline{E}_b(\bar{r})$ includes all interactions between object and flat interface. $\overline{E}_c(\bar{r})$ in Eq. (3.34) is the sum of the radiated field from the "equivalent source" and its reflection, as illustrated in Fig. (3-3). The reflected field of the equivalent source can be obtained by writing the unbounded dyadic Green's function in integral form as in Appendix B, thus the radiated field of the equivalent source $\overline{E}_i^{(1)}$

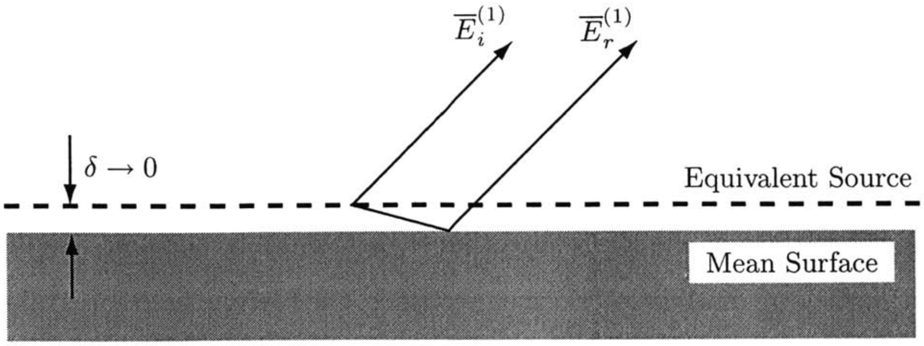

Figure 3-3: Radiation and reflection of the equivalent source.

is expressed as the sum of plane waves. By using the Fresnel reflection coefficient for each plane wave component, it is easy to write the reflected field $\overline{E}_r^{(1)}$ by multiplying with R^{TE} and R^{TM} to obtain the reflected TE and TM waves, respectively. For a non-penetrable surface $R^{TE} = -1$ and $R^{TM} = 1$, thus we find

$$\overline{E}_r^{(1)}(\bar{r}) = \overline{E}_i^{(1)}(\bar{r}). \tag{3.37}$$

Therefore the returned field due to the equivalent source is simply

$$\overline{E}_c(\bar{r}) = 2\overline{E}_i^{(1)}(\bar{r}). \tag{3.38}$$

It can also be shown that the returned field $\overline{E}_c(\bar{r})$ as in Eq. (3.38) is the same as the first order SPM solution for a conducting rough surface if we let the induced current $\overline{J}_1^{(0)} = 0$ when evaluating the surface field $\bar{a}_\perp^{(0)}(\bar{r}'_\perp)$ in Eq. (3.31). Therefore, we call $\overline{E}_c(\bar{r})$ the "incoherent" returned field from the rough surface under the influence of the object. The returned field $\overline{E}_d(\bar{r})$ is the radiated field of the first order induced current $\overline{J}_1^{(1)}$ excited by the "incoherent" field $\overline{E}_c(\bar{r})$. Since the layered Green's function is used to calculate the induced current $\overline{J}_1^{(1)}$ and its radiated field, the returned field $\overline{E}_d(\bar{r})$ includes all multiple interactions between the object and the conducting interface.

3.2.5 Object Half-Buried in a PEC Rough Surface

For the case that a perfectly conducting object half-buried in a rough surface, the change of the equivalent source due to the effect of touching areas on the rough surface and the surface of the PEC object must be taken into account. As illustrated in Fig. (3-4) for the general dielectric rough surface, the electric field integral equation for $\bar{r} \in S_1$ and $\bar{r} \in S_2$ can be written as follows, respectively:

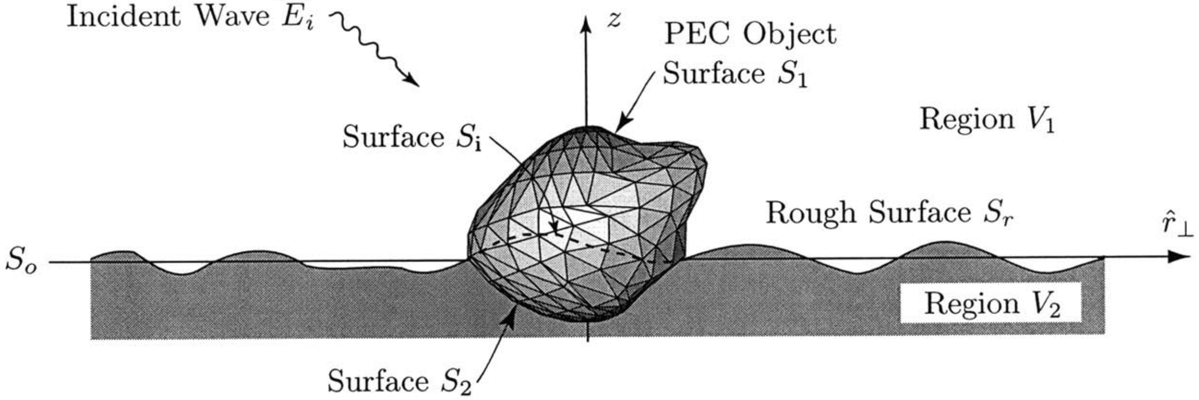

Figure 3-4: A PEC object half-buried in a rough surface.

$$\begin{aligned}\Bigg(\overline{E}_i(\bar{r}) \;+\; \int_{S_r-S_i} dS' \Big(& i\omega\mu_1\overline{\overline{G}}_1(\bar{r},\bar{r}')\cdot\big[\hat{n}_1(\bar{r}')\times\overline{H}_1(\bar{r}')\big] \\ &+\nabla\times\overline{\overline{G}}_1(\bar{r},\bar{r}')\cdot\big[\hat{n}_1(\bar{r}')\times\overline{E}_1(\bar{r}')\big]\Big) \\ &+i\omega\mu_1\int_{S_1} dS'\overline{\overline{G}}_1(\bar{r},\bar{r}')\cdot\overline{J}_1(\bar{r}')\Bigg)\times\hat{n}_o(\bar{r})=0,\end{aligned} \tag{3.39}$$

$$\begin{aligned}&\Bigg(\int_{S_r-S_i} dS' \Big(i\omega\mu_2\overline{\overline{G}}_2(\bar{r},\bar{r}')\cdot\big[\hat{n}_2(\bar{r}')\times\overline{H}_2(\bar{r}')\big]+\nabla\times\overline{\overline{G}}_2(\bar{r},\bar{r}')\cdot\big[\hat{n}_2(\bar{r}')\times\overline{E}_2(\bar{r}')\big]\Big) \\ &+i\omega\mu_2\int_{S_2} dS'\overline{\overline{G}}_2(\bar{r},\bar{r}')\cdot\overline{J}_2(\bar{r}')\Bigg)\times\hat{n}_o(\bar{r})=0.\end{aligned} \tag{3.40}$$

By applying the extinction theorem, we get the EFIEs for $\bar{r} \in V_2$ and $\bar{r} \in V_1$ regions, respectively,

$$\begin{aligned} \overline{E}_i(\bar{r}) \quad + \quad & \int_{S_r - S_i} dS' \left(i\omega\mu_1 \overline{\overline{G}}_1(\bar{r}, \bar{r}') \cdot \left[\hat{n}_1(\bar{r}') \times \overline{H}_1(\bar{r}') \right] \right. \\ & \left. + \nabla \times \overline{\overline{G}}_1(\bar{r}, \bar{r}') \cdot \left[\hat{n}_1(\bar{r}') \times \overline{E}_1(\bar{r}') \right] \right) \\ & + i\omega\mu_1 \int_{S_1} dS' \overline{\overline{G}}_1(\bar{r}, \bar{r}') \cdot \overline{J}_1(\bar{r}') = 0, \end{aligned} \tag{3.41}$$

$$\begin{aligned} & \int_{S_r - S_i} dS' \left(i\omega\mu_2 \overline{\overline{G}}_2(\bar{r}, \bar{r}') \cdot \left[\hat{n}_1(\bar{r}') \times \overline{H}_1(\bar{r}') \right] + \nabla \times \overline{\overline{G}}_2(\bar{r}, \bar{r}') \cdot \left[\hat{n}_1(\bar{r}') \times \overline{E}_1(\bar{r}') \right] \right) \\ & + i\omega\mu_2 \int_{S_2} dS' \overline{\overline{G}}_2(\bar{r}, \bar{r}') \cdot \overline{J}_2(\bar{r}') = 0. \end{aligned} \tag{3.42}$$

In the above equations, $S_r - S_i$ represents the rough surface outside the object. By defining the surface variables as in Eq. (3.4) and (3.5), and noticing that $\hat{n}_2(\bar{r}') = -\hat{n}_1(\bar{r}')$, the above integral equations can be rewritten as follows:

$$\begin{aligned} \left[\overline{E}_i(\bar{r}) \quad + \quad \right. & \int_{S_o - S_{io}} d\bar{r}'_\perp \left(ik_1 \overline{\overline{G}}_1(\bar{r}, \bar{r}') \cdot \bar{a}(\bar{r}'_\perp) + \nabla \times \overline{\overline{G}}_1(\bar{r}, \bar{r}') \cdot \bar{b}(\bar{r}'_\perp) \right) \\ & \left. + i\omega\mu_1 \int_{S_1} dS' \overline{\overline{G}}_1(\bar{r}, \bar{r}') \cdot \overline{J}_1(\bar{r}') \right] \times \hat{n}_o(\bar{r}) = 0, \end{aligned} \tag{3.43}$$

$$\begin{aligned} & \left[- \int_{S_o - S_{io}} d\bar{r}'_\perp \left(ik_2 \overline{\overline{G}}_2(\bar{r}, \bar{r}') \cdot \frac{\eta_2}{\eta_1} \bar{a}(\bar{r}'_\perp) + \nabla \times \overline{\overline{G}}_2(\bar{r}, \bar{r}') \cdot \bar{b}(\bar{r}'_\perp) \right) \right. \\ & \left. + i\omega\mu_2 \int_{S_2} dS' \overline{\overline{G}}_2(\bar{r}, \bar{r}') \cdot \overline{J}_2(\bar{r}') \right] \times \hat{n}_o(\bar{r}) = 0, \end{aligned} \tag{3.44}$$

$$\begin{aligned} \overline{E}_i(\bar{r}) \quad + \quad & \int_{S_o - S_{io}} d\bar{r}'_\perp \left(ik_1 \overline{\overline{G}}_1(\bar{r}, \bar{r}') \cdot \bar{a}(\bar{r}'_\perp) + \nabla \times \overline{\overline{G}}_1(\bar{r}, \bar{r}') \cdot \bar{b}(\bar{r}'_\perp) \right) \\ & + i\omega\mu_1 \int_{S_1} dS' \overline{\overline{G}}_1(\bar{r}, \bar{r}') \cdot \overline{J}_1(\bar{r}') = 0, \end{aligned} \tag{3.45}$$

$$
\begin{aligned}
&-\int_{S_o-S_{io}} d\bar{r}'_\perp \left(ik_2\overline{\overline{G}}_2(\bar{r},\bar{r}') \cdot \frac{\eta_2}{\eta_1}\bar{a}(\bar{r}'_\perp) + \nabla \times \overline{\overline{G}}_2(\bar{r},\bar{r}') \cdot \bar{b}(\bar{r}'_\perp) \right) \\
&+i\omega\mu_2 \int_{S_2} dS'\overline{\overline{G}}_2(\bar{r},\bar{r}') \cdot \overline{J}_2(\bar{r}') = 0, \qquad (3.46)
\end{aligned}
$$

where $S_o - S_{io}$ represents the area $S_r - S_i$ projecting on the mean surface.

To illustrate the equivalent source modified by the buried part of the object, we consider the rough surface as a perfect conductor to simplify the derivation without loss of generality. In this case the tangential electric field on the rough surface valishes and the Green's function in region 2 (conducting media) becomes zero, so the integeral equations reduce to the follows:

$$
\begin{aligned}
&\left(\overline{E}_i(\bar{r}) + ik_1 \int_{S_o-S_{io}} d\bar{r}'_\perp \overline{\overline{G}}_1(\bar{r},\bar{r}') \cdot \bar{a}(\bar{r}'_\perp) + i\omega\mu_1 \int_{S_1} dS'\overline{\overline{G}}_1(\bar{r},\bar{r}') \cdot \overline{J}_1(\bar{r}')\right) \\
&\times\hat{n}_o(\bar{r}) = 0 \qquad \text{for } \bar{r} \in S_1, \qquad (3.47) \\
&\overline{E}_i(\bar{r}) + ik_1 \int_{S_o-S_{io}} d\bar{r}'_\perp \overline{\overline{G}}_1(\bar{r},\bar{r}') \cdot \bar{a}(\bar{r}'_\perp) + i\omega\mu_1 \int_{S_1} dS'\overline{\overline{G}}_1(\bar{r},\bar{r}') \cdot \overline{J}_1(\bar{r}') = 0 \\
&\qquad \text{for } \bar{r} \in S_2. \qquad (3.48)
\end{aligned}
$$

By substituting the expanded form of Green's functions and the surface variables described in Section (3.2.2) into the above equations, and seperating the equations based on the order of rough surface height function $f(\bar{r}'_\perp)$, we obtain the n-th order electric field integeral equations as follows:

$$
\begin{aligned}
\Bigg(\overline{E}_i^{(n)}(\bar{r}) \quad &+ik_1 \int_{S_o-S_c} d\bar{r}'_\perp \overline{\overline{G}}_1(\bar{r},\bar{r}'_\perp) \cdot \bar{a}_\perp^{(n)}(\bar{r}_\perp) \\
&+ i\omega\mu_1 \int_{S_{1o}} dS'\overline{\overline{G}}_1(\bar{r},\bar{r}') \cdot \overline{J}_1^{(n)}(\bar{r}_\perp)\Bigg) \times \hat{n}_o(\bar{r}) = 0 \quad \text{for } \bar{r} \in S_1, \quad (3.49)
\end{aligned}
$$

$$
\begin{aligned}
\overline{E}_i^{(n)}(\bar{r}) \quad &+ik_1 \int_{S_o-S_c} d\bar{r}'_\perp \overline{\overline{G}}_1(\bar{r},\bar{r}'_\perp) \cdot \bar{a}_\perp^{(n)}(\bar{r}_\perp) \\
&+i\omega\mu_1 \int_{S_{1o}} dS'\overline{\overline{G}}_1(\bar{r},\bar{r}') \cdot \overline{J}_1^{(n)}(\bar{r}_\perp) = 0 \qquad \text{for } \bar{r} \in S_2, \quad (3.50)
\end{aligned}
$$

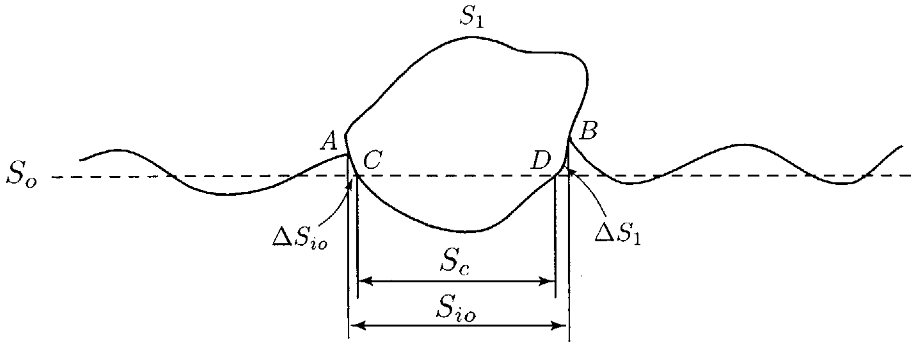

Figure 3-5: The area notations for object half-buried in a rough surface.

where, as illustrated in Fig. (3-5), S_c is the cross-section area $(C - D)$ of the object with mean surface, and S_{1o} is the surface area of object above the mean surface (area above $C - D$). ΔS_1 and ΔS_{io} are defined as $\Delta S_1 = S_{1o} - S_1$ and $\Delta S_{io} = S_{io} - S_c$, respectively. In Eq. (3.49) and (3.50) the modified equivalent source $\overline{E}_i^{(n)}$ due to the buried part is given by

$$\begin{aligned}
\overline{E}_i^{(n)}(\bar{r}) \;=\;& i\omega\mu_1 \iint_{DS_1} dS' \overline{\overline{G}}_1(\bar{r},\bar{r}') \cdot \overline{J}_1^{(n-1)}(\bar{r}_\perp) \\
&+ik_1 \sum_{m=1}^{n} \iint_{S_o-S_c} d\bar{r}'_\perp \frac{1}{m!} \left(-f(\bar{r}'_\perp)\right)^m \frac{\partial^m}{\partial z^m} \overline{\overline{G}}_1\left(\bar{r},\bar{r}'_\perp\right) \cdot \bar{a}_\perp^{(n-m)}(\bar{r}_\perp) \\
&+ik_1 \sum_{m=1}^{n} \iint_{S_o-S_{io}} d\bar{r}'_\perp \frac{1}{(m-1)!} \left(-f(\bar{r}'_\perp)\right)^{m-1} \\
&\cdot \frac{\partial^{m-1}}{\partial z^{m-1}} \overline{\overline{G}}_1\left(\bar{r},\bar{r}'_\perp\right) \cdot \left[\hat{z}\nabla'_\perp f(\bar{r}'_\perp) \cdot \bar{a}_\perp^{(n-m)}(\bar{r}'_\perp)\right] \\
&+ik_1 \sum_{m=0}^{n-1} \iint_{DS_{io}} d\bar{r}'_\perp \frac{1}{m!} \left(-f(\bar{r}'_\perp)\right)^m \frac{\partial^m}{\partial z^m} \overline{\overline{G}}_1\left(\bar{r},\bar{r}'_\perp\right) \cdot \bar{a}_\perp^{(n-1-m)}(\bar{r}_\perp) \\
&+ik_1 \sum_{m=1}^{n-1} \iint_{DS_{io}} d\bar{r}'_\perp \frac{1}{(m-1)!} \left(-f(\bar{r}'_\perp)\right)^{m-1} \\
&\cdot \frac{\partial^{m-1}}{\partial z^{m-1}} \overline{\overline{G}}_1\left(\bar{r},\bar{r}'_\perp\right) \cdot \left[\hat{z}\nabla'_\perp f(\bar{r}'_\perp) \cdot \bar{a}_\perp^{(n-1-m)}(\bar{r}'_\perp)\right],
\end{aligned} \tag{3.51}$$

with

$$\overline{E}_i^{(0)}(\bar{r}) = \overline{E}_i(\bar{r}). \tag{3.52}$$

For example, the first-order equalent source is obtained as

$$\begin{aligned}
\overline{E}_i^{(1)}(\bar{r}) = & -ik_1 \iint_{S_o-S_c} d\bar{r}'_\perp f(\bar{r}'_\perp)\frac{\partial}{\partial z}\overline{\overline{G}}_1\left(\bar{r},\bar{r}'_\perp\right)\cdot\bar{a}_\perp^{(0)}(\bar{r}_\perp) \\
& +ik_1 \iint_{S_o-S_c} d\bar{r}'_\perp\overline{\overline{G}}_1\left(\bar{r},\bar{r}'_\perp\right)\cdot\hat{z}\left[\nabla'_\perp f(\bar{r}'_\perp)\cdot\bar{a}_\perp^{(0)}(\bar{r}'_\perp)\right] \\
& +i\omega\mu_1 \iint_{DS_1} dS'\overline{\overline{G}}_1(\bar{r},\bar{r}')\cdot\overline{J}_1^{(0)}(\bar{r}_\perp) \\
& +ik_1 \iint_{DS_{io}} d\bar{r}'_\perp\frac{\partial}{\partial z}\overline{\overline{G}}_1\left(\bar{r},\bar{r}'_\perp\right)\cdot\bar{a}_\perp^{(0)}(\bar{r}_\perp). \qquad (3.53)
\end{aligned}$$

By comparing this modified equalent source with Eq. (3.36) for an object above rough surface, we find that there are following changes:

1. In the first two terms in Eq. (3.53), the integration area is $S_o - S_c$ instead of the entire mean surface area as in Eq. (3.36).

2. There are two extra terms in Eq. (3.53) due to the "corner effect" arround the touching area of the object in rough surface. In Eq. (3.53), the third term is the correction of the equivalent source due to the change of exposed surface area on the object, and the fourth term is the modification of the equivalent source due to the projecting area of rough surface on the mean surface.

3.3 Numerical Results

3.3.1 Object above a Conducting Rough Surface

In the numerical simulation, a horizontal conducting cylinder along the x-axis with 2.0λ in length and 1.0λ in diameter is considered. The distance between the bottom of the cylinder and the mean surface height of the conducting rough surface is 0.1λ so that strong interaction between object and rough surface can be expected. A rough surface with the well-known Gaussian power spectrum is used for the validation with the help of the standard method of moments (MoM). The size of the rough surface is 15.0λ by 15.0λ. The deviation and correlation length of the rough surface are $\sigma = 0.03\lambda$ and $l = 1.0\lambda$, respectively. The incident wave $\overline{E}_i$ is tapered and formed as a summation of plane waves with Gaussian-shaped footprint on the mean surface:

$$\overline{E}_i(\bar{r}) = \iint dk_x dk_y e^{i(k_x x + k_y y - k_z z)} \psi\left(k_x, k_y\right) \bar{e}\left(k_x, k_y\right), \tag{3.54}$$

where $\psi\left(k_x, k_y\right)$ is the plane wave spectrum and $\bar{e}\left(k_x, k_y\right)$ is the polarization vector of the associated plane wave. The plane wave spectrum is the Gaussian function

$$\psi\left(k_x, k_y\right) = \frac{g^2}{4\pi} \exp\left\{-\frac{g^2}{4}\left[\left(k_x - k_{ix}\right)^2 + \left(k_y - k_{iy}\right)^2\right]\right\}, \tag{3.55}$$

where factor g is the control parameter to specify the beam width. This tapered incident wave satisfies Maxwell's equations and minimizes the edge effect in the numerical calculations. The factor g, which is used to control the beam width of the tapered wave is $g = 3.0\lambda$, so that the incident electric field magnitude on the rough surface has dropped by a factor of $1/e$ at $|\bar{r}'_\perp| = 3.0\lambda$.

In the numerical calculation, the radar cross section (RCS) is defined as

$$\text{RCS} = \lim_{r\to\infty} 4\pi r^2 \frac{\left|E_s\left(\theta, \phi\right)\right|^2}{\left|E_o\left(\theta_i, \phi_i\right)\right|^2}, \tag{3.56}$$

where E_o is the maximum magnitude of the tapered incident electric field on the mean surface S_o. For monostatic (backscattering) RCS, the scattering angles are $\theta = \theta_i$ and $\phi = \phi_i$. In the numerical simulations for bistatic RCS, we let the scattering angle θ be 40° and vary the azimuthal angle ϕ from 0° to 360°. $\phi = 0°$ is the backscattering direction. For the monostatic RCS simulations, the incident $\bar{k}_i$ vector remains in the xz plane and the incident angle θ_i varies from 0° to 90°.

The plots shown in Fig. (3-6)(3-7) and Fig. (3-8)(3-9) are bistatic RCSs for the individual terms of Eq. (3.32) for TE and TM incident waves, respectively. The plot labeled as E_r is the reflected field of the incident tapered wave from the flat interface in absence of the object. A peak of co-polarized component of $\overline{E}_r$ appears in the specular direction $\phi = 180°$ as expected. The plot labeled as E_b is the returned field as in Eq. (3.33). The E_c plot is evaluated by using Eq. (3.34), and the E_d plot is calculated from Eq. (3.35). It can be seen that most of the energy of the "incoherent" field $\overline{E}_c$ concentrates in the forward scattering direction. The curves shown in the E_b plot represent the scattering from the object excited by the fields $\overline{E}_i$ and $\overline{E}_r$, while the secondary scattering field in the E_d plot is the returned field from the object excited by the "incoherent" field $\overline{E}_c$ from the rough surface. We note that the cross-polarized returns VH and HV in the backscattering direction are zero in the E_b plot. This is due to the symmetry of the geometry and the incident wave. The secondary returned fields of cross-polarized VH and HV in the plot labeled E_d are no longer zero in the backscattering direction due to the asymmetry of the "incoherent" field $\overline{E}_c$. The "incoherent" field $\overline{E}_c$ as well as the secondary returned field $\overline{E}_d$ from the object are both proportional to the surface height function $f(\bar{r}'_\perp)$ of the rough surface. It can easily be checked that both $\overline{E}_c$ and $\overline{E}_d$ become zero when the surface height function is zero.

The sum of the four terms $\overline{E}_r + \overline{E}_b + \overline{E}_c + \overline{E}_d$ as in Eq. (3.32) is the total returned field up to the first order, and the corresponding RCS are shown in Fig. (3-10) and Fig. (3-11) for TE and TM incident wave, respectively. The bistatic RCS for the total returned field with TE incident wave are compared with standard MoM results. In the MoM simulation, both the rough surface and the conducting object are discretized and the surface unknowns are solved together by using the conjugate gradient algorithm. In these simulations, a single rough surface with Gaussian power spectrum is used. The deviation of the surface height is $\sigma = 0.03\lambda$ and the correlation length is $l = 1.0\lambda$. Again the results show good agreement with the standard MoM. It is noted that the curves are no longer symmetrical with respect to the plane of incidence when the surface is rough.

Monte Carlo simulation results with 100 realizations are shown in Fig. (3-12) and

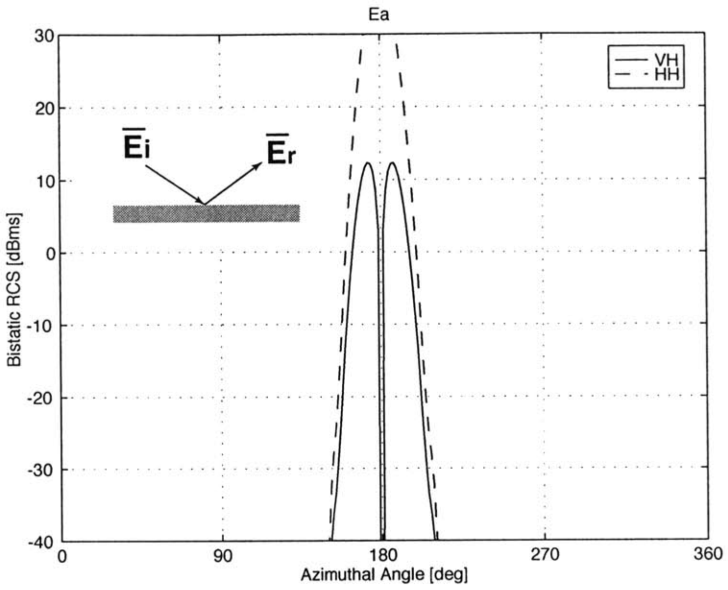

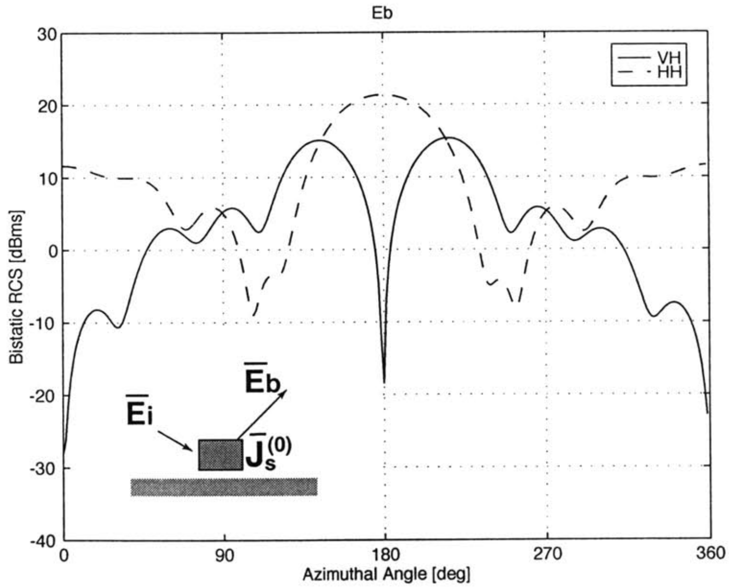

Figure 3-6: Bistatic RCS of individual terms $\overline{E}_r$ and $\overline{E}_b$ for TE incident wave.

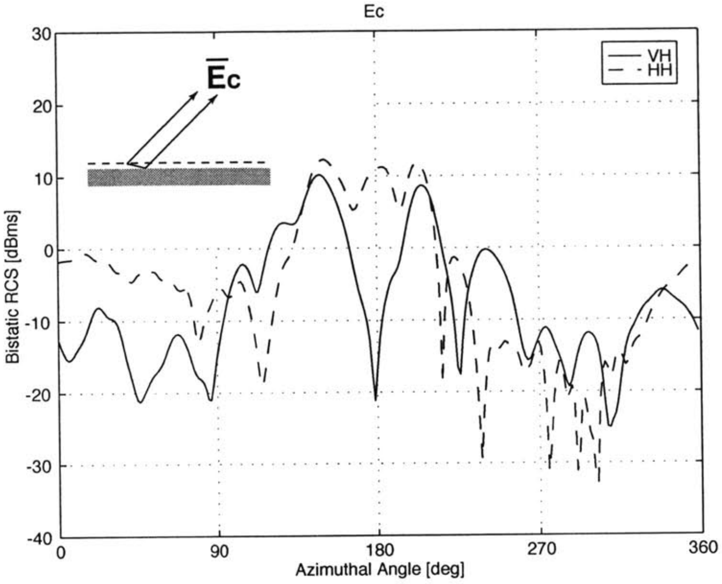

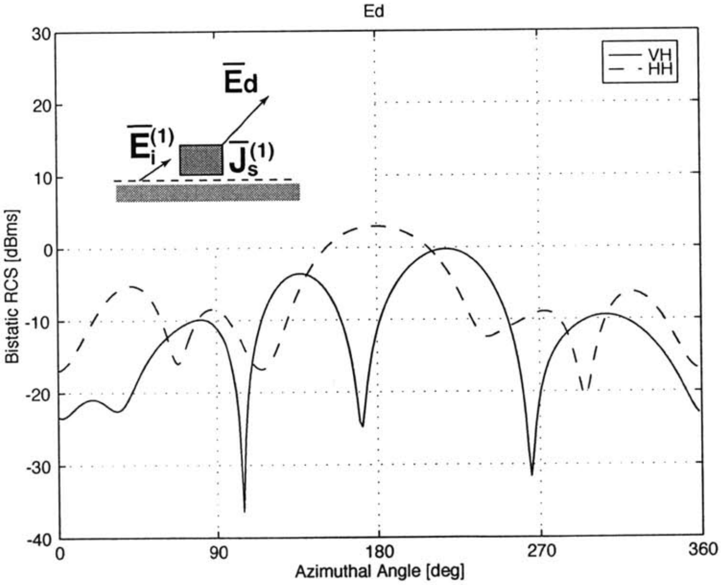

Figure 3-7: Bistatic RCS of individual terms $\overline{E}_c$ and $\overline{E}_d$ for TE incident wave.

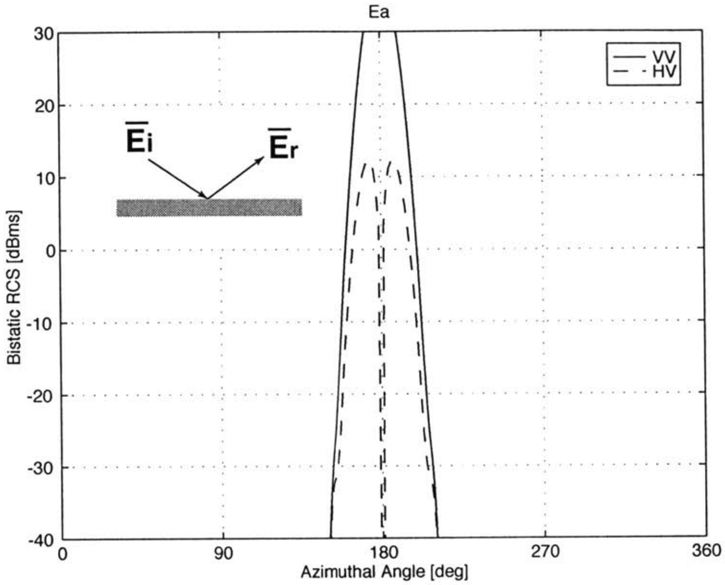

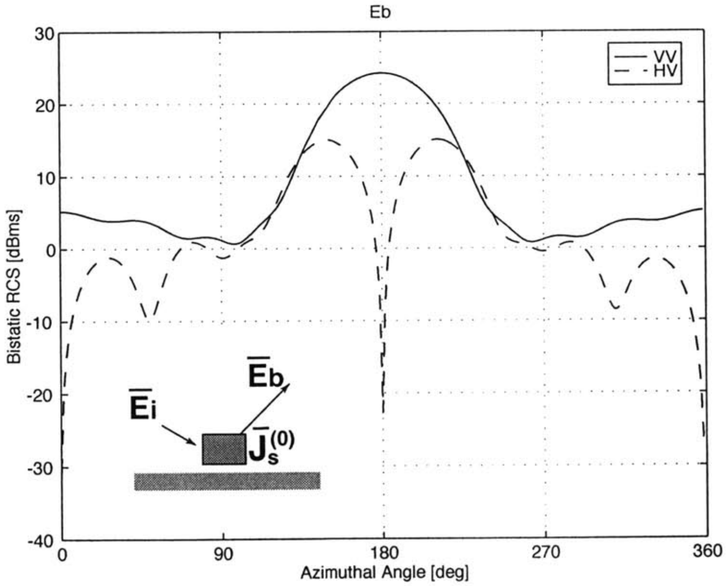

Figure 3-8: Bistatic RCS of individual terms $\overline{E}_r$ and $\overline{E}_b$ for TM incident wave.

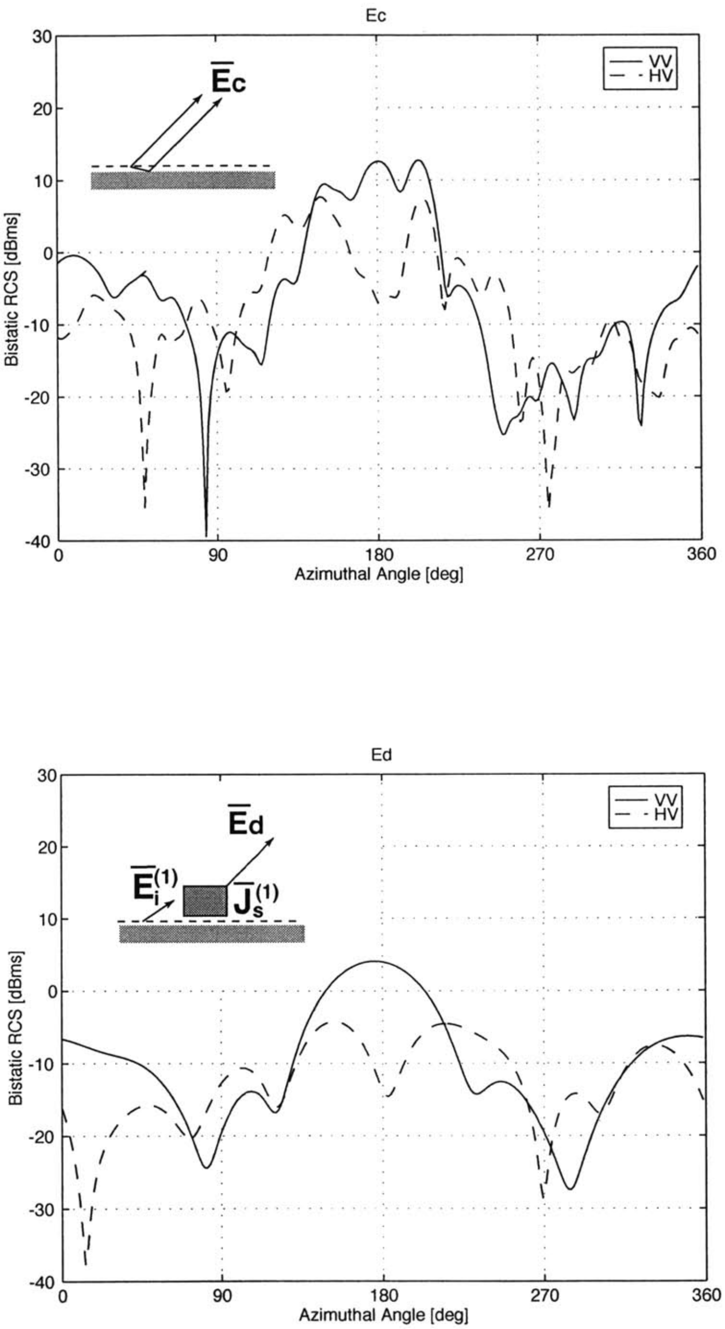

Figure 3-9: Bistatic RCS of individual terms $\overline{E}_c$ and $\overline{E}_d$ for TM incident wave.

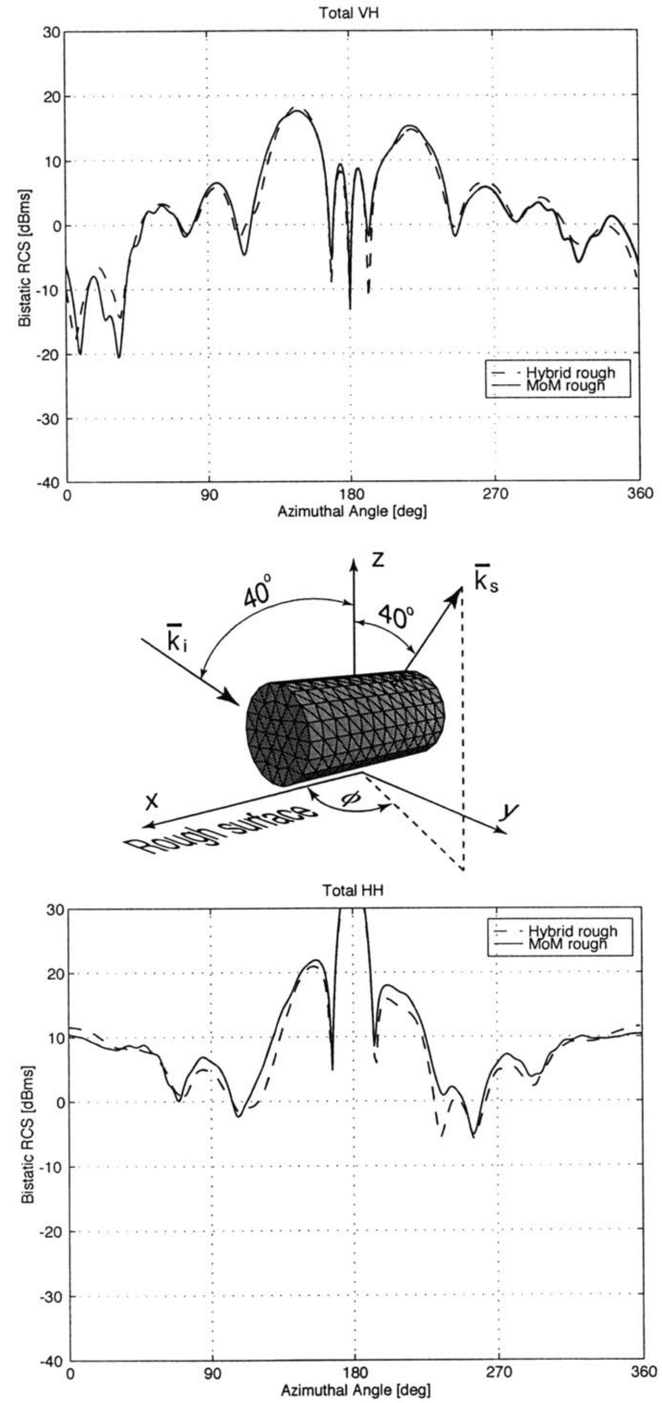

Figure 3-10: Bistatic RCS of the total returned field $\overline{E}_r+\overline{E}_b+\overline{E}_c+\overline{E}_d$ for TE incident wave: Object above a rough surface.

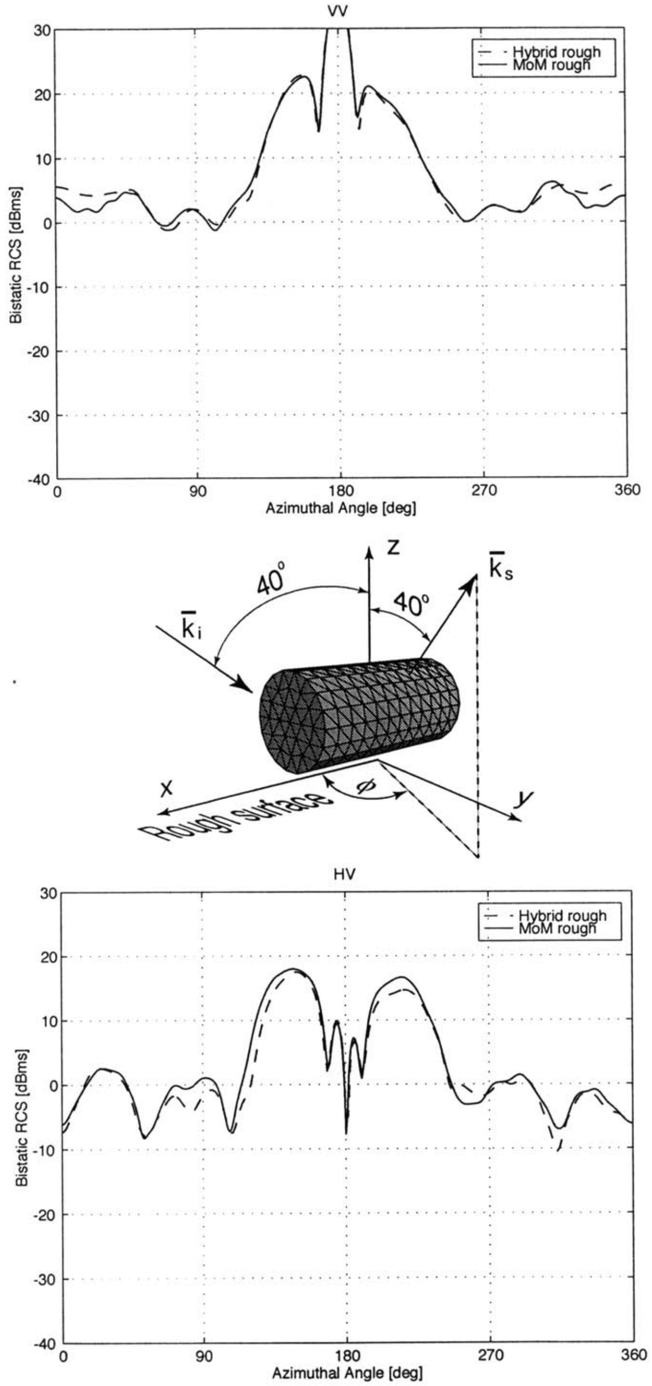

Figure 3-11: Bistatic RCS of the total returned field $\overline{E}_r + \overline{E}_b + \overline{E}_c + \overline{E}_d$ for TM incident wave: Object above a rough surface.

Fig. (3-13) for TE and TM incident waves, respectively. Statistically independent rough surfaces with power law spectrum are generated. The method of generating random rough surface is presented in Appendix C. The power law spectrum is $W(k) = a_o/k^4$, which more closely represents ocean surfaces than the Gaussian power spectrum. Here k is the spatial wavenumber of the rough surface and $a_o = 0.008/2\pi$ which is the amplitude used for the Durden-Vesecky spectrum [75]. The upper cut-off spatial wavenumber k_h is chosen to be $k_h = 2.5k_1$ which corresponds to the band width for $1/5\lambda_1$ spatial resolution of sampling on the rough surface, where k_1 and λ_1 are electromagnetic wavenumber and wavelength of the incident wave, respectively. The lower cut-off spatial wavenumber k_l is chosen according to the standard deviation of the rough surface height using the following relation:

$$\sigma^2 = \int W(k) d^2k = \pi a_o \left(\frac{1}{k_l^2} - \frac{1}{k_h^2} \right). \tag{3.57}$$

In Fig. (3-12) and Fig. (3-13), the deviations of the rough surface $k_1\sigma = 0.1,\ 0.2,\ 0.4$ correspond to the lower cut-off spatial wavenumbers $k_l/k_1 = 0.6131,\ 0.3137,\ 0.1578$, respectively. It is noted that the Monte Carlo simulations converge with respect to the number of realizations. The averaged cross-polarized RCS increases with the deviation of the rough surface over a wide range of scattering angles.

Fig. (3-14) and Fig. (3-15) show the Monte Carlo simulation for the monostatic (backscattering) RCS for TE and TM incident waves, respectively. Here 100 rough surfaces with power law spectrum and $k_1\sigma = 0.4$ are used. The backscattering direction varies from $\theta = 0°$ to $\theta = 90°$ with 45 steps in between. The azimuthal angle ϕ remains zero degree. We note that the cross-polarized VH and HV are significant in the presence of a rough surface. Analytically the cross-polarized returns should be zero for the considered geometry when the surface is flat. We note that the non-zero values for flat surface are produced numerically. Changes of co-polarized monostatic RCS due to the rough surface can be found at some scattering angles. At small grazing angles, the rough surface effect on co-polarized backscattering RCS is not

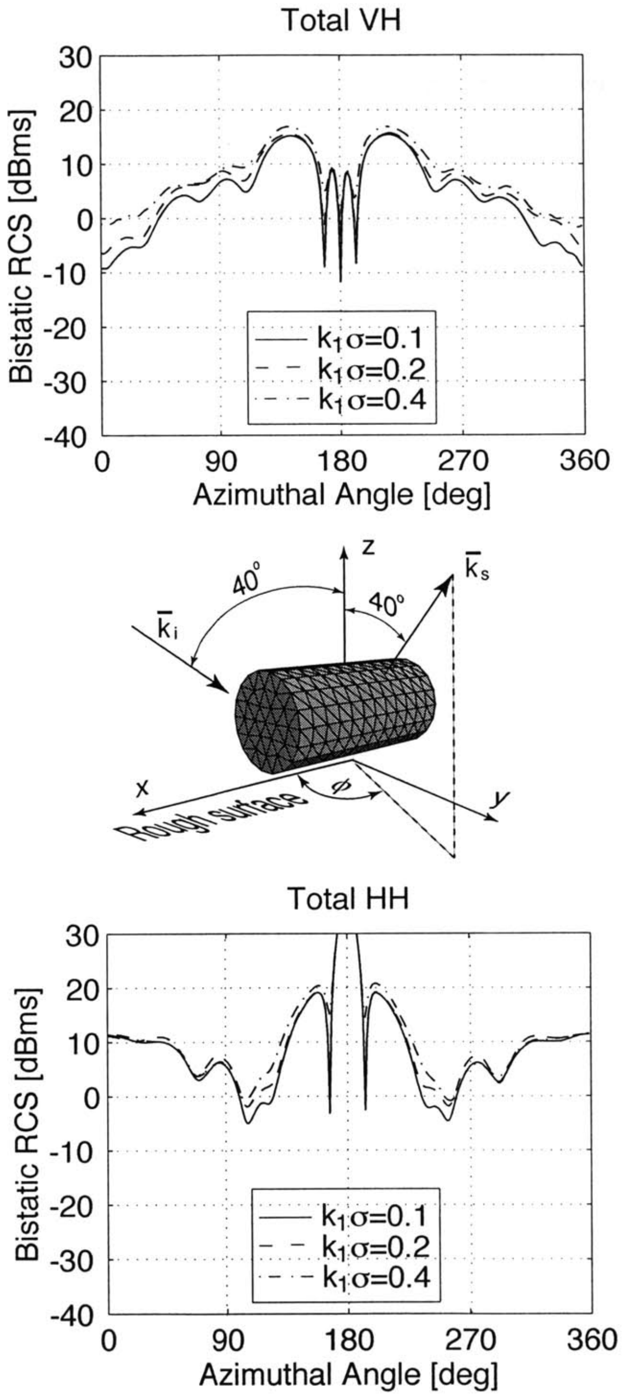

Figure 3-12: Monte Carlo simulation for the bistatic RCS of the total returned field $\overline{E}_r + \overline{E}_b + \overline{E}_c + \overline{E}_d$ for TE incident wave.

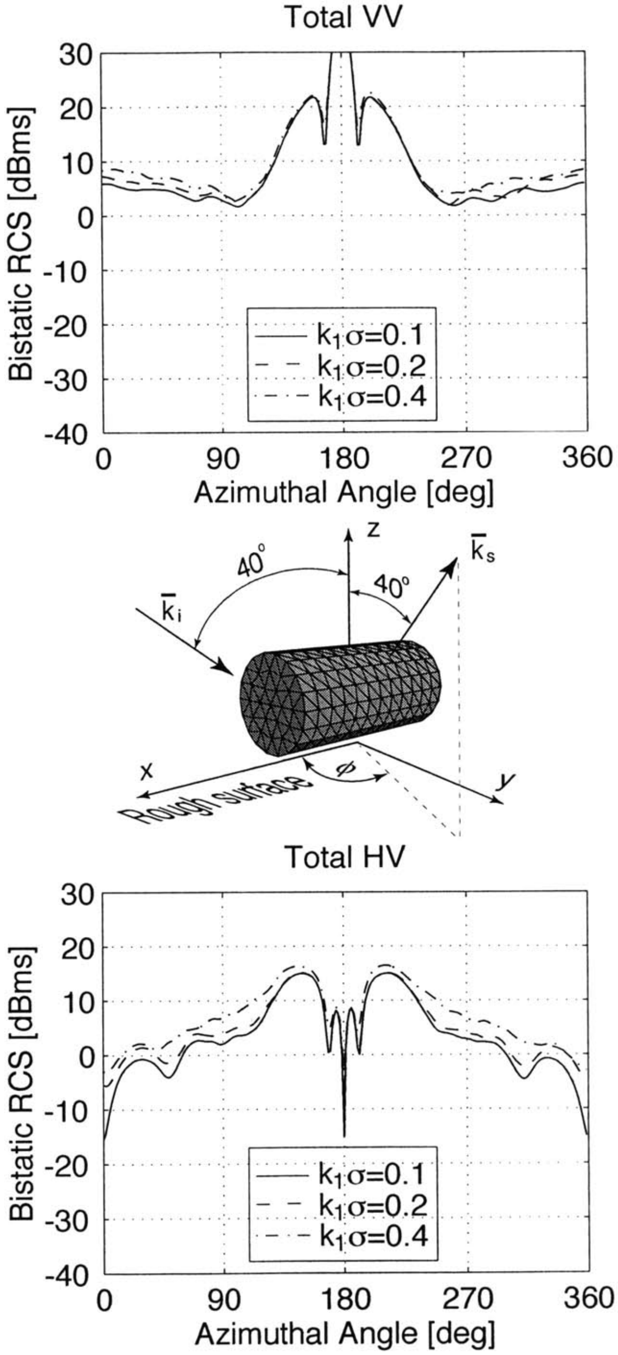

Figure 3-13: Monte Carlo simulation for the bistatic RCS of the total returned field $\overline{E}_r + \overline{E}_b + \overline{E}_c + \overline{E}_d$ for TM incident wave.

	MoM	Hybrid
Number of unknowns	17,252	972
CPU time		
single bistatic	1 hr 14 min	5 min
100 realizations	5 days (estimated)	40 min
single monostatic	23 hr	3 hr 15 min
100 monostatic	3 months (estimated)	17 hr

Table 3.1: Comparison of computational effort for standard MoM and hybrid codes, respectively.

significant.

The computational performance of the hybrid technique and the standard MoM are listed in Table 3.1 for the testing cases discussed above, where we have used a Microway Screamer 500 workstation which contains a 500 MHz Digital Alpha 21164A processor with 2 MB L3 Cache and 2 GB RAM. The CPU time for monostatic simulations is based on 45 incident angles.

3.3.2 Object Half Buried in a Conducting Rough Surface

Fig. (3-16) shows the simulation results of individual terms in Eq. (3.32) for the bistatic RCSs of a horizontal cylinder half buried in a conducting rough surface with TE and TM incident wave, respectively. The geometry of this problem is the same as in Fig. (2-14). The rough surface is generated by using the Gaussian spectrum with rms height $\sigma = 0.03\lambda$ and correlation length $l = 1\lambda$. The plot labeled as E_r is the reflected field of the incident tapered wave from the flat interface in the absence of the object. The E_b plot shows the RCS of the scattered field due to the zeroth order induced current on the cylinder on a flat surface. It is noticed that the co-polarized wave has a maximum and the cross-polarized wave a zero minimum in the specular direction due to the symmetry of the geometry. The E_c plot is the result that shows the radiation field of the equivalent source due to the rough surface. It is found that the scattered field due to the rough surface is random and the intensity is significant even though the roughness is small. The E_c plot is the result of the

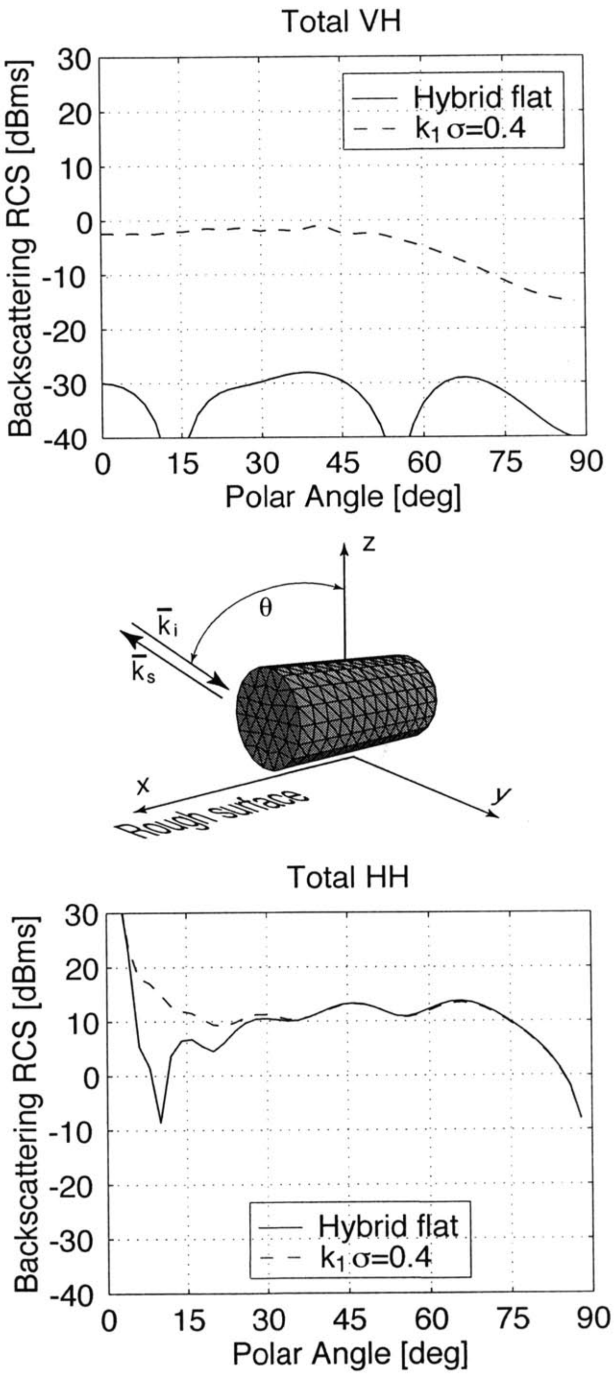

Figure 3-14: Monte Carlo simulation for the monostatic RCS of the total returned field $\overline{E}_r + \overline{E}_b + \overline{E}_c + \overline{E}_d$ for TE incident wave.

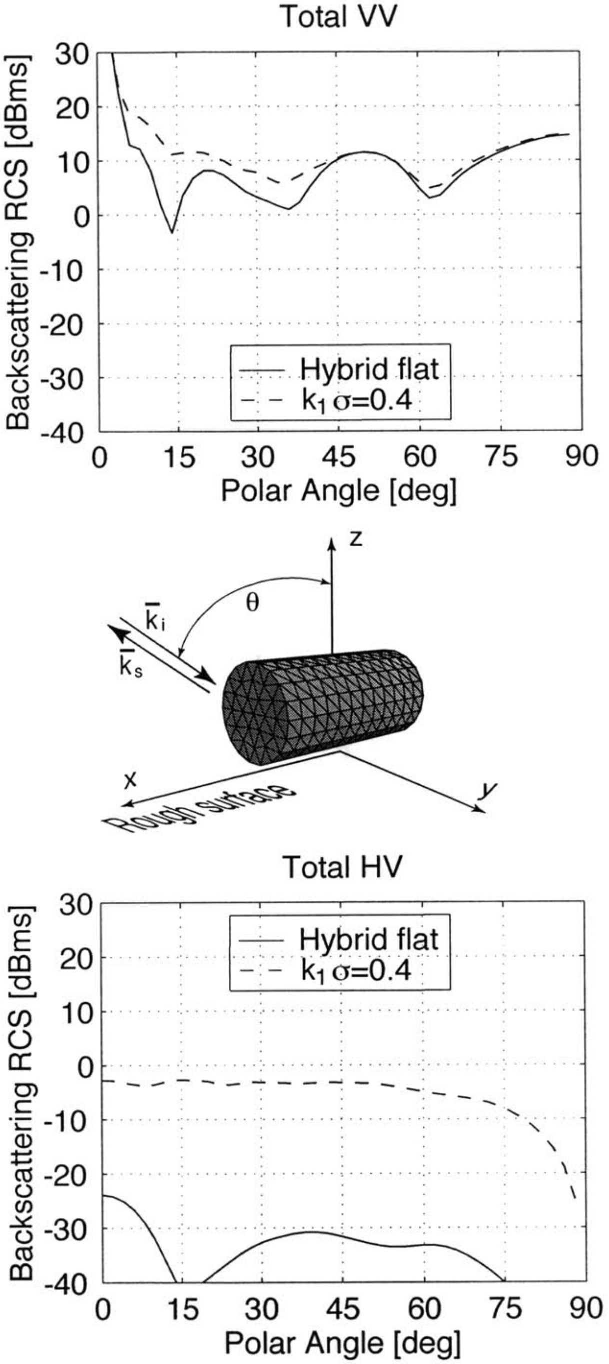

Figure 3-15: Monte Carlo simulation for the monostatic RCS of the total returned field $\overline{E}_r + \overline{E}_b + \overline{E}_c + \overline{E}_d$ for TM incident wave.

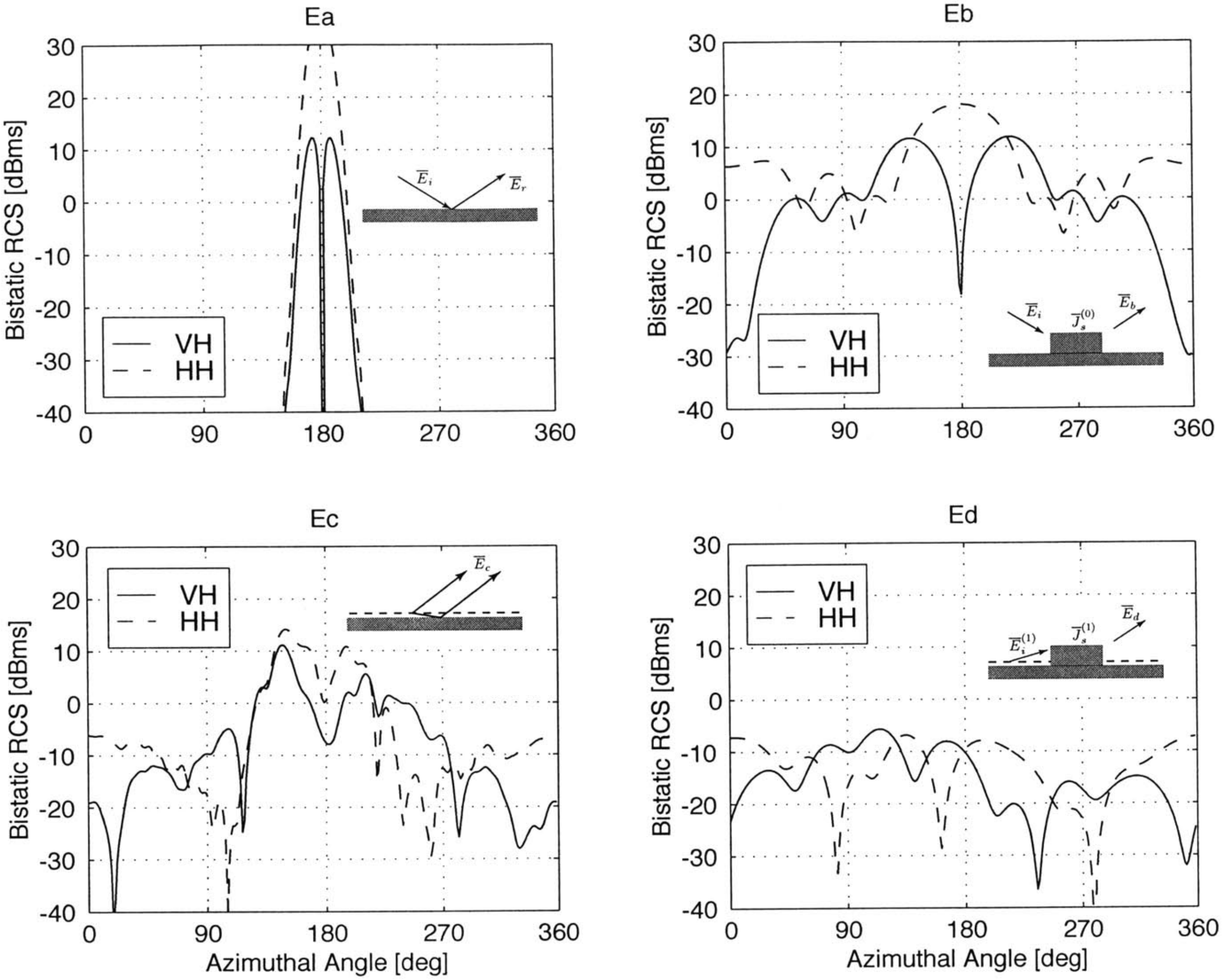

Figure 3-16: The bistatic RCS of individual terms $\overline{E}_r$ and $\overline{E}_b$ for TE incident wave.

secondary scattering of the cylinder illuminated by the radiation of the equivalent source as shown in the E_c plot. In this case the secondary scattering is relatively small in comparison with the zeroth order scattering field as shown in the E_b plot.

The bistatic RCS for the total returned field $\overline{E}_r + \overline{E}_b + \overline{E}_c + \overline{E}_d$ of the cylinder half buried in the flat surface with TE and TM incident waves are shown in Fig. (3-18) and (3-19), respectively. The plots in the top rows of Fig. (3-18) and Fig. (3-19) are the bistatic RCS of the zeroth order solution using the hybrid technique and the standard MoM solution. In the simulations shown in the bottom rows of Fig. (3-

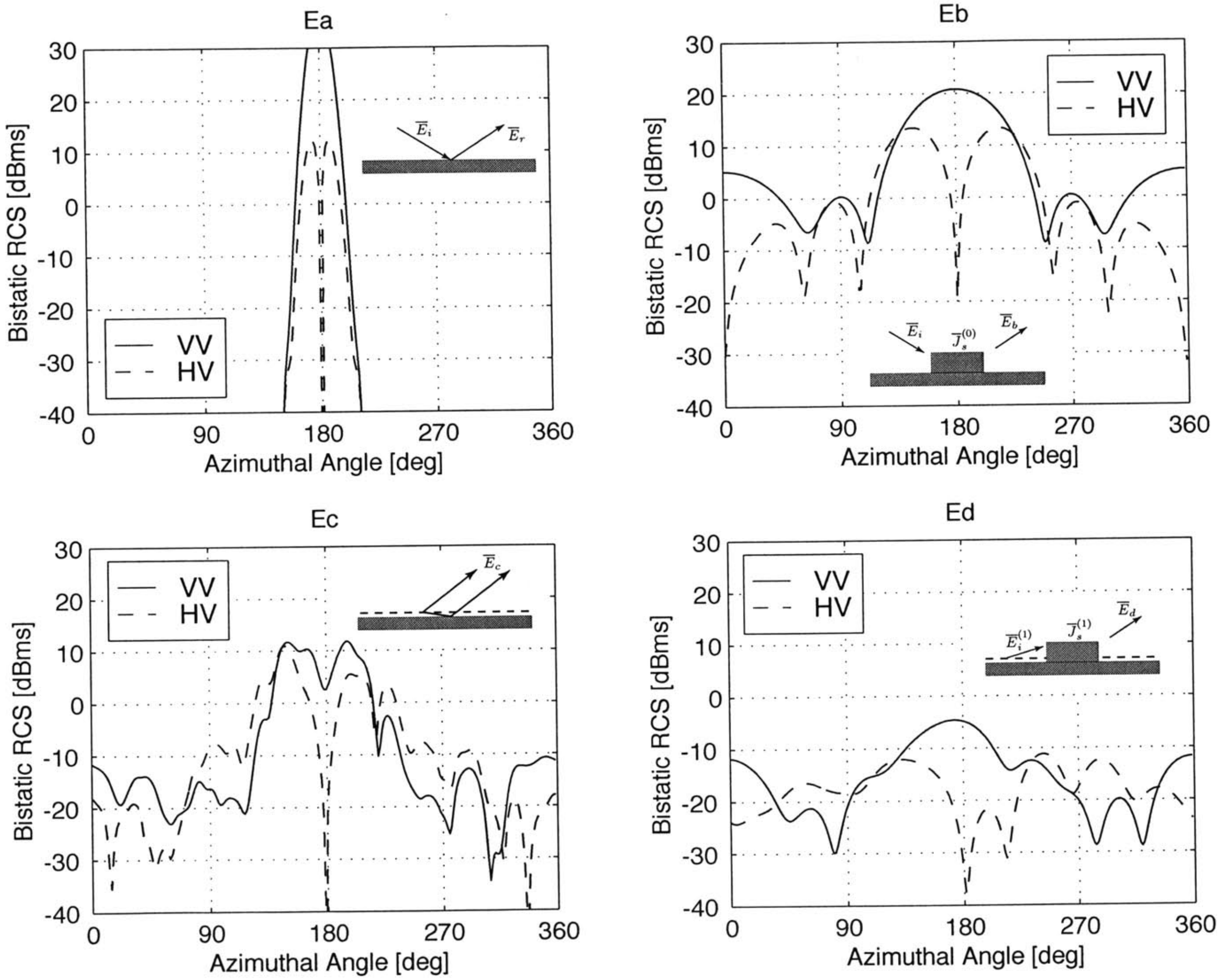

Figure 3-17: The bistatic RCS of individual terms $\overline{E}_r$ and $\overline{E}_b$ for TM incident wave.

18) and Fig. (3-19), the rough surface with Gaussian power spectrum is used. The deviation of the surface height is $\sigma = 0.03\lambda$ and the correlation length is $l = 1.0\lambda$. The results agree reasonably well with the standard MoM.

3.4 Conclusions

This chapter has presented a hybrid technique of SPM and MoM for electromagnetic wave scattering from a perfectly conducting (PEC) object above a rough surface. The formulations are derived for general penetrable rough surfaces (dielectric medium). With the expansion of the Green's function and surface variables in terms of the surface height function on the flat mean surface, the electric field integral equations are decomposed into different orders. The equations of each order represent the EM scattering problem with the same object above the mean surface and different incident field from an equivalent source that can then be evaluated by using lower order solutions. The equivalence with a flat surface problem allows us to use the dyadic Green's function for layered media, so that we do not need to solve for tangential fields on the rough surface, leaving only unknowns on the conducting object. Compared to the standard MoM, this hybrid technique demonstrates a dramatic increase in computational efficiency without loss of accuracy. The separation of the returned fields into the sum of individual interaction terms allows us to identify the coherent and incoherent returned field, and thus to characterize the rough surface effects quantitatively.

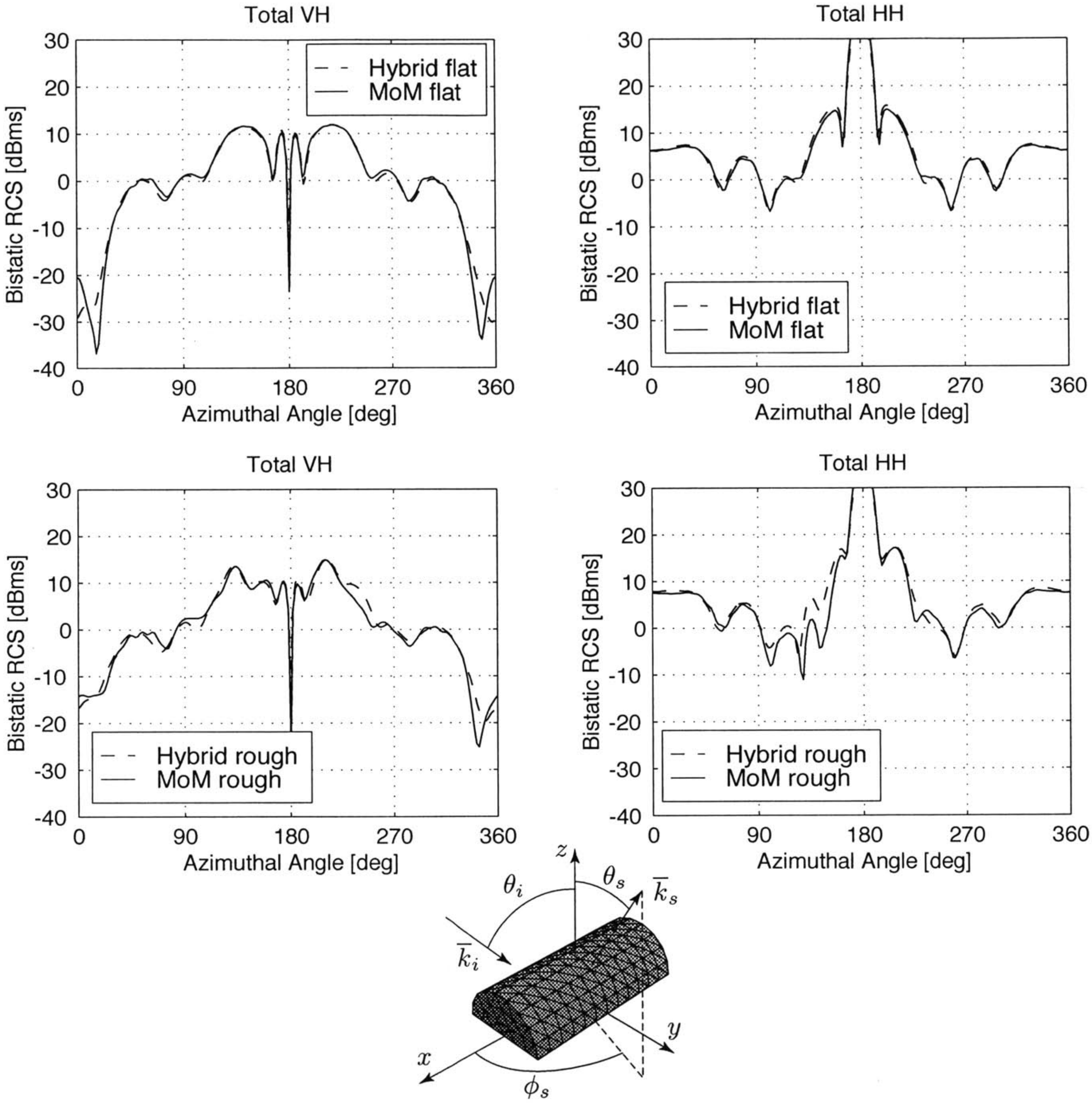

Figure 3-18: The bistatic RCS of total returned field $\overline{E}_r + \overline{E}_b + \overline{E}_c + \overline{E}_d$ for TE incident wave: Object half buried in a flat PEC surface.

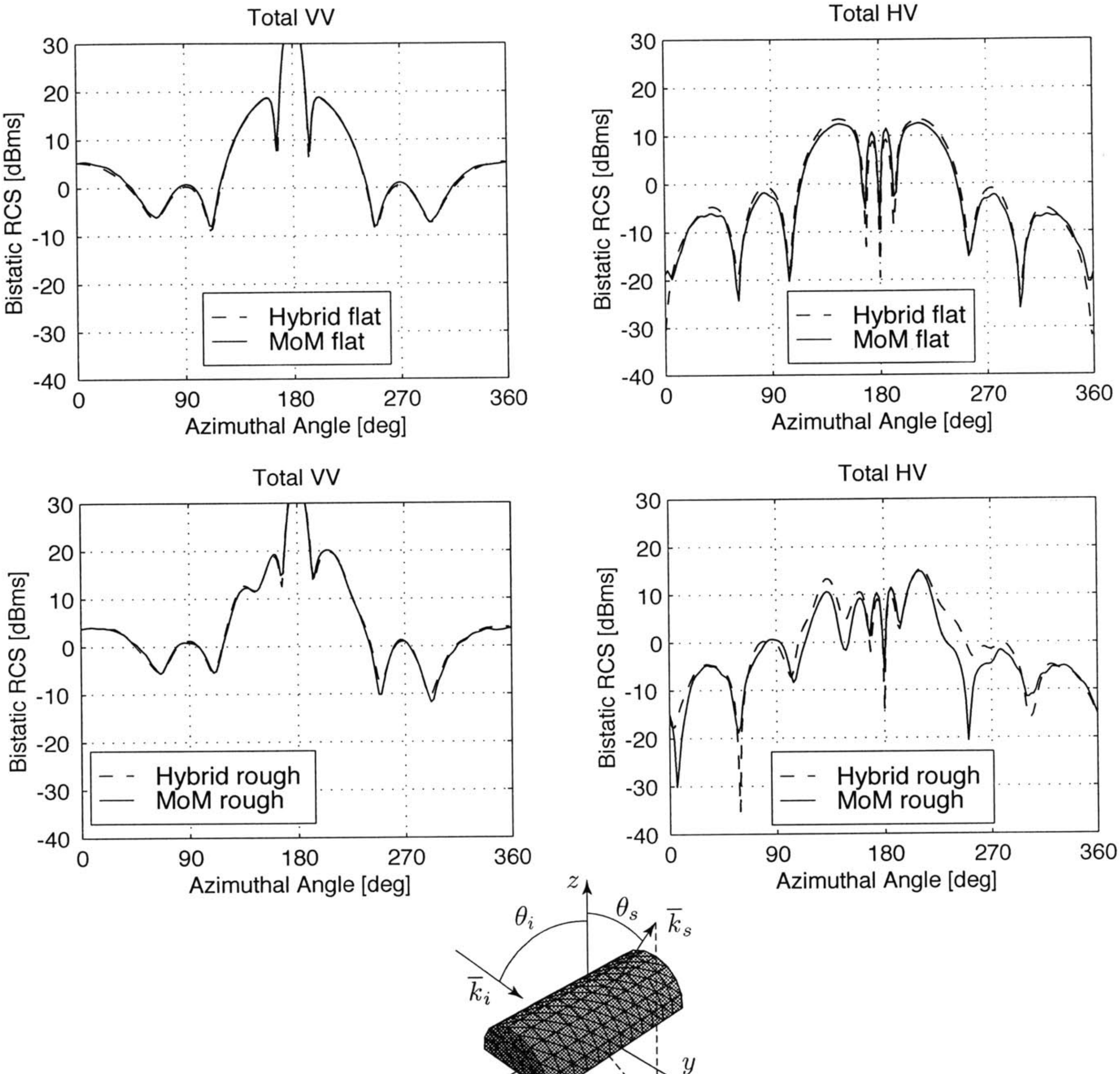

Figure 3-19: The bistatic RCS of total returned field $\overline{E}_r + \overline{E}_b + \overline{E}_c + \overline{E}_d$ for TM incident wave: Object half buried in a flat PEC surface.

Chapter 4

Electromagnetic Wave Scattering from a Rough Surface using the Equivalent Source Formulation

4.1 Introduction

Consider the electromagnetic wave scattering by a rough surface with the height function $f(\bar{r}'_\perp)$ as shown in Fig. (4-1). In Chapter 3, we derived the radiation field

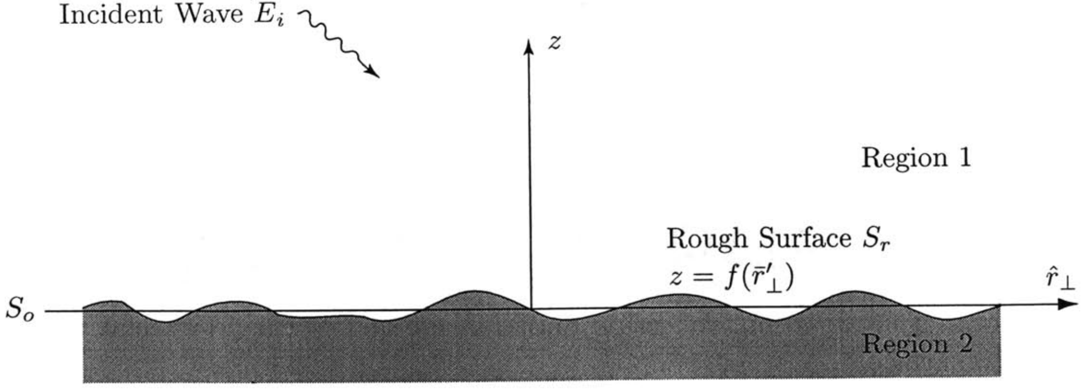

Figure 4-1: Electromagnetic wave scattering by a rough surface.

from the "equivalent source" and concluded that the field scattered by the rough surface is the same as the radiation field from the equivalent source. By using the iterative scheme, we found that the n-th order radiation field from the equivalent source can be evaluated by using the lower order surface variables $\bar{a}$ and $\bar{b}$, which represent the tangential magnetic and electric fields on the rough surface, respectively. In this chapter, we will show that, up to the first order, the radiation field from the equivalent source on a perfectly conducting (PEC) and small rough surface is the same as the scattered field derived directly from the conventional small perturbation method (SPM) when the incident wave is a plane wave. Also we will compare the numerical result of the radiation field from the equivalent source with the standard method of moments (MoM) when the incident wave is tapered.

4.2 Formulations of Equivalent Sources

We use the notation $\overline{E}_i^{(n)}$ as in Chapter 3 to represent the n-th order radiation field from the equivalent source on the mean surface. Therefore, by denoting the corresponding reflected field of the equivalent source on the mean surface as $\overline{E}_r^{(n)}$ and the transmitted field of the equivalent source in the lower region as $\overline{E}_{t2}^{(n)}$ [Fig. (4-2], we

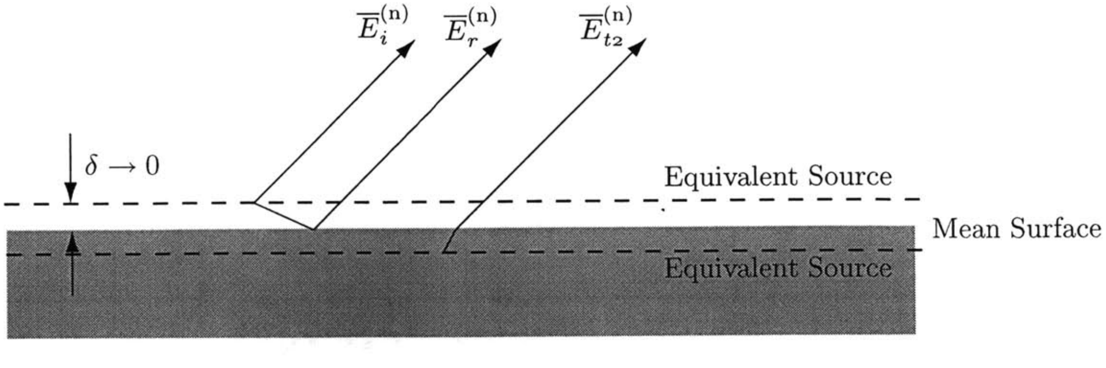

Figure 4-2: The radiation, reflection and transmission of the equivalent sources on the mean surface.

obtain the total scattered field from the rough surface excited by the incident wave

$\overline{E}_i$,

$$\overline{E}_s(\bar{r}) = \sum_{n=1}^{\infty} \left(\overline{E}_i^{(n)}(\bar{r}) + \overline{E}_r^{(n)}(\bar{r}) \right) + \sum_{n=1}^{\infty} \overline{E}_{t2}^{(n)}(\bar{r}). \tag{4.1}$$

The n-th order radiation fields from the equivalent source are given as following [from Eqs.(3.25) and (3.26) in Chapter 3],

$$\begin{aligned} \overline{E}_i^{(n)}(\bar{r}) \;=\; & \sum_{m=1}^{n} \frac{1}{m!} \int d\bar{r}'_\perp \left[-f(\bar{r}'_\perp) \right]^m \\ & \frac{\partial^m}{\partial z^m} \left\{ ik_1 \overline{\overline{G}}_1(\bar{r}, \bar{r}'_\perp) \cdot \bar{a}_\perp^{(n-m)}(\bar{r}'_\perp) + \nabla \times \overline{\overline{G}}_1(\bar{r}, \bar{r}'_\perp) \cdot \bar{b}_\perp^{(n-m)}(\bar{r}'_\perp) \right\} \\ & + \sum_{m=1}^{n} \frac{1}{(m-1)!} \int d\bar{r}'_\perp \left[-f(\bar{r}'_\perp) \right]^{m-1} \\ & \frac{\partial^{m-1}}{\partial z^{m-1}} \left\{ ik_1 \overline{\overline{G}}_1(\bar{r}, \bar{r}'_\perp) \cdot \hat{z} \left[\nabla'_\perp f(\bar{r}'_\perp) \cdot \bar{a}_\perp^{(n-m)}(\bar{r}'_\perp) \right] \right. \\ & \left. + \nabla \times \overline{\overline{G}}_1(\bar{r}, \bar{r}'_\perp) \cdot \hat{z} \left[\nabla'_\perp f(\bar{r}'_\perp) \cdot \bar{b}_\perp^{(n-m)}(\bar{r}'_\perp) \right] \right\}, \end{aligned} \tag{4.2}$$

and

$$\begin{aligned} \overline{E}_{i2}^{(n)}(\bar{r}) \;=\; & \sum_{m=1}^{n} \frac{1}{m!} \int d\bar{r}'_\perp \left[-f(\bar{r}'_\perp) \right]^m \\ & \frac{\partial^m}{\partial z^m} \left\{ ik_2 \frac{\eta_2}{\eta_1} \overline{\overline{G}}_2(\bar{r}, \bar{r}'_\perp) \cdot \bar{a}_\perp^{(n-m)}(\bar{r}'_\perp) + \nabla \times \overline{\overline{G}}_2(\bar{r}, \bar{r}'_\perp) \cdot \bar{b}_\perp^{(n-m)}(\bar{r}'_\perp) \right\} \\ & + \sum_{m=1}^{n} \frac{1}{(m-1)!} \int d\bar{r}'_\perp \left[-f(\bar{r}'_\perp) \right]^{m-1} \\ & \frac{\partial^{m-1}}{\partial z^{m-1}} \left\{ ik_2 \frac{\eta_2}{\eta_1} \overline{\overline{G}}_2(\bar{r}, \bar{r}'_\perp) \cdot \hat{z} \left[\nabla'_\perp f(\bar{r}'_\perp) \cdot \bar{a}_\perp^{(n-m)}(\bar{r}'_\perp) \right] \right. \\ & \left. + \nabla \times \overline{\overline{G}}_2(\bar{r}, \bar{r}'_\perp) \cdot \hat{z} \left[\nabla'_\perp f(\bar{r}'_\perp) \cdot \bar{b}_\perp^{(n-m)}(\bar{r}'_\perp) \right] \right\}. \end{aligned} \tag{4.3}$$

Consider the first order solutions ($n = 1$),

$$\begin{aligned} \overline{E}_i^{(1)}(\bar{r}) \;=\; & \int d\bar{r}'_\perp \left[-f(\bar{r}'_\perp) \right] \\ & \frac{\partial}{\partial z} \left\{ ik_1 \overline{\overline{G}}_1(\bar{r}, \bar{r}'_\perp) \cdot \bar{a}_\perp^{(0)}(\bar{r}'_\perp) + \nabla \times \overline{\overline{G}}_1(\bar{r}, \bar{r}'_\perp) \cdot \bar{b}_\perp^{(0)}(\bar{r}'_\perp) \right\} \\ & + \int d\bar{r}'_\perp \left\{ ik_1 \overline{\overline{G}}_1(\bar{r}, \bar{r}'_\perp) \cdot \hat{z} \left[\nabla'_\perp f(\bar{r}'_\perp) \cdot \bar{a}_\perp^{(0)}(\bar{r}'_\perp) \right] \right. \end{aligned}$$

$$+ \nabla \times \overline{\overline{G}}_1(\bar{r}, \bar{r}'_\perp) \cdot \hat{z} \left[\nabla'_\perp f(\bar{r}'_\perp) \cdot \bar{b}^{(0)}_\perp(\bar{r}'_\perp) \right] \Big\} , \tag{4.4}$$

and

$$\begin{aligned} \overline{E}^{(1)}_{i2}(\bar{r}) \;=\; & \int d\bar{r}'_\perp \left[-f(\bar{r}'_\perp) \right] \\ & \frac{\partial}{\partial z} \left\{ ik_2 \frac{\eta_2}{\eta_1} \overline{\overline{G}}_2(\bar{r}, \bar{r}'_\perp) \cdot \bar{a}^{(0)}_\perp(\bar{r}'_\perp) + \nabla \times \overline{\overline{G}}_2(\bar{r}, \bar{r}'_\perp) \cdot \bar{b}^{(0)}_\perp(\bar{r}'_\perp) \right\} \\ & + \int d\bar{r}'_\perp \Big\{ ik_2 \frac{\eta_2}{\eta_1} \overline{\overline{G}}_2(\bar{r}, \bar{r}'_\perp) \cdot \hat{z} \left[\nabla'_\perp f(\bar{r}'_\perp) \cdot \bar{a}^{(0)}_\perp(\bar{r}'_\perp) \right] \\ & + \nabla \times \overline{\overline{G}}_2(\bar{r}, \bar{r}'_\perp) \cdot \hat{z} \left[\nabla'_\perp f(\bar{r}'_\perp) \cdot \bar{b}^{(0)}_\perp(\bar{r}'_\perp) \right] \Big\} , \end{aligned} \tag{4.5}$$

where $\eta_2/\eta_1 = k_1/k_2$ for $\mu_1 = \mu_2$. Since the integrations are conducted along the mean surface, we can place the equivalent sources on the upper and lower mean surface which radiate the electromagnetic waves $\overline{E}^{(1)}_i(\bar{r})$ and $\overline{E}^{(1)}_{i2}(\bar{r})$ in the unbounded region 1 and 2. Taking the field $\overline{E}^{(1)}_i(\bar{r})$ as an example, if we place the equivalent source above the mean surface, the total field will be the superposition of $\overline{E}^{(1)}_i(\bar{r})$ and its reflection $\overline{E}^{(1)}_r(\bar{r})$ from the mean surface as shown in Fig. (4-3).

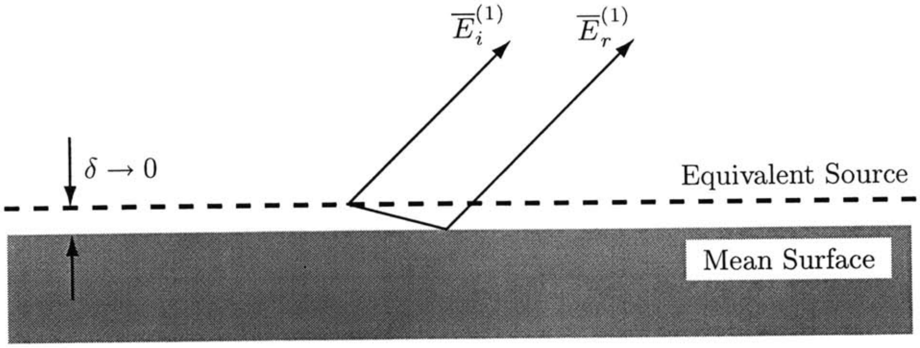

Figure 4-3: The radiation and reflection of the equivalent source on the mean surface of a PEC rough surface.

4.2.1 Surface Variables

The surface variables are defined as

$$\bar{a}(\bar{r}'_\perp) = \frac{dS'}{d\bar{r}'_\perp}\eta_1 \hat{n} \times \overline{H}(\bar{r}'), \tag{4.6}$$

$$\bar{b}(\bar{r}'_\perp) = \frac{dS'}{d\bar{r}'_\perp}\hat{n} \times \overline{E}(\bar{r}'), \tag{4.7}$$

where $\overline{E}(\bar{r}')$ and $\overline{H}(\bar{r}')$ are the total electric and magnetic fields on the rough surface, dS' is the infinitesimal area on the rough surface and is related to its projection on the mean surface by

$$dS' = d\bar{r}'_\perp \sqrt{\left(\partial f(\bar{r}'_\perp)/\partial x'\right)^2 + \left(\partial f(\bar{r}'_\perp)/\partial y'\right)^2 + 1}. \tag{4.8}$$

The normal vector is given by

$$\hat{n}(\bar{r}'_\perp) = \frac{-\hat{x}\partial f(\bar{r}'_\perp)/\partial x' - \hat{y}\partial f(\bar{r}'_\perp)/\partial y' + \hat{z}}{\sqrt{\left(\partial f(\bar{r}'_\perp)/\partial x'\right)^2 + \left(\partial f(\bar{r}'_\perp)/\partial y'\right)^2 + 1}}. \tag{4.9}$$

Therefore the surface variables can be rewritten as

$$\bar{a}(\bar{r}'_\perp) = \eta_1 \left(-\nabla'_\perp f(\bar{r}'_\perp) + \hat{z}\right) \times \overline{H}(\bar{r}'), \tag{4.10}$$

$$\bar{b}(\bar{r}'_\perp) = \left(-\nabla'_\perp f(\bar{r}'_\perp) + \hat{z}\right) \times \overline{E}(\bar{r}'). \tag{4.11}$$

Writing the surface variables and the total electric and magnetic fields in series form, we obtain

$$\begin{aligned} \bar{a}^{(0)}_\perp(\bar{r}'_\perp) + \bar{a}^{(1)}(\bar{r}'_\perp) + \cdots &= \eta_1 \left(-\nabla'_\perp f(\bar{r}'_\perp) + \hat{z}\right) \times \\ &\quad \left[\overline{H}^{(0)}(\bar{r}'_\perp) + \overline{H}^{(1)}(\bar{r}'_\perp) + \cdots\right], \end{aligned} \tag{4.12}$$

$$\begin{aligned} \bar{b}^{(0)}_\perp(\bar{r}'_\perp) + \bar{b}^{(1)}(\bar{r}'_\perp) + \cdots &= \left(-\nabla'_\perp f(\bar{r}'_\perp) + \hat{z}\right) \times \\ &\quad \left[\overline{E}^{(0)}(\bar{r}'_\perp) + \overline{E}^{(1)}(\bar{r}'_\perp) + \cdots\right]. \end{aligned} \tag{4.13}$$

We assume $\nabla'_\perp f(\bar{r}'_\perp)$ to be of the same order as $f(\bar{r}'_\perp)$, therefore, by matching the order on both sides, we get the surface variables for each order as follows:

$$\begin{align}
\bar{a}_\perp^{(0)}(\bar{r}'_\perp) &= \eta_1 \hat{z} \times \overline{H}^{(0)}(\bar{r}'_\perp), \tag{4.14}\\
\bar{a}^{(1)}(\bar{r}'_\perp) &= -\eta_1 \nabla'_\perp f(\bar{r}'_\perp) \times \overline{H}^{(0)}(\bar{r}'_\perp) + \eta_1 \hat{z} \times \overline{H}^{(1)}(\bar{r}'_\perp), \tag{4.15}\\
\bar{a}^{(n)}(\bar{r}'_\perp) &= -\eta_1 \nabla'_\perp f(\bar{r}'_\perp) \times \overline{H}^{(n-1)}(\bar{r}'_\perp) + \eta_1 \hat{z} \times \overline{H}^{(n)}(\bar{r}'_\perp), \tag{4.16}
\end{align}$$

and

$$\begin{align}
\bar{b}_\perp^{(0)}(\bar{r}'_\perp) &= \hat{z} \times \overline{E}^{(0)}(\bar{r}'_\perp), \tag{4.17}\\
\bar{b}^{(1)}(\bar{r}'_\perp) &= -\nabla'_\perp f(\bar{r}'_\perp) \times \overline{E}^{(0)}(\bar{r}'_\perp) + \hat{z} \times \overline{E}^{(1)}(\bar{r}'_\perp), \tag{4.18}\\
\bar{b}^{(n)}(\bar{r}'_\perp) &= -\nabla'_\perp f(\bar{r}'_\perp) \times \overline{E}^{(n-1)}(\bar{r}'_\perp) + \hat{z} \times \overline{E}^{(n)}(\bar{r}'_\perp). \tag{4.19}
\end{align}$$

Note that only the tangential components of the surface variables are used in the calculation of the radiation fields from the equivalent sources. Therefore

$$\begin{align}
\bar{a}_\perp^{(0)}(\bar{r}'_\perp) &= \eta_1 \hat{z} \times \overline{H}^{(0)}(\bar{r}'_\perp), \tag{4.20}\\
\bar{a}_\perp^{(1)}(\bar{r}'_\perp) &= \eta_1 \hat{z} \times \left[\nabla'_\perp f(\bar{r}'_\perp) H_z^{(0)}(\bar{r}'_\perp) + \overline{H}^{(1)}(\bar{r}'_\perp) \right], \tag{4.21}\\
\bar{a}_\perp^{(n)}(\bar{r}'_\perp) &= \eta_1 \hat{z} \times \left[\nabla'_\perp f(\bar{r}'_\perp) H_z^{(n-1)}(\bar{r}'_\perp) + \overline{H}^{(n)}(\bar{r}'_\perp) \right], \tag{4.22}
\end{align}$$

and

$$\begin{align}
\bar{b}_\perp^{(0)}(\bar{r}'_\perp) &= \hat{z} \times \overline{E}^{(0)}(\bar{r}'_\perp), \tag{4.23}\\
\bar{b}_\perp^{(1)}(\bar{r}'_\perp) &= \hat{z} \times \left[\nabla'_\perp f(\bar{r}'_\perp) E_z^{(0)}(\bar{r}'_\perp) + \overline{E}^{(1)}(\bar{r}'_\perp) \right], \tag{4.24}\\
\bar{b}_\perp^{(n)}(\bar{r}'_\perp) &= \hat{z} \times \left[\nabla'_\perp f(\bar{r}'_\perp) E_z^{(n-1)}(\bar{r}'_\perp) + \overline{E}^{(n)}(\bar{r}'_\perp) \right]. \tag{4.25}
\end{align}$$

4.2.2 Iterative Scheme

Eqs. (4.2) and (4.3) provide the formulation of the electric field from the equivalent source in terms of the lower order surface variables. The following is the iterative procedure to calculate the scattering field from the rough surface:

1. The zeroth order scattered field: Calculate the reflected $\overline{E}_r(\bar{r})$ and $\overline{H}_r(\bar{r})$ of the incident fields $\overline{E}_i(\bar{r})$ and $\overline{H}_i(\bar{r})$ from the mean surface. Thus the zeroth order scattered field is the same as the reflected field $\overline{E}_s^{(0)}(\bar{r}) = \overline{E}_r(\bar{r})$ and $\overline{H}_s^{(0)}(\bar{r}) = \overline{H}_r(\bar{r})$.

2. The first order scattered field: Calculate the total zeroth order fields on the mean surface

$$\begin{aligned} \overline{E}^{(0)}(\bar{r}) &= \overline{E}_i(\bar{r}) + \overline{E}_s^{(0)}(\bar{r}), & (4.26)\\ \overline{H}^{(0)}(\bar{r}) &= \overline{H}_i(\bar{r}) + \overline{H}_s^{(0)}(\bar{r}). & (4.27) \end{aligned}$$

Then calculate the surface variables

$$\begin{aligned} \bar{a}_\perp^{(0)}(\bar{r}'_\perp) &= \eta_1 \hat{z} \times \overline{H}^{(0)}(\bar{r}'_\perp), & (4.28)\\ \bar{b}_\perp^{(0)}(\bar{r}'_\perp) &= \hat{z} \times \overline{E}^{(0)}(\bar{r}'_\perp). & (4.29) \end{aligned}$$

Thus the first order scattered field can be calculated by

$$\begin{aligned} \overline{E}_s^{(1)}(\bar{r}) &= \overline{E}_i^{(1)}(\bar{r}) + \overline{E}_r^{(1)}(\bar{r}) + \overline{E}_{t2}^{(1)}(\bar{r}), & (4.30)\\ \overline{H}_s^{(1)}(\bar{r}) &= \overline{H}_i^{(1)}(\bar{r}) + \overline{H}_r^{(1)}(\bar{r}) + \overline{H}_{t2}^{(1)}(\bar{r}), & (4.31) \end{aligned}$$

where $\overline{E}_i^{(1)}(\bar{r})$ and $\overline{H}_i^{(1)}(\bar{r})$ are the fields of the first order equivalent source which can be calculated by using Eq. (4.4), $\overline{E}_r^{(1)}(\bar{r})$ and $\overline{H}_r^{(1)}(\bar{r})$ are the reflected fields of the equivalent source in the upper region, and $\overline{E}_{t2}^{(1)}(\bar{r})$ and $\overline{H}_{t2}^{(1)}(\bar{r})$ are the transmitted fields from the equivalent source in the lower region.

3. Calculate the n-th order scattered field: Calculate the surface variables

$$\begin{aligned}
\bar{a}_\perp^{(n)}(\bar{r}'_\perp) &= \eta_1 \hat{z} \times \left[\nabla'_\perp f(\bar{r}'_\perp) H_z^{(n-1)}(\bar{r}'_\perp) + \overline{H}^{(n)}(\bar{r}'_\perp)\right], && (4.32)\\
\bar{b}_\perp^{(n)}(\bar{r}'_\perp) &= \hat{z} \times \left[\nabla'_\perp f(\bar{r}'_\perp) E_z^{(n-1)}(\bar{r}'_\perp) + \overline{E}^{(n)}(\bar{r}'_\perp)\right]. && (4.33)
\end{aligned}$$

Thus the n-th order scattered field can be calculated by

$$\begin{aligned}
\overline{E}_s^{(n)}(\bar{r}) &= \overline{E}_i^{(n)}(\bar{r}) + \overline{E}_r^{(n)}(\bar{r}) + \overline{E}_{t2}^{(n)}(\bar{r}), && (4.34)\\
\overline{H}_s^{(n)}(\bar{r}) &= \overline{H}_i^{(n)}(\bar{r}) + \overline{H}_r^{(n)}(\bar{r}) + \overline{H}_{t2}^{(n)}(\bar{r}), && (4.35)
\end{aligned}$$

where $\overline{E}_i^{(n)}(\bar{r})$ and $\overline{H}_i^{(n)}(\bar{r})$ are the fields of the n-th order equivalent source, $\overline{E}_r^{(n)}(\bar{r})$ and $\overline{H}_r^{(n)}(\bar{r})$ are the reflected fields of the equivalent source in the upper region, and $\overline{E}_{t2}^{(n)}(\bar{r})$ and $\overline{H}_{t2}^{(n)}(\bar{r})$ are the transmitted fields from the equivalent source in the lower region.

4.3 Integral Representation of Equivalent Source

The integral representation of dyadic Green's function in region 1 and 2 can be written as [65], respectively,

$$\begin{aligned}
\overline{\overline{G}}_1(\bar{r}, \bar{r}') &= -\hat{z}\hat{z}\frac{\delta(\bar{r}, \bar{r}')}{k_1^2} \\
&\quad + \begin{cases} \dfrac{i}{8\pi^2} \displaystyle\int d\bar{k}_\perp \frac{1}{k_{1z}} \overline{\overline{A}}_1(k_{1z}) e^{i\bar{k}_1\cdot(\bar{r}-\bar{r}')} & z > z', \\ \displaystyle\int d\bar{k}_\perp \frac{1}{k_{1z}} \overline{\overline{A}}_1(-k_{1z}) e^{i\overline{K}_1\cdot(\bar{r}-\bar{r}')} & z < z', \end{cases} && (4.36)
\end{aligned}$$

and

$$\overline{\overline{G}}_2(\bar{r}, \bar{r}') = -\hat{z}\hat{z}\frac{\delta(\bar{r}, \bar{r}')}{k_2^2}$$

$$
+\begin{cases} \dfrac{i}{8\pi^2}\displaystyle\int d\bar{k}_\perp \frac{1}{k_{2z}} \overline{\overline{A}}_2(k_{2z}) e^{i\bar{k}_2\cdot(\bar{r}-\bar{r}')} & z > z', \\ \dfrac{i}{8\pi^2}\displaystyle\int d\bar{k}_\perp \frac{1}{k_{2z}} \overline{\overline{A}}_2(-k_{2z}) e^{i\overline{K}_2\cdot(\bar{r}-\bar{r}')} & z < z', \end{cases} \tag{4.37}
$$

where we define

$$
\begin{aligned}
\overline{\overline{A}}_1(k_{1z}) &= \hat{e}_1(k_{1z})\hat{e}_1(k_{1z}) + \hat{h}_1(k_{1z})\hat{h}_1(k_{1z}), & (4.38)\\
\overline{\overline{A}}_2(k_{2z}) &= \hat{e}_2(k_{2z})\hat{e}_2(k_{2z}) + \hat{h}_2(k_{2z})\hat{h}_2(k_{2z}), & (4.39)
\end{aligned}
$$

and $\hat{e}_{1,2}$ and $\hat{h}_{1,2}$ are unit polarization vectors defined in Appendix B. The up-going wave vectors $\bar{k}_1$ and $\bar{k}_2$ are expressed as $\bar{k}_1 = \hat{x}k_x + \hat{y}k_y + \hat{z}k_{1z}$ and $\bar{k}_2 = \hat{x}k_x + \hat{y}k_y + \hat{z}k_{2z}$, respectively, and the down-going wave vectors $\overline{K}_1$ and $\overline{K}_2$ are expressed as $\overline{K}_1 = \hat{x}k_x + \hat{y}k_y - \hat{z}k_{1z}$ and $\overline{K}_2 = \hat{x}k_x + \hat{y}k_y - \hat{z}k_{2z}$, respectively, where k_x and k_y are considered as the same in both regions due to phase matching. Defining the dyads

$$
\begin{aligned}
\overline{\overline{B}}_1(k_{1z}) &= \hat{k}_1 \times \overline{\overline{A}}_1(k_{1z}) = -\hat{h}_1(k_{1z})\hat{e}_1(k_{1z}) + \hat{e}_1(k_{1z})\hat{h}_1(k_{1z}), & (4.40)\\
\overline{\overline{B}}_2(k_{2z}) &= \hat{k}_2 \times \overline{\overline{A}}_2(k_{2z}) = -\hat{h}_2(k_{2z})\hat{e}_2(k_{2z}) + \hat{e}_2(k_{2z})\hat{h}_2(k_{2z}), & (4.41)
\end{aligned}
$$

we write the expressions for $\nabla \times \overline{\overline{G}}_{1,2}(\bar{r}, \bar{r}')$ in terms of the integral of $\overline{\overline{B}}_{1,2}$ as in Appendix B. The operator $\partial^m/\partial z^m$ operating on $\overline{\overline{G}}_{1,2}(\bar{r}, \bar{r}')$ and $\nabla \times \overline{\overline{G}}_{1,2}(\bar{r}, \bar{r}')$ creates the following eigenvalues

$$
\frac{\partial^m}{\partial z^m} = \begin{cases} (ik_{1,2z})^m & z > z', \\ (-ik_{1,2z})^m & z < z'. \end{cases} \tag{4.42}
$$

Therefore, the radiation field from the equivalent source on top of the mean surface can be written as follows:

For up-going wave $(z > z')$

$$
\overline{E}_i^{(n)}(\bar{r}) = -\frac{i}{8\pi^2}k_1 \sum_{m=1}^{n} \frac{1}{m!} \int d\bar{r}'_\perp \left[-f(\bar{r}'_\perp)\right]^m
$$

$$\begin{aligned}
&\left\{\int d\bar{k}_\perp\,(ik_{1z})^{m-1}\,\overline{\overline{A}}_1(k_{1z})e^{i\bar{k}_1\cdot(\bar{r}-\bar{r}')}\cdot\bar{a}_\perp^{(n-m)}(\bar{r}'_\perp)\right.\\
&\left.+\int d\bar{k}_\perp\,(ik_{1z})^{m-1}\,\overline{\overline{B}}_1(k_{1z})e^{i\bar{k}_1\cdot(\bar{r}-\bar{r}')}\cdot\bar{b}_\perp^{(n-m)}(\bar{r}'_\perp)\right\}\\
&-\frac{i}{8\pi^2}k_1\sum_{m=1}^{n}\frac{1}{(m-1)!}\int d\bar{r}'_\perp\,[-f(\bar{r}'_\perp)]^{m-1}\\
&\left\{\int d\bar{k}_\perp\,(ik_{1z})^{m-2}\,\overline{\overline{A}}_1(k_{1z})e^{i\bar{k}_1\cdot(\bar{r}-r')}\cdot\hat{z}\left[\nabla'_\perp f(\bar{r}'_\perp)\cdot\bar{a}_\perp^{(n-m)}(\bar{r}'_\perp)\right]\right.\\
&\left.+\int d\bar{k}_\perp\,(ik_{1z})^{m-2}\,\overline{\overline{B}}_1(k_{1z})e^{i\bar{k}_1\cdot(\bar{r}-\bar{r}')}\cdot\hat{z}\left[\nabla'_\perp f(\bar{r}'_\perp)\cdot\bar{b}_\perp^{(n-m)}(\bar{r}'_\perp)\right]\right\},
\end{aligned}\tag{4.43}$$

$$\begin{aligned}
\overline{E}_{i2}^{(n)}(\bar{r}) \;=\;& -\frac{ik_2}{8\pi^2}\sum_{m=1}^{n}\frac{1}{m!}\int d\bar{r}'_\perp\,[-f(\bar{r}'_\perp)]^{m}\\
&\left\{\frac{\eta_2}{\eta_1}\int d\bar{k}_\perp\,(ik_{2z})^{m-1}\,\overline{\overline{A}}_2(k_{2z})e^{i\bar{k}_2\cdot(\bar{r}-\bar{r}')}\cdot\bar{a}_\perp^{(n-m)}(\bar{r}'_\perp)\right.\\
&\left.+\int d\bar{k}_\perp\,(ik_{2z})^{m-1}\,\overline{\overline{B}}_2(k_{2z})e^{i\bar{k}_2\cdot(\bar{r}-\bar{r}')}\cdot\bar{b}_\perp^{(n-m)}(\bar{r}'_\perp)\right\}\\
&-\frac{ik_2}{8\pi^2}\sum_{m=1}^{n}\frac{1}{(m-1)!}\int d\bar{r}'_\perp\,[-f(\bar{r}'_\perp)]^{m-1}\\
&\left\{\frac{\eta_2}{\eta_1}\int d\bar{k}_\perp\,(ik_{2z})^{m-2}\,\overline{\overline{A}}_2(k_{2z})e^{i\bar{k}_2\cdot(r-r')}\cdot\hat{z}\left[\nabla'_\perp f(\bar{r}'_\perp)\cdot\bar{a}_\perp^{(n-m)}(\bar{r}'_\perp)\right]\right.\\
&\left.+\int d\bar{k}_\perp\,(ik_{2z})^{m-2}\,\overline{\overline{B}}_2(k_{2z})e^{i\bar{k}_2\cdot(r-r')}\cdot\hat{z}\left[\nabla'_\perp f(\bar{r}'_\perp)\cdot\bar{b}_\perp^{(n-m)}(\bar{r}'_\perp)\right]\right\}.
\end{aligned}\tag{4.44}$$

For down-going wave ($z < z'$)

$$\begin{aligned}
\overline{E}_{i}^{(n)}(\bar{r}) \;=\;& \frac{ik_1}{8\pi^2}\sum_{m=1}^{n}\frac{1}{m!}\int d\bar{r}'_\perp\,[-f(\bar{r}'_\perp)]^{m}\\
&\left\{\int d\bar{k}_\perp\,(-ik_{1z})^{m-1}\,\overline{\overline{A}}_1(-k_{1z})e^{i\overline{K}_1\cdot(\bar{r}-\bar{r}')}\cdot\bar{a}_\perp^{(n-m)}(\bar{r}'_\perp)\right.\\
&\left.+\int d\bar{k}_\perp\,(-ik_{1z})^{m-1}\,\overline{\overline{B}}_1(-k_{1z})e^{i\overline{K}_1\cdot(\bar{r}-\bar{r}')}\cdot\bar{b}_\perp^{(n-m)}(\bar{r}'_\perp)\right\}\\
&+\frac{ik_1}{8\pi^2}\sum_{m=1}^{n}\frac{1}{(m-1)!}\int d\bar{r}'_\perp\,[-f(\bar{r}'_\perp)]^{m-1}
\end{aligned}$$

$$\left\{\int d\bar{k}_\perp\,(-ik_{1z})^{m-2}\overline{\overline{A}}_1(-k_{1z})e^{i\overline{K}_1\cdot(\bar{r}-\bar{r}')}\cdot\hat{z}\left[\nabla'_\perp f(\bar{r}'_\perp)\cdot\bar{a}_\perp^{(n-m)}(\bar{r}'_\perp)\right]\right.$$
$$\left.+\int d\bar{k}_\perp\,(-ik_{1z})^{m-2}\overline{\overline{B}}_1(-k_{1z})e^{i\overline{K}_1\cdot(\bar{r}-\bar{r}')}\cdot\hat{z}\left[\nabla'_\perp f(\bar{r}'_\perp)\cdot\bar{b}_\perp^{(n-m)}(\bar{r}'_\perp)\right]\right\}, \tag{4.45}$$

$$\begin{aligned}
\overline{E}_{i2}^{(n)}(\bar{r}) = {} & \frac{ik_2}{8\pi^2}\sum_{m=1}^{n}\frac{1}{m!}\int d\bar{r}'_\perp\,[-f(\bar{r}'_\perp)]^m \\
& \left\{\frac{\eta_2}{\eta_1}\int d\bar{k}_\perp\,(-ik_{2z})^{m-1}\,\overline{\overline{A}}_2(-k_{2z})e^{i\overline{K}_2\cdot(\bar{r}-\bar{r}')}\cdot\bar{a}_\perp^{(n-m)}(\bar{r}'_\perp)\right. \\
& \left.+\int d\bar{k}_\perp\,(-ik_{2z})^{m-1}\overline{\overline{B}}_2(-k_{2z})e^{i\overline{K}_2\cdot(r-r')}\cdot\bar{b}_\perp^{(n-m)}(\bar{r}'_\perp)\right\} \\
& +\frac{ik_2}{8\pi^2}\sum_{m=1}^{n}\frac{1}{(m-1)!}\int d\bar{r}'_\perp\,[-f(\bar{r}'_\perp)]^{m-1} \\
& \left\{\frac{\eta_2}{\eta_1}\int d\bar{k}_\perp\,(-ik_{2z})^{m-2}\,\overline{\overline{A}}_2(-k_{2z})e^{i\overline{K}_2\cdot(\bar{r}-\bar{r}')}\cdot\hat{z}\left[\nabla'_\perp f(\bar{r}'_\perp)\cdot\bar{a}_\perp^{(n-m)}(\bar{r}'_\perp)\right]\right. \\
& \left.+\int d\bar{k}_\perp\,(-ik_{2z})^{m-2}\overline{\overline{B}}_2(-k_{2z})e^{i\overline{K}_2\cdot(\bar{r}-\bar{r}')}\cdot\hat{z}\left[\nabla'_\perp f(\bar{r}'_\perp)\cdot\bar{b}_\perp^{(n-m)}(\bar{r}'_\perp)\right]\right\}.
\end{aligned} \tag{4.46}$$

The down-going wave $\overline{E}_i^{(n)}$ and up-going wave $\overline{E}_{i2}^{(n)}$ will be reflected by and transmitted through the mean surface, respectively.

4.3.1 Reflected Field of Equivalent Source

To calculate the reflected wave of the equivalent source, we decompose $\overline{E}_i^{(n)}$ into a sum of TE and TM waves. Recalling the definition for $\overline{\overline{A}}_1$, $\overline{\overline{B}}_1$, $\overline{\overline{A}}_2$, and $\overline{\overline{B}}_2$, we know that the product of $\hat{e}_1(-k_{1z})\hat{e}_1(-k_{1z})$ or $\hat{e}_1(-k_{1z})\hat{h}_1(-k_{1z})$ with any polarization will be a TE wave, and the product of $\hat{h}_1(-k_{1z})\hat{h}_1(-k_{1z})$ or $\hat{h}_1(-k_{1z})\hat{e}_1(-k_{1z})$ with any polarization will be a TM wave. To get the reflected wave for the down-going wave $\overline{E}_i^{(n)}$ for $z < z'$, we do the following:

1. Multiply the TE wave terms by $R^{TE}(k_{1z})$ and the TM wave terms by $R^{TM}(k_{1z})$

in the integral representation of the down-going wave $\overline{E}_i^{(n)}$,

2. Change the sign of k_{1z} for the first unit polarization vector in the tensors $\overline{\overline{A}}_1$ and $\overline{\overline{B}}_1$, and
3. Change the down-going wave vector $\overline{K}_1$ to the up-going wave vector $\bar{k}_1$ in the exponential terms.

Thus we find

$$
\begin{aligned}
\overline{E}_r^{(n)}(\bar{r}) = {} & \frac{ik_1}{8\pi^2}\sum_{m=1}^{n}\frac{1}{m!}\int d\bar{r}'_\perp\,[-f(\bar{r}'_\perp)]^m \\
& \Bigg\{\int d\bar{k}_\perp\,(-ik_{1z})^{m-1}\Big(R^{TE}(k_{1z})\hat{e}_1(k_{1z})\hat{e}_1(-k_{1z})+R^{TM}(k_{1z})\hat{h}_1(k_{1z})\hat{h}_1(-k_{1z})\Big) \\
& e^{i\bar{k}_1\cdot(\bar{r}-\bar{r}')}\cdot\bar{a}_\perp^{(n-m)}(\bar{r}'_\perp) \\
& +\int d\bar{k}_\perp\,(-ik_{1z})^{m-1}\Big(-R^{TM}(k_{1z})\hat{h}_1(k_{1z})\hat{e}_1(-k_{1z})+R^{TE}(k_{1z})\hat{e}_1(k_{1z})\hat{h}_1(-k_{1z})\Big) \\
& e^{i\bar{k}_1\cdot(\bar{r}-\bar{r}')}\cdot\bar{b}_\perp^{(n-m)}(\bar{r}'_\perp)\Bigg\} \\
& +\frac{ik_1}{8\pi^2}\sum_{m=1}^{n}\frac{1}{(m-1)!}\int d\bar{r}'_\perp\,[-f(\bar{r}'_\perp)]^{m-1} \\
& \Bigg\{\int d\bar{k}_\perp\,(-ik_{1z})^{m-2}\Big(R^{TE}(k_{1z})\hat{e}_1(k_{1z})\hat{e}_1(-k_{1z})+R^{TM}(k_{1z})\hat{h}_1(k_{1z})\hat{h}_1(-k_{1z})\Big) \\
& e^{i\bar{k}_1\cdot(\bar{r}-\bar{r}')}\cdot\hat{z}\left[\nabla'_\perp f(\bar{r}'_\perp)\cdot\bar{a}_\perp^{(n-m)}(\bar{r}'_\perp)\right] \\
& +\int d\bar{k}_\perp\,(-ik_{1z})^{m-2}\Big(-R^{TM}(k_{1z})\hat{h}_1(k_{1z})\hat{e}_1(-k_{1z})+R^{TE}(k_{1z})\hat{e}_1(k_{1z})\hat{h}_1(-k_{1z})\Big) \\
& e^{i\bar{k}_1\cdot(\bar{r}-\bar{r}')}\cdot\hat{z}\left[\nabla'_\perp f(\bar{r}'_\perp)\cdot\bar{b}_\perp^{(n-m)}(\bar{r}'_\perp)\right]\Bigg\}. \qquad (4.47)
\end{aligned}
$$

In the above equation, the Fresnel reflection coefficients are defined as follows:

$$
\begin{aligned}
R^{TE}(k_{1z}) &= \frac{k_{1z}-k_{2z}}{k_{1z}+k_{2z}}, && (4.48)\\
R^{TM}(k_{1z}) &= \frac{\epsilon_2 k_{1z}-\epsilon_1 k_{2z}}{\epsilon_2 k_{1z}+\epsilon_1 k_{2z}}, && (4.49)\\
R^{TE}(k_{2z}) &= -R^{TE}(k_{1z}) = -\frac{k_{1z}-k_{2z}}{k_{1z}+k_{2z}}, && (4.50)
\end{aligned}
$$

$$R^{TM}(k_{2z}) = -R^{TM}(k_{1z}) = -\frac{\epsilon_2 k_{1z} - \epsilon_1 k_{2z}}{\epsilon_2 k_{1z} + \epsilon_1 k_{2z}}, \tag{4.51}$$

where $R^{TE}(k_{1z})$ and $R^{TM}(k_{1z})$ are the reflection coefficients for TE and TM waves incident from region 1 to region 2, respectively; $R^{TE}(k_{2z})$ and $R^{TM}(k_{2z})$ are the reflection coefficients for TE and TM waves incident from region 2 to region 1, respectively.

4.3.2 Transmitted Field of Equivalent Source

To get the transmitted wave from the equivalent source in the lower region, we work on the up-going wave $\overline{E}^{(n)}_{i2}$ as in Eq. (4.44):

1. Multiply the terms with $\hat{e}_2$ as the first vector in the tensors with T^{TE}, and multiply the terms with $\hat{h}_2$ as the first vector in the tensors $\overline{\overline{A}}_2$ and $\overline{\overline{B}}_2$ with T^{TM},
2. Change the first vectors $\hat{e}_2(k_{2z})$ and $\hat{h}_2(k_{2z})$ in the polarization tensors to $\hat{e}_1(k_{1z})$ and $\hat{h}_1(k_{1z})$, and
3. Change the up-going wave vector $\overline{k}_2$ to $\overline{k}_1$ in the exponential terms.

Thus we get

$$\begin{aligned}
\overline{E}^{(n)}_{t2}(\bar{r}) &= -\frac{ik_2}{8\pi^2}\sum_{m=1}^{n}\frac{1}{m!}\int d\bar{r}'_\perp\,[-f(\bar{r}'_\perp)]^m \\
&\quad \Big\{\frac{\eta_2}{\eta_1}\int d\bar{k}_\perp\,(ik_{2z})^{m-1}\Big(T^{TE}(k_{2z})\hat{e}_1(k_{1z})\hat{e}_2(k_{2z}) + T^{TM}(k_{2z})\hat{h}_1(k_{1z})\hat{h}_2(k_{2z})\Big) \\
&\quad e^{i\bar{k}_1\cdot(\bar{r}-\bar{r}')}\cdot\bar{a}^{(n-m)}_\perp(\bar{r}'_\perp) \\
&\quad + \int d\bar{k}_\perp\,(ik_{2z})^{m-1}\Big(-T^{TM}(k_{2z})\hat{h}_1(k_{1z})\hat{e}_2(k_{2z}) + T^{TE}(k_{2z})\hat{e}_1(k_{1z})\hat{h}_2(k_{2z})\Big) \\
&\quad e^{i\bar{k}_1\cdot(\bar{r}-\bar{r}')}\cdot\bar{b}^{(n-m)}_\perp(\bar{r}'_\perp)\Big\} \\
&\quad -\frac{ik_2}{8\pi^2}\sum_{m=1}^{n}\frac{1}{(m-1)!}\int d\bar{r}'_\perp\,[-f(\bar{r}'_\perp)]^{m-1} \\
&\quad \Big\{\frac{\eta_2}{\eta_1}\int d\bar{k}_\perp\,(ik_{2z})^{m-2}\Big(T^{TE}(k_{2z})\hat{e}_1(k_{1z})\hat{e}_2(k_{2z}) + T^{TM}(k_{2z})\hat{h}_1(k_{1z})\hat{h}_2(k_{2z})\Big)
\end{aligned}$$

$$
\begin{aligned}
& e^{i\bar{k}_1\cdot(\bar{r}-\bar{r}')}\cdot\hat{z}\left[\nabla'_\perp f(\bar{r}'_\perp)\cdot\bar{a}_\perp^{(n-m)}(\bar{r}'_\perp)\right] \\
& +\int d\bar{k}_\perp\,(ik_{2z})^{m-2}\left(-T^{TM}(k_{2z})\hat{h}_1(k_{1z})\hat{e}_2(k_{2z})+T^{TE}(k_{2z})\hat{e}_1(k_{1z})\hat{h}_2(k_{2z})\right) \\
& e^{i\bar{k}_1\cdot(\bar{r}-\bar{r}')}\cdot\hat{z}\left[\nabla'_\perp f(\bar{r}'_\perp)\cdot\bar{b}_\perp^{(n-m)}(\bar{r}'_\perp)\right]\Bigg\},
\end{aligned}
\tag{4.52}
$$

where the transmission coefficients are defined as follows:

$$T^{TE}(k_{1z}) = 1+R^{TE}(k_{1z})=\frac{2k_{1z}}{k_{1z}+k_{2z}}, \tag{4.53}$$

$$T^{TM}(k_{1z}) = \frac{\eta_2}{\eta_1}\left(1+R^{TM}(k_{1z})\right)=\frac{\eta_2}{\eta_1}\frac{2\epsilon_2 k_{1z}}{\epsilon_2 k_{1z}+\epsilon_1 k_{2z}}, \tag{4.54}$$

$$T^{TE}(k_{2z}) = 1+R^{TE}(k_{2z})=\frac{2k_{2z}}{k_{1z}+k_{2z}}, \tag{4.55}$$

$$T^{TM}(k_{2z}) = \frac{\eta_1}{\eta_2}\left(1+R^{TM}(k_{2z})\right)=\frac{\eta_1}{\eta_2}\frac{2\epsilon_1 k_{2z}}{\epsilon_2 k_{1z}+\epsilon_1 k_{2z}}. \tag{4.56}$$

4.4 The First Order Field Scattered by PEC Rough Surface

For the perfectly conducting rough surface, the tangential electric field is zero, $\bar{b}_\perp^{(0)}=0$. Therefore the first order field of the equivalent source can be written as [from Eq. (4.43)]

$$
\begin{aligned}
\overline{E}_i^{(1)}(\bar{r}) = {} & \frac{ik_1}{8\pi^2}\int d\bar{r}'_\perp f(\bar{r}'_\perp)\int d\bar{k}_\perp\overline{\overline{A}}_1(k_{1z})e^{i\bar{k}_1\cdot(\bar{r}-\bar{r}')}\cdot\bar{a}_\perp^{(0)}(\bar{r}'_\perp) \\
& -\frac{ik_1}{8\pi^2}\int d\bar{r}'_\perp\int d\bar{k}_\perp\frac{1}{ik_{1z}}\overline{\overline{A}}_1(k_{1z})e^{i\bar{k}_1\cdot(\bar{r}-\bar{r}')}\cdot\hat{z} \\
& \left[\nabla'_\perp f(\bar{r}'_\perp)\cdot\bar{a}_\perp^{(0)}(\bar{r}'_\perp)\right].
\end{aligned}
\tag{4.57}
$$

Also notice that the Fresnel reflection coefficients of the TE and TM waves for perfectly conducting surface are $R^{TE}(k_{1z})=-1$ and $R^{TM}(k_{1z})=1$. Therefore, from Eq. (4.47), the first order ($n=1$) wave of the equivalent source reflected by the perfectly conducting surface is

$$\begin{aligned}
\overline{E}_r^{(1)}(\bar{r}) &= \frac{ik_1}{8\pi^2}\int d\bar{r}'_\perp f(\bar{r}'_\perp)\int d\bar{k}_\perp\Big(\hat{e}_1(k_{1z})\hat{e}_1(k_{1z}) \\
&\quad +\hat{h}_1(k_{1z})\hat{h}_1(k_{1z})\Big)e^{i\bar{k}_1\cdot(\bar{r}-\bar{r}')}\cdot\bar{a}_\perp^{(0)}(\bar{r}'_\perp) \\
&\quad -\frac{ik_1}{8\pi^2}\int d\bar{r}'_\perp\int d\bar{k}_\perp\frac{1}{ik_{1z}}\Big(\hat{e}_1(k_{1z})\hat{e}_1(k_{1z}) \\
&\quad +\hat{h}_1(k_{1z})\hat{h}_1(k_{1z})\Big)e^{i\bar{k}_1\cdot(\bar{r}-\bar{r}')}\cdot\hat{z}\left[\nabla'_\perp f(\bar{r}'_\perp)\cdot\bar{a}_\perp^{(0)}(\bar{r}'_\perp)\right] \\
&= \frac{ik_1}{8\pi^2}\int d\bar{r}'_\perp f(\bar{r}'_\perp)\int d\bar{k}_\perp\overline{\overline{A}}_1(k_{1z})e^{i\bar{k}_1\cdot(\bar{r}-\bar{r}')}\cdot\bar{a}_\perp^{(0)}(\bar{r}'_\perp) \\
&\quad -\frac{ik_1}{8\pi^2}\int d\bar{r}'_\perp\int d\bar{k}_\perp\frac{1}{ik_{1z}}\overline{\overline{A}}_1(k_{1z})e^{i\bar{k}_1\cdot(\bar{r}-\bar{r}')}\cdot\hat{z} \\
&\quad \left[\nabla'_\perp f(\bar{r}'_\perp)\cdot\bar{a}_\perp^{(0)}(\bar{r}'_\perp)\right]. \qquad (4.58)
\end{aligned}$$

Notice that the first order wave reflected by the mean surface of the perfectly conducting rough surface [Eq. (4.58)] is the same as the first order radiated field of the equivalent source [Eq. (4.57)]. The transmitted field $\overline{E}_{t2}^{(1)}$ is zero, thus the total scattered field is

$$\begin{aligned}
\overline{E}_s^{(1)}(\bar{r}) &= \overline{E}_i^{(1)}(\bar{r})+\overline{E}_{1r}^{(1)}(\bar{r}) = 2\overline{E}_i^{(1)}(\bar{r}) \\
&= -2ik_1\int d\bar{r}'_\perp f(\bar{r}'_\perp)\frac{\partial}{\partial z}\left\{\overline{\overline{G}}_1(\bar{r},\bar{r}'_\perp)\cdot\bar{a}_\perp^{(0)}(\bar{r}'_\perp)\right\} \\
&\quad +2ik_1\int d\bar{r}'_\perp\overline{\overline{G}}_1(\bar{r},\bar{r}'_\perp)\cdot\hat{z}\left[\nabla'_\perp f(\bar{r}'_\perp)\cdot\bar{a}_\perp^{(0)}(\bar{r}'_\perp)\right]. \qquad (4.59)
\end{aligned}$$

4.4.1 Comparison with Conventional SPM Result

Consider the plane wave $\overline{E}_i(\bar{r}) = \overline{E}_i^{(0)}(\bar{r}) = \hat{e}_i E_o e^{i\bar{k}_i\cdot\bar{r}}$ incident upon a perfectly conducting rough surface. The SPM solution of the zeroth order surface variable $\bar{a}_\perp^{(0)}$ is [65]

$$\bar{a}_\perp^{(0)}(\bar{r}'_\perp) = \tilde{a}_\perp^{(0)}(\bar{k}_{i\perp})e^{i\bar{k}_{i\perp}\cdot\bar{r}'_\perp}, \qquad (4.60)$$

where

$$\tilde{a}_{\perp}^{(0)}(\bar{k}_{i\perp}) = \hat{q}_i a_q^{(0)}(\bar{k}_{i\perp}) + \hat{p}_i a_p^{(0)}(\bar{k}_{i\perp}), \tag{4.61}$$

$$\begin{aligned} a_q^{(0)}(\bar{k}_{i\perp}) &= 2\left[\hat{e}_i \cdot \hat{e}(-k_{iz})\right] E_o \frac{k_{iz}}{k_1}, \\ a_p^{(0)}(\bar{k}_{i\perp}) &= 2\left[\hat{e}_i \cdot \hat{h}(-k_{iz})\right] E_o, \end{aligned} \tag{4.62}$$

and the basis vectors are defined as follows:

$$\begin{aligned} \hat{q}_i &= \frac{1}{k_{i\rho}}(\hat{x}k_{iy} - \hat{y}k_{ix}), \\ \hat{p}_i &= \hat{z}_i \times \hat{q}_i = \frac{1}{k_{i\rho}}(\hat{x}k_{ix} + \hat{y}k_{iy}), \\ \hat{z}_i &= \hat{z}. \end{aligned} \tag{4.63}$$

Defining the Fourier transform pair

$$F(\bar{k}_{\perp}) = \frac{1}{(2\pi)^2}\int d\bar{r}'_{\perp} e^{-i\bar{k}_{\perp}\cdot\bar{r}'_{\perp}} f(\bar{r}'_{\perp}), \tag{4.64}$$

$$f(\bar{r}'_{\perp}) = \int d\bar{k}'_{\perp} e^{i\bar{k}'_{\perp}\cdot\bar{r}'_{\perp}} F(\bar{k}'_{\perp}), \tag{4.65}$$

and the delta function

$$\delta(\bar{k}_{\perp}) = \frac{1}{(2\pi)^2}\int d\bar{r}'_{\perp} e^{-i\bar{k}_{\perp}\cdot\bar{r}'_{\perp}}, \tag{4.66}$$

we can write the following relations as

$$\frac{\partial f(\bar{r}'_{\perp})}{\partial x'} = i\int d\bar{k}'_{\perp} e^{i\bar{k}'_{\perp}\cdot\bar{r}'_{\perp}} k'_x F(\bar{k}'_{\perp}), \tag{4.67}$$

$$\frac{\partial f(\bar{r}'_{\perp})}{\partial y'} = i\int d\bar{k}'_{\perp} e^{i\bar{k}'_{\perp}\cdot\bar{r}'_{\perp}} k'_y F(\bar{k}'_{\perp}), \tag{4.68}$$

$$\nabla'_{\perp} f(\bar{r}'_{\perp}) = i\int d\bar{k}'_{\perp} e^{i\bar{k}'_{\perp}\cdot\bar{r}'_{\perp}} \left(k'_x\hat{x} + k'_y\hat{y}\right) F(\bar{k}'_{\perp}). \tag{4.69}$$

Making use of the vector products

$$\begin{aligned}
(\hat{x}k_x + \hat{y}k_y)\cdot\hat{q}_i &= \frac{k_xk_{iy} - k_yk_{ix}}{k_{i\rho}}, \\
(\hat{x}k_x + \hat{y}k_y)\cdot\hat{p}_i &= \frac{k_xk_{ix} + k_yk_{iy}}{k_{i\rho}}, \\
(\hat{x}k_{ix} + \hat{y}k_{iy})\cdot\hat{q}_i &= 0, \\
(\hat{x}k_{ix} + \hat{y}k_{iy})\cdot\hat{p}_i &= k_{i\rho},
\end{aligned} \tag{4.70}$$

and

$$\begin{aligned}
\hat{e}_1(k_{1z})\cdot\hat{q}_i &= \frac{k_{iy}k_y + k_{ix}k_x}{k_\rho k_{i\rho}}, \\
\hat{e}_1(k_{1z})\cdot\hat{p}_i &= \frac{k_{ix}k_y - k_{iy}k_x}{k_\rho k_{i\rho}},
\end{aligned} \tag{4.71}$$

the first order scattered field in Eq. (4.59) is obtained by integrating the transverse wavenumber as follows:

$$\begin{aligned}
\overline{E}_s^{(1)}(\bar{r}) = {} & E_o \int d\bar{k}_\perp e^{i\bar{k}_1\cdot\bar{r}} iF(\bar{k}_\perp - \bar{k}_{i\perp})\hat{e}_1(k_{1z}) \left(2k_1 \frac{k_{iy}k_y + k_{ix}k_x}{k_\rho k_{i\rho}} \frac{k_{iz}}{k_1}\right) [\hat{e}_i\cdot\hat{e}(-k_{iz})] \\
& + E_o \int d\bar{k}_\perp e^{i\bar{k}_1\cdot\bar{r}} iF(\bar{k}_\perp - \bar{k}_{i\perp})\hat{e}_1(k_{1z}) \left(2k_1 \frac{k_{ix}k_y - k_{iy}k_x}{k_\rho k_{i\rho}}\right) \left[\hat{e}_i\cdot\hat{h}(-k_{iz})\right] \\
& + E_o \int d\bar{k}_\perp e^{i\bar{k}_1\cdot\bar{r}} iF(\bar{k}_\perp - \bar{k}_{i\perp})\hat{h}_1(k_{1z}) \left(-2\frac{k_1k_{iz}}{k_{1z}k_\rho} \frac{k_xk_{iy} - k_yk_{ix}}{k_{i\rho}}\right) [\hat{e}_i\cdot\hat{e}(-k_{iz})] \\
& + E_o \int d\bar{k}_\perp e^{i\bar{k}_1\cdot\bar{r}} iF(\bar{k}_\perp - \bar{k}_{i\perp})\hat{h}_1(k_{1z}) \left(-2\frac{k_1^2}{k_{1z}k_\rho} \frac{k_xk_{ix} + k_yk_{iy}}{k_{i\rho}} + 2\frac{k_\rho k_{i\rho}}{k_{1z}}\right) \\
& \left[\hat{e}_i\cdot\hat{h}(-k_{iz})\right].
\end{aligned} \tag{4.72}$$

By rewriting the scattered electric field in matrix form as

$$\begin{aligned}
\overline{E}^{(1)}(\bar{r}) &= \begin{bmatrix} E_e^{(1)}(\bar{r}) \\ E_h^{(1)}(\bar{r}) \end{bmatrix} \\
&= \int d\bar{k}_\perp e^{i\bar{k}_1\cdot\bar{r}} iF(\bar{k}_\perp - \bar{k}_{i\perp}) \begin{bmatrix} f_{ee} & f_{eh} \\ f_{he} & f_{hh} \end{bmatrix} \begin{bmatrix} \hat{e}_i\cdot\hat{e}(-k_{iz})E_o \\ \hat{e}_i\cdot\hat{h}(-k_{iz})E_o \end{bmatrix},
\end{aligned} \tag{4.73}$$

the scattering matrix can be written as

$$\begin{bmatrix} f_{ee} & f_{eh} \\ f_{he} & f_{hh} \end{bmatrix} = \begin{bmatrix} 2k_1 \frac{k_{iy}k_y + k_{ix}k_x}{k_\rho k_{i\rho}} \frac{k_{iz}}{k_1} & 2k_1 \frac{k_{ix}k_y - k_{iy}k_x}{k_\rho k_{i\rho}} \\ -2\frac{k_1 k_{iz}}{k_{1z}k_\rho} \frac{k_x k_{iy} - k_y k_{ix}}{k_{i\rho}} & -2\frac{k_1^2}{k_{1z}k_\rho} \frac{k_x k_{ix} + k_y k_{iy}}{k_{i\rho}} + 2\frac{k_\rho k_{i\rho}}{k_{1z}} \end{bmatrix}. \tag{4.74}$$

Expressing the wavenumber components by using angles θ, ϕ, θ_i, and ϕ_i, we find the scattering matrix

$$\begin{bmatrix} f_{ee} & f_{eh} \\ f_{he} & f_{hh} \end{bmatrix} = \begin{bmatrix} 2k_{iz}\cos(\phi - \phi_i) & 2k_1 \sin(\phi - \phi_i) \\ \frac{2k_1 k_{iz}}{k_{1z}} \sin(\phi - \phi_i) & \frac{2k_1^2}{k_{1z}} [\sin\theta \sin\theta_i - \cos(\phi - \phi_i)] \end{bmatrix}. \tag{4.75}$$

Notice that the components of the scattering matrix [Eq. (4.74)] derived above using the equivalent source formulation are the same as the ones using conventional SPM as given in [40] for the limiting case of $k_2 \to \infty$.

4.5 Numerical Result

In this section, the backscattering coefficients will be calculated by using the first order equivalent source formulation and compared with the standard method of moments. For plane incident wave, the backscattering coefficient of the field scattered by rough surface is defined as

$$\sigma_{ab} = \lim_{r\to\infty} 4\pi r^2 \frac{\left\langle |E_a^s - \langle E_a^s \rangle|^2 \right\rangle}{A\,|E_b^i|^2}, \tag{4.76}$$

where $a, b = h, v$ denotes the polarizations of the scattered and incident waves, respectively. For an arbitrarily incident wave, the backscattering coefficient is defined as

$$\sigma_{ab} = \lim_{r\to\infty} 4\pi r^2 \frac{\left\langle |E_a^s - \langle E_a^s \rangle|^2 \right\rangle}{P_i}, \tag{4.77}$$

where $P_i = \int \left|E_b^i\right|^2 dA$ is the power of the incident wave on the illuminated area with the integral over the mean surface. For example, on the mean surface, the electric field of a Gaussian tapered wave can be written as $E_b^i = E_o e^{-r^2/g^2}$, where g is a factor specifying the beam width. Therefore we get, for the incident Gaussian tapered wave,

$$P_i = \int_0^\infty r dr \int_0^{2\pi} d\phi \left|E_o\right|^2 e^{-2r^2/g^2} = \left|E_o\right|^2 \frac{\pi g^2}{2}. \tag{4.78}$$

In the numerical calculation, the expected backscattering coefficient are calculated by averaging samples of the scattered field, thus

$$\begin{aligned} \sigma_{ab} &= \lim_{r\to\infty} 4\pi r^2 \frac{\left\langle \left|E_a^s - \langle E_a^s\rangle\right|^2 \right\rangle}{P_i} \\ &\sim \lim_{r\to\infty} \frac{4\pi r^2}{P_i} \left[\frac{1}{N-1} \sum_{n=1}^{N} \left|E_a^s\right|^2 - \frac{1}{N(N-1)} \left| \sum_{n=1}^{N} E_a^s \right|^2 \right] \\ &= \lim_{r\to\infty} \frac{4\pi r^2}{P_i} \frac{N}{N-1} \left[\frac{1}{N} \sum_{n=1}^{N} \left|E_a^s\right|^2 - \left| \frac{1}{N} \sum_{n=1}^{N} E_a^s \right|^2 \right], \end{aligned} \tag{4.79}$$

where N is the number of realizations in the Monte Carlo simulation and "$\sim$" means statistically estimated. The method of generating random rough surfaces is presented in Appendix C. It is convenient if we use the standard deviation to normalize the calculated profile $f(x,y)$. The standard deviation σ can be obtained by

$$\sigma^2 = \int_0^\infty kdk \int_0^{2\pi} d\alpha W(k,\alpha). \tag{4.80}$$

In the numerical simulation, we use the power law spectrum to generate random rough surfaces. The power law spectrum function for rough surfaces is defined as

$$W(k,\alpha) = \frac{\sigma^2 k_c^2 k_{\max}^2}{\pi\left(k_{\max}^2 - k_c^2\right) k^4}, \tag{4.81}$$

where σ is the rms height, and k_c and $k_{\max}$ are the low and high cutoff wavenumbers of the rough surface, respectively.

Figure (4-4) is the numerical result for the backscattering coefficients of the co-

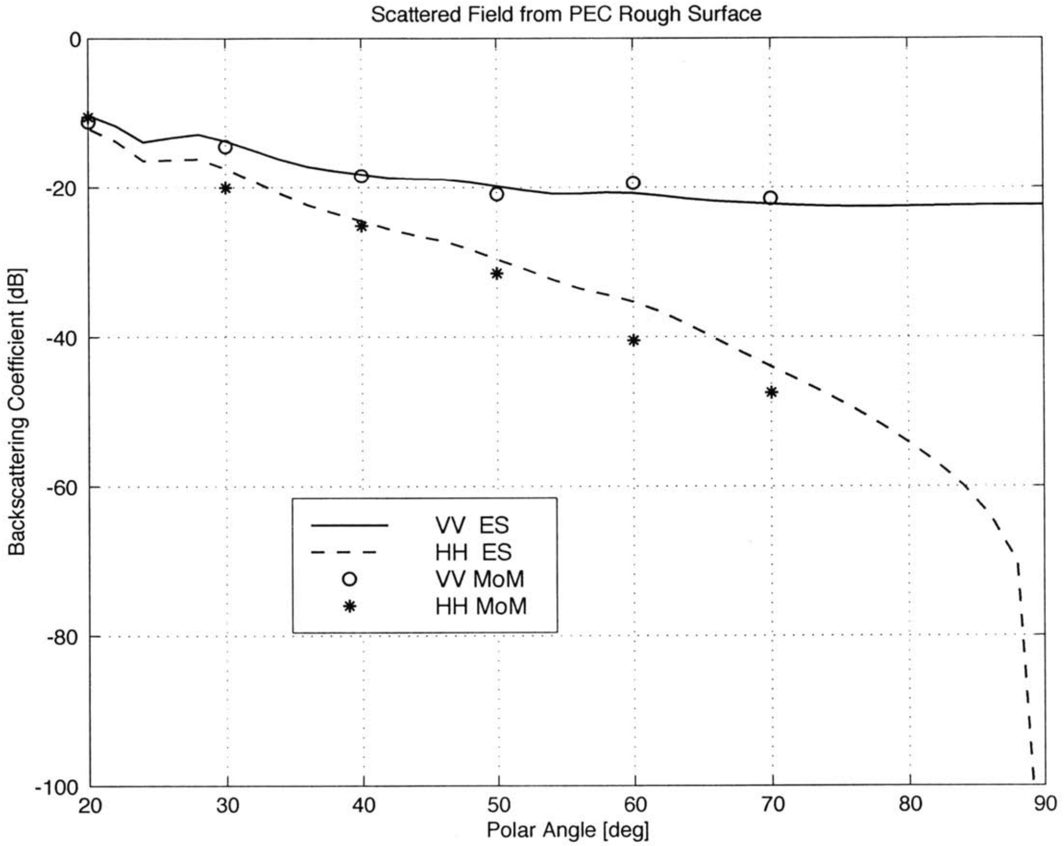

Figure 4-4: Comparison of the scattered field calculated by using the equivalent source (ES) formulation with the result from the standard method of moments (MoM).

polarized waves σ_{hh} and σ_{vv} by using the equivalent source formulation in comparison with the standard MoM. The rms height of the rough surface is $\sigma = 0.01\lambda$ and the number of realizations is $N = 30$. The incident wave is tapered with the factor $g = 3.0\lambda$. The central plane wave of the incident tapered wave varies its polar angle from 20° to 70° in order to avoid the strong specular reflection of the incident beam close to the normal incident and numerical problems of the standard MoM at low grazing angles. A comparison of the results demonstrates good agreement between the two different methods. At low grazing angles, the MoM code does not provide correct results due to the difficulty to increase the size of rough surface at these angles [76]. The equivalent source formulation gives reasonable results at low grazing angles where σ_{hh} drops to zero and σ_{vv} tends to a constant when the grazing angle approaches zero.

4.6 Conclusions

In this chapter, up to the first order, we have proved that the total field of the equivalent source on a PEC rough surface is the field scattered by the rough surface. The proof for dielectric rough surfaces and for arbitrary orders requires much more effort since the Sommerfeld integrals are involved. By considering a plane incident wave, we have found that the total field of the equivalent source is the same as the field scattered by the rough surface obtained by using the traditional small perturbation method (SPM). From the SPM point of view, we conclude that the n-th order scattered field is the n-th order field of the equivalent source on the mean surface. Particularly for the PEC rough surface, the equivalent source formulation in Eq. (4.59) is more suited for calculating the scattered field than the conventional SPM, since

1. The incident wave $\overline{E}_i$ is arbitrary but not constrained to be a plane wave as in SPM.

2. Unlike SPM, the equivalent source formulation can be used to calculate the scattered field in the near field.

In comparison with the standard MoM, the equivalent source method is much faster in the case of PEC rough surfaces. In addition to the good agreement in the numerical comparison with the MoM, the equivalent source method works well at low grazing angles, while it is hard at these angles to obtain correct results with the MoM, owing to the difficulty of sampling a large rough surface.

Chapter 5

Polarimetric Thermal Emission from Foam-Covered Wind-Driven Ocean Surface

5.1 Introduction

In the microwave remote sensing of ocean surface, the use of polarimetric passive techniques has shown potential for enhancing the retrieval of wind speed and directions [40]. Recent theoretical and experimental research activities have concentrated on studies of polarimetric thermal emissions regarding the anisotropic ocean surface assuming a smoothly varying surface profile [40, 41, 77, 78]. However, under high wind conditions, the presence of breaking water waves, foam patches and bubbles will affect the polarimetric brightness temperatures of the plain ocean surface. The significance of foam on the ocean surface was recognized a long time ago [42], and several subsequent experiments performed have verified its importance [43, 44]. Previous studies of the foam contribution to the emissivity of ocean surface were based on empirical formulations [45, 46] derived from experimental data. Although several attempts at theoretically modeling the foam have been presented [47, 48], it is difficult to incorporate them with rough ocean surface. The more realistic modeling for foam-covered ocean surface has been proposed by Huang et al. [79], who consider the sea foam to be a layer with water particles over a rough sea surface.

However, it is not suited to model the sea foam as the layer of spherical water particles, since the sea foam is dominated by water bubbles [80]. In this chapter, we present the theoretical study on the polarimetric thermal emissions from foam-covered ocean surface based on a composite volume and rough surface scattering model using the radiative transfer theory. We model the locally foam-covered ocean surface as a random layer with water bubbles. The small perturbation method (SPM) is used for random rough ocean surface, where the bistatic scattering is calculated up to the second order. The radiative transfer equations for foam layer are solved using an iterative technique. The model predictions are compared with measurement data [49].

5.2 Formulations for Foam Emission

5.2.1 RT Equations for Foam Layer

Sea-foam is made of spray, small water droplets and air bubbles which are generated by wind tearing and further processions such as bubble production, bubble downward entrainment, and droplet produced by bubble bursting as illustrated in Fig. (5-1) [80]. Since the thermal emission from sea-foam is dominated by water bubbles, we simplify the sea-foam as a water bubble layer as shown in Fig. (5-2). For simplicity, the top surface of the foam layer is considered to be a flat surface. Above the foam layer (region 1) is a half free space that is labeled as region 0 with ϵ_o, μ_o. The foam layer is specified by a foam thickness d_1, the inner bubble radius R, bubble film thinkness δ and permittivity ϵ_1, the fractional volume f_v of bubbles, the extinction coefficient κ_e, and the temperature profile $T(z)$. The background of the foam layer is considered to be free space with ϵ_o, μ_o. The sea water (region 2) is in the lower half space

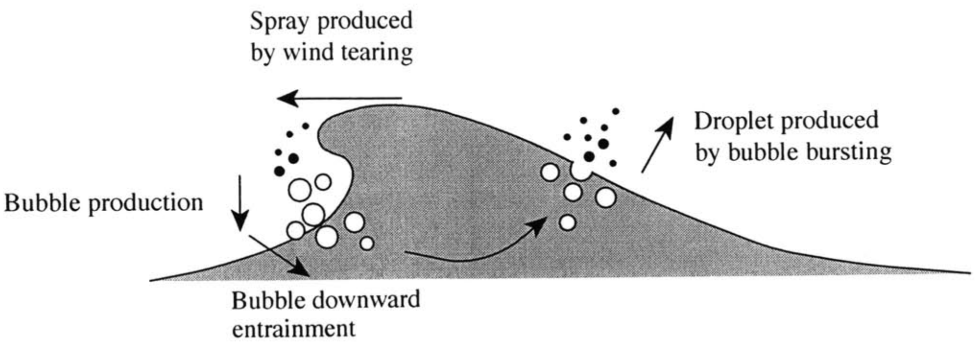

Figure 5-1: The generation of sea-foam.

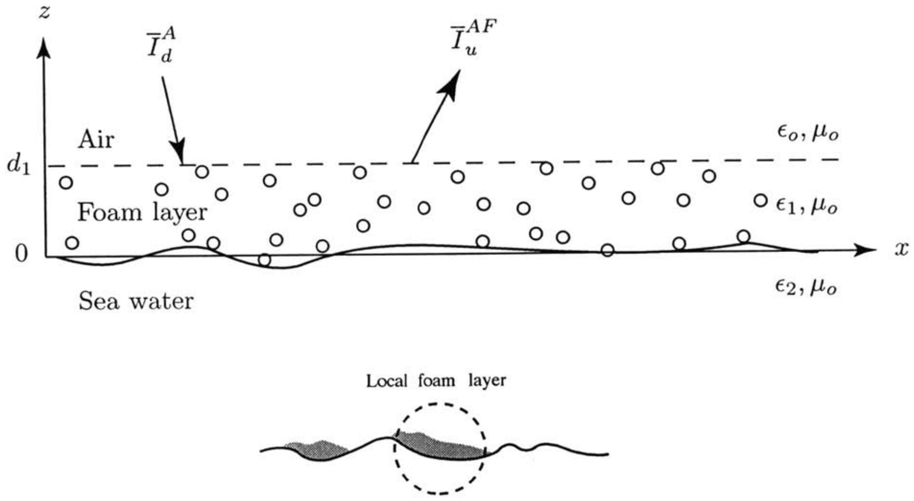

Figure 5-2: The configuration of local foam layer on wind-driven rough ocean surface.

with permittivity ϵ_2, salinity S, and physical temperature T_o. The foam coverage is denoted by F, thus the coverage of the plain ocean surface is $1 - F$.

In the foam layer, the radiative transfer equation [81, page 229] is given by

$$\begin{aligned} \cos\theta \frac{d}{dz}\overline{I}(\theta,\phi,z) &= -\overline{\overline{\kappa}}_e(\theta,\phi)\cdot\overline{I}(\theta,\phi,z) \\ &\quad + \int_{4\pi} d\Omega'\,\overline{\overline{P}}(\theta,\phi,\theta',\phi')\cdot\overline{I}(\theta',\phi',z) + \overline{I}_T(\theta,\phi,z), \end{aligned} \tag{5.1}$$

where $\overline{\overline{P}}(\theta,\phi,\theta',\phi')$ is the phase matrix which is derived by using Mie theory in Appendix D. The phase matrix provides the contributions to the specific intensity

$\overline{I}(\theta, \phi, z)$ in the direction (θ, ϕ) from the direction (θ', ϕ'). $\overline{\overline{\kappa}}_e$ is the extinction tensor. In this thesis, the specific intensity with the unit of $\mathrm{W/m^2}$ is defined as

$$\overline{I}(\theta, \phi, z) = \frac{1}{\eta} \begin{bmatrix} \left\langle |E_v|^2 \right\rangle \\ \left\langle |E_h|^2 \right\rangle \\ 2\mathrm{Re}\left\langle E_v E_h^* \right\rangle \\ 2\mathrm{Im}\left\langle E_v E_h^* \right\rangle \end{bmatrix}, \tag{5.2}$$

where $\eta = \sqrt{\mu_o/\epsilon_o}$ is the free space impedance. $\overline{I}_T(\theta, \phi, z)$ is the intensity of the physical temperature and it is written as $\overline{I}_T(\theta, \phi, z) = \overline{\kappa}_a(\theta, \phi)CT(z)$. In this expression, $\overline{\kappa}_a$ is the absorption coefficient vector, $C = K_B/\lambda^2$ where K_B is the Boltzmann constant ($K_B = 1.380658 \times 10^{-23}$ J/K) and λ is the electromagnetic wavelength. We assume that the scatterers are bubbles and the absorption is isotropic, thus

$$\overline{\kappa}_a = \kappa_a \left[1 \quad 1 \quad 0 \quad 0\right]^T. \tag{5.3}$$

As mentioned in the previous section, the foam layer is modeled as the composition of spherical water bubbles randomly distributed in the foam layer, therefore the extinction coefficient $\overline{\overline{\kappa}}_e(\theta, \phi)$ is a scalar, i.e., $\overline{\overline{\kappa}}_e(\theta, \phi) = \kappa_e$. The formulations of calculating κ_e and κ_a are provided in Appendix D. We assume that the temperature $T(z)$ in the foam layer is independent of elevation and it is equal to the temperature of the sea water, i.e., $T(z) = T_o$. Thus

$$\overline{I}_T(\theta, \phi, z) = \overline{\kappa}_a(\theta, \phi)CT_o. \tag{5.4}$$

Define the new specific intensities for $0 \leq \theta < \pi/2$ as

$$\begin{aligned} \overline{I}_u(\theta, \phi, z) &= \overline{I}(\theta, \phi, z), & (5.5) \\ \overline{I}_d(\theta, \phi, z) &= \overline{I}(\pi - \theta, \phi, z), & (5.6) \\ \overline{I}_{Tu}(\theta, \phi, z) &= \overline{I}_T(\theta, \phi, z), & (5.7) \end{aligned}$$

$$\overline{I}_{Td}(\theta, \phi, z) = \overline{I}_T(\pi - \theta, \phi, z), \tag{5.8}$$

the RT equation (5.1) is split into two:

$$\begin{aligned} \cos\theta \frac{d}{dz} \overline{I}_u(\theta, \phi, z) &= -\kappa_e \overline{I}_u(\theta, \phi, z) + \int_{\text{upper } 2\pi} d\Omega' \,\overline{\overline{P}}(\theta, \phi, \theta', \phi') \cdot \overline{I}_u(\theta', \phi', z) \\ &+ \int_{\text{lower } 2\pi} d\Omega' \,\overline{\overline{P}}(\theta, \phi, \pi - \theta', \phi') \cdot \overline{I}_d(\theta', \phi', z) + \overline{I}_{Tu}(\theta, \phi), \end{aligned} \tag{5.9}$$

$$\begin{aligned} -\cos\theta \frac{d}{dz} \overline{I}_d(\theta, \phi, z) &= -\kappa_e \overline{I}_d(\theta, \phi, z) + \int_{\text{upper } 2\pi} d\Omega' \,\overline{\overline{P}}(\pi - \theta, \phi, \theta', \phi') \cdot \overline{I}_u(\theta', \phi', z) \\ &+ \int_{\text{lower } 2\pi} d\Omega' \,\overline{\overline{P}}(\pi - \theta, \phi, \pi - \theta', \phi') \cdot \overline{I}_d(\theta', \phi', z) + \overline{I}_{Td}(\theta, \phi). \end{aligned} \tag{5.10}$$

We assume that the thickness of the foam layer is much larger than the penetration depth of the electromagnetic wave. Under this assumption, there is no returned wave from the bottom of the foam layer. Thus the boundary conditions are:

on the upper boundary ($z = d_1$)

$$\overline{I}_d(\theta, \phi, d_1) = \overline{I}_d^A(\theta, \phi, d_1), \tag{5.11}$$

on the lower boundary ($z = 0$)

$$\overline{I}_u(\theta, \phi, 0) = 0, \tag{5.12}$$

where $\overline{I}_d^A(\theta, \phi, d_1)$ is the specific intensity of the atmospheric layer.

5.2.2 Solution of the RT Equation

To solve the RT equations (5.9) and (5.10), the iterative and numerical methods can be used. The iterative method is applied to scattering problems with small absorption which is the case for the foam layer, while the numerical method can be applied for strong absorption problems.

In the iterative method of solving the RT equations, we consider the integral terms as known from the lower order solutions, thus the RT equations for each step are in the form of an ordinary differential equation (ODE). The general form of the first order ODE is written as

$$\frac{dy(z)}{dz} + f(z)y(z) = g(z), \tag{5.13}$$

with the boundary condition $y(z_o) = y_o$. The solution of the ODE is

$$y(z) = \left[\int_{z_o}^{z} g(z') e^{\int_{z_o}^{z'} f(z'')dz''} dz' + y_o \right] e^{-\int_{z_o}^{z} f(z')dz'} . \tag{5.14}$$

The zeroth order RT solution

To solve the RT equations for the zeroth order, we first ignore the scattering by assuming $\overline{\overline{P}} = 0$. Thus we obtain

$$\cos\theta \frac{d}{dz} \overline{I}_u^{(0)}(\theta, \phi, z) = -\kappa_e \overline{I}_u^{(0)}(\theta, \phi, z) + \overline{I}_{Tu}(\theta, \phi), \tag{5.15}$$

$$-\cos\theta \frac{d}{dz} \overline{I}_d^{(0)}(\theta, \phi, z) = -\kappa_e \overline{I}_d^{(0)}(\theta, \phi, z) + \overline{I}_{Td}(\theta, \phi), \tag{5.16}$$

with the boundary conditions

$$\overline{I}_d^{(0)}(\theta, \phi, d_1) = \overline{I}_d^{A}(\theta, \phi, d_1), \tag{5.17}$$

$$\overline{I}_u^{(0)}(\theta, \phi, 0) = 0. \tag{5.18}$$

From the formula of the general solution (5.14) of the first order ODE, the zeroth order solutions of the RT equations (5.9) and (5.10) can be derived as follows:

$$\overline{I}_u^{(0)}(\theta, \phi, z) = \overline{I}_{Tu}(\theta, \phi)\frac{1 - e^{-z\sec\theta\kappa_e}}{\kappa_e}, \tag{5.19}$$

$$\overline{I}_d^{(0)}(\theta, \phi, z) = \overline{I}_{Td}(\theta, \phi)\frac{1 - e^{-(d_1 - z)\sec\theta\kappa_e}}{\kappa_e} + \overline{I}_d^{A}(\theta, \phi, d_1)e^{-(d_1 - z)\sec\theta\kappa_e}. \tag{5.20}$$

The first order RT solution

Plugging the zeroth order solutions (5.19) and (5.20) into the RT equations (5.9) and (5.10), and defining the terms from the zeroth order solutions as follows:

$$\begin{aligned}\overline{I}_{Tu}^{(1)}(\theta, \phi, z) &= \int_{\text{upper } 2\pi} d\Omega' \,\overline{\overline{P}}(\theta, \phi, \theta', \phi') \cdot \overline{I}_u^{(0)}(\theta', \phi', z) \\ &\quad + \int_{\text{lower } 2\pi} d\Omega' \,\overline{\overline{P}}(\theta, \phi, \pi - \theta', \phi') \cdot \overline{I}_d^{(0)}(\theta', \phi', z) + \overline{I}_{Tu}(\theta, \phi),\end{aligned} \tag{5.21}$$

$$\begin{aligned}\overline{I}_{Td}^{(1)}(\theta, \phi, z) &= \int_{\text{upper } 2\pi} d\Omega' \,\overline{\overline{P}}(\pi - \theta, \phi, \theta', \phi') \cdot \overline{I}_u^{(0)}(\theta', \phi', z) \\ &\quad + \int_{\text{lower } 2\pi} d\Omega' \,\overline{\overline{P}}(\pi - \theta, \phi, \pi - \theta', \phi') \cdot \overline{I}_d^{(0)}(\theta', \phi', z) + \overline{I}_{Td}(\theta, \phi),\end{aligned} \tag{5.22}$$

we set up the first order RT equations as

$$\cos\theta\frac{d}{dz}\overline{I}_u^{(1)}(\theta, \phi, z) = -\kappa_e\overline{I}_u^{(1)}(\theta, \phi, z) + \overline{I}_{Tu}^{(1)}(\theta, \phi, z), \tag{5.23}$$

$$-\cos\theta\frac{d}{dz}\overline{I}_d^{(1)}(\theta, \phi, z) = -\kappa_e\overline{I}_d^{(1)}(\theta, \phi, z) + \overline{I}_{Td}^{(1)}(\theta, \phi, z), \tag{5.24}$$

with the boundary conditions

$$\overline{I}_d^{(1)}(\theta,\phi,d_1)=\overline{I}_d^{A}(\theta,\phi,d_1), \tag{5.25}$$

$$\overline{I}_u^{(1)}(\theta,\phi,0)=0. \tag{5.26}$$

Again by using the general solution (5.14) of the ODE, the solutions of the first order RT equations are obtained as

$$\overline{I}_u^{(1)}(\theta,\phi,z)=\left[\int\limits_0^z \sec\theta\,\overline{I}_{Tu}^{(1)}(\theta,\phi,z')\,e^{z'\sec\theta\kappa_e}\,dz'\right]e^{-z\sec\theta\kappa_e}, \tag{5.27}$$

$$\overline{I}_d^{(1)}(\theta,\phi,z)=\left[-\sec\theta\int\limits_{d_1}^{z}\overline{I}_{Td}^{(1)}(\theta,\phi,z')e^{-z'\sec\theta\kappa_e}dz'+\overline{I}_d^{A}(\theta,\phi,d_1)e^{-d_1\sec\theta\kappa_e}\right]e^{z\sec\theta\kappa_e}. \tag{5.28}$$

The specific intensity in the foam layer we are interested in is the up-going intensity at $z=d_1$. By integrating over the elevation in Eq. (5.27), the first order intensity of the up-going wave at the top of the foam layer can be written as

$$\begin{aligned}
\overline{I}_u^{(1)}(\theta,\phi,d_1) = {} & \overline{I}_{Tu}(\theta,\phi)\frac{1-e^{-d_1\sec\theta\kappa_e}}{\kappa_e} \\
& +\sec\theta\int\limits_{\text{upper }2\pi} d\Omega'\,\overline{\overline{P}}(\theta,\phi,\theta',\phi')\cdot\overline{I}_{Tu}(\theta',\phi')\frac{1}{\kappa_e^2} \\
& \left(\frac{1-e^{-d_1\sec\theta\kappa_e}}{\sec\theta}-\frac{e^{-d_1\sec\theta'\kappa_e}-e^{-d_1\sec\theta\kappa_e}}{\sec\theta-\sec\theta'}\right) \\
& +\sec\theta\int\limits_{\text{lower }2\pi} d\Omega'\,\overline{\overline{P}}(\theta,\phi,\pi-\theta',\phi')\cdot\overline{I}_{Td}(\theta',\phi')\frac{1}{\kappa_e^2} \\
& \left(\frac{1-e^{-d_1\sec\theta\kappa_e}}{\sec\theta}-\frac{1-e^{-d_1(\sec\theta+\sec\theta')\kappa_e}}{\sec\theta+\sec\theta'}\right) \\
& +\sec\theta\int\limits_{\text{lower }2\pi} d\Omega'\,\overline{\overline{P}}(\theta,\phi,\pi-\theta',\phi')\cdot\overline{I}_d^{A}(\theta',\phi',d_1) \\
& \frac{1-e^{-d_1(\sec\theta+\sec\theta')\kappa_e}}{(\sec\theta+\sec\theta')\kappa_e}.
\end{aligned} \tag{5.29}$$

Assuming $d_1\kappa_e \gg 1$, the Stokes vector of the thick foam layer is given as follows

$$\begin{aligned}
\overline{I}_u^{AF}(\theta,\phi,d_1) &\approx \overline{I}_u^{(1)}(\theta,\phi,d_1) \\
&\approx \overline{I}_{Tu}(\theta,\phi)\frac{1}{\kappa_e} + \int_{\text{upper }2\pi} d\Omega'\,\overline{\overline{P}}(\theta,\phi,\theta',\phi')\cdot\overline{I}_{Tu}(\theta',\phi')\frac{1}{\kappa_e^2} \\
&\quad + \int_{\text{lower }2\pi} d\Omega'\,\overline{\overline{P}}(\theta,\phi,\pi-\theta',\phi')\cdot\overline{I}_{Td}(\theta',\phi')\frac{1}{\kappa_e^2}\left(1-\frac{\sec\theta}{\sec\theta+\sec\theta'}\right) \\
&\quad + \int_{\text{lower }2\pi} d\Omega'\,\overline{\overline{P}}(\theta,\phi,\pi-\theta',\phi')\cdot\overline{I}_d^{A}(\theta',\phi',d_1)\frac{\sec\theta}{(\sec\theta+\sec\theta')\kappa_e},
\end{aligned} \tag{5.30}$$

where the first term denotes the direct emission due to the physical temperature of the foam layer, the second and the third term are the scattering of emission by the scatterers in the foam layer, and the fourth term is the scattering of the atmospheric emission. Notice that the up-going and down-going specific intensities due to the physical temperature in the foam layer are direction independent and they are given by

$$\overline{I}_{Tu}(\theta,\phi) = \overline{I}_{Td}(\theta,\phi) = \bar{\kappa}_a C T_o = \kappa_a C T_o \begin{bmatrix} 1 \\ 1 \\ 0 \\ 0 \end{bmatrix}. \tag{5.31}$$

5.2.3 Foam Coverage

Let the foam coverage be F, thus the total brightness temperature is [45]

$$\overline{T}_u^{T}(\theta,\phi,d_1) = F\cdot\overline{T}_u^{AF}(\theta,\phi,0) + (1-F)\cdot\overline{T}_u^{AS}(\theta,\phi,0), \tag{5.32}$$

where $\overline{T}_u^{AF}(\theta,\phi,d_1)$ is the emission of the 100% foam as in Eq. (5.30), and $\overline{T}_u^{AS}(\theta,\phi,0)$ is the emission of the plain ocean surface with the consideration of the reflection of atmospheric emission that will be discussed in the following sections. Notice that, at this stage, we only consider the emission at the zero elevation height ($z = 0$). We need to consider atmospheric attenuation and radiation if we calculate the total brightness temperature at the height of the radiometer ($z = d_2$). The empirical formula of the foam coverage F as the function of the wind speed U_w, the polar angle θ, and the operating frequency f was provided by Stogryn [45] and later used by Pandey [46] among others. The foam coverage is expressed as [45]

$$F = b_0 + b_1 U_w + b_2 U_w^2, \tag{5.33}$$

where the coefficients b_0, b_1 and b_2 are frequency dependent, and they are given by

$$\begin{aligned} b_0 &= 1.707 \times 10^{-2} + 8.560 \times 10^{-4} f + 1.120 \times 10^{-5} f^2, \\ b_1 &= -1.501 \times 10^{-2} + 1.821 \times 10^{-3} f - 4.634 \times 10^{-5} f^2, \\ b_2 &= 2.442 \times 10^{-4} - 2.282 \times 10^{-6} f + 4.194 \times 10^{-7} f^2. \end{aligned} \tag{5.34}$$

In (5.33) and (5.34), the units of the wind speed and the frequency are m/s and GHz, respectively.

5.3 Thermal Emission from Plain Ocean Surface

In local regions without foam, the thermal emission from the ocean surface is the sum of the reflection of the atmospheric emission and the thermal emission from the plain ocean surface, i.e.,

$$\overline{I}_u^{AS}(\theta, \phi, 0) = \int_{\text{lower } 2\pi} d\Omega' \,\overline{\overline{R}}(\theta, \phi, \pi - \theta', \phi') \cdot \overline{I}_d^A(\theta', \phi', 0) + \overline{I}_u^S(\theta, \phi, 0), \tag{5.35}$$

where $\overline{\overline{R}}$ is the reflection matrix of the rough sea surface, $\overline{I}_d^A(\theta', \phi', 0)$ is the thermal emission of the atmosphere, and $\overline{I}_u^S$ is the thermal emission of the plain ocean surface. The details of calculating the atmospheric emission $\overline{I}_d^A(\theta', \phi', 0)$ will be discussed in Section 5.3.2.

Considering that the ocean water is in thermal equilibrium, the Stokes vector is related to the emissivity $\bar{e}$ by

$$\overline{I}_u^S(\theta, \phi, 0) = \frac{K_B}{\lambda^2}\bar{e}(\theta, \phi)T_s, \tag{5.36}$$

where T_s is the physical temperature of the rough ocean surface. By Kirchhoff's law, the emissivity vector $\bar{e}(\theta, \phi)$ is the intensity of incident wave with unit amplitude minus the total intensity of the reflected waves,

$$\bar{e}(\theta, \phi) = \overline{I}_i - \int \overline{I}_r(\theta, \phi; \theta_i, \phi_i; 0)d\Omega_i, \tag{5.37}$$

where

$$\overline{I}_i = \frac{1}{\eta}\begin{bmatrix} \left\langle |E_{vi}|^2 \right\rangle \\ \left\langle |E_{hi}|^2 \right\rangle \\ 2\mathrm{Re}\left\langle E_{vi}E_{hi}^* \right\rangle \\ 2\mathrm{Im}\left\langle E_{vi}E_{hi}^* \right\rangle \end{bmatrix} = \begin{bmatrix} 1 \\ 1 \\ 0 \\ 0 \end{bmatrix}. \tag{5.38}$$

The amplitude of the v and h-polarized incident electric fields is unity, and $\overline{I}_r$ is the reflection Stokes vector of the plane wave with incident angles θ_i and ϕ_i.

5.3.1 Stokes Vector of Reflected Wave

We apply the small perturbation method (SPM) to calculate the reflection matrix $\overline{\overline{R}}$ of the rough surface and then calculate the reflection Stokes vector $\overline{I}_r$. The reflection Stokes vector can be written as

$$\overline{I}_r(\theta, \phi, \theta_i, \phi_i; 0) = \overline{\overline{R}}(\theta, \phi, \theta_i, \phi_i) \cdot \overline{I}_i(\theta_i, \phi_i; 0), \tag{5.39}$$

where $\overline{\overline{R}}$ is the reflection matrix for the Stokes vector.

In the zeroth order SPM solution, the scattered field is specular and is equivalent to the flat-surface scattering problem; thus the reflection coefficients of the zeroth order solution are the Fresnel reflection coefficients. Using the ensemble average, the second order solution from SPM is also specular. Therefore we call both the zeroth and second-order terms coherent. The averaged field of the first order solution by SPM is zero, hence it is incoherent. By including solutions up to the second order using SPM, the reflection matrix is the sum of coherent and incoherent parts, $\overline{\overline{R}}^c$ and $\overline{\overline{R}}^i$, respectively, so that

$$\overline{\overline{R}} = \overline{\overline{R}}^c + \overline{\overline{R}}^i. \tag{5.40}$$

Since the scattered field from the zeroth and second order SPM solutions is specular, the coherent reflection matrix of the Stokes vector can be written as

$$\begin{aligned}\overline{\overline{R}}^c(\theta, \phi, \pi - \theta_i, \phi_i) &= \left[R^c_{ij}\right] \delta(\cos\theta - \cos\theta_i)\delta(\phi - \phi_i) \\ &= \begin{bmatrix} R^c_{11} & R^c_{12} & R^c_{13} & R^c_{14} \\ R^c_{21} & R^c_{22} & R^c_{23} & R^c_{24} \\ R^c_{31} & R^c_{32} & R^c_{33} & R^c_{34} \\ R^c_{41} & R^c_{42} & R^c_{43} & R^c_{44} \end{bmatrix} \delta(\cos\theta - \cos\theta_i)\delta(\phi - \phi_i).\end{aligned} \tag{5.41}$$

Note that the subscripts i and j are associated with the scattered and incident components of the Stokes vector, respectively. The element R^c_{ij} $(i, j = 1, 2, 3, 4)$ is related to the reflection coefficient $R_{\alpha\beta}$ with subscripts $\alpha, \beta = v, h$, where

$$\begin{bmatrix} E^c_{vs} \\ E^c_{hs} \end{bmatrix} = \begin{bmatrix} R^c_{vv}(\theta_i, \phi_i) & R^c_{vh}(\theta_i, \phi_i) \\ R^c_{hv}(\theta_i, \phi_i) & R^c_{hh}(\theta_i, \phi_i) \end{bmatrix} \begin{bmatrix} E_{vi} \\ E_{hi} \end{bmatrix}, \tag{5.42}$$

and the subscript v and h represent vertically and horizontally polarized waves, respectively. By writing

$$\overline{I}^c_u = \frac{1}{\eta} \begin{bmatrix} |E^c_{vs}|^2 \\ |E^c_{hs}|^2 \\ 2\mathrm{Re}\{E^c_{vs}E^{c*}_{hs}\} \\ 2\mathrm{Im}\{E^c_{vs}E^{c*}_{hs}\} \end{bmatrix}$$

and expressing E^c_{vs} and E^c_{hs} in terms of E^c_{vi} and E^c_{hi} using Eq. (5.42), it can be shown that

$$\overline{I}^c_u = \left[R^c_{ij}\right] \cdot \overline{I}_i, \tag{5.43}$$

where

$$\left[R^c_{ij}\right] =$$
$$\begin{bmatrix} |R^c_{vv}|^2 & |R^c_{vh}|^2 & \mathrm{Re}(R^c_{vv}R^{*c}_{vh}) & -\mathrm{Im}(R^c_{vv}R^{*c}_{vh}) \\ |R^c_{hv}|^2 & |R^c_{hh}|^2 & \mathrm{Re}(R^c_{hv}R^{*c}_{hh}) & -\mathrm{Im}(R^c_{hv}R^{*c}_{hh}) \\ 2\mathrm{Re}(R^c_{vv}R^{*c}_{hv}) & 2\mathrm{Re}(R^c_{vh}R^{*c}_{hh}) & \mathrm{Re}\left(R^c_{vv}R^{*c}_{hh} + R^c_{vh}R^{*c}_{hv}\right) & -\mathrm{Im}\left(R^c_{vv}R^{*c}_{hh} - R^c_{vh}R^{*c}_{hv}\right) \\ 2\mathrm{Im}(R^c_{vv}R^{*c}_{hv}) & 2\mathrm{Im}(R^c_{vh}R^{*c}_{hh}) & \mathrm{Im}\left(R^c_{vv}R^{*c}_{hh} + R^c_{vh}R^{*c}_{hv}\right) & \mathrm{Re}\left(R^c_{vv}R^{*c}_{hh} - R^c_{vh}R^{*c}_{hv}\right) \end{bmatrix} \tag{5.44}$$

and the incident Stokes vector $\overline{I}_i$ is defined as in Eq. (5.38). Using SPM, $R^c_{\alpha\beta}$ $(\alpha, \beta = v, h)$ can be obtained as

$$R^c_{\alpha\beta} = \begin{bmatrix} R^{(0)}_{vv} + R^{(2)}_{vv} & R^{(0)}_{vh} + R^{(2)}_{vh} \\ R^{(0)}_{hv} + R^{(2)}_{hv} & R^{(0)}_{hh} + R^{(2)}_{hh} \end{bmatrix}, \tag{5.45}$$

where the zeroth order $R^{(0)}_{\alpha\beta}$ is the Fresnel reflection coefficient of a flat surface, which is given by

$$\begin{cases} R^{(0)}_{vv} = \dfrac{\epsilon_2 k_{1z} - \epsilon_1 k_{2z}}{\epsilon_2 k_{1z} + \epsilon_1 k_{2z}}, \\ R^{(0)}_{hh} = \dfrac{k_{1z} - k_{2z}}{k_{1z} + k_{2z}}, \\ R^{(0)}_{vh} = R^{(0)}_{hv} = 0. \end{cases} \tag{5.46}$$

The second order reflection coefficient $R^{(2)}_{\alpha\beta}$ is given by

$$R^{(2)}_{\alpha\beta} = \int\limits_{-\infty}^{\infty}\int\limits_{-\infty}^{\infty} dk_x dk_y W(k_{xi} - k_x, k_{yi} - k_y) f^{(2)}_{\alpha\beta}, \tag{5.47}$$

where $W(k_{xi} - k_x, k_{yi} - k_y)$ is the spectral density function of the rough ocean surface, and $f_{\alpha\beta}^{(2)}$ is the second-order scattering coefficient as in [40].

The incoherent reflection matrix $\overline{\overline{R}}^i(\theta, \phi; \theta_i, \phi_i)$ can be calculated by considering the first order SPM solution. By expressing the scattering fields as

$$\begin{bmatrix} E_{vs} \\ E_{hs} \end{bmatrix} = \frac{e^{ik_1 r}}{r} \begin{bmatrix} f_{vv}(\theta, \phi; \theta_i, \phi_i) & f_{vh}(\theta, \phi; \theta_i, \phi_i) \\ f_{hv}(\theta, \phi; \theta_i, \phi_i) & f_{hh}(\theta, \phi; \theta_i, \phi_i) \end{bmatrix} \begin{bmatrix} E_{vi} \\ E_{hi} \end{bmatrix}, \tag{5.48}$$

where $f_{\alpha\beta}(\theta, \phi; \theta_i, \phi_i)$ is the polarimetric scattering coefficient $(\alpha, \beta = h, v)$, the reflection matrix can be calculated by [82]

$$\overline{\overline{R}}^i = \frac{1}{A \cos\theta} \overline{\overline{L}}^i, \tag{5.49}$$

where

$$\overline{\overline{L}}^i(\theta, \phi; \theta_i, \phi_i) = \\ \begin{bmatrix} \left\langle |f_{vv}|^2 \right\rangle & \left\langle |f_{vh}|^2 \right\rangle & \mathrm{Re}\left\langle (f_{vv} f_{vh}^*) \right\rangle & -\mathrm{Im}\left\langle (f_{vv} f_{vh}^*) \right\rangle \\ \left\langle |f_{hv}|^2 \right\rangle & \left\langle |f_{hh}|^2 \right\rangle & \mathrm{Re}\left\langle (f_{hv} f_{hh}^*) \right\rangle & -\mathrm{Im}\left\langle (f_{hv} f_{hh}^*) \right\rangle \\ 2\mathrm{Re}\left\langle (f_{vv} f_{hv}^*) \right\rangle & 2\mathrm{Re}\left\langle (f_{vh} f_{hh}^*) \right\rangle & \mathrm{Re}\left\langle (f_{vv} f_{hh}^* + f_{vh} f_{hv}^*) \right\rangle & -\mathrm{Im}\left\langle (f_{vv} f_{hh}^* - f_{vh} f_{hv}^*) \right\rangle \\ 2\mathrm{Im}\left\langle (f_{vv} f_{hv}^*) \right\rangle & 2\mathrm{Im}\left\langle (f_{vh} f_{hh}^*) \right\rangle & \mathrm{Im}\left\langle (f_{vv} f_{hh}^* + f_{vh} f_{hv}^*) \right\rangle & \mathrm{Re}\left\langle (f_{vv} f_{hh}^* - f_{vh} f_{hv}^*) \right\rangle \end{bmatrix}. \tag{5.50}$$

and A is the illuminated area. The ensemble averaged product of the scattering coefficients is related to the polarimetric bistatic scattering coefficient as following:

$$\gamma_{\alpha\beta\mu\nu}^i(\theta, \phi; \theta_i, \phi_i) = \frac{4\pi \left\langle f_{\alpha\beta}(\theta, \phi; \theta_i, \phi_i) f_{\mu\nu}^*(\theta, \phi; \theta_i, \phi_i) \right\rangle}{A \cos\theta_i}. \tag{5.51}$$

From expression (5.49), (5.50) and (5.51), it can be easily derived that

$$\overline{\overline{R}}^i = \frac{\cos\theta_i}{4\pi\cos\theta}\begin{bmatrix} \gamma^i_{vvvv} & \gamma^i_{vhvh} & \mathrm{Re}\gamma^i_{vvvh} & -\mathrm{Im}\gamma^i_{vvvh} \\ \gamma^i_{hvhv} & \gamma^i_{hhhh} & \mathrm{Re}\gamma^i_{hvhh} & -\mathrm{Im}\gamma^i_{hvhh} \\ 2\mathrm{Re}\gamma^i_{vvhv} & 2\mathrm{Re}\gamma^i_{vhhh} & \mathrm{Re}\left(\gamma^i_{vvhh}+\gamma^i_{vhhv}\right) & -\mathrm{Im}\left(\gamma^{i*}_{vvhh}-\gamma^i_{vhhv}\right) \\ 2\mathrm{Im}\gamma^i_{vvhv} & 2\mathrm{Im}\gamma^i_{vhhh} & \mathrm{Im}\left(\gamma^i_{vvhh}+\gamma^i_{vhhv}\right) & \mathrm{Re}\left(\gamma^{i*}_{vvhh}-\gamma^i_{vhhv}\right) \end{bmatrix} \tag{5.52}$$

with

$$\gamma^i_{\alpha\beta\mu\nu}(\theta,\phi;\theta_i,\phi_i) = \frac{4\pi k_1^2\cos^2\theta\,\Gamma_{\alpha\beta\mu\nu}(\theta,\phi;\theta_i,\phi_i)W(\theta,\phi;\theta_i,\phi_i)}{\cos\theta_i}, \tag{5.53}$$

where $\Gamma_{\alpha\beta\mu\nu}$ is the coefficient with explicit form given in [40]. Finally, by knowing the coherent reflection matrix $\overline{\overline{R}}^c$ from Eq. (5.41) and the incoherent reflection matrix $\overline{\overline{R}}^i$ from Eq. (5.52), we obtain the total reflection $\overline{\overline{R}} = \overline{\overline{R}}^c + \overline{\overline{R}}^i$ [Eq. (5.40)]. Therefore the reflection Stokes vector $\overline{I}_r$ is obtained as

$$\overline{I}_r\left(\theta,\phi,\theta_i,\phi_i;0\right) = \left(\overline{\overline{R}}^c + \overline{\overline{R}}^i\right)\cdot\overline{I}_i, \tag{5.54}$$

and the emissivity can be calculated from Eq. (5.37) as

$$\begin{aligned} \bar{e}(\theta,\phi) &= \overline{I}_i - \int\left(\overline{\overline{R}}^c + \overline{\overline{R}}^i\right)\cdot\overline{I}_i d\Omega_i \\ &= \overline{I}_i - \int_0^{\pi/2}\sin\theta_i d\theta_i\int_0^{2\pi}d\phi_i\left(\overline{\overline{R}}^c + \overline{\overline{R}}^i\right)\cdot\overline{I}_i. \end{aligned} \tag{5.55}$$

5.3.2 Reflection of Atmospheric Thermal Emission

We write the term representing the reflection of the atmospheric thermal emission from the rough surface as

$$\overline{I}_r^A(\theta,\phi;0) = \int d\Omega'\,\overline{\overline{R}}(\theta,\phi,\pi-\theta',\phi')\cdot\overline{I}_d^A(\theta',\phi';0). \tag{5.56}$$

From Eq. (5.40) we know that the reflection of the rough surface can be written as the sum of the coherent and incoherent parts, therefore

$$\overline{I}_r^A(\theta,\phi;0) = \int d\Omega' \left(\overline{\overline{R}}^c + \overline{\overline{R}}^i\right) \cdot \overline{I}_d^A(\theta',\phi';0). \tag{5.57}$$

Thus the total Stokes vector in Eq. (5.35) can be written as

$$\begin{aligned} \overline{I}_u^{AS}(\theta,\phi;0) &= \int d\Omega' \left(\overline{\overline{R}}^c + \overline{\overline{R}}^i\right) \cdot \overline{I}_d^A(\theta',\phi';0) \\ &\quad + \frac{K_B}{\lambda^2} T_s \left[\overline{I}_i - \int d\Omega_i \left(\overline{\overline{R}}^c + \overline{\overline{R}}^i\right) \cdot \overline{I}_i\right]. \end{aligned} \tag{5.58}$$

Noticing that $d\Omega' = d\Omega_i$ for the down-going Stokes vector from the atmospheric layer, therefore it can be shown that

$$\overline{I}_u^{AS}(\theta,\phi;0) = \frac{K_B}{\lambda^2} T_s \overline{I}_i - \frac{K_B}{\lambda^2} T_s \int d\Omega_i \left(\overline{\overline{R}}^c + \overline{\overline{R}}^i\right) \cdot \left[\overline{I}_i - \frac{\lambda^2}{K_B T_s} \overline{I}_d^A(\theta_i,\phi_i;0)\right]. \tag{5.59}$$

Converting the Stokes vector to the brightness temperature, the brightness temperature of the plain ocean surface can be written as

$$\begin{aligned} \overline{T}_u^{AS}(\theta,\phi;0) &= \frac{\lambda^2}{K_B} \overline{I}_u^{AS}(\theta,\phi;0) \\ &= \overline{T}_i - \int d\Omega_i \left(\overline{\overline{R}}^c + \overline{\overline{R}}^i\right) \cdot \left[\overline{T}_i - \overline{T}_d^A(\theta_i,\phi_i;0)\right], \end{aligned} \tag{5.60}$$

where $\overline{T}_i = T_s \overline{I}_i$, and $\overline{T}_d^A(\theta_i,\phi_i;0) = \frac{\lambda^2}{K_B} \overline{I}_d^A(\theta_i,\phi_i;0)$ is the down-going brightness temperature of the atmosphere at the ocean surface. The down-going specific intensity $\overline{I}_d^A(\theta_i,\phi_i;0)$ from the atmosphere can be found from Eq. (5.77) and its approximation can be found in Eq. (5.89) as

$$\overline{I}_d^A(\theta,\phi,d_1) = \sec\theta \int_{d_1}^{d_2} \bar{\kappa}_a(z') C T(z') e^{-\sec\theta \int_{d_1}^{z'} \kappa_a(z'') dz''} dz'$$

$$\approx \quad CT(z_o)\,\frac{\bar{\kappa}_a}{\kappa_a}\left[1-e^{-\sec\theta\int\limits_{d_1}^{d_2}\kappa_a(z'')dz''}\right], \tag{5.61}$$

where $T(z')$ is the temperature profile of the atmosphere, and κ_a is the absorption coefficient. The median elevation z_o can be calculated by solving the following equation:

$$\int\limits_{d_1}^{z_o}\kappa_a(z')dz' = \frac{1}{2}\int\limits_{d_1}^{d_2}\kappa_a(z')dz'. \tag{5.62}$$

5.3.3 Power Spectrum of Rough Ocean Surface

The ocean surface spectrum applied in this thesis was proposed by Durden and Vesecky [75]. This surface spectrum is based on experimental data fitting and thus it is an empirical model. The Durden-Vesecky surface spectrum is given by

$$W(k,\phi) = \frac{a_0}{2\pi k^4}\Phi\left(k,\phi\right)S\left(k\right), \tag{5.63}$$

where

$$\Phi\left(k,\phi\right) = \left(1+c(1-e^{-sk^2})\cos 2\phi\right), \tag{5.64}$$

$$S\left(k\right) = \begin{cases} e^{-0.74\left(\frac{g}{U_{19.5}^2 k}\right)^2} & \text{if } 0 < k < 2, \\ \left(\frac{bku_*^2}{g+\gamma k^2}\right)^{a\log_{10}(k/2)} & \text{if } k > 2. \end{cases} \tag{5.65}$$

The wind friction velocity u_* can be found from the following equation

$$U_h = \frac{u_*}{0.4}\log\frac{h}{6.84\times 10^{-5}/u_* + 4.28\times 10^{-3}u_*^2 - 4.43\times 10^{-4}}, \tag{5.66}$$

where U_h is the wind speed in the unit of m/s at the elevation height h in meters above the mean ocean surface. k is the ocean surface spatial wavenumber, ϕ is the azimuthal angle with respect to wind direction, a_0, a, b, g, γ, and s are constants with the values of $a_0 = 0.008$, $a = 0.225$, $b = 1.25$, $g = 9.81$, $\gamma = 7.25\times 10^{-5}$, $s = 1.5\times 10^{-4}$. The parameter c, which serves as the coefficient for the azimuthal-dependent term in the spectrum, is given by

$$c = \frac{2\,(1-R)\,/\,(1+R)}{1-D}, \tag{5.67}$$

where

$$R = \frac{0.003 + 1.92 \times 10^{-3} U_{12.5}}{3.16 \times 10^{-3} U_{12.5}}, \tag{5.68}$$

$$D = \frac{\int\limits_0^\infty dk\, k^2\, S(k)\, e^{-(k/89.44)^2}}{\int\limits_0^\infty dk\, k^2\, S(k)}. \tag{5.69}$$

For example, for the wind speed $U_h = 12\,\text{m/s}$ at height $h = 19.5\,\text{m}$, it can be calculated that $u_* = 0.46388$ and $c = 0.65139$. To consider certain hydrodynamic effects of the ocean waves, we multiply the parameter c in the spectrum density function $W(k, \phi)$ by $(1 - d_0 \cos\phi)$, where the parameter d_0 is determined by data matching. The hydrodynamic modulation was also modeled differently by multiplying the ocean surface spectrum with a parameter h' based on the slope of the long waves [75, 83]. The modulated spectrum is written as

$$W(k, \phi, S_x) = h'\, W(k, \phi), \tag{5.70}$$

where S_x is the slope of the large-scale waves on the ocean surface and h' is calculated as

$$h' = \begin{cases} 1 - 0.5\,\text{sgn}\,(S_x) & \text{if } |S_x/S_u| > 1.25, \\ 1 - 0.4\, S_x/S_u & \text{if } |S_x/S_u| \leq 1.25, \end{cases} \tag{5.71}$$

where S_u is the rms upwind surface slope which can be calculated by using Eq. (5.110). The hydrodynamic modulation of the ocean surface spectrum using the parameter h' is useful for the two-scale model of the ocean surface. A detailed study can be found in Section (5.5).

5.4 Radiative Transfer Equations for Atmosphere

The atmospheric contribution to the brightness temperature of the ocean surface must be taken into account since (1) the airborne radiometer is usually at a very high altitude, hence the accumulated thermal emission along the path from the ocean surface to the radiometer may be significant, and/or the attenuation for the brightness temperature propagating from the ocean surface up to the radiometer cannot be negligible, and (2) there may be a significant amount of down-going thermal emission from the atmosphere being reflected by the ocean surface. In clear air conditions, the main concerns about the atmosphere for passive remote sensing are the atmospheric emission and attenuation due to the contributions from gaseous oxygen (O_2), water vapor (H_2O), and suspended water droplets (hydrosols) [84]. In the adverse conditions, cloud and rainfall need to be addressed [84, 85]. In clear air and at microwave frequencies, the electromagnetic wave scattering by atmospheric gases can be ignored [86], thus the radiative transfer (RT) equations that are used to model the wave propagation in the atmosphere reduce to uncoupled first-order differential equations.

The atmosphere can be modeled as an inhomogeneous layer with the extinction coefficient $\kappa_e(z)$, the absorption coefficient $\kappa_a(z)$, and the temperature profile $T(z)$ in terms of the height z as shown in Fig. (5-3). We assume that the scatterers such as water vapor, droplets and gaseous oxygen are small thus the scattering is ignored ($\kappa_e = \kappa_s + \kappa_a \approx \kappa_a$). Therefore the radiative transfer equations for the specific intensity $\overline{I}_u^A$ and $\overline{I}_d^A$ have the following simple form [81, 87]

$$\cos\theta \frac{\partial}{\partial z}\overline{I}_u^A(\theta,\phi,z) = -\kappa_a(z)\overline{I}_u^A(\theta,\phi,z) + \bar{\kappa}_a C T(z), \tag{5.72}$$

$$-\cos\theta \frac{\partial}{\partial z}\overline{I}_d^A(\theta,\phi,z) = -\kappa_a(z)\overline{I}_d^A(\theta,\phi,z) + \bar{\kappa}_a C T(z), \tag{5.73}$$

where $C = K_B/\lambda^2$, K_B is Boltzmann constant and λ is the electromagnetic wave-

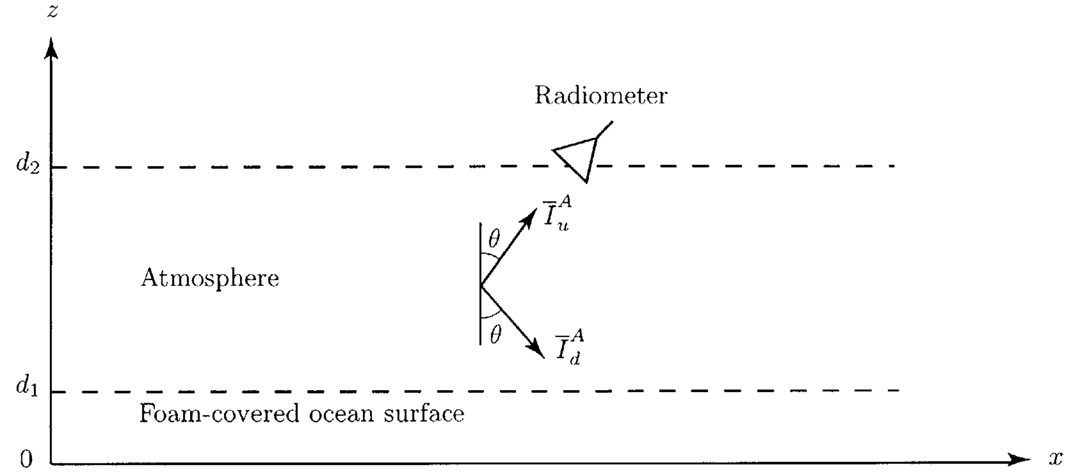

Figure 5-3: The atmospheric layer above a foam-covered ocean surface.

length.

Assuming that there is no thermal emission from the upper space at $z = d_2$, the boundary conditions for Eqs. (5.72) and (5.73) are given by

$$\overline{I}_u^A(\theta, \phi, d_1) = \overline{I}_u^T(\theta, \phi, d_1), \tag{5.74}$$

$$\overline{I}_d^A(\theta, \phi, d_2) = 0, \tag{5.75}$$

where $\overline{I}_u^T(\theta, \phi, d_1)$ denotes the emission from the lower boundary at $z = d_1$ (the foam-covered ocean surface). From Eq. (5.14), the solution of the RT equations (5.72) and (5.73) are obtained as

$$\begin{aligned}\overline{I}_u^A(\theta, \phi, d_2) \;&=\; \sec\theta \int_{d_1}^{d_2} \bar{\kappa}_a(z') C T(z')\, e^{-\sec\theta \int_{z'}^{d_2} \kappa_a(z'')dz''} dz' \\ &\quad + \overline{I}_u^T(\theta, \phi, d_1)\, e^{-\sec\theta \int_{d_1}^{d_2} \kappa_a(z')dz'}, \end{aligned} \tag{5.76}$$

$$\overline{I}_d^A(\theta, \phi, d_1) = \sec\theta \int_{d_1}^{d_2} \bar{\kappa}_a(z') C T(z')\, e^{-\sec\theta \int_{d_1}^{z'} \kappa_a(z'')dz''} dz'. \tag{5.77}$$

The specific intensity of the down-going wave in Eq. (5.77) can be calculated for any polar angle θ from the absorption and temperature profiles. From the equation of the down-going wave in Eq. (5.77) we find that the assumption that down-going wave at height d_2 is zero as in Eq. (5.75) is due to the fact that the absorption coefficient κ_a at $z = d_2$ is very small. In the next sections, we will see from the numerical results for the US Standard Atmosphere [55] that the value of the absorption coefficient is negligible for altitude larger than 10 km. In the RT theory, if the scattering is ignored for the propagating wave, the absorption coefficient κ_a is two times the imaginary part of the complex wavenumber,

$$\kappa_a = 2\mathrm{Im}\left\{k\right\} = 2\mathrm{Im}\left\{\left(10^{-6}N + 1\right) k_o\right\}, \tag{5.78}$$

where k_o is the wavenumber in free space, and N is the complex refractivity. In the following sections, we will use Liebe's millimeter-wave propagation model (MPM) [54] to calculate the complex refractivity in the atmosphere.

The extinction coefficient κ_e is the sum of the scattering coefficient κ_s and the absorption coefficient of the background κ_a. Quantitatively, we find that $\kappa_s \ll \kappa_a$, therefore we use κ_a to approximate κ_e. The dominant scattering in the atmosphere is due to water vapor and suspended water droplets (hydrosols). The scattering and absorption coefficient are given by [81, page 157–158]

$$\kappa_s = 2 f_v k^4 a^3 \left|y\right|^2, \tag{5.79}$$

$$\kappa_a = f_v k \frac{\epsilon_s''}{\epsilon} \left|\frac{3\epsilon}{\epsilon_s + 2\epsilon}\right|^2, \tag{5.80}$$

where f_v is the fractional volume occupied by the water particles, a is the radius of a water particle, and

$$y = \frac{\epsilon_s - \epsilon}{\epsilon_s + 2\epsilon}. \tag{5.81}$$

For water droplets in the atmosphere, the typical values are $a \sim 5\,\mu\mathrm{m}$, $f_v \sim 5 \times 10^{-7}$, and $\epsilon_s \sim 30 + i40$ for $f = 20\,\mathrm{GHz}$. Therefore $\kappa_s \sim 10^{-12}\,\mathrm{m}^{-1}$ and $\kappa_a \sim 10^{-5}\,\mathrm{m}^{-1}$, thus $\kappa_s \ll \kappa_a$ and we can ignore κ_s and let $\kappa_e \approx \kappa_a$. The gaseous oxygen ($O_2$), water vapor ($H_2O$), and suspended water droplets in the atmosphere are considered as the principal absorbers in moist air [84].

5.4.1 The Millimeter-Wave Propagation Model

The millimeter-wave propagation model (MPM) model developed by Liebe [54] can be used to calculate the complex refractivity N that is related to the complex refractive index n by $N = 10^6(n-1)$. By writing the refractive index as $n = n' + in''$, the effective permittivity of moist air is found as following:

$$\epsilon_e = (n' + in'')^2 = \left(n'^2 - n''^2\right) + i\left(2n'n''\right), \tag{5.82}$$

where k_o is the wavenumber in free space. Thus the complex wavenumber is given by

$$k = \omega\sqrt{\mu_e \epsilon_e} = k_o n, \tag{5.83}$$

assuming $\mu_e = \mu_o$. The measurable parameters of atmosphere are (1) barometric pressure P in kilopascal ($1\,\mathrm{kPa} = 10\,\mathrm{mbar}$), (2) temperature T in degrees Kelvin (K), (3) relative humidity RH, and (4) mass concentration in grams per cubic meter. The four measurable parameters can be converted to the internal variables which are useful in the MPM model as shown in Appendix E.

The typical barometric pressure profile is given in [55] and it is plotted in Fig. (5-4). As an example, we consider the frequency $f = 19.35\,\mathrm{GHz}$ and use the US Standard Atmosphere 1976 temperature, barometric pressure and humidity profiles to calculate the complex wavenumber k for an electromagnetic wave propagating in the atmosphere. The numerical result of the absorption coefficient is plotted in Fig. (5-5), where the real and imaginary parts are plotted separately in terms of the wavenumber in free space k_o.

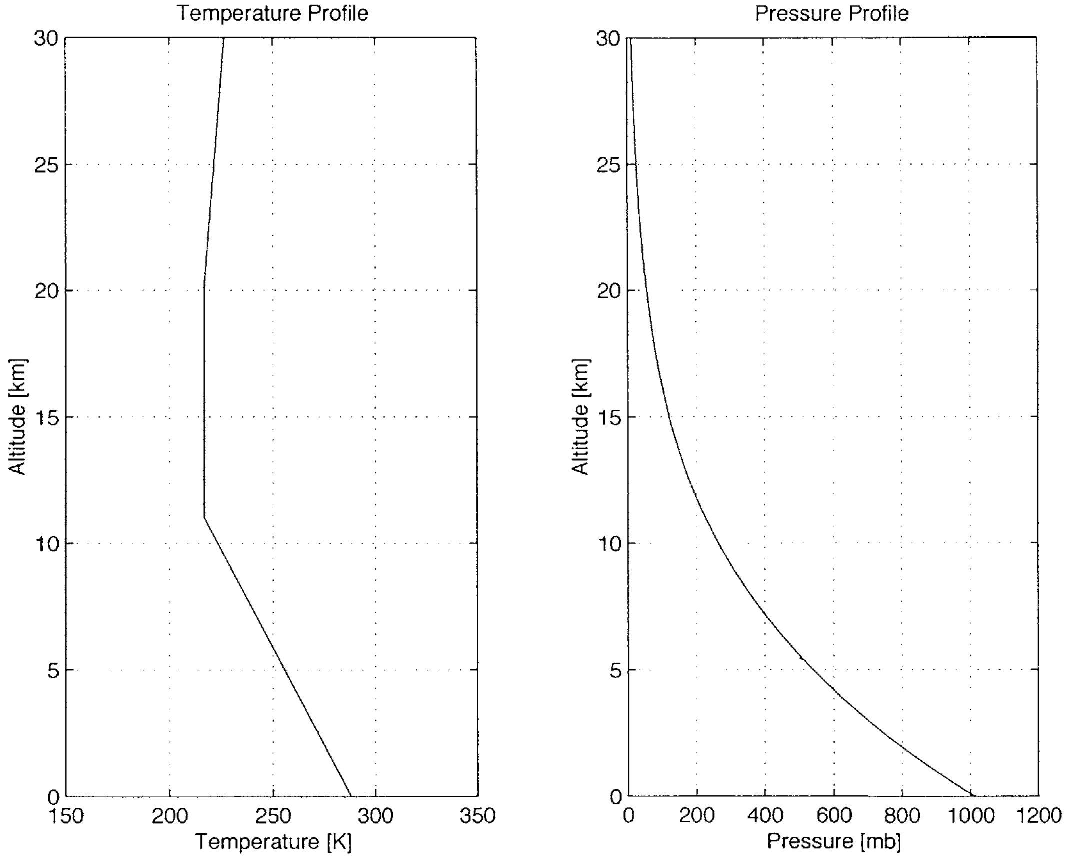

Figure 5-4: Temperature and barometric pressure profiles in the US Standard Atmosphere 1976.

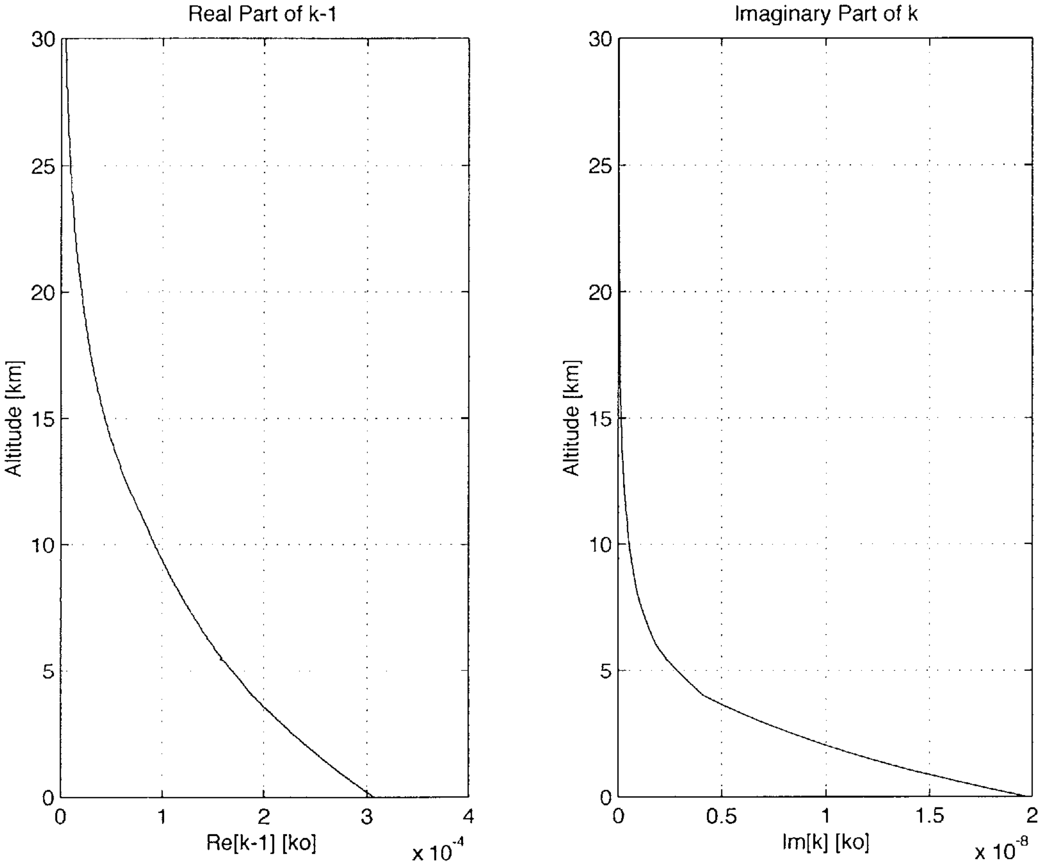

Figure 5-5: The complex wavenumber of electromagnetic wave with $f = 19.35\,\text{GHz}$ propagating in the atmosphere in terms of the wavenumber in free space.

5.4.2 Attenuation and Emission of Atmosphere

Once we obtained the key parameter — the absorption coefficient κ_a from the MPM model, the thermal emission of the standard atmosphere and its attenuation for the propagating waves can be calculated by using the RT solutions (5.76) and (5.77). The first term in Eq. (5.76) represents the up-going thermal emission of the atmosphere and can be written as

$$\bar{I}_{u1}^{A}(\theta, \phi, d_2) = \sec\theta \int_{d_1}^{d_2} \bar{\kappa}_a(z') CT(z') e^{-\sec\theta \int_{z'}^{d_2} \kappa_a(z'') dz''} dz'. \tag{5.84}$$

The down-going wave in Eq. (5.77) represents the down-going thermal emission of the atmosphere,

$$\bar{I}_{d}^{A}(\theta, \phi, d_1) = \sec\theta \int_{d_1}^{d_2} \bar{\kappa}_a(z') CT(z') e^{-\sec\theta \int_{d_1}^{z'} \kappa_a(z'') dz''} dz'. \tag{5.85}$$

The up and down-going thermal emissions can be calculated using the result of absorption and temperature profiles from the MPM. We can show numerically that they are very close to each other quantitatively.

The up-going thermal emission as in Eq. (5.84) can be written as

$$\bar{I}_{u1}^{A}(\theta, \phi, d_2) = CT(z_o) \sec\theta \int_{d_1}^{d_2} \bar{\kappa}_a(z') e^{-\sec\theta \int_{z'}^{d_2} \kappa_a(z'') dz''} dz', \tag{5.86}$$

where z_o is between d_1 and d_2. The down-going wave as in Eq. (5.85) can also be written as

$$\bar{I}_{d}^{A}(\theta, \phi, d_1) = CT(z_o') \sec\theta \int_{d_1}^{d_2} \bar{\kappa}_a(z') e^{-\sec\theta \int_{d_1}^{z'} \kappa_a(z'') dz''} dz', \tag{5.87}$$

where z_o' is between d_1 and d_2 but different from z_o. It can be shown that

$$\begin{aligned}\int_{d_1}^{d_2} \kappa_a(z') e^{-\sec\theta \int_{z'}^{d_2} \kappa_a(z'')dz''} dz' &= \int_{d_1}^{d_2} \kappa_a(z') e^{-\sec\theta \int_{d_1}^{z'} \kappa_a(z'')dz''} dz' \\ &= \cos\theta \left[1 - e^{-\sec\theta \int_{d_1}^{d_2} \kappa_a(z'')dz''} \right]. \qquad (5.88)\end{aligned}$$

Since the temperature profile $T(z)$ does not change much for the entire integral path, i.e. $T(z_o) \approx T(z_o')$,

$$\overline{I}^A_{u1}(\theta, \phi, d_2) \approx \overline{I}^A_d(\theta, \phi, d_1) \approx CT(z_o) \frac{\bar{\kappa}_a}{\kappa_a} \left[1 - e^{-\sec\theta \int_{d_1}^{d_2} \kappa_a(z'')dz''} \right], \qquad (5.89)$$

where z_o is the median elevation as defined in Eq. (5.62). Figure (5-6) shows the numerical result of the down-going, up-going and approximated brightness temperatures by carrying out the integration for Eqs.(5.84) and (5.85) numerically or using approximation formula Eq. (5.89) for the standard atmosphere at $f = 19.35\,\text{GHz}$, $d_2 = 30\,\text{km}$ and $d_1 = 0$.

In the second term of the up-going wave in Eq. (5.76), the factor

$$\exp\left(-\sec\theta \int_{d_1}^{d_2} \kappa_a(z')dz' \right)$$

is the attenuation for the thermal emission from the foam-covered ocean surface. For the US standard atmosphere at $f = 19.35\,\text{GHz}$, $d_2 = 30\,\text{km}$ and $d_1 = 0$, we can calculate the attenuation using the numerical κ_a from the MPM. Fig (5-7) shows the attenuation in terms of the polar angle.

After the total brightness temperature on the ocean surface is calculated by [also

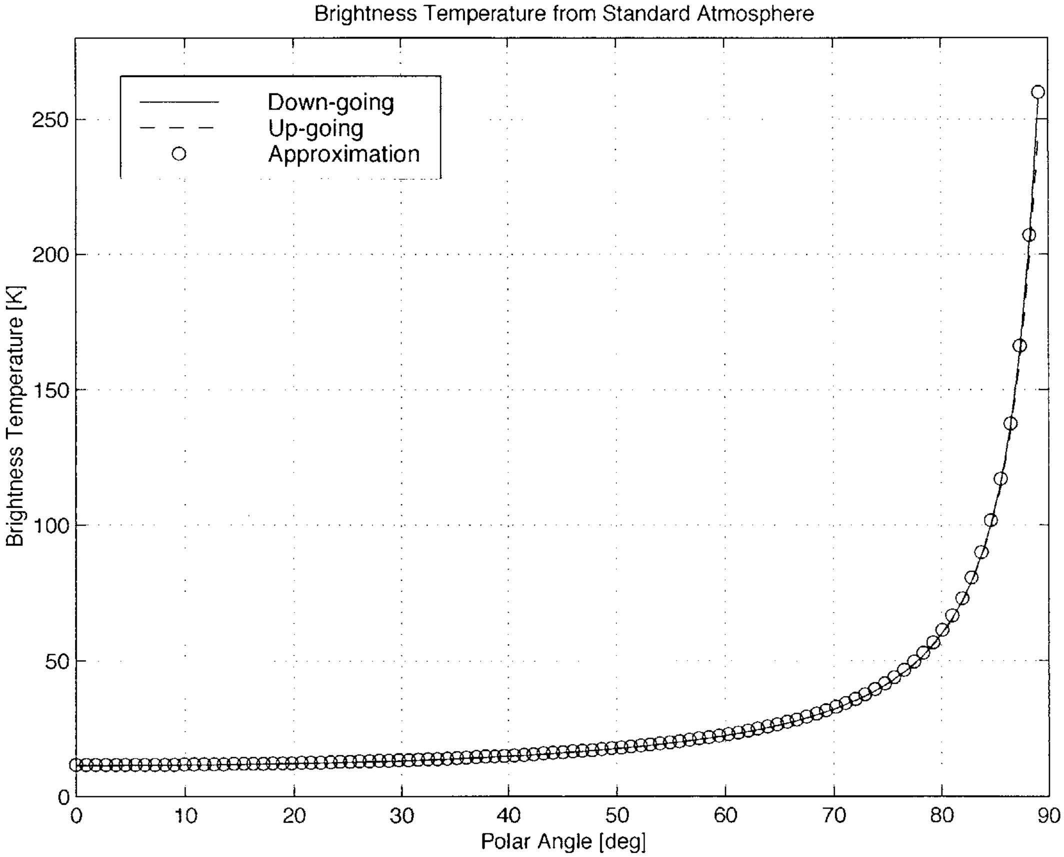

Figure 5-6: The brightness temperature of down-going and up-going waves and their comparison with the approximation formula for $f = 19.35\,\mathrm{GHz}$.

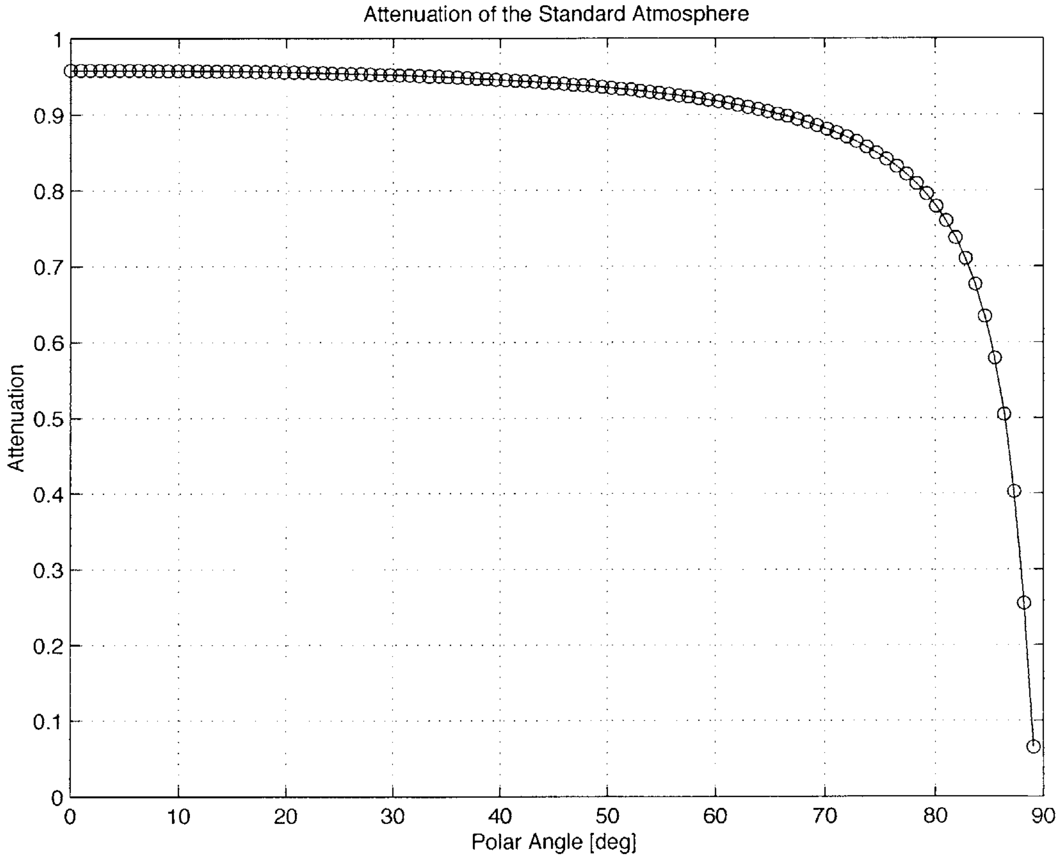

Figure 5-7: The attenuation of the standard atmosphere for $f = 19.35\,\text{GHz}$, $d_2 = 30\,\text{km}$ and $d_1 = 0$.

from Eq. (5.32)]

$$\overline{T}_u^T(\theta,\phi,d_1) = F\cdot\overline{T}_u^{AF}(\theta,\phi,d_1) + (1-F)\cdot\overline{T}_u^{AS}(\theta,\phi,0), \tag{5.90}$$

we can calculate the brightness temperature at the height of the radiometer. Between the ocean surface and the radiometer, the atmospheric emission and the attenuation must be taken into account. At the radiometer height $z = d_2$, by dividing the constant $C = K_B/\lambda^2$ on both sides of Eq. (5.76), the total brightness temperature can be written as

$$\overline{T}_u^A(\theta,\phi,d_2) = \sec\theta\int_{d_1}^{d_2}\bar{\kappa}_a(z')T(z')e^{-\sec\theta\int_{z'}^{d_2}\kappa_a(z'')dz''}dz' + \overline{T}_u^T(\theta,\phi,d_1)e^{-\sec\theta\int_{d_1}^{d_2}\kappa_a(z')dz'}, \tag{5.91}$$

where the first term is the thermal emission of the atmosphere and the exponential factor in the second term is the atmospheric attenuation for the wave traveling from the ocean surface to the radiometer. In order to study individually the contributions from the plain ocean surface, the foam and the atmosphere, we re-label the terms in Eq. (5.90) and Eq. (5.91) as

$$\overline{T}_S = (1-F)\cdot\overline{T}_u^{AS}(\theta,\phi,0)e^{-\sec\theta\int_0^{d_2}\kappa_a(z')dz'}, \tag{5.92}$$

$$\overline{T}_F = F\cdot\overline{T}_u^{AF}(\theta,\phi,d_1)e^{-\sec\theta\int_{d_1}^{d_2}\kappa_a(z')dz'}, \tag{5.93}$$

$$\overline{T}_A = \sec\theta\int_{d_1}^{d_2}\bar{\kappa}_a(z')T(z')e^{-\sec\theta\int_{z'}^{d_2}\kappa_a(z'')dz''}dz'. \tag{5.94}$$

In the above expressions, $\overline{T}_S$ is the brightness temperature of the plain ocean surface with the consideration of reflection of atmospheric emission by water bubbles and the attenuation when the wave travels from the ocean surface to the radiometer. $\overline{T}_F$ is the brightness temperature of the foam layer with the consideration of scattering of atmospheric emission and attenuation. T_A is the brightness temperature due to the thermal emission of the atmosphere.

5.4.3 Equivalent Polar Angle of the Spherical Atmospheric Layer

Consider a radiometer placed at point A with zenith height H as shown in Fig. (5-8). We create a flat atmospheric layer to approximate the spherical layer so that it is easier to apply the geometry for the RT theory. On the flat layer, the equivalent position of the radiometer is at point C, where we assume $\overline{AB} = \overline{BC}$. It can be found that in the equivalent flat-layer model of the atmosphere, the polar angle θ' is different from θ in the spherical model. By projecting the lines $\overline{AO}$ and $\overline{AB}$ on the x- and z-axis, respectively, we find

$$\overline{AB} \cdot \sin\theta = (R+H)\sin\theta_o, \tag{5.95}$$

$$R + \overline{AB} \cdot \cos\theta = (R+H)\cos\theta_o. \tag{5.96}$$

By eliminating the angle θ_o from Eqs. (5.95) and (5.96), it yields

$$\overline{AB} = \sqrt{R^2\cos^2\theta + 2RH + H^2} - R\cos\theta. \tag{5.97}$$

Considering the triangle BCD, it can be shown that

$$\cos\theta' = {}^{H}\!\big/_{\overline{AB}}. \tag{5.98}$$

Therefore the modified polar angle in the equivalent flat atmospheric layer is

$$\theta' = \cos^{-1}\frac{H}{\sqrt{R^2\cos^2\theta + 2RH + H^2} - R\cos\theta}. \tag{5.99}$$

For example, let the radiometer height $H = 30,000\,\mathrm{m}$, and the earth radius $R =$

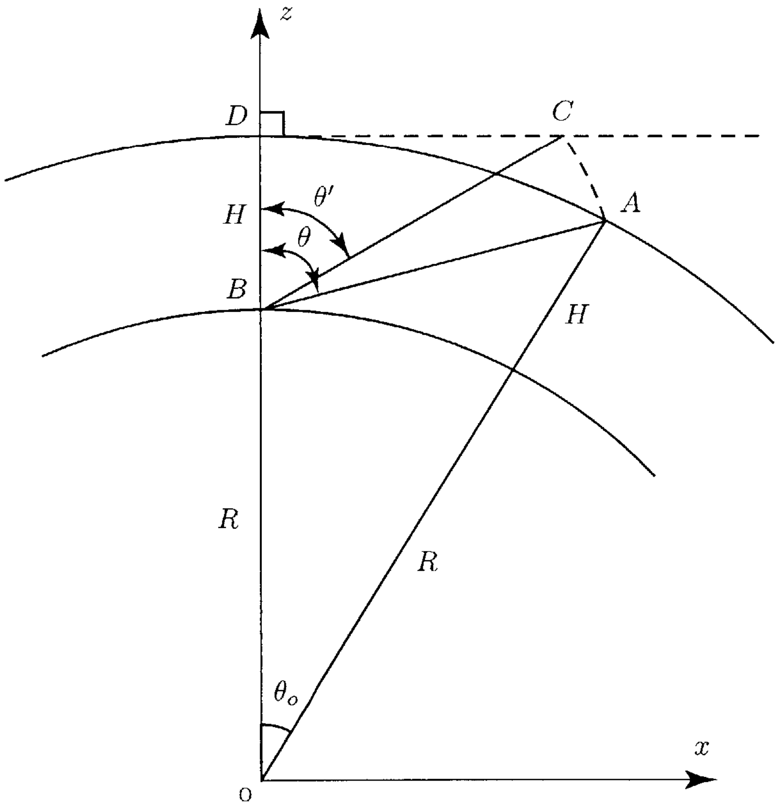

Figure 5-8: Geometry of the spherical atmospheric layer.

6.37×10^6 m. For the zero grazing angle ($\theta = 90°$), the modified polar angle can be calculated as

$$\theta' = \cos^{-1} \frac{H}{\sqrt{2RH + H^2}} = \cos^{-1} \frac{3}{\sqrt{2 \times 637 \times 3 + 3^2}} = 87.2°. \tag{5.100}$$

5.5 Two-Scale Model of Rough Ocean Surface

In the previous section, we only considered the rough ocean surface with wavenumber less than 5 times the electromagnetic wavelength by defining the cutoff wavenumber $k_d = k_o/5$, where k_o is the electromagnetic wavenumber. For numerical purposes, the variable l is defined as $l = 1/k$ so that the integration for l is from 0 to $1/k_d$ instead of from 0 to ∞ for k. Therefore numerically k_d cannot be zero, and the waves are separated into large-scale ($k < k_d$) and small-scale ($k > k_d$) categories. If we only consider the small-scale waves, the total brightness temperature is not sensitive to the value of k_d (k_d around $k_o/5$) that will be demonstrated in Fig. (5-14) in the numerical simulation section. The large-scale wave operates as tilted facet. The two-scale model takes care of the tilted polar angle on the local facet due to the large scale or long waves of the ocean surface. In the two-scale model, the brightness temperature vector is calculated by averaging the local values over the slope distribution of the large scale waves [88, 83]. The averaged brightness temperature at the ocean surface is written as

$$\overline{T}(\theta, \phi, 0) = \int_{-\infty}^{\infty} dS_x \int_{-\cot\theta}^{\infty} dS_y \overline{T}_l(\theta', \phi) P_s\left(S'_x, S'_y, \theta\right), \tag{5.101}$$

where $\overline{T}_l(\theta', \phi)$ is the brightness temperature of the local facet at the local looking angle θ', P_s is the slope distribution of the large-scale waves as viewed at the local looking angle θ', S_x and S_y are the surface slopes along the global x and y axis, respectively, while S'_x and S'_y are the surface slopes with respect to the radiometer observation direction (θ', ϕ). Notice that S_x is limited to $-\cot\theta$ due to shadowing by large-scale waves [83]. The transformation of the global slopes to the slopes with

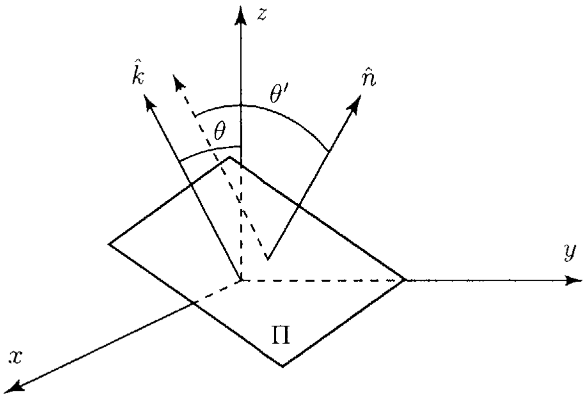

Figure 5-9: The local polar angle with respect to the global looking angle and the slope of the facet.

respect to the radiometer observation direction is given by

$$S'_x = S_x \cos\phi + S_y \sin\phi, \tag{5.102}$$

$$S'_y = -S_x \sin\phi + S_y \cos\phi. \tag{5.103}$$

To calculate the polar angle θ' with respect to the local facet Π for a given looking angle θ with respect to the global coordinate (x, y, z) as shown in Fig. (5-9), we write the unit normal vector of the local facet as

$$\hat{n} = \frac{\hat{z} - S_x\hat{x} - S_y\hat{y}}{\sqrt{1 + S_x^2 + S_y^2}}, \tag{5.104}$$

and the unit wave vector with the orientation angles θ and ϕ as

$$\hat{k} = \hat{x}\sin\theta\cos\phi + \hat{y}\sin\theta\sin\phi + \hat{z}\cos\theta. \tag{5.105}$$

Thus the polar angle with respect to the local facet is

$$\theta' = \cos^{-1}\hat{k}\cdot\hat{n} = \cos^{-1}\frac{-S_x\sin\theta\cos\phi - S_y\sin\theta\sin\phi + \cos\theta}{\sqrt{1 + S_x^2 + S_y^2}}. \tag{5.106}$$

The slope distribution P_s was studied by Cox and Munk [89] by measuring the ocean surface, and it can be written as

$$P_s\left(S'_x, S'_y, \theta\right) = \left(1 + S_x \tan\theta\right) P\left(S'_x, S'_y\right), \tag{5.107}$$

where $P(S'_x, S'_y)$ is assumed to be a Gaussian distribution function

$$P\left(S'_x, S'_y\right) = \frac{F\left(S'_x, S'_y\right)}{2\pi S_u S_c} \exp\left[-\left(\frac{S_x'^{\,2}}{2S_u^2} + \frac{S_y'^{\,2}}{2S_c^2}\right)\right] \tag{5.108}$$

with the function $F(S'_x; S'_y)$ defined as

$$\begin{aligned} F\left(S'_x, S'_y\right) &= 1 - \frac{C_{21}}{2}\left(\frac{S_y'^{\,2}}{S_c^2} - 1\right)\frac{S'_x}{S_u} - \frac{C_{03}}{6}\left(\frac{S_x'^{\,3}}{S_u^3} - 3\frac{S'_x}{S_u}\right) \\ &\quad + \frac{C_{40}}{24}\left(\frac{S_y'^{\,4}}{S_c^4} - 6\frac{S_y'^{\,3}}{S_c^3} + 3\right) + \frac{C_{22}}{4}\left(\frac{S_y'^{\,2}}{S_c^2} - 1\right)\left(\frac{S_x'^{\,2}}{S_u^2} - 1\right) \\ &\quad + \frac{C_{04}}{24}\left(\frac{S_x'^{\,4}}{S_u^4} - 6\frac{S_u'^3}{S_u^3} + 3\right). \end{aligned} \tag{5.109}$$

In the above expression, the coefficients are $C_{40} = 0.4$, $C_{22} = 0.12$, $C_{04} = 0.23$, $C_{21} = 0.01 - 0.0086U_w$, and $C_{03} = 0.04 - 0.033U_w$, where U_w is the wind speed in m/s.

The upwind and crosswind slope variances are calculated as follows:

$$S_u^2 = \int_0^{k_d} dk \int_0^{2\pi} d\phi k^3 \cos^2\phi W\left(k, \phi\right), \tag{5.110}$$

$$S_c^2 = \int_0^{k_d} dk \int_0^{2\pi} d\phi k^3 \sin^2\phi W\left(k, \phi\right). \tag{5.111}$$

In the numerical evaluation of Eq. (5.101), the integration limits of S_x and S_y are truncated as $5\,S_u$ and $5\,S_c$, respectively. The local brightness temperature $\overline{T}_l$ is assigned to be the one of the plain ocean surface $\overline{T}_u^{AS}$ as in Eq. (5.60) or of the foam $\overline{T}_u^{F}$ as in

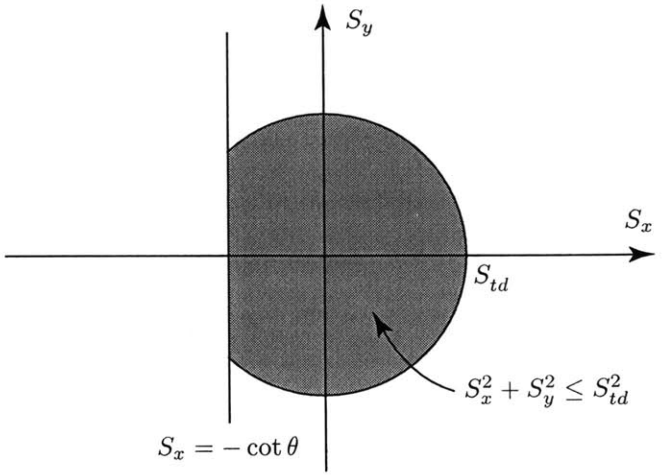

Figure 5-10: The integration area for determining the slope threshold.

Eq. (5.30) based on the slope of the surface $S = \sqrt{S_x^2 + S_y^2}$. To the best of our knowledge, there is presently no literature on the study of the foam assignment according to the slope of the ocean surface. In this thesis, we assume a threshold S_{td} and assign the foam brightness temperature $\overline{T}_u^F$ to the local $\overline{T}_l$ if the slope $\sqrt{S_x^2 + S_y^2} \geq S_{td}$. The slope threshold S_{td} can be found by calculating the integral within the area [as shown in Fig. (5-10)] of $\left\{(S_x, S_y) : S_x^2 + S_y^2 \leq S_{td}^2, S_x \geq -\cot\theta\right\}$, so that the integral value is equal to the foam coverage F in Eq. (5.33), i.e.

$$F = \int dS_y \int dS_x P_s\left(S'{}_x, S'_x\right). \tag{5.112}$$

5.6 Numerical Results

In this section, we calculate the brightness temperature of the wind-driven ocean surface and compare the simulation results with the data from JPL's WINDRAD experiment [49]. In the experiment, a K-band (19.35 GHz) radiometer was mounted on the NASA DC-8 aircraft flying in a circle at the height of 30,000 ft (9,144 m). The data was collected in November 1993 near the northern Californian coast. During the experiment, weather was clear and there was a wind speed of 12 m/s. The brightness temperatures were measured for the Stokes parameters T_v, T_h, and U with the polar angles of 30, 40, and 50 degrees. In the simulation, the frequency of the brightness temperatures is $f = 19.35\,\mathrm{MHz}$, the ocean wind speed is $U_w = 12\,\mathrm{m/s}$ at height $h = 19.5\,\mathrm{m}$. The physical temperature of the sea water is $T_o = 12\,^\circ\mathrm{C}$, and the salinity is $S = 3.5\%$.

Fig. (5-11), (5-12) and (5-13) show the simulation results of the brightness temperatures by varying the azimuth angle ϕ of the observation with nadir looking angle $\theta = 30^\circ$, 40° and 50°, respectively. The ocean surface spectrum is the empirical formula proposed by Durden and Vesecky [75]. For the foam layer, the internal radius of water bubble is $R = 4.3\,\mathrm{mm}$, the bubble film thickness is $d = 0.13\,\mathrm{mm}$ and the fractional volume of water bubbles is $f_v = 0.01$. The extinction and absorption coefficients are calculated as $\kappa_e = 8.298\,\mathrm{m}^{-1}$ and $\kappa_a = 2.273\,\mathrm{m}^{-1}$. The permittivity of the bubble film is the same as of the ocean water, and the permittivity of the background is ϵ_o. The elevation height of the radiometer is 30,000 ft (9,144 m). In these figures, the open circles are the WINDRAD experimental data. In the plots of the first and second Stokes parameters T_v and T_h, the lines (from bottom to top) are the plots for the numerical simulation considering (1) only the plain ocean surface [$\overline{T}_S$ in Eq. (5.92)], (2) plain ocean surface plus the foam emission [$\overline{T}_S + \overline{T}_F$ in Eq. (5.92) and (5.93)], and (3) plain ocean surface plus the foam and the atmospheric emissions [$\overline{T}_S + \overline{T}_F + \overline{T}_A$ in Eq. (5.92), (5.93) and (5.94)]. In the plots for the third and fourth Stokes parameters U and V, the total emissions are considered. In comparison with experiment data, we notice that both the foam and the atmospheric emission are significant to correct the emission of the plain ocean surface for T_v and T_h.

The Durden-Vesecky spectrum is similar to the power law $W(k) = a_0/k^4$ that describes the relative portion of the large scale and small scale roughness of the ocean surface by specifying the lower cutoff wavenumber k_d. The smaller k_d is, the

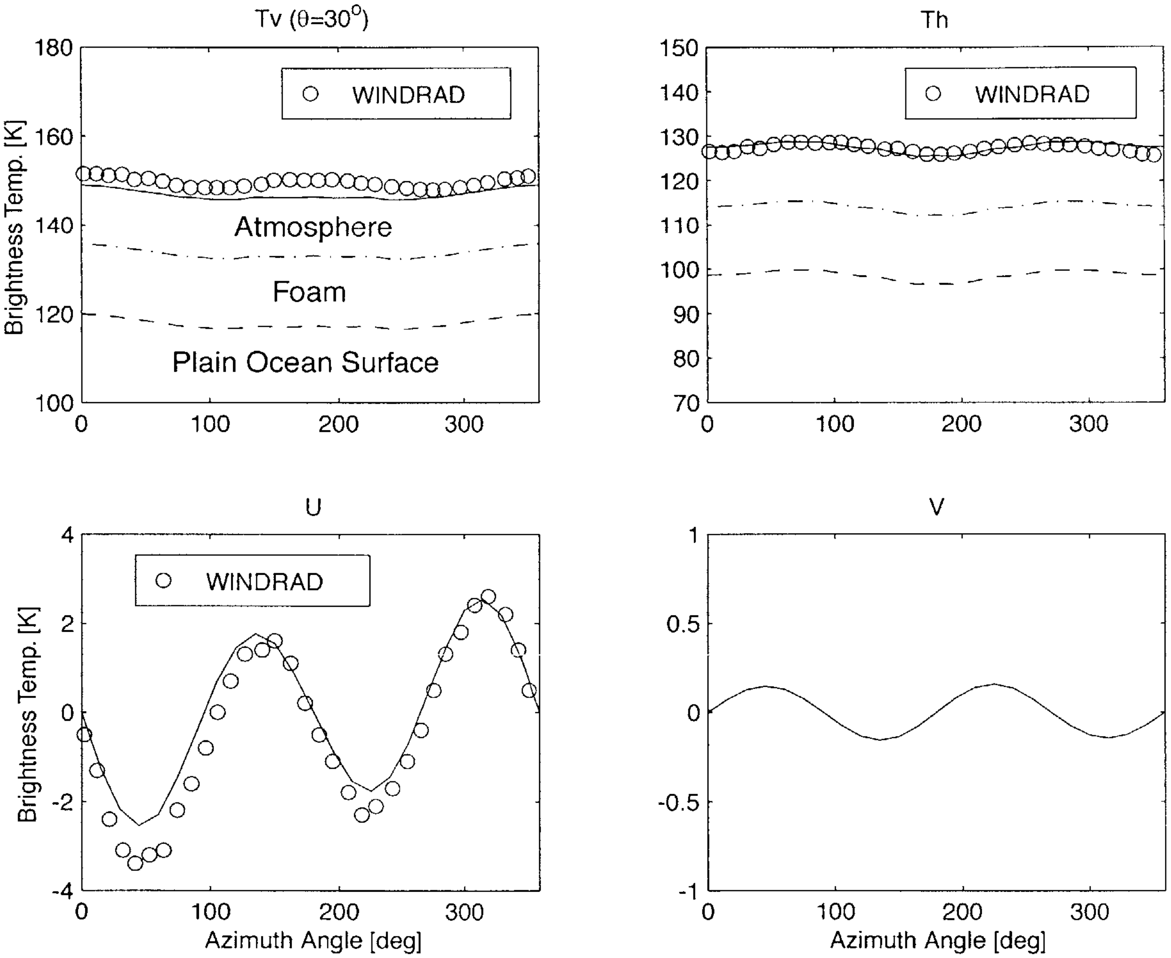

Figure 5-11: The brightness temperature of wind-driven ocean surface for nadir looking angle $\theta = 30^\circ$ and the lower cutoff wavenumber $k_d = 80\,\mathrm{m}^{-1}$.

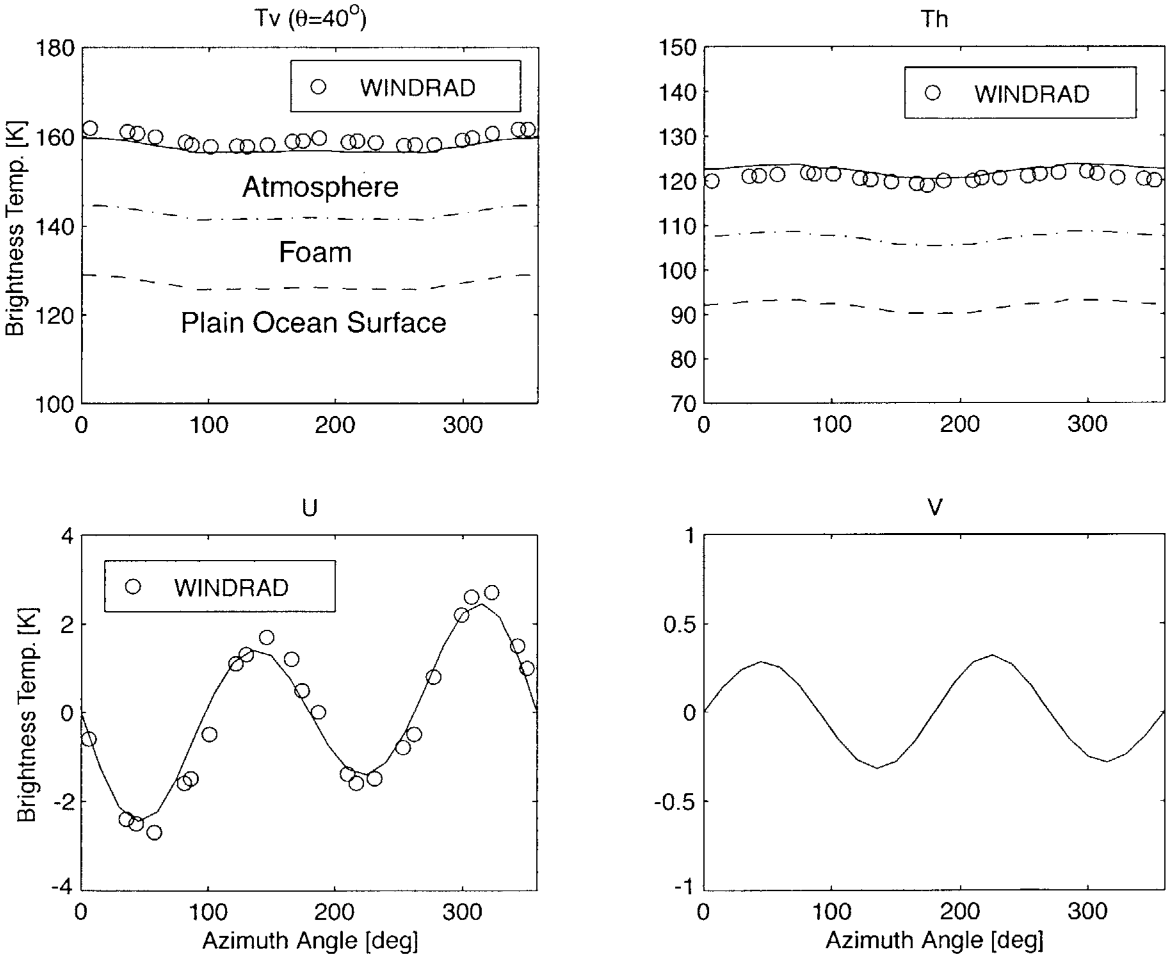

Figure 5-12: The brightness temperature of wind-driven ocean surface for nadir looking angle $\theta = 40°$ and the lower cutoff wavenumber $k_d = 80\,\mathrm{m}^{-1}$.

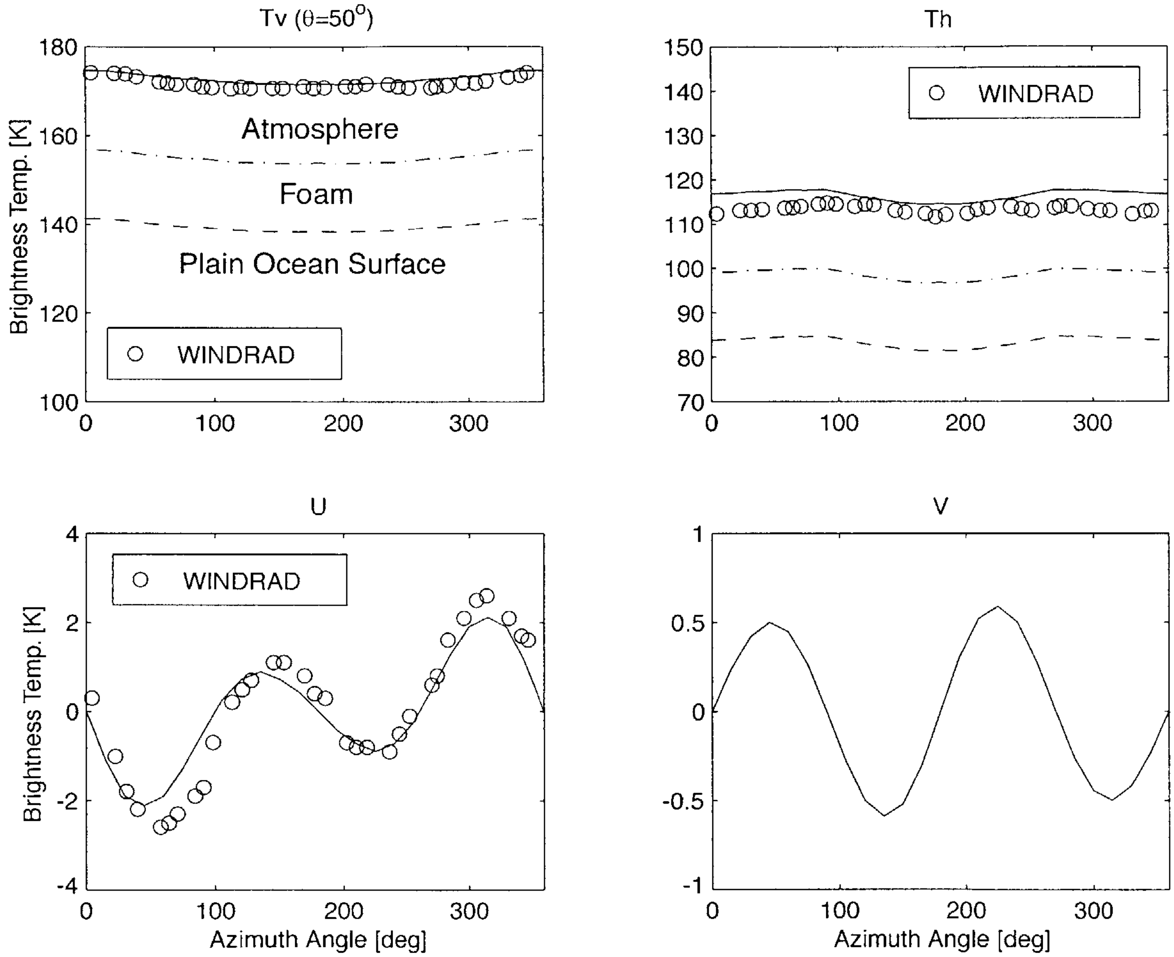

Figure 5-13: The brightness temperature of wind-driven ocean surface for nadir looking angle $\theta = 50°$ and the lower cutoff wavenumber $k_d = 80\,\mathrm{m}^{-1}$.

higher the long waves. However, in the simulation for the thermal emission from the ocean surface, the brightness temperatures are obtained by integrating over the entire reflected waves due to Kirchhoff's law. Therefore there is no significant difference between the collection of reflected waves from very long ocean waves or from a flat surface. In SPM, the zeroth and the second order reflected waves are specular, thus they include the dominant reflections from the long waves. The bistatic pattern of the field scattered by rough ocean surface is dominated by small scale roughness (Bragg scattering) which is included in the first order solution in SPM. Therefore the value of the lower cutoff wavenumber k_d is not sensitive to the calculation of the emissivity from the rough ocean surface. This can be demonstrated by re-calculating the brightness temperatures shown in Figs. (5-11), (5-12) and (5-13) with lower cutoff wavenumbers. In Figs. (5-11), (5-12) and (5-13), the lower cutoff wavenumber is $k_d = 80\,\mathrm{m}^{-1}$ which is about 5λ of the electromagnetic wave. Fig. (5-14) shows the brightness temperatures for the polar angle $\theta = 40°$ and the lower cutoff wavenumber $k_d = 120\,\mathrm{m}^{-1}$. Not much change is observed for the result in comparison with Fig. (5-12) for $k_d = 80\,\mathrm{m}^{-1}$.

With the same simulation conditions as in Fig. (5-11)–(5-13), we compare the numerical results obtained by using the one-scale and two-scale models as shown in Fig. (5-15)–(5-17). Notice that the T_v and T_h terms in these figures match better with the measurement data in the two-scale model for $\theta = 30°$ and $40°$, but there is an irregular offset in Fig. (5-17), which may be due to the shadowing effect at large polar angles.

5.7 Conclusions

In this chapter, one-scale and two-scale electromagnetic models to calculate the brightness temperature of wind-driven ocean with foam coverage have been presented. The one-scale emissivity model is the local thermal contribution by small roughness

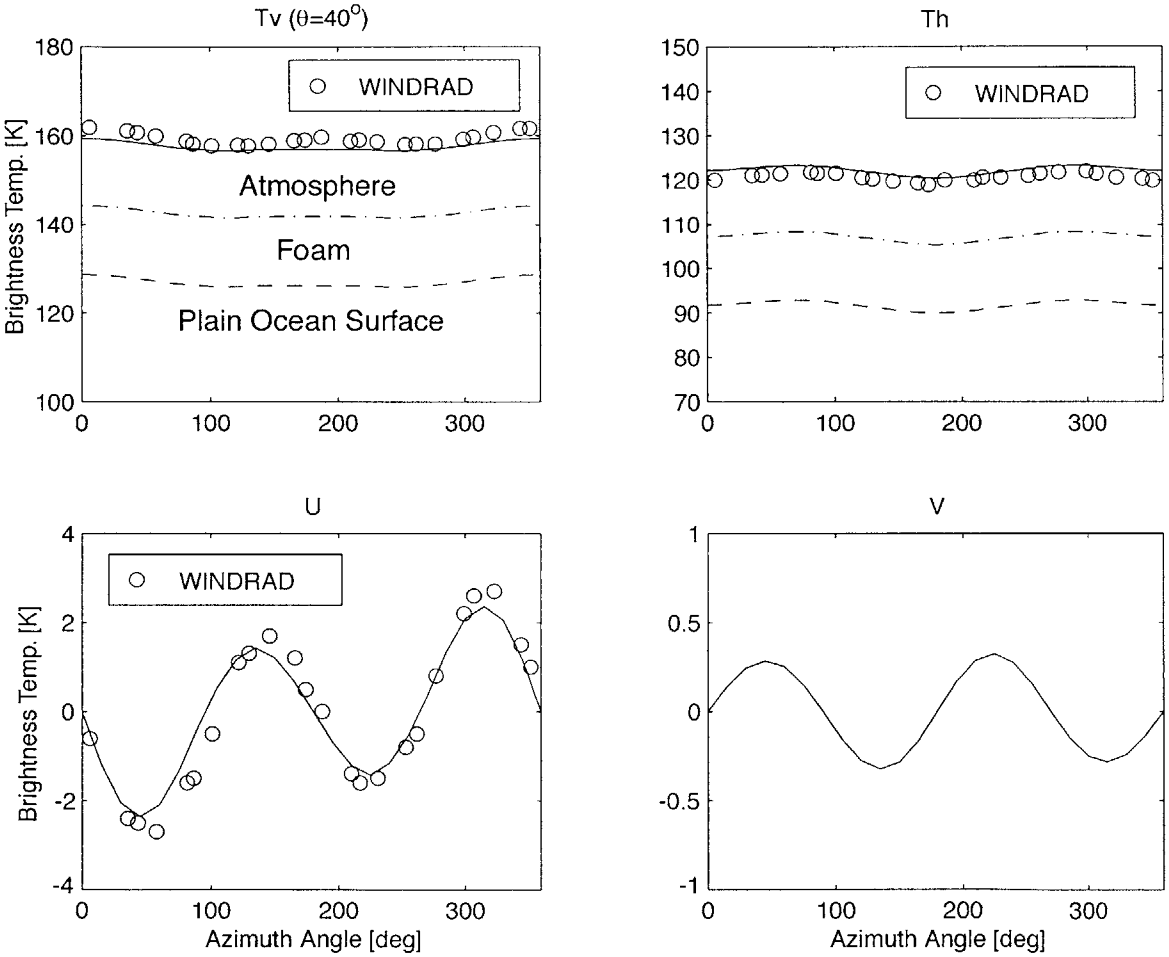

Figure 5-14: The brightness temperature of wind-driven ocean surface for nadir looking angle $\theta = 40°$ and the lower cutoff wavenumber $k_d = 120\,\mathrm{m}^{-1}$.

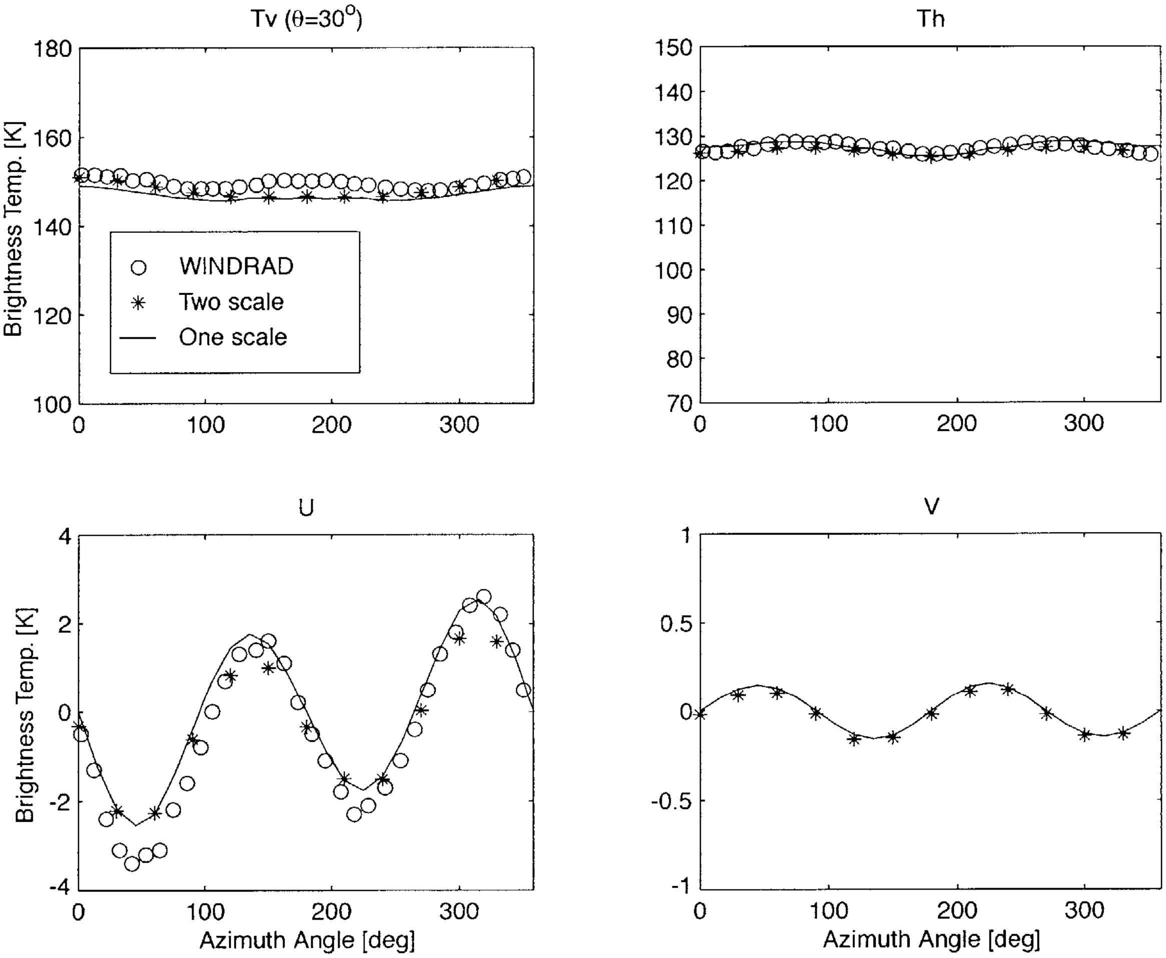

Figure 5-15: The comparison of the one-scale and two-scale models at $\theta = 30°$.

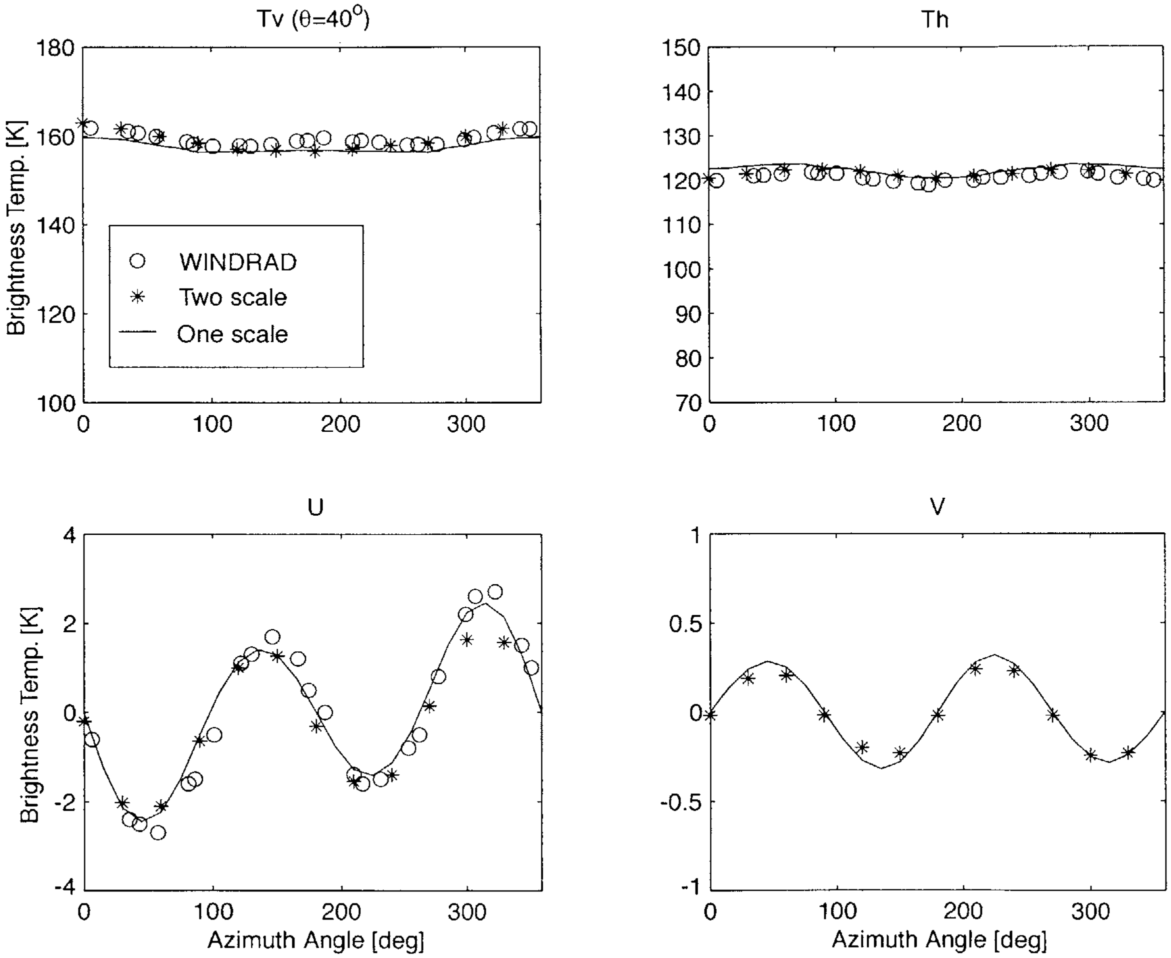

Figure 5-16: The comparison of the one-scale and two-scale models at $\theta = 40°$.

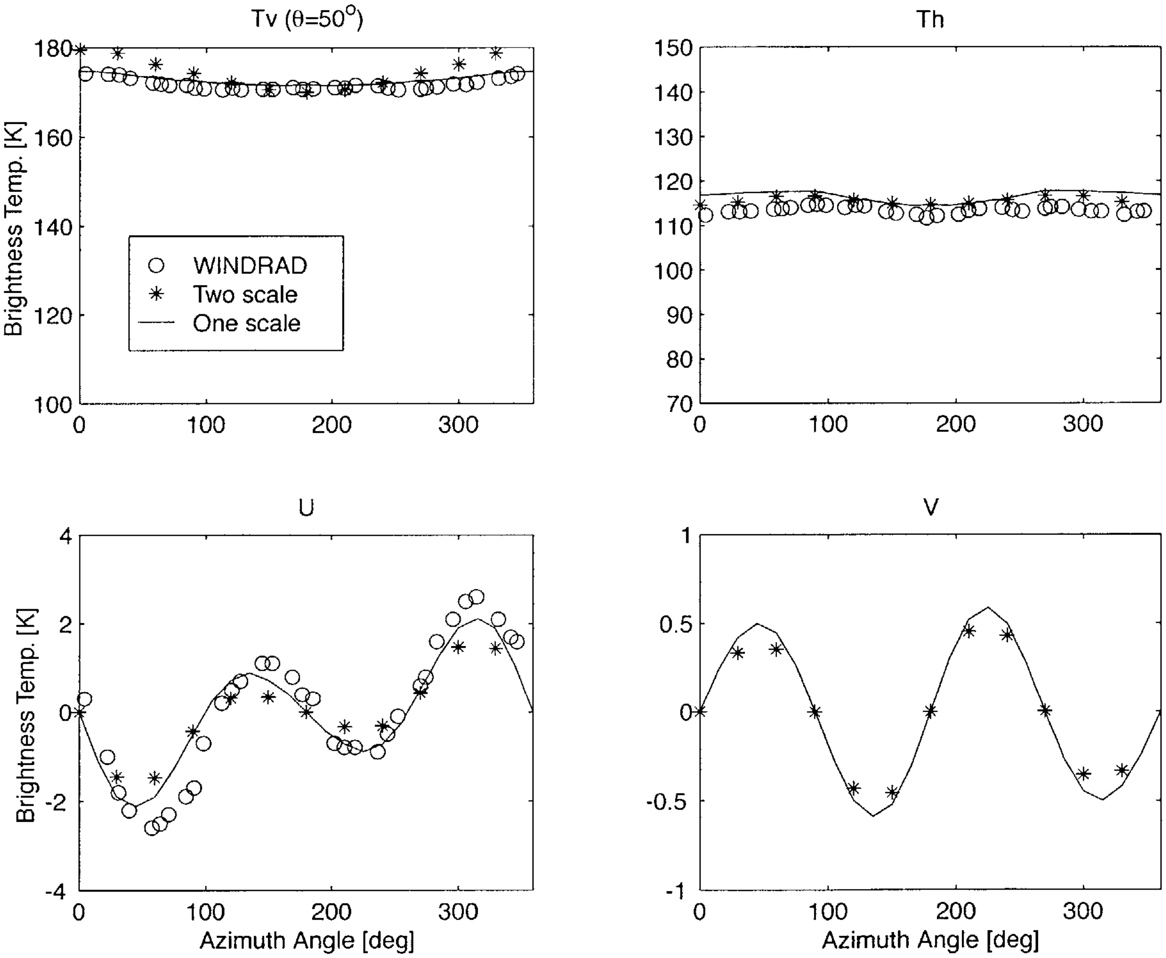

Figure 5-17: The comparison of the one-scale and two-scale models at $\theta = 50°$.

of the foam-covered ocean surface, while the two-scale model is the average of one-scale emissivity over large-scale slope of the rough ocean surface with the weight described by the slope distribution function. The overall brightness temperature is contributed by three portions — plain ocean surface, foam, and atmospheric layer. The interactions between the different regions are described by boundary conditions. For the plain ocean surface, the emissivity has been calculated using Kirchhoff's law by calculating the reflectivity of rough ocean surface. The coupling to the wind speed is through the power spectrum of ocean surface by which the ocean rough surface is described. The radiative transfer theory (RT) is used to model the foam layer in which we assume the scatterers are spherical thin-film water bubbles. The closed form solution of the RT equations for the foam layer is obtained using the iterative approach up to the first order. In the RT equations for the atmospheric layer, the scattering due to the water vapor and other gases in the air is ignored, hence a closed form of the RT solution is obtained. The simulation results, both from one-scale and two-scale models, are compared with the WINDRAD experimental data with good agreements. The results show that both the one-scale and two-scale models agree well with the WINDRAD data. However the one-scale model is much faster in computation than the two-scale model, since few integrals are involved in the one-scale model.

It has to be pointed out that, although the foam model with water bubbles is more realistic than water particles, more studies need to be conducted to model the foam layer more accurately. For example, it is suggested the multiple scattering among water bubbles to be considered by using the dense medium radiative transfer theory [81], and the top foam surface to be rough instead of flat as considered in this thesis for simplification.

Chapter 6

Electromagnetic Inversion of Plasma Medium

6.1 Introduction

Reconstruction of dielectric profiles of one-dimensional inhomogeneous material from electromagnetic scattered waves has attracted many investigators. In 1961, Kay [50] developed the inverse scattering theory to reconstruct the scattering potential of a plasma media with one-dimensional electron density profile. Kay's inverse theory is applicable to plasma medium with the permittivity $\epsilon = \epsilon_o \left(1 - \omega_p^2/\omega^2\right)$, where ω_p is the plasma frequency. The Helmhotz wave equation for plasma medium can be expressed as the Schrödinger equation from which the Gel'fand-Levitan-Marchenko (GLM) integral equation is obtained [90]. If the reflection coefficient is a rational function of the wavenumber, the GLM integral equation can be solved in a closed form to get the dielectric profile of the plasma medium [50, 91]. The GLM inverse scattering for rational reflection coefficient and its applications have been studied extensively by Jordan et al. [51],[91]–[98]. Theoretically, the GLM integral equation can be solved analytically if the reflection coefficient is given as a rational function. However when the number of poles exceeds three or there are zeroes in the rational reflection coefficient, the analytical solution of the GLM integral equation becomes difficult. For non-rational functions of the reflection coefficient, in general, an analytical solution of the GLM equation does not exist.

In 1982, Kritikos et al.[99] applied an iterative method to solve the GLM integral equation for an arbitrary reflection coefficient. In 1994 and 1996, Ge et al.[52, 56] again used the iterative numerical method with relaxation to solve the GLM inverse problem for the design of optical waveguides. The iterative numerical scheme works well for small thickness of the inhomogeneous plasma medium, but does not converge for large thickness with large reflection coefficient [52]. In this chapter, we review the GLM inverse theory and introduce a new numerical method to solve the integral equation. The new numerical scheme is based on the discretization of space and time, and changing the integral equation to a matrix equation. For each step of the spatial discretization, we solve the matrix equation to get the kernel function. After solving all kernel functions, we calculate the scattering potential, which is related to the electron density of the plasma medium.

6.2 Formulations

The geometry of the problem is shown in Fig. (6-1). Region I and III are homogeneous media characterized by ϵ_o, μ_o independent of electromagnetic frequency. Region II is the 1-D inhomogeneous plasma medium, i.e., the electron density $N(x)$ varies in $\hat{x}$ direction only. The permittivity of the plasma medium is given by

$$\epsilon_1(x,\omega) = \epsilon_o \left[1 - \frac{\omega_p^2(x)}{\omega^2}\right], \tag{6.1}$$

where ω_p is the plasma frequency

$$\omega_p(x) = \sqrt{\frac{e^2 N(x)}{m\epsilon_o}}. \tag{6.2}$$

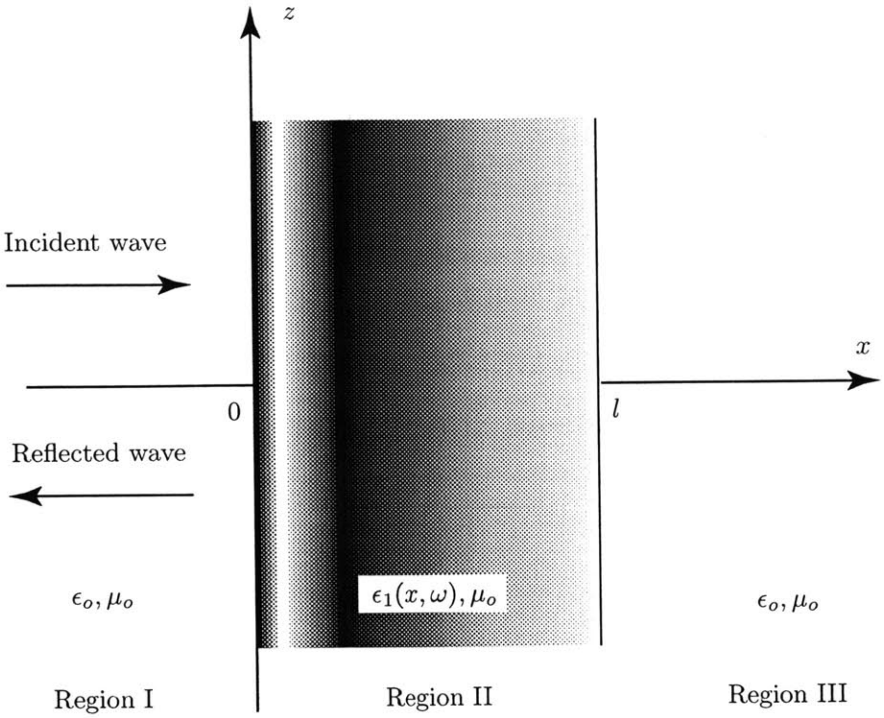

Figure 6-1: The configuration of an inhomogeneous medium.

In the above expression for ω_p, e is the charge of electron, $N(x)$ is the electron density, and m is the mass of electron. Writing the wavenumber in the homogeneous regions I and III as

$$k = \omega\sqrt{\epsilon_o \mu_o}, \tag{6.3}$$

and the wavenumber in the inhomogeneous region II as

$$k_1(x,\omega) = \omega\sqrt{\epsilon_1(x,\omega)\mu_o}, \tag{6.4}$$

we can define the scattering potential of the plasma medium as

$$q(x,\omega) = k^2 - k_1^2(x,\omega). \tag{6.5}$$

Since the wavenumber (6.3) in the homogeneous region is proportional to the frequency ω, it is convenient to rewrite the scattering potential as a function of x and

k

$$\begin{aligned} q(x,k) &= k^2 - k_1^2(x,k) = \omega_p^2(x)\epsilon_o\mu_o \\ &= \frac{e^2\mu_o N(x)}{m}. \end{aligned} \tag{6.6}$$

Notice that the scattering potential $q(x,k)$ is independent of the wavenumber k.

Consider an electromagnetic wave polarized in $\hat{y}$ direction normally incident upon the inhomogeneous plasma medium. The time-harmonic electric wave equation in the inhomogeneous medium is

$$\frac{\partial^2}{\partial x^2}E_y(x,k) + k_1^2(x)E_y(x,k) = 0. \tag{6.7}$$

Substiting Eq. (6.5) into Eq. (6.7), we get the Schrödinger-type wave equation

$$\frac{\partial^2}{\partial x^2}E_y(x,k) - q(x)E_y(x,k) = -k^2E_y(x,k). \tag{6.8}$$

The electric field $E_y(x,k)$ in Eq. (6.8) can be transformed to $\Psi(x,t)$ by

$$\Psi(x,t) = c\int E_y(x,k)e^{-ickt}dk, \tag{6.9}$$

where c is the speed of light in the homogeneous media I and III. Plugging Eq. (6.9) into Eq. (6.8), the wave equation in the time domain for the plasma region can be written as

$$\frac{\partial^2}{\partial x^2}\Psi(x,t) - \frac{1}{c^2}\frac{\partial^2}{\partial t^2}\Psi(x,t) - q(x)\Psi(x,t) = 0. \tag{6.10}$$

Let the field $\Psi(x,t)$ in the inhomogeneous plasma region II be

$$\Psi(x,t) = \Psi_o(x,t) + \int_{-x}^{x} K(x,y)\Psi_o(y,t)dy, \tag{6.11}$$

where the total field $\Psi_o(x,t)$ in region I is the sum of the incident impulse $\delta(x-ct)$

and the reflection transient $R(x+ct)$, which can be written as

$$\psi_o(x,t) = \delta(x-ct) + R(x+ct). \tag{6.12}$$

Substituting Eq. (6.12) into Eq. (6.11) and using the causality condition

$$R(x+ct) = 0, \qquad \text{for } x+ct \leq 0, \tag{6.13}$$

the integral equation becomes

$$R(x+ct) + K(x,ct) + \int_{-ct}^{x} K(x,y)R(y+ct)dy = \psi(x,t) - \delta(x-ct). \tag{6.14}$$

We know that $\psi(x,t)$ is a wave moving in positive $\hat{x}$ direction, therefore

$$\psi(x,t) = 0, \qquad \text{for } x \geq ct. \tag{6.15}$$

Then the integral equation (6.14) becomes

$$R(x+ct) + K(x,ct) + \int_{-ct}^{x} K(x,y)R(y+ct)dy = 0, \quad \text{for } x > ct. \tag{6.16}$$

Now we prove that if Eq. (6.16) is solved by considering the boundary conditions

$$K(x,-x) = 0, \tag{6.17}$$

and

$$2\frac{dK(x,x)}{dx} = q(x), \tag{6.18}$$

then the wave function described by Eq. (6.11) satisfies the wave equation (6.10). The result is that the boundary condition (6.18) gives the formula to reconstruct the scattering potential profile $q(x)$ once the kernel function $K(x,x)$ has been found.

Proof:

Using the following differentiation relation

$$\frac{\partial^2}{\partial x^2}\int\limits_{-t}^{x} K(x,y)R(y+ct)dy = \int\limits_{-t}^{x} \frac{\partial^2}{\partial x^2}K(x,y)R(y+ct)dy + 2\frac{\partial}{\partial x}K(x,x)R(x+ct), \tag{6.19}$$

$$\frac{\partial^2}{\partial t^2}\int\limits_{-t}^{x} K(x,y)R(y+ct)dy = \int\limits_{-ct}^{x} K(x,y)\frac{\partial^2}{\partial t^2}R(y+ct)dy, \tag{6.20}$$

where

$$\begin{aligned} R(y+ct)\big|_{y=-ct} &= 0, \\ \frac{\partial}{\partial t}R(y+ct)\bigg|_{y=-ct} &= 0, \end{aligned} \tag{6.21}$$

we apply the operator

$$\frac{\partial^2}{\partial x^2} - \frac{\partial^2}{\partial (ct)^2} - q(x) \tag{6.22}$$

to the integral equation (6.16) and use the boundary conditions (6.17) and (6.18). The result is

$$\begin{aligned} &\left[\frac{\partial^2}{\partial x^2}K(x,ct) - \frac{\partial^2}{\partial (ct)^2}K(x,ct) - q(x)K(x,ct)\right] \\ &+ \int\limits_{-t}^{x}\left[\frac{\partial^2}{\partial x^2}K(x,y) - \frac{\partial^2}{\partial y^2}K(x,y) - q(x)K(x,y)\right] R(y+ct)dy = 0. \end{aligned} \tag{6.23}$$

This integral equation is homogeneous for the function in the square brackets. If this function is unique, it must be zero. This statement yields

$$\frac{\partial^2}{\partial x^2}K(x,ct) - \frac{\partial^2}{\partial (ct)^2}K(x,ct) - q(x)K(x,ct) = 0. \tag{6.24}$$

Eq. (6.16) is a Fredholm integral equation for $K(x,ct)$ as a function of t with x as a constant parameter. According to the uniqueness theorem for Fredholm integral equations, $K(x,t)$ is unique, hence the function in the square bracket in Eq. (6.23) must be unique, too. Next, with the use of boundary conditions (6.17), (6.18), and Eq. (6.24), we verify that the wave function $\psi(x,t)$ satisfies the wave equation (6.10).

Assume that the wave function in the homogeneous region I, where $q(x) = 0$, satisfies the wave equation

$$\frac{\partial^2}{\partial x^2}\psi_o(x,t) - \frac{1}{c^2}\frac{\partial^2}{\partial t^2}\psi_o(x,t) = 0. \tag{6.25}$$

Inserting Eq. (6.11) into Eq. (6.10), we obtain

$$\begin{aligned}\frac{\partial^2}{\partial x^2}\psi(x,t) \quad - \quad & \frac{1}{c^2}\frac{\partial^2}{\partial t^2}\psi(x,t) - q(x)\psi(x,t) \\ = & \frac{\partial^2}{\partial x^2}\int\limits_{-x}^{x} K(x,y)\psi_o(y,t)dy - \frac{1}{c^2}\frac{\partial^2}{\partial t^2}\int\limits_{-x}^{x} K(x,y)\psi_o(y,t)dy \\ & -q(x)\psi_o(x,t) - q(x)\int\limits_{-x}^{x} K(x,y)\psi_o(y,t)dy. \end{aligned} \tag{6.26}$$

By using the relation

$$\begin{aligned}\frac{\partial^2}{\partial x^2}\int\limits_{-x}^{x} K(x,y)\psi_o(y,t)dy \quad = \quad & \int\limits_{-x}^{x}\frac{\partial^2}{\partial x^2}K(x,y)\psi_o(y,t)dy + \frac{\partial}{\partial x}K(x,y)\psi_o(y,t)\bigg|_{y=x} \\ & + \frac{\partial}{\partial x}K(x,y)\psi_o(y,t)\bigg|_{y=-x} + \frac{\partial}{\partial x}K(x,x)\psi_o(x,t) \\ & +K(x,x)\frac{\partial}{\partial x}\psi_o(x,t), \end{aligned} \tag{6.27}$$

we get

$$\begin{aligned} & \frac{\partial^2}{\partial x^2}\psi(x,t) - \frac{1}{c^2}\frac{\partial^2}{\partial t^2}\psi(x,t) - q(x)\psi(x,t) \\ & = \int\limits_{-x}^{x}\left[\frac{\partial^2}{\partial x^2}K(x,y) - \frac{\partial^2}{\partial y^2}K(x,y) - q(x)K(x,y)\right]\psi_o(y,t)dy. \end{aligned} \tag{6.28}$$

Noticing that the function in the square bracket on the right hand side of Eq. (6.28) is zero according to Eq. (6.24), we then have proved that the wave function $\psi(x,t)$ satisfies the wave equation (6.10)

$$\frac{\partial^2}{\partial x^2}\psi(x,t) - \frac{1}{c^2}\frac{\partial^2}{\partial t^2}\psi(x,t) - q(x)\psi(x,t) = 0. \tag{6.29}$$

Once the kernel function $K(x,t)$ has been solved from Eq. (6.16) with a given transient reflection coefficient $R(x+ct)$, the scattering potential can be calculated by using the boundary condition Eq. (6.18).

6.3 Solution of the GLM Integral Equation

6.3.1 Analytical Solution

For convenience, we use $\tau = ct$ in the rest of this chapter. Note that τ has the same unit as position x. In general, there is no closed form solution of the GLM integral equation (6.16) for an arbitrary type of function $R(x+\tau)$. Perhaps the only exception is when the reflection coefficient in the frequency domain $r(k)$ has a rational form

$$r(k) = \frac{\prod\limits_{m=1}^{M}(k-\mu_m)}{\prod\limits_{n=1}^{N}(k-k_n)}, \tag{6.30}$$

where μ_m is the location of zeroes, and k_n is the location of poles. Jordan and Lakshmanasamy [93] discussed the method to solve the GLM integral equation analytically for the reflection coefficient $r(k)$ with the form of a rational function. In their approach, the operator $f(p) = \prod\limits_{n=1}^{N}(p+ik_n)$, where $p = \partial/\partial\tau$, is applied to the integral equation (6.16) to be changed to a differential equation. In the following part of this section, we will use the similar procedure provided by Jordan and Ahn [92] to solve the GLM integral equation analytically for the rational $r(k)$ with 3 poles ($M = 0$ and $N = 3$), and use the results to validate the numerical solution in the next section.

Let the reflection coefficient be

$$r(k) = \frac{-i}{k^3 - i^3} = \frac{-i}{\left[k - \left(-\sqrt{3}/2 - i/2\right)\right]\left[k - \left(\sqrt{3}/2 - i/2\right)\right](k - i)}, \tag{6.31}$$

thus

$$\begin{aligned} k_1 &= -\sqrt{3}/2 - i/2, \\ k_2 &= \sqrt{3}/2 - i/2, \\ k_3 &= i. \end{aligned} \tag{6.32}$$

The reflection coefficient can also be written in terms of poles and residues

$$r(k) = \frac{r_1}{k - k_1} + \frac{r_2}{k - k_2} + \frac{r_3}{k - k_3}, \tag{6.33}$$

where the residues are

$$\begin{aligned} r_1 &= \frac{k_1 k_2 k_3}{(k_1 - k_2)(k_1 - k_3)} = -\frac{2}{3(\sqrt{3} - i)}, \\ r_2 &= \frac{k_1 k_2 k_3}{(k_2 - k_1)(k_2 - k_3)} = \frac{2}{3(\sqrt{3} + i)}, \\ r_3 &= \frac{k_1 k_2 k_3}{(k_3 - k_1)(k_3 - k_2)} = \frac{i}{3}. \end{aligned} \tag{6.34}$$

Therefore the transient reflection coefficient is

$$\begin{aligned} R(x+\tau) &= -i \sum_{n=1}^{3} r_n e^{-ik_n(x+\tau)} \\ &= -\frac{2}{3} \cos\left(\frac{\sqrt{3}(x+\tau)}{2} - \frac{\pi}{3}\right) e^{-\frac{x+\tau}{2}} + \frac{1}{3} e^{(x+\tau)}. \end{aligned} \tag{6.35}$$

Defining the operator $f(p) = p^3 - 1$, where $p = \partial/\partial\tau$ and applying it to the integral equation (6.16), we can write

$$f(p)K(x,\tau)+K(x,-\tau)=0, \tag{6.36}$$

and by symmetry

$$f(-p)K(x,-\tau)+K(x,\tau)=0. \tag{6.37}$$

Eliminating $K(x,-\tau)$ from the above equations, it yields

$$f(-p)f(p)K(x,\tau)-K(x,\tau)=0, \tag{6.38}$$

or

$$\frac{\partial^6}{\partial\tau^6}K(x,\tau)=0. \tag{6.39}$$

The boundary conditions for the kernel function $K(x,\tau)$ are

$$\begin{aligned} K(x,\tau)\big|_{\tau=-x} &= -R(0)=0, \\ \frac{\partial}{\partial\tau}K(x,\tau)\bigg|_{\tau=-x} &= -\frac{\partial}{\partial\tau}R(x+\tau)\bigg|_{\tau=-x}=0, \\ \frac{\partial^2}{\partial\tau^2}K(x,\tau)\bigg|_{\tau=-x} &= -\frac{\partial^2}{\partial\tau^2}R(x+\tau)\bigg|_{\tau=-x}=-1. \end{aligned} \tag{6.40}$$

Let the solution of Eq. (6.39) be

$$K(x,\tau)=C_5(x)\tau^5+C_4(x)\tau^4+C_3(x)\tau^3+C_2(x)\tau^2+C_1(x)\tau+C_0(x), \tag{6.41}$$

where the coefficient functions $C_0(x),\cdots,C_5(x)$ can be obtained from the differential equations and the boundary conditions. Finally we obtain

$$K(x,\tau)=-\frac{x}{8x^3+12}\tau^4+\frac{x^3-3}{4x^3+6}\tau^2-\frac{3x}{2x^3+3}\tau-\frac{x^5+6x^2}{8x^3+12}. \tag{6.42}$$

Thus the scattering potential is obtained as

$$q(x) = 2\frac{\partial}{\partial x}K(x,x) = \frac{24x(x^3-3)}{(2x^3+3)^2}. \tag{6.43}$$

6.3.2 Numerical Solution

In the previous section, we solved the GLM integral equation (6.16) analytically for the case of a rational reflection coefficient. However for an arbitrary reflection coefficient, there is no closed form solution of the GLM integral equation. In this section, we discuss the method of solving the GLM integral equation numerically for an arbitrary function of transient reflection coefficient $R(x+\tau)$.

Using $\tau = ct$, the GLM integral equation (6.16) is given by

$$K(x,\tau) + R(x+\tau) + \int_{-x}^{x} K(x,y)R(y+\tau)dy = 0, \tag{6.44}$$

with the boundary conditions

$$\begin{aligned} R(x+\tau) &= 0, &\quad& \text{for } x+\tau \le 0, &(6.45)\\ K(x,y) &= 0, && \text{for } y < x \text{ or } y \ge -x. &(6.46)\end{aligned}$$

Notice that the lower limit of the integral in Eq. (6.44) is $-x$ instead of $-\tau$ as in Eq. (6.16). The consistency of these two equations is ensured by the boundary condition (6.45). We discretize the time variables τ and y into $N+1$ grid steps with equal spacing $h = 2x/N$, thus the time variables can be expressed by

$$\begin{aligned} y &= -x + \frac{2x}{N}j, &\quad& (j = 0,1,2,\cdots,N), &(6.47)\\ \tau &= -x + \frac{2x}{N}i, && (i = 0,1,2,\cdots,N). &(6.48)\end{aligned}$$

Notice that x is considered as a fixed parameter for each time step when solving the

GLM integral equation. For each time step, x is discretized as

$$x = \frac{x_{\max}}{M} m, \qquad (m = 0, 1, 2, \cdots, M), \tag{6.49}$$

where the total number of grid points for x is $M+1$, and $x_{\max}$ is the maximum depth for the solution. Plugging the discretized time variables τ and y, and the spatial variable x into Eq. (6.44), we get the following equation

$$K_{mi} + R_{mi} + \sum_{j=0}^{N} c_j h K_{mj} R_{ji} = 0, \tag{6.50}$$

where

$$K_{mi} = K(x, \tau) = K\left(\frac{x_{\max}}{M} m, -\frac{x_{\max}}{M} m + \frac{2x_{\max}}{MN} mi\right), \tag{6.51}$$

$$R_{mi} = R(x + \tau) = R\left(\frac{2x_{\max}}{MN} mi\right), \tag{6.52}$$

$$K_{mj} = K(x, y) = K\left(\frac{x_{\max}}{M} m, -\frac{x_{\max}}{M} m + \frac{2x_{\max}}{MN} mj\right), \tag{6.53}$$

$$R_{ji} = R(y + \tau) = R\left(\frac{2x_{\max}}{M} m \left(\frac{i+j}{N} - 1\right)\right). \tag{6.54}$$

The coefficient c_j, by the trapezoidal rule, has the value

$$c_j = \begin{cases} 0.5 & \text{for } j = 0 \text{ or } N, \\ 1 & \text{otherwise.} \end{cases} \tag{6.55}$$

Letting $K_{mi} = \delta_{ij} K_{mj}$, Eq. (6.50) can be rewritten as

$$\sum_{j=0}^{N} \left[\delta_{ij} + c_j h R_{ji}\right] K_{mj} = -R_{mi}, \tag{6.56}$$

which is a matrix equation with the form

$$\overline{\overline{A}} \cdot \overline{a}_m = \overline{b}_m \tag{6.57}$$

for each spatial sampling point m, where

$$\overline{\overline{A}} = \delta_{ij} + c_j h R_{ji}, \tag{6.58}$$

$$\overline{a}_m = K_{mj}, \tag{6.59}$$

$$\overline{b}_m = -R_{mi}. \tag{6.60}$$

Figure (6-2) displays the non-zero entries of matrix $\overline{\overline{A}}$. The zero entries in the plot are due to the causality condition of $R(x+\tau) = 0$ for $x + \tau \leq 0$. The kernel function $K(x, \tau)$ can then be solved numerically by

$$K_{mj} = \overline{a}_m = \overline{\overline{A}}^{-1} \cdot \overline{b}_m. \tag{6.61}$$

Thus the scattering potential can be calculated numerically by

$$q(x_m) = 2\frac{K_{mN} - K_{m-1,N}}{\Delta x} = \frac{2M}{x_{\mathsf{max}}}\left(K_{mN} - K_{m-1,N}\right). \tag{6.62}$$

6.4 Validation of Numerical Method using the Closed Form Solution

The advantage of the numerical method is that it can be applied to the inverse scattering problem for plasma medium by using arbitrary reflection coefficient. To verify the numerical code, we compare the numerical result of scattering potential with the closed form solution obtained in Eq. (6.43),

$$q(x) = 2\frac{\partial}{\partial x}K(x, x) = \frac{24x(x^3 - 3)}{(2x^3 + 3)^2}, \tag{6.63}$$

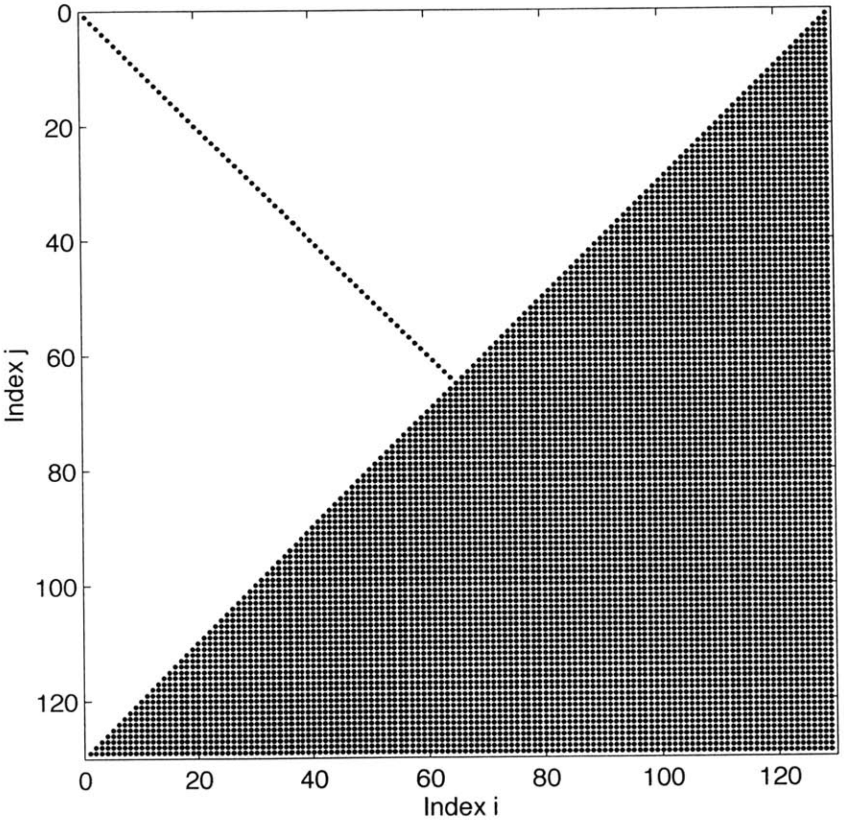

Figure 6-2: The nonzero entries of the matrix $\overline{\overline{A}}$.

where the reflection coefficient as in Eq. (6.31) is

$$r(k) = \frac{-i}{k^3 - i}. \tag{6.64}$$

The three poles in the above rational function are located at [Eq. (6.32)]

$$\begin{aligned} k_1 &= -\sqrt{3}/2 - i/2, \\ k_2 &= \sqrt{3}/2 - i/2, \\ k_3 &= i, \end{aligned} \tag{6.65}$$

and the transient reflection coefficient is [Eq. (6.35)]

$$R(x+\tau) = -\frac{2}{3}\cos\left(\frac{\sqrt{3}(x+\tau)}{2} - \frac{\pi}{3}\right) e^{-\frac{x+\tau}{2}} + \frac{1}{3}e^{(x+\tau)}. \tag{6.66}$$

In the numerical calculation, the transient reflection coefficient (6.66) is used to fill the matrix $\overline{\overline{A}}$ and the vector $\bar{b}_m$ using Eq. (6.58) and Eq. (6.60), respectively. Fig. (6-3) is the numerical result of the reconstructed scattering potential in comparison with the analytical solution as in Eq. (6.63)

Notice that the agreement of the numerical result and the analytical solution is excellent. The reflection coefficient $r(k)$ has low-pass characteristics which is shown in Fig. (6-4).

6.5 Numerical Reconstruction of Plasma Profile

In the previous section, we validated the numerical solution of the GLM integral equation by using the closed form analytical solution for a given reflection coefficient in the form of a rational function. In this section, we start from a given plasma profile to calculate the reflection coefficient analytically and then to solve the GLM equation numerically to reconstruct the plasma profile. We use the inverted result to compare

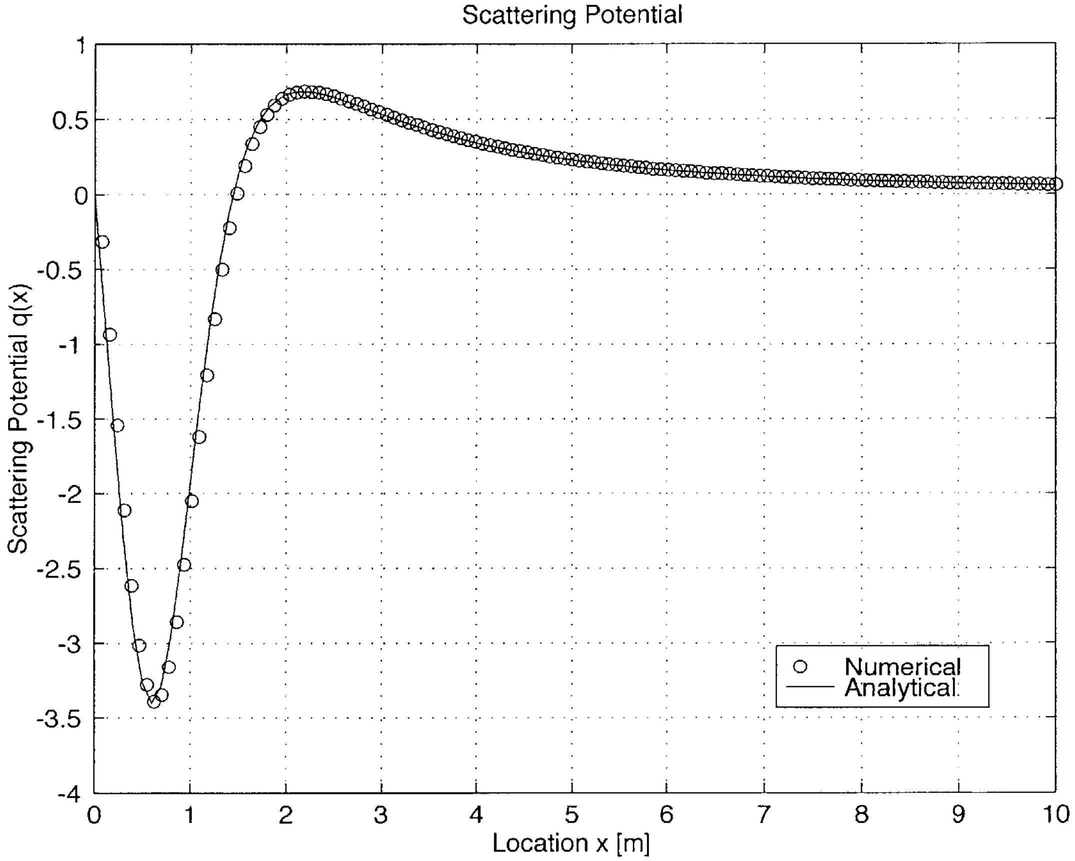

Figure 6-3: Numerical result of the scattering potential in comparison with the closed form solution for a rational reflection coefficient with three poles.

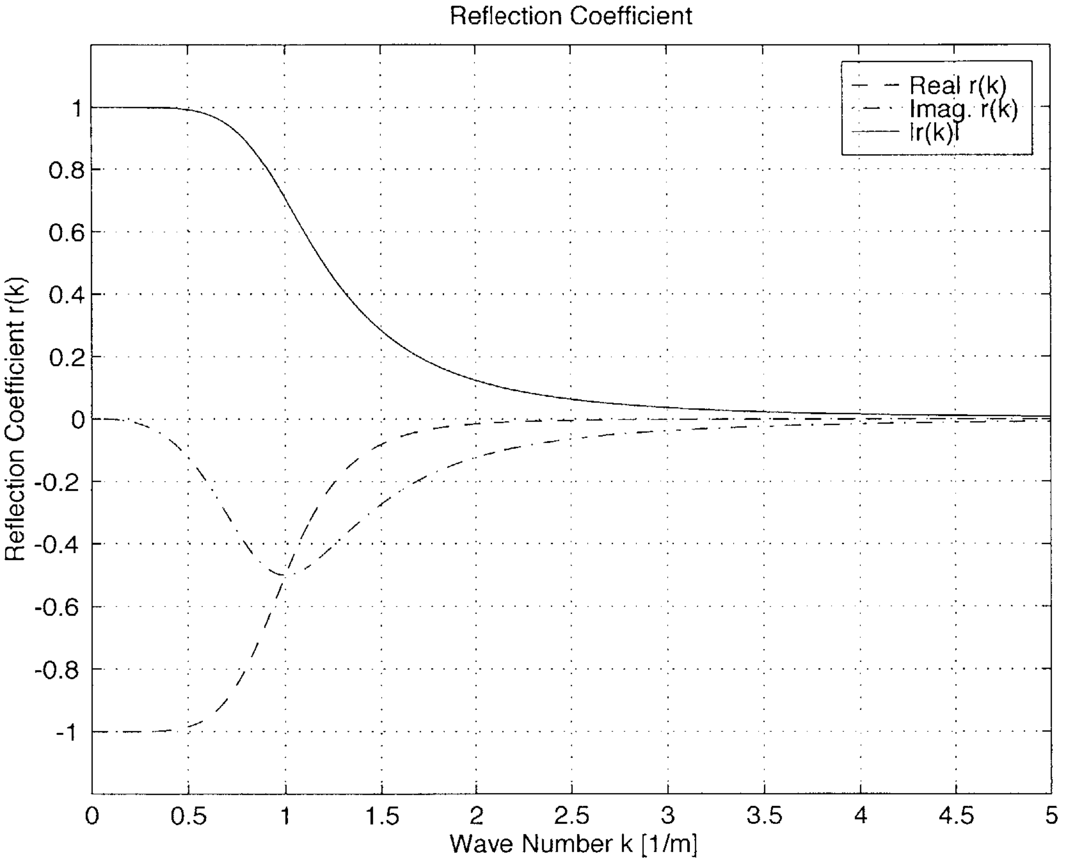

Figure 6-4: The reflection coefficient $r(k) = -i/(k^3 - i)$ with three poles.

with the given plasma profile.

6.5.1 Reflection Coefficient of a Homogeneous Plasma Slab

Consider a plasma slab as shown in Fig. (6-1). Let the depth of the slab be l and assume that the electron density $N(x)$ is constant. For the normal incident wave polarized in $\hat{y}$ direction, the wave equation is given by

$$\left(-\frac{\partial^2}{\partial x^2} + q(x)\right) E(x,k) = k^2 E(x,k), \tag{6.67}$$

where $q(x)$ is zero for region I and III, and $q(x)$ is a constant for region II.

The waves are assumed to be

$$E_1(x) = e^{ikx} + r(k)e^{-ikx} \qquad \text{in region I,} \tag{6.68}$$

$$E_2(x) = Ae^{ik_1x} + Be^{-ik_1x} \qquad \text{in region II,} \tag{6.69}$$

$$E_3(x) = Ce^{ikx} \qquad \text{in region III,} \tag{6.70}$$

where $k_1 = \omega\sqrt{\epsilon_1(x)\mu_o} = \sqrt{k^2 - k_p^2}$ and $k_p = \omega_p\sqrt{\epsilon_o\mu_o}$. On the boundaries at $x = 0$ and $x = l$, the tangential electric and magnetic fields are continuous, thus

$$1 + r(k) = A + B, \tag{6.71}$$

$$k - kr(k) = k_1A - k_1B, \tag{6.72}$$

and

$$Ae^{ik_1l} + Be^{-ik_1l} = Ce^{ikl}, \tag{6.73}$$

$$k_1Ae^{ik_1l} - k_1Be^{-ik_1l} = kCe^{ikl}. \tag{6.74}$$

Solving for $r(k)$ by eliminating A, B and C, thus the reflection coefficient is obtained as

$$r(k) = \frac{1-\gamma^2}{(1+\gamma^2) + i2\gamma\cot(k_1 l)}, \tag{6.75}$$

where

$$\gamma = k_1/k = \sqrt{1 - \frac{k_p^2}{k^2}}. \tag{6.76}$$

The scattering potential of the plasma slab is related to the plasma wavenumber by Eq. (6.6). Therefore

$$\gamma = \frac{k_1}{k} = \frac{\sqrt{k^2 - q(x)}}{k}. \tag{6.77}$$

Using the symmetry property $r(-k) = r^*(k)$, the reflection transient can be calculated by

$$\begin{aligned} R(\tau) &= \frac{1}{2\pi}\int_{-\infty}^{\infty} r(k)e^{-ik\tau}dk \\ &= \frac{1}{\pi}\int_{0}^{\infty} \{\mathrm{Re}\,[r(k)]\cos(k\tau) + \mathrm{Im}\,[r(k)]\sin(k\tau)\}\,dk. \end{aligned} \tag{6.78}$$

6.5.2 Numerical Results of the Profile Reconstruction

In the numerical simulation, we let $q(x) = 2\,\mathrm{m}^{-2}$ and $l = 1.5\,\mathrm{m}$, thus

$$\gamma = \frac{\sqrt{k^2-2}}{k}. \tag{6.79}$$

The reflection coefficient $r(k)$ of the homogeneous plasma slab is plotted in Fig. (6-5). The corresponding transient reflection coefficient is shown in Fig. (6-6). Figure (6-7) is the numerical result of the reconstruction for the corresponding scattering potential $q(x)$ with the given profile. The ripples of the numerical result are due to the truncation of the reflection coefficient $r(k)$ in the calculation of the transient reflection coefficient $R(x+\tau)$ in Eq. (6.78). In Fig. (6-7), the cutoff wavenumber $k_{\mathrm{max}} = 10\,\mathrm{m}^{-1}$ is used for the truncation of $r(k)$. A better numerical reconstruction result can be obtained by choosing a larger cutoff wavenumber. Figure (6-8) shows the result for

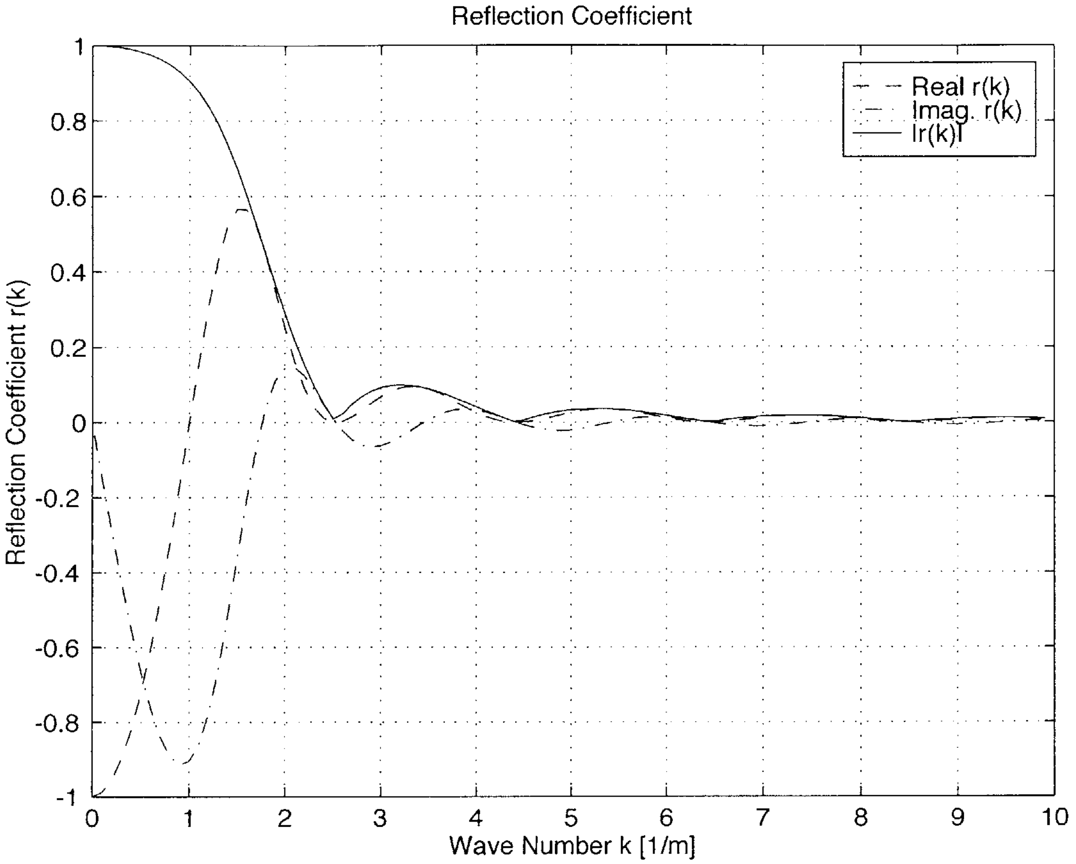

Figure 6-5: The reflection coefficient of a homogeneous plasma slab with $q(x) = 2\,\mathrm{m}^{-2}$ and $l = 1.5\,\mathrm{m}$.

the cutoff wavenumber $k_{\max} = 20\,\mathrm{m}^{-1}$, and we notice that much more accurate results are obtained. For both cases, the number of sampling points for space and time is $N = M = 256$.

6.6 Conclusions

In this section, we have studied the Gel'fand-Levitan-Marchenko (GLM) inverse theory and derived its integral equation. The GLM integral equation is solved in closed form for the reflection coefficient having the form of a rational function with 3 poles. It becomes very difficult to solve the GLM equation in a closed form when the number of poles exceeds 3 or zeroes appear in the rational function of the reflection coefficient.

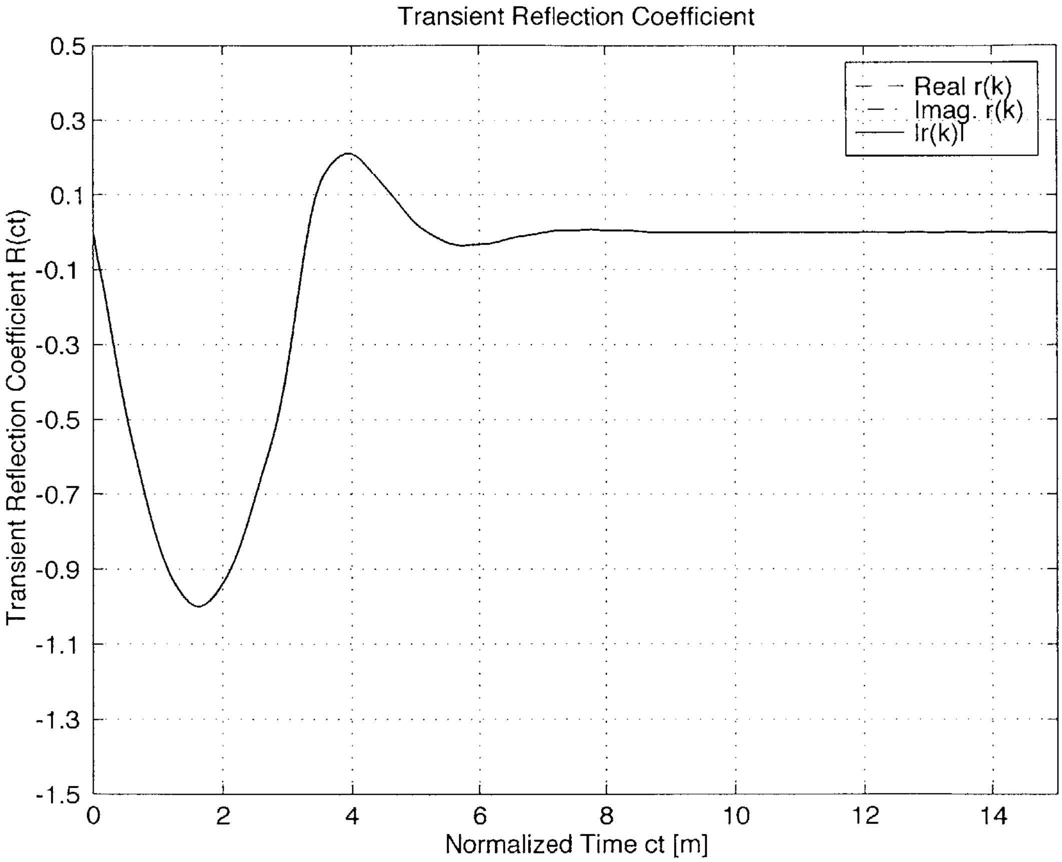

Figure 6-6: The transient reflection coefficient of a homogeneous plasma slab with $q(x) = 2\,\mathrm{m}^{-2}$ and $l = 1.5\,\mathrm{m}$.

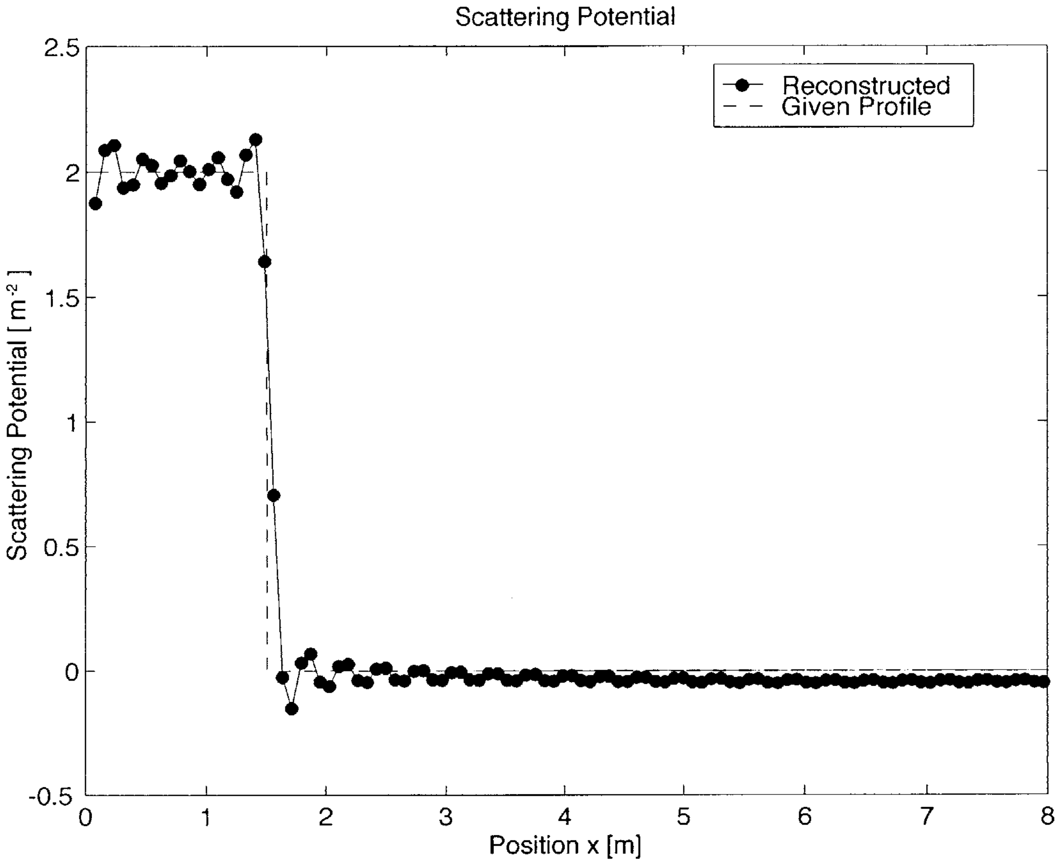

Figure 6-7: The reconstruction of a homogeneous plasma slab with $q(x) = 2\,\mathrm{m}^{-2}$ and $l = 1.5\,\mathrm{m}$. The cutoff wavenumber is $k_{\mathrm{max}} = 10\,\mathrm{m}^{-1}$. The numbers of sampling points for space and time are $N = 256$ and $M = 256$, respectively.

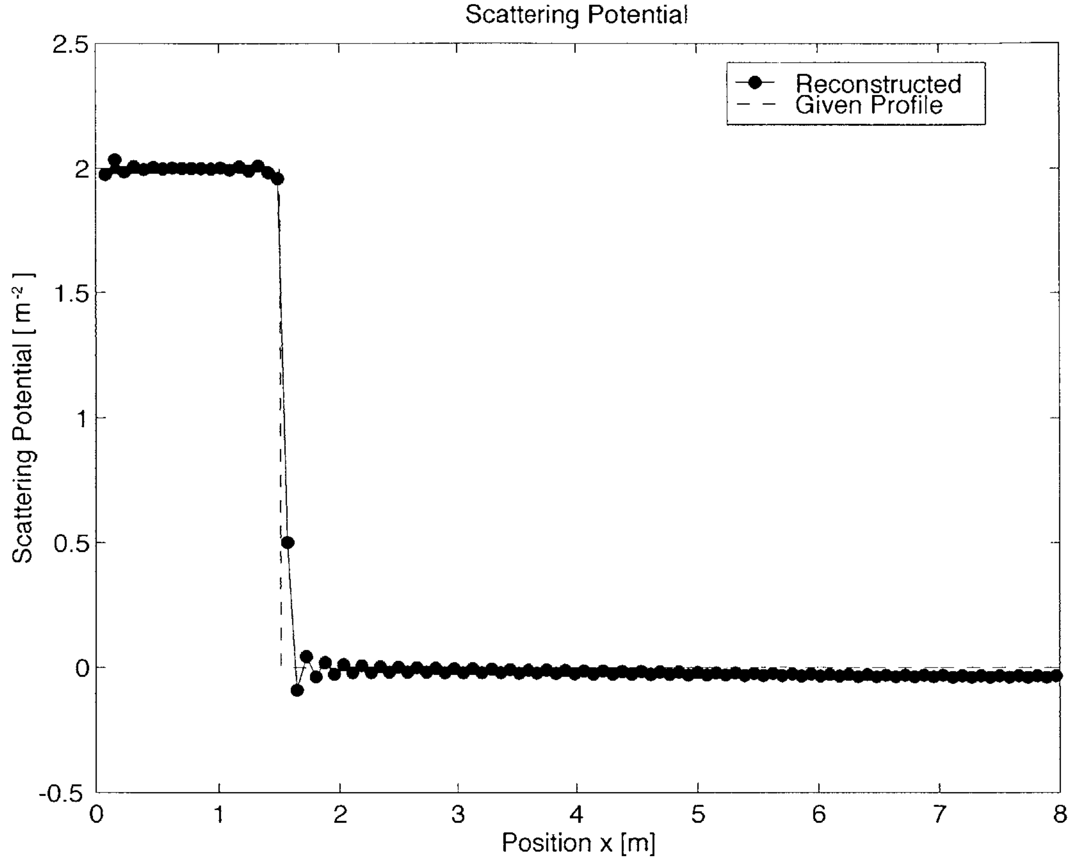

Figure 6-8: The reconstruction of a homogeneous plasma slab with $q(x) = 2\,\mathrm{m}^{-2}$ and $l = 1.5\,\mathrm{m}$. The cutoff wavenumber is $k_{\max} = 20\,\mathrm{m}^{-1}$. The numbers of sampling points for space and time are $N = 256$ and $M = 256$, respectively.

In general, there is no closed form solution for the GLM equation for a reflection coefficient with arbitrary form of reflection coefficient. Hence a numerical method has been developed by discretizing the kernel and transient reflection coefficient function in space and time, and solving the GLM equation by matrix inversion. In comparison with the iterative approach with relaxation, this numerical method is faster and much more accurate. The numerical result of the scattering potential has been validated by comparison with the analytical solution with closed form, and the reconstructed electron density profile of a plasma slab. It has been found that the accuracy of the reconstructed profile is sensitive to the cutoff wavenumber in the transformation of reflection coefficient $r(k)$ to the transient function $R(x + ct)$. However if the numerical inversion is directly performed by using the transient reflection coefficient R, the accuracy of the reconstructed profile is affected only in the region defined by the distance traveled by a wave corresponding to the time of the truncation of the transient R. Further study for the accuracy of the reconstruction is suggested when noise is taken into account in the reflection coefficient.

Chapter 7

Summary and Suggestions for Future Work

In this thesis, we have presented various analytical and numerical methods for solving microwave remote sensing problems. First we considered a perfectly conducting object in free space or on a flat surface, and calculated its radar cross section (RCS) by solving the electric field integral equation (EFIE) derived from Huygens' principle. In the EFIE formulation for a PEC object on a flat surface, we considered the case of a perfectly conducting flat interface. It is possible to use the same approach and consider the interface as dielectric, however the computational complexity increases because of the need to evaluate the Sommerfeld integral in the determination of the dyadic Green's function [28, 100].

For the geometry of a PEC object on a rough surface, a hybrid method consisting of SPM and MoM has been presented. The formulation was derived in a general form and was applicable to the dielectric rough surface. Using the expansion of the Green's function and surface variables on the rough surface, the EFIEs were decomposed in terms of the order of the rough surface height function. The equations of each order represent the EM scattering problem with the same object on the mean surface but different incident field radiated from the "equivalent source". The equivalent source field can be obtained using the lower order solutions, such that an iterative method can be applied. The equivalence of the rough surface problem to the flat surface problem allows us to use the zeroth order MoM solution developed in Chapter 2 to calculate the RCS of the PEC object on a flat surface by using the different incident field (equivalent source). In comparison with the standard MoM, this hybrid method demonstrates a dramatic increase in computational efficiency without loss of accuracy. Another significant achievement of this hybrid method is that the total returned field, as the one obtained by the standard MoM, is the sum of individual terms in the hybrid method, each of which has a clear physical meaning of the electromagnetic wave interactions between the PEC object and the rough surface.

Furthermore, we have proved that the first order field of the equivalent source on a PEC rough surface is the same as the one derived from the traditional SPM by considering a plane incident wave. So the solutions from the traditional SPM are essentially the radiation field from the equivalent source on the mean surface. The equivalent source can be evaluated using the lower order solution of the surface field and the rough surface profile. From the formulation of the equivalent source, we found that it is not limited to the plane incident wave as in the traditional SPM. By using a tapered wave as the incident wave, we calculated the radiation field of the first order equivalent source on a PEC rough surface, and got good agreement in comparison with the standard MoM. The calculation of the field scattered by PEC rough surface using the equivalent source is much faster than the standard MoM. In addition, the equivalent source gives reasonable numerical results at low grazing angles, while it is difficult for the standard MoM to produce the correct result because of the difficulty in sampling a large rough surface at these angles. Although the equivalent source has been used to calculate the first order field scattered by a PEC rough surface, it is not so obvious that the equivalent source approach will still show its advantage for obtaining higher order scattered fields or for dielectric rough surfaces in comparison with other analytical or numerical methods.

We have also developed composite models in Chapter 5 to obtain the thermal emission of the wind-driven and foam-covered ocean surface, including atmosphere contribution. We modeled the foam as a volume with thin-film water bubbles and the radiative transfer equations were set up in this volume with the boundary conditions linking the atmosphere and the ocean surface. At the frequency we were interested in, we assumed the penetration depth of the electromagnetic wave in the foam layer to be much shorter than the foam thickness, the electromagnetic wave interaction between the foam layer and the ocean surface was ignored and the formulation was greatly simplified. The RT equations in the foam layer were solved by using an iterative method, and a closed form solution was obtained up to the first order. In the solution of the RT equations in the foam layer, the terms provide the physical meaning of the wave propagation and interaction between the atmosphere and the water bubbles in the foam. For the interface of the atmosphere and the open ocean surface, thermal emission is the sum of the reflection of down-going atmospheric thermal emission and the thermal emission from the plain ocean surface. The total thermal emission at the radiometer is the sum of the contribution from the atmosphere-foam interface and the atmosphere-plain ocean surface interface, weighted by the foam coverage. In the one-scale model, in which only the small-scale ocean waves are taken into account, we found that the atmospheric thermal emission is comparable to the foam's thermal emission for the co-polarized waves. The two-scale model is more realistic in comparison with the one-scale model, however it requires much more computational time since two more folds of integration are needed for averaging over the slope of large-scale ocean waves. Eventhough we included the hydrodynamic model by simply multiplying an up-wind and down-wind dependent factor to the power spectrum of the rough ocean surface, a better hydrodynamic model is expected to describe more accurately the asymmetry of the wind-driven waves and the breaking waves.

The propagation of the specific intensity is also modeled using the RT theory for the atmosphere. Since the scattering in the atmosphere is ignored, the only existing parameter in the RT equations is the absorption coefficient that can be obtained from the millimeter-wave propagation model (MPM) with the use of standard atmospheric profile data available in the US Standard Atmosphere 1976. Although it is difficult to obtain the atmospheric profile data at the particular measurement site, further study to validate the atmospheric emission model using measurement data is important and worthy.

In Chapter 6, the GLM inverse theory was studied and a numerical method of solving its integral equation to reconstruct the electron density profile for a plasma medium was presented. A numerical method was developed by discretizing the kernel function and the transient reflection coefficient in the space and time domains, so that the integral equation was converted to a matrix equation and the solution was obtained by inverting the matrix for arbitrary form of reflection coefficient. This numerical method is much faster and more accurate than other methods such as the iterative method with relaxation. The numerical method was validated by comparing with the analytical solution for the special case where the reflection coefficient is rational with respect to the wavenumber. The numerical method was also validated by solving the GLM integral equation for a reflection coefficient from an assumed plasma profile. While this numerical model for the GLM inverse problem was proved to be very efficient and accurate, a sensitivity-to-noise study and the application of this model to measurement data are suggested.

Appendix A

The Inner Product of Scattered Field with the Basis Function

Considering the fact that there is no surface current accumulation and the current does not cross the open edges, we get

$$\int\limits_S dS\nabla \cdot \left(\phi(\bar{r})\overline{f}_m(\bar{r})\right) = \oint\limits_c dl\, \hat{n}_l \cdot \left(\phi(\bar{r})\overline{f}_m(\bar{r})\right) = 0. \tag{A.1}$$

The inner product of the scattered electric field with the vector basis function is

$$\begin{aligned}
&\int\limits_S dS\overline{E}_s(\bar{r}) \cdot \overline{f}_m(\bar{r}) \\
&\quad = i\omega \int\limits_S dS\overline{A}(\bar{r}) \cdot \overline{f}_m(\bar{r}) - \int\limits_S dS\nabla\phi(\bar{r}) \cdot \overline{f}_m(\bar{r}) \\
&\quad = i\omega \int\limits_S dS\overline{A}(\bar{r}) \cdot \overline{f}_m(\bar{r}) - \int\limits_S dS\nabla \cdot \left(\phi(\bar{r})\overline{f}_m(\bar{r})\right) + \int\limits_S dS\phi(\bar{r})\nabla \cdot \overline{f}_m(\bar{r}) \\
&\quad = i\omega \int\limits_S dS\overline{A}(\bar{r}) \cdot \overline{f}_m(\bar{r}) + \int\limits_S dS\phi(\bar{r})\nabla \cdot \overline{f}_m(\bar{r}) \\
&\quad = i\omega \int\limits_{T_m^+} dS\overline{A}(\bar{r}) \cdot \frac{l_m}{2A_m^+}\bar{\rho}_m^+(\bar{r}) + i\omega \int\limits_{T_m^-} dS\overline{A}(\bar{r}) \cdot \frac{l_m}{2A_m^-}\bar{\rho}_m^-(\bar{r})
\end{aligned}$$

$$
\begin{aligned}
&+\int\limits_{T_m^+} dS\phi(\bar{r})\frac{l_m}{A_m^+} - \int\limits_{T_m^-} dS\phi(\bar{r})\frac{l_n}{A_m^-} \\
&\approx i\omega l_m\left[\overline{A}(\bar{r}_m^{c+})\cdot\frac{\bar{\rho}_m^+(\bar{r}_m^{c+})}{2} + \overline{A}(\bar{r}_m^{c-})\cdot\frac{\bar{\rho}_m^-(\bar{r}_m^{c-})}{2}\right] \\
&+l_m\left[\phi(\bar{r}_m^{c+}) - \phi(\bar{r}_m^{c-})\right].
\end{aligned}
\tag{A.2}
$$

Appendix B

The Basis Vectors and Green's Functions

The polarization basis vectors in homogeneous region 1 and 2 with a flat interface are defined as

$$\hat{e}_1(\pm k_{1z}) = \frac{\hat{k}_1 \times \hat{z}}{\left|\hat{k}_1 \times \hat{z}\right|} = \frac{\hat{x}k_y - \hat{y}k_x}{\sqrt{k_x^2 + k_y^2}}, \tag{B.1}$$

$$\hat{h}_1(\pm k_{1z}) = \hat{e}_1(\pm k_{1z}) \times \hat{k}_1 = \mp \frac{k_{1z}}{k_1\sqrt{k_x^2 + k_y^2}}\left(\hat{x}k_x + \hat{y}k_y\right) + \hat{z}\frac{\sqrt{k_x^2 + k_y^2}}{k_1}, \tag{B.2}$$

$$\hat{e}_2(\pm k_{2z}) = \frac{\hat{x}k_y - \hat{y}k_x}{\sqrt{k_x^2 + k_y^2}}, \tag{B.3}$$

$$\hat{h}_2(\pm k_{2z}) = \hat{e}(\pm k_{2z}) \times \hat{k}_2 = \mp \frac{k_{2z}}{k_2\sqrt{k_x^2 + k_y^2}}\left(\hat{x}k_x + \hat{y}k_y\right) + \hat{z}\frac{\sqrt{k_x^2 + k_y^2}}{k_2}. \tag{B.4}$$

The integral representation of the dyadic Green's function in unbounded space is given by [65]

$$\overline{\overline{G}}_1(\bar{r}, \bar{r}') = -\hat{z}\hat{z}\frac{\delta(\bar{r}, \bar{r}')}{k_1^2}$$

$$+\begin{cases} \dfrac{i}{8\pi^2}\displaystyle\int d\bar{k}_\perp \dfrac{1}{k_{1z}}\left[\hat{e}(k_{1z})\hat{e}(k_{1z})+\hat{h}(k_{1z})\hat{h}(k_{1z})\right]e^{i\bar{k}_1\cdot(\bar{r}-\bar{r}')} & z > z', \\ \dfrac{i}{8\pi^2}\displaystyle\int d\bar{k}_\perp \dfrac{1}{k_{1z}}\left[\hat{e}(-k_{1z})\hat{e}(-k_{1z})+\hat{h}(-k_{1z})\hat{h}(-k_{1z})\right]e^{i\overline{K}_1\cdot(\bar{r}-\bar{r}')} & z < z'. \end{cases} \tag{B.5}$$

The curl of the Green's function is

$$\nabla \times \overline{\overline{G}}_\alpha(\bar{r},\bar{r}') = \begin{cases} -\dfrac{1}{8\pi^2}\displaystyle\int d\bar{k}_\perp \dfrac{k_\alpha}{k_{1z}}\overline{\overline{B}}_\alpha(k_{1z})e^{i\bar{k}_\alpha\cdot(\bar{r}-\bar{r}')} & z > z', \\ -\dfrac{1}{8\pi^2}\displaystyle\int d\bar{k}_\perp \dfrac{k_\alpha}{k_{1z}}\overline{\overline{B}}_\alpha(-k_{1z})e^{i\overline{K}_\alpha\cdot(\bar{r}-\bar{r}')} & z < z', \end{cases} \tag{B.6}$$

where $\alpha = 1, 2$.

Appendix C

Simulation of Random Rough Surfaces

To generate the 2-D rough surface for Monte Carlo simulation, we define the Fourier transform pair

$$f(x,y) = \iint F(k_x,k_y)e^{-i(k_xx+k_yy)}dk_xdk_y, \tag{C.1}$$

$$F(k_x,k_y) = \frac{1}{(2\pi)^2}\iint f(x,y)e^{i(k_xx+k_yy)}dxdy. \tag{C.2}$$

Since the elevation height $f(x,y)$ of rough surface is real, we get

$$F(k_x,k_y) = F^*(-k_x,-k_y), \tag{C.3}$$

$$F(k_x,-k_y) = F^*(-k_x,k_y). \tag{C.4}$$

Thus we obtain the relations of the real and imaginary parts in the function $F(k_x,k_y)$ as follows:

$$\begin{cases} F_R(k_x,k_y) = F_R(-k_x,-k_y), \\ F_I(k_x,k_y) = -F_I(-k_x,-k_y), \end{cases} \tag{C.5}$$

$$\begin{cases} F_R(k_x, -k_y) = F_R(-k_x, k_y), \\ F_I(k_x, -k_y) = -F_I(-k_x, k_y). \end{cases} \tag{C.6}$$

Assuming that the rough surface spectrum function W has the following symmetrical property:

$$W(k_x, k_y) = W(\pm k_x, \pm k_y), \tag{C.7}$$

which is true for the spectrum functions under study in the thesis, and letting

$$\begin{cases} F_R(k_x, k_y) = a(k_x, k_y)\sqrt{W(k_x, k_y)}, \\ F_I(k_x, k_y) = b(k_x, k_y)\sqrt{W(k_x, k_y)}, \end{cases} \tag{C.8}$$

we get

$$\begin{cases} a(k_x, k_y) = a(-k_x, -k_y), \\ b(k_x, k_y) = -b(-k_x, -k_y), \end{cases} \tag{C.9}$$

where $a(k_x, k_y)$ and $b(k_x, k_y)$ are independent random numbers of Gaussian distribution with zero mean and unit variance. Notice that the average of roughness [65, page 557] is

$$\Big\langle F(k_x, k_y)F^*(k'_x, k'_y)\Big\rangle \tag{C.10}$$

$$= \Big(a(k_x, k_y)a(k'_x, k'_y) + b(k_x, k_y)b(k'_x, k'_y)\Big) \sqrt{W(k_x, k_y)}\sqrt{W(k'_x, k'_y)}, \tag{C.11}$$

therefore the deviation of the random number must be

$$\Big\langle a(k_x, k_y)a(k'_x, k'_y)\Big\rangle = \Big\langle b(k_x, k_y)b(k'_x, k'_y)\Big\rangle = \frac{\delta(k_x - k'_x, k_y - k'_y)}{2}. \tag{C.12}$$

Using the symmetrical property in Eq. (C.6), the elevation height of rough surface in Eq. (C.2) can be evaluated from

$$f(x, y) = \iint F(k_x, k_y)e^{-i(k_x x + k_y y)}dk_x dk_y$$

$$\begin{aligned} &= \int_0^\infty dk_x \int_0^\infty dk_y \sqrt{W(k_x,k_y)} a(k_x,k_y) 2\cos(k_x x + k_y y) \\ &\quad + \int_0^\infty dk_x \int_0^\infty dk_y \sqrt{W(k_x,k_y)} a(k_x,-k_y) 2\cos(k_x x - k_y y) \\ &\quad + \int_0^\infty dk_x \int_0^\infty dk_y \sqrt{W(k_x,k_y)} b(k_x,-k_y) 2\sin(k_x x - k_y y) \\ &\quad + \int_0^\infty dk_x \int_0^\infty dk_y \sqrt{W(k_x,k_y)} b(k_x,k_y) 2\sin(k_x x + k_y y). \end{aligned} \tag{C.13}$$

By changing the coordinates,

$$\begin{aligned} k_x &= k\cos\alpha, \\ k_y &= k\sin\alpha, \end{aligned} \tag{C.14}$$

we get

$$\begin{aligned} f(x,y) &= 2\int_0^\infty kdk \int_0^\pi d\alpha \sqrt{W(k,\alpha)} a(k,\alpha) \cos k(x\cos\alpha + y\sin\alpha) \\ &\quad +2\int_0^\infty kdk \int_0^\pi d\alpha \sqrt{W(k,\alpha)} b(k,\alpha) \sin k(x\cos\alpha + x\sin\alpha). \end{aligned} \tag{C.15}$$

Appendix D

Phase Matrix for Water Bubbles

Consider an electromagnetic plane wave propagating in $+\hat{z}'$ direction and incident upon a thin-film water bubble in (x', y', z') coordinates with inner radius R and film thickness d as shown in Fig. (D-1). Let the wavenumber in the core and outside be k, the wavenumber in the film be k_1, and the polarization angle be β. On $y'z'$ plane, the scattered field with scattering angles θ' and $\phi' = 90°$ in radiation zone is given in a closed form as follows [101]:

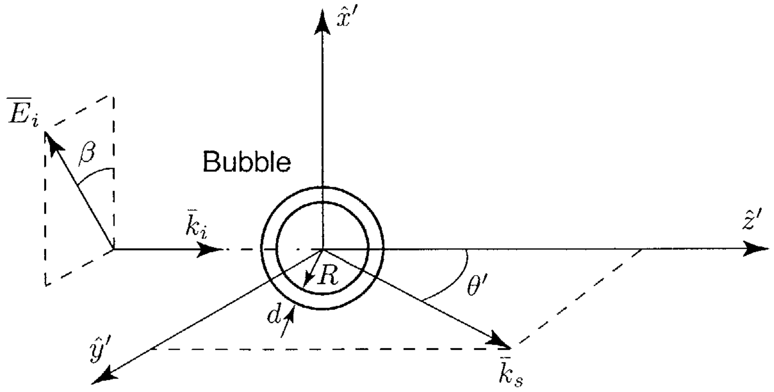

Figure D-1: EM scattering by a bubble in (x', y', z') coordinates.

$$E_{\phi'} = \frac{ie^{ikr}}{kr} S_1 \cos\beta, \tag{D.1}$$

$$E_{\theta'} = -\frac{ie^{ikr}}{kr} S_2 \sin\beta, \tag{D.2}$$

where

$$S_1 = i\delta(m^2-1)\alpha^2 \left[j_o(x) - \frac{m^2-1}{m^2}\frac{j_1(x)}{x} \right], \tag{D.3}$$

$$\begin{aligned} S_2 &= i\delta(m^2-1)\alpha^2 \Bigg\{ j_o(x)\cos\theta' \\ &+ \frac{m^2-1}{m^2}\left[\frac{j_1(x)}{x} + \frac{1+\cos\theta'}{2}\left(\frac{j_1(x)}{x} - j_o(x) \right) \right] \Bigg\}, \end{aligned} \tag{D.4}$$

in which $m = k_1/k$, $x = \dfrac{4\pi}{\lambda} R \sin(\theta'/2)$, $\delta = 2\pi d/\lambda$, $\alpha = 2\pi R/\lambda$, $j_o(x)$ and $j_1(x)$ are the zeroth and first order spherical Bessel's functions, respectively. The geometry of the wave scattering in (x', y', z') coordinates is general because of the symmetrical property of the spherical water bubble.

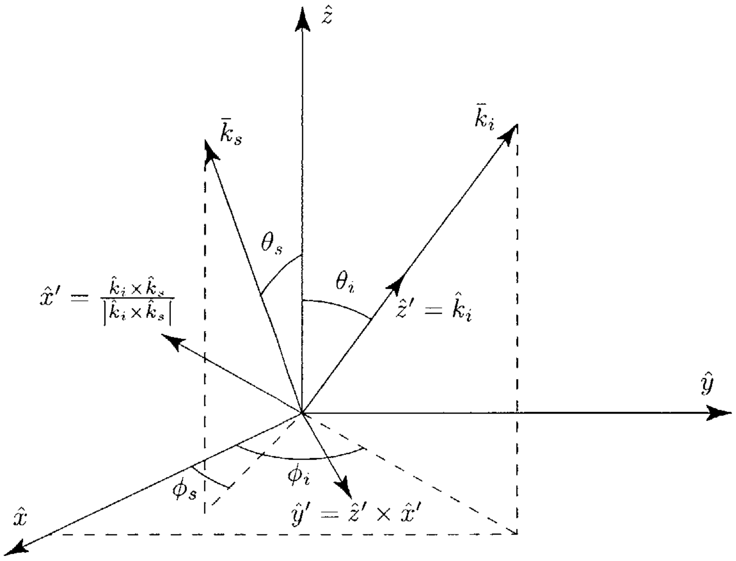

Figure D-2: The transformation of coordinates.

In the (x, y, z) coordinate system, the incident wave is written as

$$\overline{E}_i = \hat{e}_i E_o e^{i k_i \cdot \bar{r}}, \tag{D.5}$$

where $\hat{e}_i = \hat{v}_i$ or $\hat{h}_i$, $E_{e_i} = E_{v_i}$ or E_{h_i}, and

$$\bar{k}_i = k\hat{k}_i = k\left(\hat{x}\sin\theta_i\cos\phi_i + \hat{y}\sin\theta_i\sin\phi_i + \hat{z}\cos\theta_i\right),$$

and the incident angles θ_i and ϕ_i are with respect to the (x, y, z) coordinates as shown in Fig. (D-2). The polarization vectors are defined as

$$\begin{cases} \hat{v}_i = \hat{h}_i \times \hat{k}_i = \hat{x}\cos\theta_i\cos\phi_i + \hat{y}\cos\theta_i\sin\phi_i - \hat{z}\sin\theta_i \\ \hat{h}_i = \dfrac{\hat{z}\times\hat{k}_i}{\left|\hat{z}\times\hat{k}_i\right|} = -\hat{x}\sin\phi_i + \hat{y}\cos\phi_i. \end{cases} \tag{D.6}$$

In the (x, y, z) coordinate system, we set up the coordinates (x', y', z') so that

$$\begin{cases} \hat{x}' = \dfrac{\hat{k}_i \times \hat{k}_s}{\left|\hat{k}_i \times \hat{k}_s\right|} \\ \hat{y}' = \dfrac{\hat{k}_i \times \hat{k}_i \times \hat{k}_s}{\left|\hat{k}_i \times \hat{k}_i \times \hat{k}_s\right|} = \dfrac{\hat{k}_i\left(\hat{k}_i \cdot \hat{k}_s\right) - \hat{k}_s}{\left|\hat{k}_i\left(\hat{k}_i \cdot \hat{k}_s\right) - \hat{k}_s\right|} \\ \hat{z}' = \hat{k}_i, \end{cases} \tag{D.7}$$

where

$$\hat{k}_s = \hat{x}\sin\theta_s\cos\phi_s + \hat{y}\sin\theta_s\sin\phi_s + \hat{z}\cos\theta_s$$

is the wave vector of the scattered field. Therefore the transformation relation of the two coordinate systems is

$$\begin{cases} \hat{x}' = \hat{x}a_{11} + \hat{y}a_{12} + \hat{z}a_{13} \\ \hat{y}' = \hat{x}a_{21} + \hat{y}a_{22} + \hat{z}a_{23} \\ \hat{z}' = \hat{x}a_{31} + \hat{y}a_{32} + \hat{z}a_{33} \end{cases} \tag{D.8}$$

or

$$\begin{bmatrix} \hat{x}' \\ \hat{y}' \\ \hat{z}' \end{bmatrix} = \overline{\overline{A}} \begin{bmatrix} \hat{x} \\ \hat{y} \\ \hat{z} \end{bmatrix} \tag{D.9}$$

where

$$\begin{cases} a_{11} = \begin{vmatrix} a_{22} & a_{23} \\ a_{32} & a_{33} \end{vmatrix} \\ a_{12} = \begin{vmatrix} a_{31} & a_{33} \\ a_{21} & a_{23} \end{vmatrix} \\ a_{13} = \begin{vmatrix} a_{21} & a_{31} \\ a_{22} & a_{32} \end{vmatrix} \end{cases} \tag{D.10}$$

$$\begin{cases} a_{21} = \dfrac{A_{21}}{\sqrt{A_{21}^2 + A_{22}^2 + A_{23}^2}} \\ a_{22} = \dfrac{A_{22}}{\sqrt{A_{21}^2 + A_{22}^2 + A_{23}^2}} \\ a_{23} = \dfrac{A_{23}}{\sqrt{A_{21}^2 + A_{22}^2 + A_{23}^2}}, \end{cases} \tag{D.11}$$

$$\begin{cases} a_{31} = \sin\theta_i \cos\phi_i \\ a_{32} = \sin\theta_i \sin\phi_i \\ a_{33} = \cos\theta_i \end{cases} \tag{D.12}$$

$$\begin{cases} A = \sin\theta_i \sin\theta_s \cos(\phi_i - \phi_s) + \cos\theta_i \cos\theta_s \\ A_{21} = A \sin\theta_i \cos\phi_i - \sin\theta_s \cos\phi_s \\ A_{22} = A \sin\theta_i \sin\phi_i - \sin\theta_s \sin\phi_s \\ A_{23} = A\cos\theta_i - \cos\theta_s. \end{cases} \tag{D.13}$$

By using the identity $\overline{\overline{A}}^{-1} = \overline{\overline{A}}^{T}$, the transformation of a vector from one coordinate system to another can the expressed as

$$\overline{E}' = E'^{T} \begin{bmatrix} \hat{x}' \\ \hat{y}' \\ \hat{z}' \end{bmatrix} = E'^{T}\overline{\overline{A}} \begin{bmatrix} \hat{x} \\ \hat{y} \\ \hat{z} \end{bmatrix} \equiv \overline{E}. \tag{D.14}$$

Thus $E = \overline{\overline{A}}^{T} E'$ and $E' = \overline{\overline{A}} E$.

By writing the incident field in (x, y, z) coordinates as

$$\overline{E}_i = \hat{e}_i E_o e^{i\bar{k}_i \cdot \bar{r}} = E_o \left[(\hat{e}_i \cdot \hat{x})\,\hat{x} + (\hat{e}_i \cdot \hat{y})\,\hat{y} + (\hat{e}_i \cdot \hat{z})\,\hat{z} \right] e^{i\bar{k}_i \cdot \bar{r}}, \tag{D.15}$$

thus the transformation of the incident field is

$$\overline{E}_i' = \begin{bmatrix} E_{x'}^i \\ E_{y'}^i \\ E_{z'}^i \end{bmatrix} = \overline{\overline{A}} \begin{bmatrix} (\hat{e}_i \cdot \hat{x}) \\ (\hat{e}_i \cdot \hat{y}) \\ (\hat{e}_i \cdot \hat{z}) \end{bmatrix} E_o = \begin{bmatrix} a_{11} & a_{12} & a_{13} \\ a_{21} & a_{22} & a_{23} \\ a_{31} & a_{32} & a_{33} \end{bmatrix} \begin{bmatrix} (\hat{e}_i \cdot \hat{x}) \\ (\hat{e}_i \cdot \hat{y}) \\ (\hat{e}_i \cdot \hat{z}) \end{bmatrix} E_o, \tag{D.16}$$

we can calculate the polarization angle β and scattering angle θ' in the (x', y', z') coordinates as follows:

$$\beta = \cos^{-1} \frac{\overline{E}_i' \cdot \hat{y}'}{\left|\overline{E}_i'\right|} = \cos^{-1} \frac{b_2}{C}, \tag{D.17}$$

$$\theta' = \cos^{-1} \hat{k}_s \cdot \hat{z}' = \cos^{-1} \left[\sin\theta_i \sin\theta_s \cos(\phi_s - \phi_i) + \cos\theta_i \cos\theta_s\right], \tag{D.18}$$

where

$$\begin{aligned} b_1 &= a_{11}(\hat{e}_i \cdot \hat{x}) + a_{12}(\hat{e}_i \cdot \hat{y}) + a_{13}(\hat{e}_i \cdot \hat{z}), && \text{(D.19)} \\ b_2 &= a_{21}(\hat{e}_i \cdot \hat{x}) + a_{22}(\hat{e}_i \cdot \hat{y}) + a_{23}(\hat{e}_i \cdot \hat{z}), && \text{(D.20)} \\ b_3 &= a_{31}(\hat{e}_i \cdot \hat{x}) + a_{32}(\hat{e}_i \cdot \hat{y}) + a_{33}(\hat{e}_i \cdot \hat{z}), && \text{(D.21)} \\ C &= \sqrt{b_1^2 + b_2^2 + b_3^2}. && \text{(D.22)} \end{aligned}$$

In the (x', y', z') coordinate system, we write the scattered field as

$$\begin{aligned} \overline{E}_s' &= E_{\theta'}\hat{\theta}' + E_{\phi'}\hat{\phi}' = E_{\theta'}(\hat{y}'\cos\theta' - \hat{z}'\sin\theta') - E_{\phi'}\hat{x}' \\ &= \begin{bmatrix} -E_{\phi'} \\ E_{\theta'}\cos\theta' \\ -E_{\theta'}\sin\theta' \end{bmatrix}, \end{aligned} \tag{D.23}$$

where, by droping out the factor $\dfrac{e^{ikr}}{r}$ for scattering coefficient calculation,

$$\begin{aligned} E_{\phi'} &= \frac{i}{k} S_1 \cos\beta, && \text{(D.24)} \\ E_{\theta'} &= -\frac{i}{k} S_2 \sin\beta. && \text{(D.25)} \end{aligned}$$

The scattered field in the (x, y, z) coordinate system is thus

$$\begin{aligned}\overline{E}_s &= \overline{\overline{A}}^T \overline{E}'_s = \begin{bmatrix} a_{11} & a_{21} & a_{31} \\ a_{12} & a_{22} & a_{32} \\ a_{13} & a_{23} & a_{33} \end{bmatrix} \begin{bmatrix} -E_{\phi'} \\ E_{\theta'}\cos\theta' \\ -E_{\theta'}\sin\theta' \end{bmatrix} \\ &= \begin{bmatrix} -E_{\phi'}a_{11} + E_{\theta'}\cos\theta' a_{21} - E_{\theta'}\sin\theta' a_{31} \\ -E_{\phi'}a_{12} + E_{\theta'}\cos\theta' a_{22} - E_{\theta'}\sin\theta' a_{32} \\ -E_{\phi'}a_{13} + E_{\theta'}\cos\theta' a_{23} - E_{\theta'}\sin\theta' a_{33} \end{bmatrix}. \end{aligned} \tag{D.26}$$

By writing the polarization vectors of the scattered field as

$$\begin{cases} \hat{v}_s = \hat{h}_s \times \hat{k}_s = \hat{x}\cos\theta_s\cos\phi_s + \hat{y}\cos\theta_s\sin\phi_s - \hat{z}\sin\theta_s \\ \hat{h}_s = \dfrac{\hat{z}\times\hat{k}_s}{\left|\hat{z}\times\hat{k}_s\right|} = -\hat{x}\sin\phi_s + \hat{y}\cos\phi_s, \end{cases} \tag{D.27}$$

the v and h-components are obtained as follows:

$$\begin{aligned} E_v^s &= \overline{E}_s \cdot \hat{v}_s = (-E_{\phi'}a_{11} + E_{\theta'}\cos\theta' a_{21} - E_{\theta'}\sin\theta' a_{31})\cos\theta_s\cos\phi_s \\ &\quad + (-E_{\phi'}a_{12} + E_{\theta'}\cos\theta' a_{22} - E_{\theta'}\sin\theta' a_{32})\cos\theta_s\sin\phi_s \\ &\quad + (E_{\phi'}a_{13} - E_{\theta'}\cos\theta' a_{23} + E_{\theta'}\sin\theta' a_{33})\sin\theta_s, \end{aligned} \tag{D.28}$$

$$\begin{aligned} E_h^s &= \overline{E}_s \cdot \hat{h}_s = (E_{\phi'}a_{11} - E_{\theta'}\cos\theta' a_{21} + E_{\theta'}\sin\theta' a_{31})\sin\phi_s \\ &\quad - (E_{\phi'}a_{12} - E_{\theta'}\cos\theta' a_{22} + E_{\theta'}\sin\theta' a_{32})\cos\phi_s. \end{aligned} \tag{D.29}$$

Therefore the scattering coefficients are $f_{vv} = E_v^s$, $f_{hv} = E_h^s$ for $\hat{e}_i = \hat{v}_i$ and $E_o = 1$; $f_{vh} = E_v^s$, $f_{hh} = E_h^s$ for $\hat{e}_i = \hat{h}_i$ and $E_o = 1$. Define the matrix

$$\overline{\overline{L}}(\theta_s, \phi_s; \theta_i, \phi_i) = \begin{bmatrix} |f_{vv}|^2 & |f_{vh}|^2 & \mathrm{Re}(f_{vv}f_{vh}^*) & -\mathrm{Im}(f_{vv}f_{vh}^*) \\ |f_{hv}|^2 & |f_{hh}|^2 & \mathrm{Re}(f_{hv}f_{hh}^*) & -\mathrm{Im}(f_{hv}f_{hh}^*) \\ 2\mathrm{Re}(f_{vv}f_{hv}^*) & 2\mathrm{Re}(f_{vh}f_{hh}^*) & \mathrm{Re}(f_{vv}f_{hh}^* + f_{vh}f_{hv}^*) & -\mathrm{Im}(f_{vv}f_{hh}^* - f_{vh}f_{hv}^*) \\ 2\mathrm{Im}(f_{vv}f_{hv}^*) & 2\mathrm{Im}(f_{vh}f_{hh}^*) & \mathrm{Im}(f_{vv}f_{hh}^* + f_{vh}f_{hv}^*) & \mathrm{Re}(f_{vv}f_{hh}^* - f_{vh}f_{hv}^*) \end{bmatrix}, \tag{D.30}$$

the phase matrix can be calculated as

$$\overline{\overline{P}}(\theta_s, \phi_s; \theta_i, \phi_i) = n_o \overline{\overline{L}}(\theta_s, \phi_s; \theta_i, \phi_i), \tag{D.31}$$

where n_o is the number of bubbles per unit volume.

The extinction coefficient is derived as following [81, page 147]:

$$\begin{aligned} \kappa_e &= n_o \frac{4\pi}{k} \mathrm{Im}\left\{ f_{vv}(\theta_i, \phi_i; \theta_i, \phi_i) \right\} = -n_o \frac{4\pi}{k^2} \mathrm{Im}\left\{ iS_1 \right\} \\ &= n_o \frac{4\pi}{k^2} \mathrm{Im}\left\{ \delta(m^2 - 1)\alpha^2 \left[j_o(x) - \frac{m^2 - 1}{m^2} \frac{j_1(x)}{x} \right]_{x \to 0} \right\} \\ &= n_o \frac{4\pi}{k^2} \delta\alpha^2 \mathrm{Im}\left\{ (m^2 - 1) \left(\frac{2m^2 + 1}{3m^2} \right) \right\}. \end{aligned} \tag{D.32}$$

The absorption coefficient is

$$\kappa_s = n_o \int d\Omega_s \left[\left| f_{vv}(\theta_s, \phi_s; \theta_i, \phi_i) \right|^2 + \left| f_{hv}(\theta_s, \phi_s; \theta_i, \phi_i) \right|^2 \right], \tag{D.33}$$

which can be evaluated numerically. Due to the symmetry property of the bubble, κ_s is independent on the angles θ_i and ϕ_i. The absorption coefficient is calculated as

$$\kappa_a = \kappa_e - \kappa_s. \tag{D.34}$$

Appendix E

The Parameters in the Millimeter-Wave Propagation Model

The parameters used in the MPM [54] are as follows:

Barometric pressure

$$P = p + e, \tag{E.1}$$

where p is dry air pressure and e is partial water vapor pressure. The unit of the barometric pressure is kPa.

Temperature

$$T = 300/t, \tag{E.2}$$

where the unit of the temperature is Kelvin (K), and t is the inverse temperature parameter. The typical temperature profile is given in [55] and plotted in Fig. (5-4).

Relative humidity

$$RH = \frac{e}{e_s} \times 100 = 41.51 \frac{e}{t^5} \times 10^{\frac{9.834}{t^{10}}}, \tag{E.3}$$

where e_s is the saturation pressure over liquid phase.

Dry air and vapor densities

$$\begin{aligned} u &= 11.612pt, \\ v &= 7.217et, \end{aligned} \tag{E.4}$$

where the unit of the densities is g/m^3.

Complex refractivity

$$N = N_0 + N'(f) + iN''(f), \tag{E.5}$$

where N_0, $N'(f)$ and $N''(f)$ are real and called the frequency-independent term, refractive dispersion and absorption, respectively. f is frequency in gigahertz (GHz).

Frequency-independent term

$$N_0 = (2.588p + 2.39e)t + N_v, \tag{E.6}$$

where $N_v = 41.6et^2$ is the contribution from the rotational spectrum of water vapor.

Dispersion term

$$N'(f) = \sum_{i=1}^{n_a} (S_a F'_a)_i + N'_p + \sum_{i=1}^{n_b} (S_b F'_b)_i + N'_e + N'_w, \tag{E.7}$$

Absorption term

$$N''(f) = \sum_{i=1}^{n_a} (S_a F''_a)_i + N''_p + \sum_{i=1}^{n_b} (S_b F''_b)_i + N''_e + N''_w, \tag{E.8}$$

where $S_a = a_1 p t^3 e^{a_2(1-t)}$ and $S_b = b_1 e t^{3.5} e^{b_2(1-t)}$ are the line strength in kilohertz for oxygen and water, respectively. F'_a and F'_b are the real parts of a line shape function in GHz^{-1} which can be written explicitly as

$$F'_\alpha(f) = \frac{Z_\alpha - f}{X_\alpha} + \frac{Z_\alpha + f}{Y_\alpha} - \frac{2}{v_{\alpha o}} + \delta_\alpha \left(\frac{1}{X_\alpha} - \frac{1}{Y_\alpha}\right) \frac{\gamma_\alpha f}{v_{\alpha o}}, \tag{E.9}$$

$$F''_\alpha(f) = -\delta_\alpha \left[\frac{v_{\alpha o}-f}{X_\alpha} + \frac{v_{\alpha o}+f}{Y_\alpha}\right]\frac{f}{v_{\alpha o}} + \left(\frac{1}{X_\alpha}+\frac{1}{Y_\alpha}\right)\frac{\gamma_\alpha f}{v_{\alpha o}}, \tag{E.10}$$

where $\alpha = a, b$, and

$$\begin{aligned}
X_\alpha &= (v_{\alpha o} - f)^2 + \gamma_\alpha^2, \\
Y_\alpha &= (v_{\alpha o} + f)^2 + \gamma_\alpha^2, \\
Z_\alpha &= \left(v_{\alpha o}^2 + \gamma_\alpha^2\right)\big/ v_{\alpha o}, \\
\gamma_a &= a_3\left(pt^{0.8-a_4} + 1.1et\right), \\
\gamma_b &= b_3\left(pt^{0.8} + 4.8et\right), \\
\delta_a &= a_5 pt^{a_6}, \\
\delta_b &= 0.
\end{aligned}$$

In the above expressions, v_{oa} and a_i $(i = 1, 2, \cdots, 6)$ are oxygen line parameters, v_{ob}, and b_i $(i = 1, 2, 3)$ are water vapor line parameters.

Dry air continuum

$$N'_p(f) = a_0\left\{\left[1 + (f/\gamma_0)^2\right]^{-1} - 1\right\} pt^2, \tag{E.11}$$

$$N''_p(f) = \left\{2a_0\left[\gamma_0\left(1 + (f/\gamma_0)^2\right)\left(1 + (f/60)^2\right)\right]^{-1} + a_p pt^{2.5}\right\} fpt^2, \tag{E.12}$$

where $a_0 = 3.07 \times 10^{-4}$, $a_p = 1.40\left(1 - 1.2f^{1.5}10^{-5}\right)10^{-10}$, and $\gamma_0 = 5.6 \times 10^{-3}(p + 1.1e)t^{0.8}$ GHz.

Water vapor continuum

$$N'_e(f) = b_0 f^{2.05} et^{2.4}, \tag{E.13}$$

$$N''_e(f) = \left(b_f p + b_e et^3\right) fet^{2.5}, \tag{E.14}$$

where $b_0 = 6.47 \times 10^{-6}$, $b_f = 1.40 \times 10^{-6}$ and $b_e = 5.41 \times 10^{-5}$.

Hydrosol continuum

$$N'_w(f) = 2.4 \times 10^{-3} w\epsilon', \tag{E.15}$$

$$N_w''(f) = 4.50w/\epsilon''(1+\eta^2), \tag{E.16}$$

where $\eta = (2+\epsilon')/\epsilon''$ and $\tau = 4.17 \times 10^{-5} t e^{(7.13t)}$ ns. ϵ' and ϵ'' are the real and imaginary parts of the dielectric constant of water. They can be calculated using the following empirical formulas

$$\epsilon' = 4.9 + \frac{185 - 113/t}{1+(f\tau)^2}, \tag{E.17}$$

$$\epsilon'' = \frac{(185 - 113/t)\, f\tau}{1+(f\tau)^2}. \tag{E.18}$$

Bibliography

[1] T. Dogaru, L. Carlin, B. L. Merchant, and C. F. Lee, "Electromagnetic scattering and detection of mines near a rough air-ground interface," *Proc. SPIE - Int. Soc. Opt. Eng. (USA)*, vol. 3079, pp. 704–715, Apr. 1997.

[2] Y. He, T. Uno, and S. Adachi, "Reconstruction of underground objects by imaging the secondary currents," *IEEE Antennas and Propagat. Soc. Int'l Symp.*, vol. 2, pp. 261–264, Sep. 1996.

[3] J. S. Kang and W. C. Chew, "Time-domain distorted Born iterative method for imaging buried dielectric cylinder in underground lossy media," *IEEE Antennas and Propagat. Soc. Int'l Symp.*, vol. 3, pp. 2156–2159, 1996.

[4] R. W. Moses, R. E. Kelly, and J. M. Mack, "Modeling the electromagnetic detection of buried cylindrical conductors," *Int'l Geosci. Remote Sensing Symp. (IGARSS)*, vol. 4, pp. 1938–1940, May 1996.

[5] K. Zhu, "Analysis of response of the electromagnetic induction for detecting of buried objects," *Int'l Geosci. Remote Sensing Symp. (IGARSS)*, vol. 4, pp. 2041–2043, May 1996.

[6] D. J. Daniels, "Surface-penetrating radar," *Electron. Comm. Eng. J.*, vol. 8, no. 4, pp. 165–182, Aug. 1996.

[7] K. O'Neill, R. F. Lussky, Jr., and K. D. Paulsen, "Scattering from a metallic object embedded near the randomly rough surface of a lossy dielectric," *IEEE Trans. Geosci. Remote Sensing*, vol. 34, no. 2, pp. 367–376, Mar. 1996.

[8] J. M. Bourgeois and G. S. Smith, "A full electromagnetic simulation of a ground penetrating radar: theory and experiment," *IEEE Antennas and Propagat. Soc. Int'l Symp.*, vol. 3, pp. 1442–1445, June 1994.

[9] A. Helaly, A. Sebak, and L. Shafai, "Scattering by a buried conducting object of general shape at low frequencies," *IEE Proc. H (Microwaves, Antennas and Propagat.)*, vol. 138, no. 3, pp. 213–218, June 1991.

[10] K. Tajima and S. I. Iiguchi, "Analysis of electromagnetic wave scattered from cylinders buried in the ground," *Electron. Comm. Japan: Part 1 (Communications)*, vol. 70, no. 5, pp. 86–94, May 1987.

[11] P. G. Cottis and J. D. Kanellopoulos, "Scattering from a conducting cylinder above a lossy medium," *Int'l J. Electron.*, vol. 65, no. 5, pp. 1031–1038, Nov. 1988.

[12] J. R. Barnum, "Ship detection with high-resolution HF skywave radar," *IEEE J. Oceanic Eng.*, vol. OE-11, no. 2, pp. 196–209, 1986.

[13] J. H. Richmond, "A wire-grid model for scattering by conducting bodies," *IEEE Trans. Antennas Propagat.*, vol. AP-14, no. 6, pp. 782–786, Nov. 1966.

[14] E. K. Miller and F. J. Deadrick, "Some computational aspects of thin-wire modeling," in *Numerical and Asymptotic Techniques in Electromagnetics*, R. Mittra, Ed. Springer-Verlag, New York, 1975.

[15] K. S. H. Lee, L. Marin, and J. P. Castillo, "Limitations of wire-grid modeling of a closed surface," *IEEE Trans. Electromagn. Compat.*, vol. EMC-18, no. 3, pp. 123–129, Aug. 1976.

[16] D. L. Knepp and J. Goldhirsh, "Numerical analysis of electromagnetic radiation properties of smooth conducting bodies of arbitrary shape," *IEEE Trans. Antennas Propagat.*, vol. AP-20, no. 3, pp. 383–388, May 1972.

[17] N. C. Albertsen, J. E. Hansen, and N. E. Jensen, "Computation of radiation from wire antennas on conducting bodies," *IEEE Trans. Antennas Propagat.*, vol. AP-22, no. 2, pp. 200–206, Mar. 1974.

[18] N. N. Wang, J. H. Richmond, and M. C. Gilreath, "Sinusoidal reaction formulation for radiation and scattering from conducting surfaces," *IEEE Trans. Antennas Propagat.*, vol. AP-23, no. 3, pp. 376–382, May 1975.

[19] E. H. Newman and D. M. Pozar, "Electromagnetic modeling of composite wire and surface geometries," *IEEE Trans. Antennas Propagat.*, vol. AP-26, no. 6, pp. 784–789, Nov. 1978.

[20] A. Sankar and T. C. Tong, "Current computation on complex structures by finite element method," *Electron. Lett.*, vol. 11, no. 20, pp. 481–482, Oct. 1975.

[21] J. J. H. Wang, "Numerical analysis of three-dimensional arbitrarily-shaped conducting scatterers by trilateral surface cell modeling," *Radio Sci.*, vol. 13, no. 6, pp. 947–952, Nov.–Dec 1978.

[22] J. Singh and A. T. Adams, "A non-rectangular patch model for scattering from surfaces," *IEEE Trans. Antennas Propagat.*, vol. AP-27, no. 4, pp. 531–535, July 1979.

[23] S. M. Rao, D. R. Wilton, and A. W. Glisson, "Electromagnetic scattering by surfaces of arbitrary shape," *IEEE Trans. Antennas Propagat.*, vol. AP-30, no. 3, pp. 409–418, May 1982.

[24] C. M. Butler, "Current induced on a conducting strip which resides on the planar interface between two semi-infinite half-spaces," *IEEE Trans. Antennas Propagat.*, vol. AP-32, no. 3, pp. 226–231, Mar. 1984.

[25] C. M. Butler, X. B. Xu, and A. W. Glisson, "Current induced on a conducting cylinder located near the planar interface between two semi-infinite half-spaces," *IEEE Trans. Antennas Propagat.*, vol. AP-33, no. 6, pp. 616–624, June 1985.

[26] X. B. Xu and C. M. Butler, "Current induced by TE excitation on a conducting cylinder located near the planar interface between two semi-infinite half-spaces," *IEEE Trans. Antennas Propagat.*, vol. AP-34, no. 7, pp. 880–890, July 1986.

[27] X. B. Xu and C. M. Butler, "Scattering of TM excitation by coupled and partially buried cylinders at the interface between two media," *IEEE Trans. Antennas Propagat.*, vol. AP-35, no. 5, pp. 529–538, May 1987.

[28] K. A. Michalski and D. Zheng, "Electromagnetic scattering and radiation by surfaces of arbitrary shape in layered media, part I: Theory," *IEEE Trans. Antennas Propagat.*, vol. AP-38, pp. 335–344, Mar. 1990.

[29] K. A. Michalski and D. Zheng, "Electromagnetic scattering and radiation by surfaces of arbitrary shape in layered media, part II: Implementation and results for contiguous half-spaces," *IEEE Trans. Antennas Propagat.*, vol. AP-38, pp. 345–352, Mar. 1990.

[30] S. F. Mahmoud, S. M. Ali, and J. R. Wait, "Electromagnetic scattering from a buried cylindrical inhomogeneity inside a lossy earth," *Radio Sci.*, vol. 16, no. 6, pp. 1285–1298, Nov.–Dec 1981.

[31] A. Q. Howard, "The electromagnetic fields of a subterranean cylindrical inhomogeneity excited by a line source," *Geophysics*, vol. 37, no. 6, pp. 975–984, Dec. 1972.

[32] J. R. Parry and S. H. Ward, "Electromagnetic scattering from cylinders of arbitrary cross-section in a conductive half-space," *Geophysics*, vol. 36, no. 1, pp. 67–100, Feb. 1971.

[33] C. N. Vazouras, P. G. Cottis, and J. D. Kanellopoulos, "Scattering from a conducting cylinder above a lossy medium of sinusoidal interface," *Radio Sci.*, vol. 27, no. 6, pp. 883–892, Nov.–Dec. 1992.

[34] L. Tsang, G. Zhang, and K. Pak, "Detection of a buried object under a single random rough surface with angular correlation function in EM wave scattering," *Microwave Opt. Technol. Lett.*, vol. 11, no. 6, pp. 300–304, Apr. 1996.

[35] J. Ripoll, A. Madrazo, and M. Nieto-Vesperinas, "Scattering of electromagnetic waves from a body over a random rough surface," *Opt. Commun.*, vol. 142, no. 4–6, pp. 173–178, Oct. 1997.

[36] T. Dogaru and L. Carin, "Time-domain sensing of targets buried under a rough air-ground interface," *IEEE Trans. Antennas Propagat.*, vol. AP-46, no. 3, pp. 360–372, Mar. 1998.

[37] S. Tjuatja, Zhi-Jian Li, A. K. Fung, and C. Terre, "Numerical simulation of scattering from object embedded in a medium with randomly rough boundary," *Int'l Geosci. Remote Sensing Symp. (IGARSS)*, vol. 1, pp. 772 774, May 1996.

[38] M. Saillard and G. Toso, "Electromagnetic scattering from bounded or infinite subsurface bodies," *Radio Sci.*, vol. 32, no. 4, pp. 1347–1359, July–Aug. 1997.

[39] L. Tsang, "Polarimetric passive microwave remote sensing of random discrete scatterers and rough surfaces," *J. Electromagnetic Waves and Applications*, vol. 5, no. 1, pp. 41–57, 1991.

[40] S. H. Yueh, R. Kwok, F. K. Li, S. V. Nghiem, and W. J. Wilson, "Polarimetric passive remote sensing of ocean wind vectors," *Radio Sci.*, vol. 29, no. 4, pp. 799–814, July–Aug. 1994.

[41] S. H. Yueh, S. V. Nghiem, R. Kwok, W. J. Wilson, F. K. Li, J. T. Johnson, and J. A. Kong, "Polarimetric thermal emission from periodic water surface," *Radio Sci.*, vol. 29, no. 1, pp. 87–96, Jan.–Feb. 1994.

[42] G. F. Williams, "Microwave radiometry of the ocean and the possibility of marine wind velocity determination from satellite observations," *J. Geophys. Res.*, vol. 74, no. 18, pp. 4591–4594, Aug. 1969.

[43] G. F. Williams, "Microwave emissivity measurements of bubbles and foam," *IEEE Trans. Geosci. Electron.*, vol. GE-9, no. 4, pp. 221–224, Oct. 1971.

[44] P. M. Smith, "The emissivity of sea foam at 19 and 37 GHz," *IEEE Trans. Geosci. Remote Sensing*, vol. 26, no. 5, pp. 541–547, Sep. 1988.

[45] A. Stogryn, "The emissivity of sea foam at microwave frequencies," *J. Geophys. Res.*, vol. 77, no. 9, pp. 1658–1666, Mar. 1972.

[46] P. C. Pandey and R. K. Kakar, "An empirical microwave emissivity model for a foam-covered sea," *IEEE J. Oceanic Eng.*, vol. OE-7, no. 3, pp. 135–140, July 1982.

[47] J. D. Droppleman, "Apparent microwave emissivity of sea foam," *J. Geophys. Res.*, vol. 75, no. 3, pp. 696–698, Jan. 1970.

[48] P. W. Rosenkranz and D. H. Staelin, "Microwave emissivity of ocean foam and its effect on nadiral radiometric measurements," *J. Geophys. Res.*, vol. 77, no. 33, pp. 6528–6538, Nov. 1972.

[49] S. H. Yueh, W. J. Wilson, F. K. Li, S. V. Nghiem, and W. B. Ricketts, "Polarimetric measurements of sea surface brightness temperatures using an aircraft

K-band radiometer," *IEEE Trans. Geosci. Remote Sensing*, vol. 33, no. 1, pp. 85–92, Jan. 1995.

[50] I. Kay, "The inverse scattering problem when the reflection coefficient is a rational function," *Comm. Pure and Appl. Math.*, vol. 13, pp. 371–393, 1960.

[51] A. K. Jordan and H. N. Kritikos, "An application of one-dimensional inverse-scattering theory for inhomogeneous regions," *IEEE Trans. Antennas Propagat.*, vol. AP-21, no. 6, pp. 909–911, Nov. 1973.

[52] D. B. Ge, A. K. Jordan, and L. S. Tamil, "Numerical inverse scattering theory for the design of planar optical waveguides," *J. Opt. Soc. Am. A*, vol. 11, no. 11, pp. 2809–2815, Nov. 1994.

[53] Y. Zhang, J. A. Kong, and A. K. Jordan, "Numerical solution of the Gel'fand-Levitan-Marchenko integral equation for electromagnetic inverse scattering theory using matrix inversion," *Microwave Opt. Technol. Lett.*, vol. 15, no. 5, pp. 277–278, Aug. 1997.

[54] H. J. Liebe, "An updated model for millimeter wave propagation in moist air," *Radio Sci.*, vol. 20, no. 5, pp. 1069–1089, Sep.–Oct. 1985.

[55] *U.S. Standard Atmosphere*, National Oceanic and Atmospheric Administration, National Aeronautics and Space Administration, United States Air Force, 1976.

[56] D. B. Ge, L. S. Tamil, and A. K. Jordan, "Profile reconstruction for planar dielectric waveguide by using underrelaxed iterative method," *Acta Photonica Sinica*, vol. 25, no. 5, pp. 439–445, May 1996.

[57] J. R. Mautz and R. F. Harrington, "Radiation and scattering from bodies of revolution," *Applied Scientific Research*, vol. 20, no. 6, pp. 405–435, June 1969.

[58] J. R. Mautz and R. F. Harrington, "Generalized network parameters, radiation and scattering by conducting bodies of revolution," *IEEE Trans. Antennas Propagat.*, vol. AP-22, no. 4, pp. 630–631, July 1974.

[59] J. R. Mautz and R. F. Harrington, "A combined-source solution for radiation and scattering from a perfectly conducting body," *IEEE Trans. Antennas Propagat.*, vol. AP-27, no. 4, pp. 445–454, July 1979.

[60] J. R. Mautz and R. F. Harrington, "Electromagnetic coupling to a conducting body of revolution with a homogeneous material region," *Electromagnetics*, vol. 2, no. 4, pp. 257–308, Oct.–Dec. 1982.

[61] D. B. Davidson and D. A. McNamara, "Moment method formulation for asymmetrically excited conducting bodies of revolution," *Electron. Lett.*, vol. 24, no. 20, pp. 1280–1282, Sep. 1988.

[62] S. D. Gedney and R. Mittra, "The use of the FFT for the efficient solution of the problem of electromagnetic scattering by a body of revolution," *IEEE Trans. Antennas Propagat.*, vol. AP-38, no. 3, pp. 313–322, Mar. 1990.

[63] D. R. Wilton and R. Mittra, "A new numerical approach to the calculation of electromagnetic scattering properties of two-dimensional bodies of arbitrary cross section," *IEEE Trans. Antennas Propagat.*, vol. AP-20, no. 3, pp. 310–317, May 1972.

[64] J. J. H. Wang and C. Papanicolopulos, "Surface-patch modelling of scatterers of arbitrary shapes," *IEEE Antennas and Propagat. Soc. Int'l Symp.*, pp. 159–162, 1979.

[65] J. A. Kong, *Electromagnetic Wave Theory*, Wiley, New York, 2nd edition, 1990.

[66] J. Van Bladel, *Electromagnetic Fields*, McGraw-Hill, New York, 1964.

[67] A. W. Glisson, *On the Development of Numerical Techniques for Treating Arbitrarily-Shaped Surfaces*, Ph.D. thesis, University of Mississippi, 1978.

[68] G. Videen, "Light scattering from a sphere on or near a surface," *J. Opt. Soc. Am. A*, vol. 8, no. 3, pp. 483–489, Mar. 1991.

[69] G. Videen, "Light scattering from a sphere on or near a surface: errata," *J. Opt. Soc. Am. A*, vol. 9, no. 5, pp. 844–845, May 1992.

[70] G. Videen, "Light scattering from a particle on or near a perfectly conducting surface," *Opt. Commun.*, vol. 115, pp. 1–7, Mar. 1995.

[71] T. J. Cui, W. Wiesbeck, and A. Herschlein, "Electromagnetic scattering by multiple three-dimensional scatterers buried under multilayered media. I. Theory," *IEEE Trans. Geosci. Remote Sensing*, vol. 36, no. 2, pp. 526–534, Mar. 1998.

[72] T. J. Cui, W. Wiesbeck, and A. Herschlein, "Electromagnetic scattering by multiple three-dimensional scatterers buried under multilayered media. II. Numerical," *IEEE Trans. Geosci. Remote Sensing*, vol. 36, no. 2, pp. 535–546, Mar. 1998.

[73] Y. Zhang, Y. E. Yang, H. Braunisch, and J. A. Kong, "Electromagnetic wave interaction of conducting object with rough surface by hybrid SPM/MoM technique," *J. Electromagnetic Waves and Applications*, vol. 13, pp. 983–984, 1999.

[74] Y. Zhang, Y. E. Yang, H. Braunisch, and J. A. Kong, "Electromagnetic wave interaction of conducting object with rough surface by hybrid SPM/MoM technique," in *Progress in Electromagnetics Research (PIER 22)*, J. A. Kong, Ed., pp. 315–335. EMW Publishing, Cambridge, 1999.

[75] S. P. Durden and J. F. Vesecky, "A physical radar cross-section model for a wind-driven sea with swell," *IEEE J. Oceanic Eng.*, vol. OE-10, pp. 445–457, Oct. 1985.

[76] L. Tsang, C. H. Chan, K. Pak, and H. Sangani, "Monte-Carlo simulation of large-scale problems of random rough surface scattering and applications to grazing incidence with the BMIA/canonical grid method," *IEEE Trans. Antennas Propagat.*, vol. AP-43, no. 8, pp. 851–859, Aug. 1995.

[77] J. T. Johnson, J. A. Kong, R. T. Shin, D. H. Staelin, K. O'Neill, and A. W. Lananick, "Third Stokes parameter emission from a periodic water surface," *IEEE Trans. Geosci. Remote Sensing*, vol. 31, no. 5, pp. 1066–1080, Sep. 1993.

[78] J. T. Johnson, J. A. Kong, R. T. Shin, S. H. Yueh, S. V. Nghiem, and R. Kwok, "Polarimetric thermal emission from rough ocean surfaces," *J. Electromagnetic Waves and Applications*, vol. 8, no. 1, pp. 43–59, 1994.

[79] X. Z. Huang and Y. Q. Jin, "Scattering and emission from two-scale randomly rough sea surface with foam scatterers," *IEE Proc. H (Microwaves, Antennas and Propagat.)*, vol. 142, no. 2, pp. 109–114, Apr. 1995.

[80] E. C. Manahan and G. MacNiocaill, *Oceanic Whitecaps and Their Role in Air-Sea Exchange Processes*, D. Reidel Pub. Co., Boston, 1986.

[81] L. Tsang, J. A. Kong, and R. T. Shin, *Theory of Microwave Remote Sensing*, Wiley, New York, 1985.

[82] R. T. Shin and J. A. Kong, "Radiative transfer theory for active remote sensing of two-layer random medium," in *Progress in Electromagnetics Research (PIER 1)*, J. A. Kong, Ed. Elsevier Science, New York, 1989.

[83] S. H. Yueh, "Modeling of wind direction signals in polarimetric sea surface brightness temperature," *IEEE Trans. Geosci. Remote Sensing*, vol. 35, no. 6, pp. 1400–1418, Nov. 1997.

[84] H. J. Liebe, "MPM—an atmospheric millimeter-wave propagation model," *Int'l J. Infr. Millimeter Waves.*, vol. 10, no. 6, pp. 631–650, June 1989.

[85] G. E. Hunt, "A review of computational techniques for analysing the transfer of radiation through a model cloudy atmosphere," *J. Quant. Spectrosc. Radiat. Transfer.*, vol. 11, no. 6, pp. 655–690, June 1971.

[86] G. Brussaard and P. A. Watson, *Atmospheric Modeling and Millimeter Wave Propagation*, Chapman & Hall, 1995.

[87] C. P. Yeang, S. H. Yueh, K. H. Ding, and J. A. Kong, "Atmospheric effect on microwave polarimetric passive remote sensing of ocean surfaces," *Radio Sci.*, vol. 34, no. 2, pp. 521–37, Mar.–April. 1999.

[88] H. L. Chan and A. K. Fung, "A theory of sea scatter at large incident angles," *J. Geophys. Res.*, vol. 82, no. 24, pp. 3439–3444, Aug. 1977.

[89] C. S. Cox and W. H. Munk, "Measurement of the roughness of the sea surface from photographs of the sun glitter," *J. Opt. Soc. Am.*, vol. 44, no. 11, pp. 838–850, 1954.

[90] I. M. Gel'fand and B. M. Levitan, "On the determination of a differential equation from its spectral function," *American Math. Soc. Transl.*, vol. 1, pp. 253–304, 1955.

[91] M. H. Reilly and A. K. Jordan, "The applicability of an inverse method for reconstruction of electron-density profiles," *IEEE Trans. Antennas Propagat.*, vol. AP-29, no. 2, pp. 245–252, Mar. 1981.

[92] A. K. Jordan and S. Ahn, "Inverse scattering theory and profile reconstruction," *Proc. IEE (London)*, vol. 126, no. 10, pp. 945–950, Oct. 1979.

[93] A. K. Jordan and S. Lakshmanasamy, "Inverse scattering theory applied to the design of single-mode planar optical waveguides," *J. Opt. Soc. Am. A*, vol. 6, no. 8, pp. 1206–1212, Aug. 1989.

[94] S. Lakshmanasamy and A. K. Jordan, "Design of wide-core planar waveguides by an inverse scattering method," *Opt. Lett.*, vol. 14, no. 8, pp. 411–413, Apr. 1989.

[95] L. S. Tamil and A. K. Jordan, "Optical waveguides for imaging applications: design by an inverse scattering approach," *Int'l J. Imag. Sys. Tech.*, vol. 3, no. 1, pp. 18–26, Spring 1991.

[96] L. S. Tamil and A. K. Jordan, "Spectral inverse scattering theory for inhomogeneous dielectric waveguides and devices," *Proc. IEEE*, vol. 79, no. 10, pp. 1519–1528, Oct. 1991.

[97] L. S. Tamil and A. K. Jordan, "An inverse-scattering model for an all-optical logic gate," *J. Appl. Phys.*, vol. 70, no. 3, pp. 1882–1884, Aug. 1991.

[98] A. K. Jordan and L. S. Tamil, "Inverse scattering theory for optical waveguides and devices: synthesis from rational and nonrational reflection coefficients," *Radio Sci.*, vol. 31, no. 6, pp. 1863–1876, Nov.–Dec. 1996.

[99] H. N. Kritikos, D. L. Jaggard, and D. B. Ge, "Numeric reconstruction of smooth dielectric profiles," *Proc. IEEE*, vol. 70, no. 3, pp. 295–297, Mar. 1982.

[100] K. A. Michalski and D. Zheng, "Electromagnetic scattering and radiation by surfaces of arbitrary shape in layered media, part I: Theory," *IEEE Trans. Antennas Propagat.*, vol. AP-38, pp. 335–344, Mar. 1990.

[101] S. R. Aragón and M. Elwenspoek, "Mie scattering from thin spherical bubbles," *J. Chem. Phys.*, vol. 77, no. 7, pp. 3406–3413, Oct. 1982.